London
South Bank
University

EST 1892

HEAT FROM UNDERGROUND ENERGY LONDON (HEAT FUEL)

A thesis submitted in partial fulfilment of the requirements for the degree of Doctor of Philosophy

This research programme was carried out in collaboration with Transport for London

April 2022

Henrique Roscoe Papini Lagoeiro BSc

School of Engineering

London South Bank University

Abstract

Recovering waste heat from urban infrastructures is becoming increasingly important as governments around the world strive to decarbonise heat supply, which remains one of the main challenges in the transition towards net zero. The Bunhill Waste Heat Recovery (WHR) System represents a first-of-its-kind scheme that recovers waste heat from a ventilation shaft of the London Underground (LU) transport network. The system is based upon the installation of a heat recovery heat exchanger that consists of cooling coils and a reversible fan; the coils are connected to a heat pump (HP) that supplies low-carbon thermal energy to a heat network in the London Borough of Islington. One advantage of district-scale HP systems is the possibility of coupling them with thermal energy storage (TES) in order to reduce operating costs while delivering significant carbon savings. Furthermore, depending on the operation of the reversible fan, the WHR system enables the supply of cooled air to the Underground tunnels whilst simultaneously providing heating to the local heat network.

This thesis investigates the potential benefits that could be claimed by recovering waste heat from underground railways (URs), based upon the development of a mathematical model of the WHR system. This WHR model, which was validated with operational data, is able to calculate system performance under different heat source conditions, which vary throughout the year and depend on the operation of the reversible fan. The analysis focused on the influence of condensation and air temperatures on the performance of the WHR system, evaluating how these parameters may affect its efficiency and capacity. In order to fully realise the cooling potential when operating in a bivalent heating/cooling mode (Supply Mode), an investigation was carried out using a numerical model of the local LU environment to assess the impacts of cooling provision in terms of alleviating peak temperatures at nearby stations, with reductions of up to 7.2 K being calculated for adjacent stations in 2030.

The WHR model was also coupled with a techno-economic model of a heat network, which was applied to assess how different volumes of TES could improve the levelised cost of heat (LCH) and carbon abatement costs (CAC) when compared to meeting the same heat demand with communal air-source heat pumps (ASHPs). Results indicate that, if the WHR system operates in Supply Mode for half the year, savings of approximately 9% and 18% could be obtained for the LCH and CAC, respectively, in comparison with ASHPs. The potential for replicating this technology across the UK was also investigated, focusing on the LU and Tyne and Wear Metro networks, with 30 MW being estimated as the recoverable waste heat, which could be reclaimed to provide 351 GWh of thermal energy annually. The different analyses that were carried out indicate the opportunity for waste heat from railway tunnels to become a key resource for decarbonising heat supply in cities with underground transport systems.

Declaration

The research described in this report is the original work of the author except where otherwise specified, or acknowledgement is made by reference.

It was carried out at the School of Engineering, London South Bank University, under the supervision of Dr Akos Revesz, Dr Gareth Davies and Prof. Graeme Maidment. The PhD project was part of the LoT-NET (Low Temperature Heat Recovery and Distribution Network Technologies) research project, funded by the Engineering and Physical Science Research Council (EPSRC) under grant agreement EP/R045496/1.

The work has not been submitted for another degree or award of another academic or professional institution during the research programme.

Henrique Roscoe Papini Lagoeiro

Henrique Roscoe Papini Lagoeiro
London, April 2022

Acknowledgements

Undertaking a PhD has been a challenging yet fulfilling journey, and I am very grateful for the support and guidance I received from many people along the way.

Firstly, I would like to express my gratitude to my supervisors Prof. Graeme Maidment, Dr Gareth Davies and Dr Akos Revesz, who were encouraging, supportive and helpful throughout the project. I would like to thank Graeme particularly for his leadership and trust, which have helped me grow and learn more than I ever expected, and Gareth for providing invaluable support and advice by always sharing his vast knowledge in many of our fruitful discussions. I also thank Akos for always encouraging me to think outside the box without losing sight of the big picture. I am lucky to have had great supervisors who always had an open door and were so actively involved throughout the PhD process.

I am also grateful for the care received from all the staff at LSBU, who made sure I had the best possible experience as a student. I am particularly thankful for the support and advice from my colleagues Dr Catarina Marques, Matt Wegner and Dr Helen Turnell at the Centre for Heating and Cooling Research. I am privileged to have joined such a great team and to have had the opportunity to learn so much in our day-to-day meetings and discussions.

The engagement and assistance provided by the industrial project partner, Transport for London, is also greatly appreciated. I am very grateful to Dan Curry, Gareth Faulks, Josh Vivian and Declan Murphy for attending progress meetings and providing useful guidance and advice throughout the project. I would like to acknowledge the support of Ken Gysin, who taught me so much about the capabilities of SES and the work carried out by the modelling team at TfL. I am also grateful to Islington Council for their support in providing valuable information for this project. A special thanks to Simon Bowles for always being happy to assist and contribute to my research.

I must also thank my friends, in both the UK and Brazil, for their encouragement and for reminding me of the importance of enjoying myself even in the most stressful of times. I would also like to acknowledge how privileged I am for having an amazing family – especially my mum, Maria Angela, and my dad, Leonardo – who were always so present despite being an ocean apart! Their motivation, advice and care have been essential to my personal and professional development. Amo vocês!

Finally, a big thank you goes to my partner Sofia, who has inspired me, helped me grow over the years and kept me going with love and support even through the most challenging times. She has made this journey much more enjoyable, and I must also thank her for all her patience during the PhD – I promise to stop pestering you about heat pumps and waste heat (for) now!

Contents

List of Figures

List of Tables

List of Publications

Journal Publications

Lagoeiro, H., Revesz, A., Davies, G., Maidment, G., Curry, D., Faulks, G. & Murawa, M., 2019. Opportunities for Integrating Underground Railways into Low Carbon Urban Energy Networks: A Review. Applied Sciences 9, 3332.

Lagoeiro, H., Revesz, A., Davies, G., Gysin, K., Curry, D., Faulks, G., Murphy, D., Vivian, J. & Maidment, G., 2021. Investigating the opportunity for cooling the London Underground through waste heat recovery. Building Services Engineering Research and Technology 43, Special Issue: CIBSE Technical Symposium 2021.

Conference Publications

Lagoeiro, H., Revesz, A., Davies, G., Maidment, G., Curry, D., Faulks, G. & Bielicki, J., 2019. Heat from Underground Energy London. CIBSE Technical Symposium, Sheffield, UK.

Lagoeiro, H., Curry, D., Faulks, G., Murawa, M., Revesz, A., Davies, G. & Maidment, G., 2019. Heat Opportunities from Underground Energy in London. 7th DHC+ Student Awards, Euroheat and Power Congress, Nantes, France.

Lagoeiro, H., Curry, D., Faulks, G., Bielicki, J., Revesz, A., Davies, G. & Maidment, G., 2019. Heat from Underground Energy London. The 25th IIR International Congress of Refrigeration, Montréal, Québec, Canada.

Lagoeiro, H., Revesz, A., Davies, G., Curry, D., Faulks, G., Murawa, M. & Maidment, G., 2020. Assessing the Performance of District Heating Networks Utilising Waste Heat: A Review. ASHRAE Winter Conference, Orlando, Florida, USA.

Lagoeiro, H., Revesz, A., Davies, G., Gysin, K., Curry, D., Faulks, G., Murphy, D., Vivian, J. & Maidment, G., 2021. Waste Heat Recovery from Underground Railways – Evaluating the Cooling Potential. CIBSE Technical Symposium, UK.

Lagoeiro, H., Revesz, A., Davies, G., Curry, D., Faulks, G., Murphy, D., Vivian, J. & Maidment, G., 2022. Integrating Waste Heat Recovery from Railway Tunnels into Flexible Heat Networks. ASHRAE Winter Conference, Las Vegas, Nevada, USA.

Lagoeiro, H., Wegner, M., Revesz, A., Davies, G., Curry, D., Vivian, J., Faulks, G., Murphy, D. & Maidment, G., 2022. Recovering Waste Heat from the London Underground: Sizing the Opportunity. World Sustainable Energy Days – Young Energy Researchers Conference, Wels, Austria.

Other Publications

Lagoeiro, H., Dunham, C., Revesz, A., Marques, C. & Maidment, G., 2022. Carbon, Costs and Coefficient of Performance – New Metrics for Heat Pumps. CIBSE Technical Symposium, London, UK.

Marques, C., Tozer, R., Revesz, A., Dunham, C., Jones, P., Matabuena, R., Bond, C., Lagoeiro, H., Wegner, M. & Maidment, G., 2020. GreenSCIES – Green Smart Community Integrated Energy Systems – Integration with Data Centres. Tech talk – Institute of Refrigeration.

Marques, C., Dunham, C., Jones, P., Matabuena, R., Revesz, A., Lagoeiro, H. & Maidment, G., 2021. Integration of High Temperature Heat Networks with Low Carbon Ambient Loop Systems. ASHRAE Winter Conference, USA.

Revesz, A., Lagoeiro, H., Marques, C., Jones, P., Dunham, C. & Maidment, G., 2022. The generation gap! Are 5th generation district energy schemes better or just different? CIBSE Technical Symposium, London, UK.

Nomenclature

Symbols

Symbol	Description	Units
A	Area	m^2
b	Plate channel spacing	mm
Bo	Boiling Number	N/A
C	Specific Heat Capacity	$kJ \cdot kg^{-1} \cdot K^{-1}$
SHR	Sensible Heat Ratio	N/A
D	Depth	m
d	Diameter	mm
E	Energy	kJ
f	Friction factor	N/A
G	Mass flux	$kg \cdot s^{-1} \cdot m^{-2}$
g	Gravitational acceleration	$m \cdot s^{-2}$
Gz	Graetz number	N/A
H	Head loss	m
h	Convective heat transfer coefficient	$W \cdot m^{-2} \cdot K^{-1}$
i	Specific enthalpy	kJ/kg
K	Head loss coefficient	N/A
k	Thermal conductivity	$W \cdot m^{-1} \cdot K^{-1}$
L	Length	m
l	Litres	m^{-3}
Le	Lewis Number	N/A
$\dot{m}$	Mass flow rate	kg/s
Nu	Nusselt number	N/A

Q	Heat	kW
q''	Heat flux	$kW{\cdot}m^{-2}$
P	Pressure	Pa or kPa
P*	Pressure ratio	N/A
p	Pitch	mm
Pr	Prandtl number	N/A
R	Resistance	$K{\cdot}W^{-1}$ or $J/kg{\cdot}W^{-1}$
Re	Reynolds number	N/A
r	Radius	mm
S	Tube Pitch	mm
s	Spacing gap	mm
T	Temperature	°C or K
t	Thickness	mm
U	Overall heat transfer coefficient	$kW{\cdot}m^{-2}{\cdot}K^{-1}$
$\dot{V}$	Volumetric flow rate	$m^3{\cdot}s^{-1}$
v	Velocity	$m{\cdot}s^{-1}$
W	Work	kW
w	Width	mm
X	Dry fraction of coils	N/A
x	Quality	N/A
yr	Year	N/A
α	Weighting factor	N/A
β	Chevron angle	Degrees
Δ	Variation	N/A
ε	Roughness	µm

ϵ	Effectiveness	N/A
η	Efficiency	N/A
ϕ	Surface enlargement factor	N/A
μ	Dynamic viscosity	Pa·s
ξ	Fouling factor	$m^2 \cdot K \cdot W^{-1}$
ρ	Density	$kg \cdot m^{-3}$
$\sum$	Sum	N/A
ω	Moisture content	kg/kg_{air}

Subscripts

Subscript	**Description**
A	Air
amb	Ambient
amp	Amplitude
C	Cooling
c	Coolant
comp	Compressor
cond	Condensate or condenser/condensing
cp	Flow channels per pass
crit	Critical
D	Diagonal
d	Dry
dis	Discharge
dp	Dew point
ds	Desuperheater

e	Enthalpic
ef	Effective
eq	Equivalent
evap	Evaporator/evaporating
eve	Evening
ext	External
F	Fan
f	Fouling
fit	Fittings
fd	Fully developed
FP	Freeze protection
gas	Gaseous
H	Heating
HP	Heat Pump
hs	High stage
in	Inlet
int	Internal or intermediate
is	Isentropic
L	Longitudinal
l	Laminar
lat	Latent
liq	Liquid
ls	Low stage
lt	Long-term
m	Mass

max	Maximum
min	Minimum
mor	Morning
out	Outlet or output
P	Pumping
p	At constant pressure
proj	Projected
r	Refrigerant
rec	Recovered
S	Static
s	Surface
sat	Saturated
sen	Sensible
st	Short-term
suc	Suction
T	Transversal
t	Thermal
tb	Turbulent
tr	Transitional
vap	Vaporisation
w	Wet or water
x	At point X

Abbreviations

Abbreviation	Meaning
1D	One-dimensional
2D	Two-dimensional
3D	Three-dimensional
1GDH	1st Generation District Heating
2GDH	2nd Generation District Heating
3GDH	3rd Generation District Heating
4GDH	4th Generation District Heating
5GDHC	5th Generation District Heating and Cooling
AAHEDC	Assistance for Areas with High Electricity Distribution Costs
AC	Alternating Current
ADE	Association for Decentralised Energy
AHU	Air-handling Unit
ASHP	Air-source Heat Pump
ASHRAE	American Society of Heating, Refrigerating and Air-Conditioning Engineers
BEIS	Department for Business, Energy and Industrial Strategy
CAC	Carbon Abatement Costs
$CACl_2$	Calcium Chloride
CAD	Computer-aided Design
CAPEX	Capital Expenditure
CCC	Climate Change Committee
CCS	Carbon Capture and Storage
CFD	Computational Fluid Dynamics
CfD	Contracts for Difference

CHP	Combined Heat and Power
CIBSE	Chartered Institution of Building Services Engineers
CO_2	Carbon Dioxide
CO_2e	Carbon Dioxide Equivalent
COMEAP	Committee on the Medical Effects of Air Pollutants
COP	Coefficient of Performance
COSP	Coefficient of System Performance
CMC	Capacity Market Charges
DECC	Department of Energy and Climate Change
DEFRA	Department for Environment, Food and Rural Affairs
DHC	District Heating and Cooling
DHN	District Heating Network
DC	Direct Current
DN	Nominal Diameter
DUoS	Distribution Use of System
EA	Ethyl Alcohol
ECIU	Energy and Climate Intelligence Unit
EES	Engineering Equation Solver
EG	Ethylene Glycol
EU	European Union
EV	Electric Vehicle
FD	Finite Difference
FE	Finite Element
FIT	Feed-in Tariff
FP	Freeze Protection

GB	Great Britain
GHE	Geothermal Heat Exchanger
GHNF	Green Heat Network Fund
GIS	Geographic Information System
GHG	Greenhouse Gas
GL	Glycerol
GLA	Greater London Authority
GSHP	Ground Source Heat Pump
GWh	Gigawatt-hour
HFO	Hydrofluoroolefin
HP	Heat Pump
HRC	Heat Recovery Coils
kWh	Kilowatt-hour
LCH	Levelised Cost of Heat
LMED	Log-mean Enthalpy Difference
LMTD	Log-mean Temperature Difference
LU	London Underground
MWh	Megawatt-hour
NAEI	National Atmospheric Emissions Inventory
NaCl	Sodium Chloride
NCA	National Comprehensive Assessment
NH_3/R717	Ammonia
NO_x	Nitrogen Oxides
NPC	Net Present Cost
OPEX	Operational Expenditure

PAHU	Platform Air-handling Units
PCM	Phase-change Material
PG	Propylene Glycol
PHE	Plate Heat Exchangers
PJ	Petajoules
PSHE	Plate-and-shell Heat Exchangers
REPEX	Replacement Expenditure
RH	Relative Humidity
RO	Renewable Obligation
SD	Standard Deviation
SO_2	Sulphur Dioxide
TCES	Thermochemical Energy Storage
TEV	Thermal Expansion Valve
TES	Thermal Energy Storage
TfL	Transport for London
TPH	Trains per Hour
TWh	Terawatt-hour
UITP	International Association of Public Transport
UK	United Kingdom
UKCP09	United Kingdom Climate Projections from 2009
UNCC	United Nations Climate Change
UN DESA	United Nations Department of Economic and Social Affairs
UR	Underground Railway
USA	United States of America
WHR	Waste Heat Recovery

1. Introduction

1.1. Background and Relevance

The climate emergency is one of the greatest challenges ever faced by humanity. Since the Industrial Revolution, the economic development of the world has been based on the utilisation of fossil fuels to meet increasing global energy demands. With the threat of climate breakdown, many countries around the world have been working to accelerate the uptake of clean or low-carbon energy sources; for instance, the United Kingdom (UK) has managed to achieve, in recent years, a significant decrease in greenhouse gas (GHG) emissions, cutting them by 48.8% since 1990 (BEIS, 2021a). These results are, however, mainly due to the power sector, which has experienced the gradual phase out of coal as an energy source, whilst renewable alternatives — such as wind and solar power — have gained greater relevance. Although approximately 35% of the electricity generated in the UK in 2019 came from renewables, only around 8% of the heating demand was met using renewable sources (BEIS, 2020a). If the UK is to honour its recent pledge to reach net zero carbon emissions by 2050, much greater efforts will be required — especially from the heating sector, which currently accounts for nearly half the energy consumption and around one third of carbon emissions in the UK (BEIS, 2018).

Achieving sustainable heating is also a challenge for London, where gas boilers account for nearly 90% of the heating systems used in buildings, posing a threat not only in global warming terms but also due to air pollution. London's homes produce one third of the capital's total GHG emissions and nearly 75% of the energy consumed by dwellings is used to provide space and hot water heating; meanwhile, workplaces account for approximately 40% of the city's emissions, with half of their energy demand being related to heating (GLA, 2018a). It is clear that, if the UK aims to decarbonise its energy sector, heat generation all over the country will have to transition towards efficient and low-carbon heating systems.

Harnessing the surplus heat that is wasted in a variety of urban infrastructures represents a unique opportunity for London and other cities worldwide. Urban waste heat is typically of low grade, meaning that heat pumps (HPs) are often necessary to enable its use for the provision of space heating and domestic hot water. By utilising heat sources of higher temperature, HPs can operate with higher efficiencies, but even low temperature waste heat, e.g. 10-20°C, can be economically upgraded for reuse with HPs. The combination of HPs and heat networks could therefore unlock the potential to generate and distribute low-carbon energy locally and efficiently, helping to reduce the carbon footprint associated with heating whilst also tackling fuel poverty. In the UK today, heat networks supply around 2% of the overall heating demand (ADE, 2018), whilst 6% of the energy demand in London is supplied via district systems (GLA, 2018a). These systems do not necessarily rely on low-carbon heat sources, such as HPs, and the Climate Change Committee (CCC, 2019) has recognised that district energy based on waste heat will play an important role in decarbonising the heat supply of buildings in the UK, representing an essential mechanism for reaching the net zero GHG emission target by 2050. At a local level, the London Environment Strategy has already set a target of increasing the energy supply from district schemes and renewable sources to 15% by 2030 (GLA, 2018a).

There are a range of sources in the urban environment from which it is possible to capture waste heat. A study by the Greater London Authority (GLA) and Buro Happold (2013) reported that, in 2010, there were ca. 71 Terawatt-hour (TWh) per year of thermal energy available from secondary sources (i.e. natural and waste heat) in London, an amount greater than the city’s estimated demand of 66 TWh in that same year. One source of particular interest in London is the London Underground (LU), as its network covers a large area of the city, and the operation of its trains generate significant amounts of thermal energy. This potential led to the development of the Bunhill Waste Heat Recovery (WHR) System, a first-of-its-kind project that involves recovering waste heat from the LU and utilising it to heat buildings in the London Borough of Islington. In addition to providing low-carbon heat to a local district heating network (DHN), the Bunhill WHR system is also able to provide cooling to the underground railway (UR), potentially increasing the thermal comfort of LU passengers by reducing tunnel air temperatures. As a pioneering project, the performance of the system is still to be fully understood; the investigation described in this thesis utilises mathematical modelling to investigate the current and potential benefits that can be achieved with the WHR system.

1.2. Thesis Aim

This thesis aims to provide a holistic investigation into the potential benefits of recovering waste heat from a LU ventilation shaft, considering not only its efficiency as a heat source, but also secondary benefits such as cooling the LU environment, providing flexibility to the wider energy system and tackling air pollution. This aim guided the critical literature review, which formed the basis for identifying how this thesis can contribute to knowledge. Based on the proposed contribution, specific research objectives were defined, as detailed in Chapter 3.

1.3. Thesis Chapters

To achieve the aforementioned aim, the thesis will consist of the following chapters:

Chapter 1 – Introduction**:** provides a summary of the investigation described in this thesis.

Chapter 2 – Critical Literature Review: provides an overview of the latest literature on the topic of this research. Firstly, the critical literature review explores the importance of low-carbon heating systems in light of the climate crisis, looking at the main pathways currently being discussed as alternatives for decarbonising heat supply in buildings. The benefits of district energy are then highlighted and linked to the potential of WHR in cities, with focus on URs. Lastly, this chapter describes the modelling techniques and tools that can be applied to simulate the WHR system and achieve the aim of this thesis.

Chapter 3 – Research Methodology: defines the objectives of this investigation and proposes a methodology for achieving them.

Chapter 4 – The Bunhill Waste Heat Recovery System: introduces the WHR system in detail, highlighting its main technical components and principles of operation.

Chapter 5 – Modelling of the Waste Heat Recovery System: details the development of a mathematical model capable of estimating the performance of the WHR system based on inlet air conditions and values for HP output.

Chapter 6 – Data Collection and Model Validation: describes the operational data collected from the WHR system and the instruments used in the process, as well as the approach utilised to validate the WHR model.

Chapter 7 – Investigating the Impacts on the Underground Railway Environment: provides an overview of the principles behind the numerical model applied to simulate the UR environment. This chapter also describes how the results from the WHR model were used to estimate the air temperature reductions at the stations adjacent to the ventilation shaft.

Chapter 8 – Heat Recovery Analysis – Design and Operation: reports the results from the WHR model under different operating modes and their potential impact on the local railway tunnels. This chapter also provides recommendations for design and operation based upon critical parameters that affect heat recovery and cooling potential, with focus on condensation.

Chapter 9 – Evaluating the Benefits of Waste Heat Recovery from Underground Railways: provides economic and environmental evaluations of the performance of the WHR system against typical counterfactuals, describing how WHR can reduce costs of decarbonisation through additional value streams, such as cooling and flexibility.

Chapter 10 – Waste Heat Recovery and the Potential for Replication: investigates how the concept of the Bunhill scheme could be replicated for different ventilation shafts belonging to the underground transport systems for the cities of London and Newcastle.

Chapter 11 – Conclusion and Further Studies: presents the main findings of the investigation, highlighting the outcomes of the modelling work and how this project relates to current literature. The chapter also suggests how future research can build upon the work described in this thesis.

2. Critical Literature Review

2.1. Introduction

This critical literature review aims to identify how this research project can contribute to current knowledge related to waste heat recovery (WHR) from railway tunnels. The review first contextualises the relevance of the heating and cooling sector in terms of overall energy consumption and contribution to the climate crisis, with focus on London, the UK and Europe. The challenge of decarbonising heat is then presented based on the current strategy by the UK Government to reduce emissions associated with heating; this demonstrates the need for the deployment of low-carbon heating systems, highlighting how combining WHR with district energy networks can transform the urban energy environment while playing a key role in the fight against climate breakdown and fuel poverty. This potential is first explored by reviewing how district energy has evolved over the years and by identifying its benefits based on existing case studies that utilise waste heat. Additionally, a range of different urban waste heat sources were compared, with an emphasis on underground railways (URs).

The opportunity for using URs as a source of low-carbon heat is further investigated by reviewing studies available in current literature that report state-of-the-art technologies used to capture heat generated during the operation of underground trains. The review shows how current work has been focused on modelling and feasibility studies for either cooling railway tunnels or for using their waste heat, with some pilot projects being reported to test the potential of these technologies on a small scale. Studies on the provision of cooling for railway tunnels, as well as on other secondary benefits from WHR, are also presented and discussed. Although there are studies which analyse a combined heating and cooling potential, they are based on conceptual designs rather than a practical project. Furthermore, the combination of waste heat from URs with flexibility through thermal energy storage (TES) and its potential benefits has not been explored to date.

Finally, modelling techniques and tools commonly used for energy systems are reviewed, informing what methods could be applied for the development of models that enable the estimation of the performance of the WHR system and the evaluation of its full potential. There are several benefits that could be realised by recovering waste heat from railway tunnels, and this thesis aims to provide much needed clarity on how the combination of different value streams, e.g. cooling, heating and flexibility, should be considering when assessing the role waste heat should play in the transition towards a net zero economy. This chapter provides the context and scientific foundation that were considered when formulating the research questions that are presented in Chapter 3.

2.1.1. Sources Searched for Relevant Literature

The following databases were used to search for relevant literature as part of this investigation:

- Academic Search Complete
- American Society of Heating, Refrigerating and Air-Conditioning Engineers (ASHRAE)
- Chartered Institution of Building Services Engineers (CIBSE)
- Construction Information Service (CIS)
- British Standards Online
- Google Scholar
- Institute of Refrigeration
- London South Bank University Library
- Science Direct
- Scopus Database

The following keywords have been used when searching through these databases: Air-to-water, Ammonia, Analytical, Compressor(s), Condenser(s), Cooling, Coil(s), Cycle(s), District, Energy, Enthalpy, Environment, Evaporator(s), Fan(s), Flexibility, Heat, Heat Pump(s), Heat Exchanger(s), Heating, Humidity, London, Metro, Model(s), Modelling, Numerical, Plate, Pumping, Railway(s), Refrigeration, Secondary Heat, Storage, Temperature, Thermal, Tunnel(s), Two-stage, Underground, Waste Heat.

In total, over 300 resources were obtained (e.g. books, reports, journal and conference papers); these were catalogued utilising the Zotero Software and categorised according to their subject area and relevance to this investigation.

2.2. Heating, Cooling and the Climate Crisis

2.2.1. The Global Scenario

Earth's urban population surpassed its rural population for the first time in history in the year of 2007, rapidly growing to reach 55% of the overall global population in 2018. It is projected that this index will have risen to 68% in 2050, adding more than 2.4 billion people to cities across the globe (UN DESA, 2018). The trend is no different for the UK, as its urban residents are expected to grow from 83.7% in 2018 to 90.2% of the overall population in 2050 (UN DESA, 2018), with London's population expected to increase by approximately 26% between 2017 and 2050 (GLA, 2018b). Nowadays, cities consume about 70% of the world's resources, and it is estimated that two thirds of the energy generated globally are used to meet demands in urban areas, which account for more than 70% of the world's CO_2 emissions (C40 Cities, 2019). This is due to the density of urban population, the intensity of related economic and social activities, and to the inefficiency of the built environment (Bibri and Krogstie, 2017). This demonstrates why cities must be at the forefront of climate change mitigation and the great challenge that lies ahead, as the future expansion of urban settlements will increase the demand for services and resources. Meeting the world's target of keeping global temperatures to within 1.5°C above pre-industrial levels (IPCC, 2018) will require investments in low-carbon solutions that improve the efficiency of cities worldwide.

Currently, around 12.5% of the world's population lives in households without a reliable supply of electricity and the growing efforts to universalise energy access are likely to increase global energy demand by at least a quarter by 2040 (IEA, 2018a). This growing demand, mostly related to urban areas in emerging economies, will have to be dealt with at a time when urgent action is required to change the global energy matrix, as nearly 91% of the world's primary energy supply came from fossil fuels in 2016 (IEA, 2018b). This scenario highlights the important role to be played by energy efficiency measures and zero/low-carbon energy sources in speeding up this transition. Much of the intensive energy consumption in cities worldwide can be attributed to the built environment, as buildings and their construction processes account for about 40% of CO_2 emissions and 36% of energy demand globally, with almost a third of this demand being related to heating (IEA, 2018c). Therefore, energy efficiency and heat decarbonisation are essential to achieving the world's climate goals, as the UN calls for governments across the globe to raise their ambitions and achieve net zero greenhouse gas (GHG) emissions by 2050 (UNCC, 2021), which is defined by a state when all emissions produced are balanced by the removal of GHGs from the atmosphere.

2.2.2. Europe

In Europe, around 50% of the energy consumed in 2015 was for heating and cooling purposes, with nearly 31% accounting for space heating and domestic hot water (Heat Roadmap Europe, 2019). Despite representing a large portion of total energy use, only 19.1% of the heating and cooling demands were met using renewable energy sources in the following year (EEA, 2018).

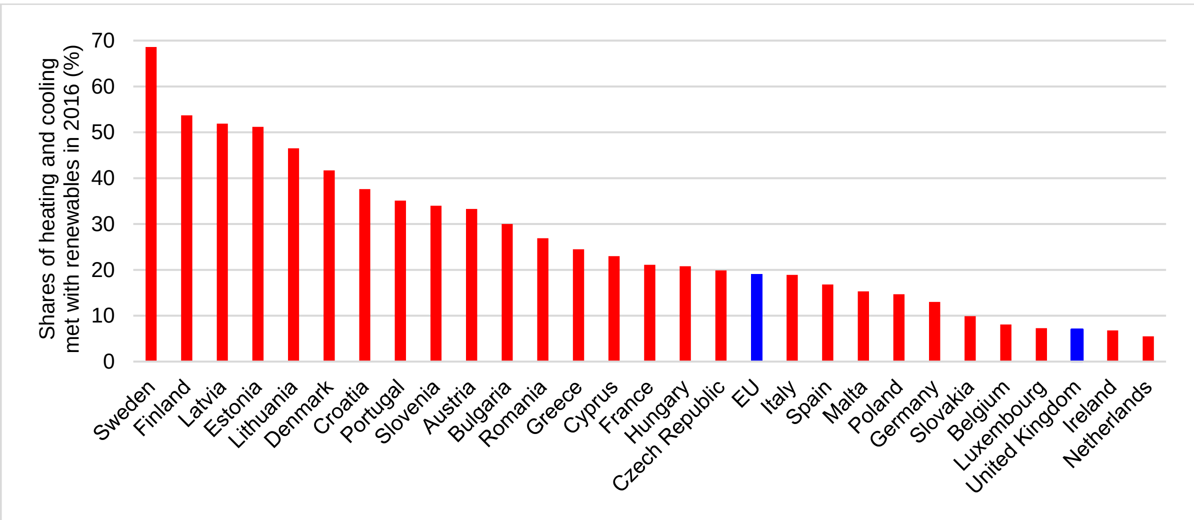

Figure 2.1 – Shares of heating and cooling demand met with renewables across the EU in 2016 (EEA, 2018).

The shares of heating and cooling demands met with renewable energy sources vary widely amongst European countries due to how different historical developments and other factors (e.g. economic stability, policy frameworks, local climate, and availability of fossil fuels) have shaped each national energy system. Figure 2.1 shows the shares of renewable energy in relation to the energy used for heating and cooling purposes for the European Union (EU) and the UK, both highlighted in blue, as well as for the 27 EU member states.

2.2.3. London and the United Kingdom

The UK has one of the lowest shares of renewable energy used to provide heating and cooling in Europe, with only 7% of its demand being met with renewables, as shown in Figure 2.1. This demonstrates the challenge the UK will face over the coming years, as the country aims to decarbonise its economy and reduce GHG emissions to net zero by 2050. This ambitious target was motivated by the progress made by the UK in recent years, as national emissions fell by 48.8% between 1990 and 2020 (BEIS, 2021a). These results are primarily attributed to the power sector, which experienced a reduction in the use of coal and an increase in the use of renewable sources for the generation of electricity. Overall, 35% of the electricity generated in 2019 came from renewables, whilst the shares of renewables for heating and transport only represented, respectively, 7.9% and 8.8% of the energy used to meet these demands nationally (BEIS, 2020a). Therefore, if the UK is to meet its carbon target, much greater efforts will be required from other sectors within the energy industry, such as heating and transport.

The heating and cooling sector will indeed play an important role in achieving those targets, particularly as heating accounts for approximately a third of carbon emissions and around half of the energy consumption in the UK (BEIS, 2018). Currently, 85% of British households are heated by natural gas and only 5% have low-carbon heating technologies (ESC, 2020a). Sustainable heating is also a problem within London, where 90% of buildings are heated with gas-fired boilers (GLA, 2018a). Additionally, recent developments based on Combined Heat and Power (CHP) systems have been introduced across the country as a cost-effective way of producing low-carbon heat. However, as the national electricity grid decarbonises, the carbon savings relating to CHP are declining and there is increasing evidence of their adverse impacts on air quality. It is clear that, if London and the UK want to decarbonise their energy systems, heat generation all over the country must be shifted towards a wide deployment of efficient and low-carbon heating sources. The Greater London Authority (GLA) has a bold plan to make London a zero-carbon city by 2050, following the latest recommendation from the Climate Change Committee (CCC) for the national emission reduction target.

2.3. Pathways for Decarbonisation

As part of a set of recommendations on how to achieve net zero, the CCC has highlighted the need for UK homes to be retrofitted with energy efficiency (insulation) measures and low-carbon heating technologies (CCC, 2019). Amongst the technologies proposed, hydrogen boilers and heat pumps (HPs), which may be linked with district heating, were highlighted as promising solutions for the decarbonisation of the UK's building stock. This is further detailed in the Sixth Carbon Budget Report (CCC, 2020), which proposes a balanced pathway to net zero that aims to raise ambitions while still being realistic when considering uncertainties around people's behaviour and the development of different technologies and their markets. This balanced pathway would involve phasing out the currently dominant heating method of gas boilers by 2033, with HPs playing a leading role in the process. Furthermore, low-carbon heat networks would grow to meet around a fifth of the UK's heat demand by 2050, with focus on densely occupied areas such as cities. According to the CCC (2020), around 93% of heat networks in the UK currently use a fossil fuel primary energy source, and these would have to shift towards low-carbon and waste heat from the mid-2020s. This can be noted from the projections for low-carbon heating stock from 2020 to 2050, as illustrated in Figure 2.2, which highlights the contributions expected from HPs and district heating to decarbonisation.

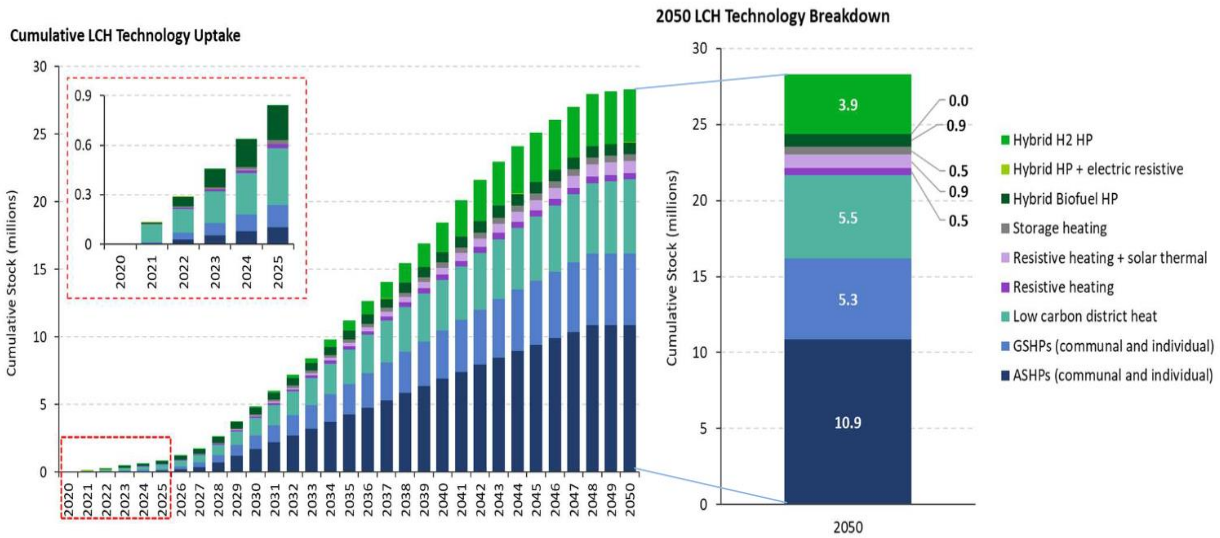

Figure 2.2 – Projected balanced pathway heating stock for the UK from 2020 to 2050 (Element Energy, 2021).

As for hydrogen, the CCC sees its applicability for heating gaining greater relevance from the 2030s, particularly as a resource to complement areas where electrification and heat networks might not be viable. The exact role of hydrogen in the decarbonisation of heat is still uncertain and future decisions will be based on trials throughout the 2020s (Element Energy, 2021). However, there is already some initial evidence on the inefficiency of hydrogen as a fuel for heating. According to Cebon (2020), low-carbon hydrogen can be produced in two different ways, namely: ‘green’ hydrogen, which is obtained through the electrolysis of pure water; and ‘blue’ hydrogen, which consists of separating the carbon atoms from methane molecules (CH_4) through a process known as steam methane reforming (SMR), which generates H_2 and CO_2 – the latter product then sequestered through carbon capture and storage (CCS). Cebon (2020) has shown how green hydrogen can be nearly 83% less efficient than HPs when providing the same amount of heat, meaning that much greater investments in low-carbon electricity generation would have to be made in order to generate green hydrogen if it were incentivised as a fuel for heating in buildings. The author also highlighted the inefficiencies and risks of fugitive emissions associated with blue hydrogen. This was further investigated by Howarth and Jacobson (2021), who estimated that GHG emissions resulting from the production of heat with blue hydrogen could be 20% higher than when generating the same amount of heat with natural gas, which is mainly due to fugitive methane emissions.

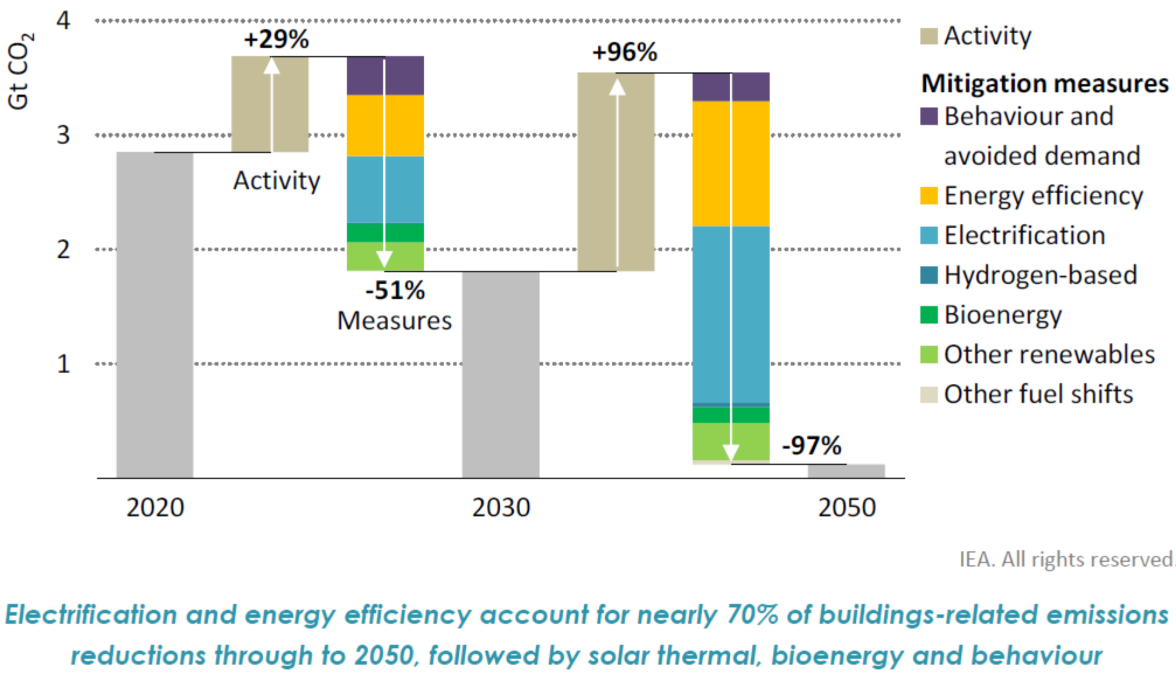

Figure 2.3 – Estimated CO_2 savings by mitigation measure for buildings in a net zero scenario (IEA, 2021).

The IEA’s roadmap to net zero in 2050 (2021) has identified energy efficiency and electrification as the two main drivers for the decarbonisation of buildings, as can be seen from Figure 2.3, which highlights how hydrogen is expected to play a minor role in the buildings sector. This is associated with an expected worldwide increase in renewable electricity generation in future decades. As the demand for electricity rises — not only due to heating and cooling, but also due to an increased uptake of electric vehicles (EV) — the deployment of solutions that prioritise energy efficiency, such as district energy and WHR, will become increasingly important, as they can help in managing growing energy demands, which is critical to achieving climate goals cost-effectively.

2.4. Current Policy Landscape

In October 2021, the UK Government announced its long-awaited Heat and Buildings Strategy (BEIS, 2021b), which provided plans for the decarbonisation of heat in UK buildings based on 2020's ten-point plan for a green industrial revolution (BEIS, 2020b). The strategy introduced guidelines that build upon previous policies, such as the Renewable Heat Incentive (RHI), the Green Homes Grant and the Heat Network Investment Project (HNIP). The RHI was a financial refund linked to the quantity of heat generated from renewable sources, for technologies such as solar thermal and biomass boilers, as well as ground-source and air-source HPs (Ofgem, 2020). The Green Homes Grant provided vouchers covering up to 100% of the installation costs for home improvements that included energy efficiency measures and low-carbon heating technologies, with a maximum contribution of £5,000 (BEIS, 2021c). As for HNIP, it consisted of a £320m fund to support the development of heat networks in the UK, which could provide up to £5 million or 50% of the capital costs of district heating projects (BEIS, 2018).

The Heat and Buildings Strategy is aligned with the recommendations from the CCC (2020), with a focus on the electrification of heat as a crucial step in the road towards net zero, with HPs being recognised as the main technology readily available for decarbonising heat supply for the UK's building stock. The Government intends to phase out the installation of new gas boilers beyond 2035 whilst incentivising HPs through the Boiler Upgrade Scheme, which will provide £5,000 and £6,000 capital grants for air-source and ground-source HPs, respectively. This £450m policy is expected to deliver around 30,000 HP installations per year, a number that is still far lower than the 2020 ten point plan target of delivering 600,000 installations per year by 2028. Hydrogen might still play a role for heating in the future, but the Government is waiting on further evidence of its potential before incentivising this technology, with plans to reach a decision on this by 2026. Another key policy in the strategy refers to plans for revising the levies and taxes applied to electricity and gas in 2022, as the current disparity in prices between natural gas and electricity represents a risk to the electrification of heat.

District heating networks (DHNs) have also been highlighted as a technology of great potential in densely occupied areas, with plans to develop heat network zones where district heating represents the lowest cost and carbon solution. The zoning policy would oblige the connection of appropriate buildings by law if they are located within a heat network zone. Furthermore, the Government plans to invest £338 million until 2025 into a broader Heat Network Transformation Programme that aims to incentivise the decarbonisation of existing DHNs and the construction of low-carbon networks through the Green Heat Network Fund (GHNF) (BEIS, 2021d). The Heat and Buildings strategy also highlights how waste heat from sources like URs can be key in the transformation of the UK's heat network market.

2.5. District Energy Systems

Traditionally, district energy systems, or district heating and cooling (DHC), can be defined as networks that provide either heating or cooling from a central point of generation to multiple buildings within a district, neighbourhood, or city (Euroheat and Power, 2019). These systems have been widely applied as a way of providing low-carbon energy to end users, leading to significant financial and environmental benefits. From an economic perspective, DHC systems benefit from economies of scale, as utilising the heat produced from one larger source can often be more efficient than using heat from a variety of smaller sources. In terms of environmental benefits, heating and cooling networks allow the use of locally available energy sources that either can be renewable or based on the recovery of energy which would otherwise be wasted. Another advantage of district energy systems is their ability to operate with different generating plants, avoiding being locked into technologies that may become obsolete in future decades. By enabling the integration of a variety of energy sources, end users are not dependent upon one single source, which leads to greater energy security and permits alternating between different forms of supply to guarantee a cost-effective and low-carbon operation.

The UN’s District Energy Initiative (2019) provides a similar definition but calls for the adoption of a modernised description of district energy that would combine renewable power generation with DHC networks. This involves utilising renewable electricity to power devices that can generate heat or coolth for end users, helping to manage the fluctuating supply of renewable power by using TES. This concept would entail generating heat when costs are lower and storing that energy to be used later when meeting peak demands over daily or seasonal periods. The coupling of the electricity and heating sectors represents an essential feature of future energy systems, particularly as it can help in alleviating high peak demands from the electricity grid and allow heat to be produced with lower carbon intensities.

The recovery of waste heat involves capturing thermal energy that would otherwise be rejected during a given process, such as in the operation of a variety of urban infrastructures (e.g. sewage systems, electricity distribution systems, supermarkets, data centres, and railway tunnels). Urban waste heat is, therefore, widely available in cities and typically of low grade, meaning that HPs must be deployed to upgrade it to appropriate temperatures for distribution and domestic use. The upgrade can occur either next to the WHR site or closer to end users, depending upon the heat distribution temperature. Historically, the evolutionary trend amongst district heating has been towards lower operating temperatures, higher energy efficiency and lower use of fossil fuels. Therefore, the latest generations of heat networks, characterised by lower operating temperatures, provide a greater opportunity for harnessing waste heat.

2.5.1. Historical Development

The deployment of district energy within a specific country depends on a complex framework that involves market, technical, environmental, and institutional contexts. Werner (2017) found that district energy networks have been historically associated with the supply of heat rather than coolth and also noted a low utilisation rate of these systems globally, although there are varying implementation levels amongst countries due to different local driving forces. This is illustrated in Figure 2.4, which shows the percentage of citizens served by district heating in some European countries in the year of 2013, highlighting how the UK had one of the lowest shares of citizens connected to DHNs in Europe at that time.

Through the analysis of the dissemination of district heating in different countries, Werner (2017) also noticed common driving factors for the deployment of DHNs. On the supply side, the main driving force was the potential primary energy savings related to the recycling of heat from a variety of processes, such as waste-to-energy. There was also an advantage for consumers: the convenience of avoiding the responsibility for maintaining boilers and purchasing fuel. Other factors have been identified in the context of specific countries; for example, legislative incentives and high fuel taxes were particularly favourable in Denmark and Sweden, whilst the UK has lacked corresponding policies. These factors, along with access to abundant natural gas reserves in the North Sea, have shaped the heating sector in the UK to be severely dependent on natural gas, with an underdeveloped heat network market.

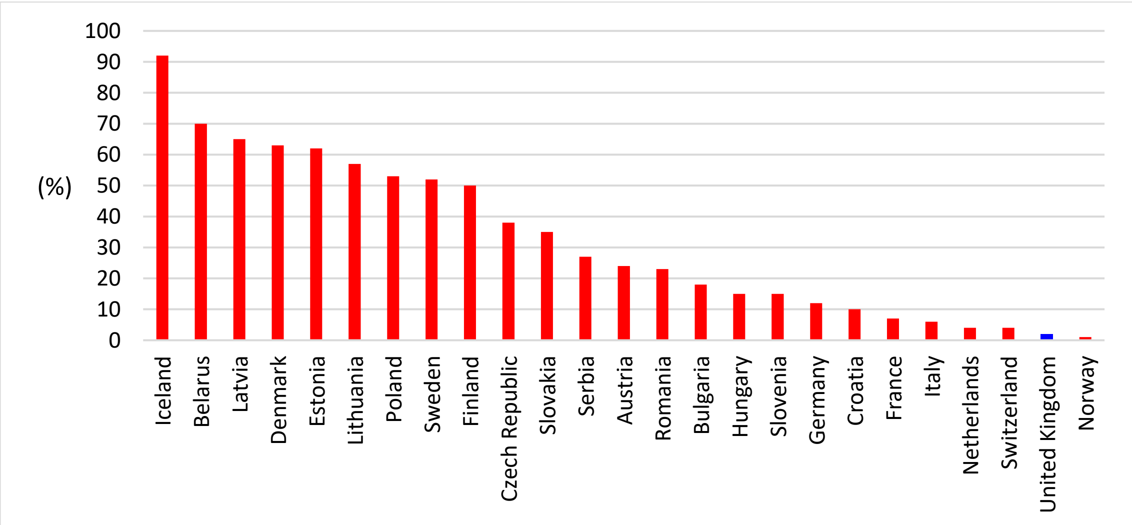

Figure 2.4 – The percentage of citizens served by district heating in 25 European countries in 2013, with the UK highlighted in blue (Euroheat and Power, 2015).

Over the years, district heating has evolved significantly. The 1st Generation of District Heating (1GDH), dating back to the 1880s in the USA, was defined by the use of steam as the heat carrier, typically transported in insulated steel pipes within concrete ducts. According to Werner (2017) and Lund et al. (2014), the 2nd Generation of District Heating (2GDH) introduced pressurised water, usually above 100°C, as a more efficient medium to transport heat, a technological advancement driven by the introduction of cogeneration systems applied to increase the efficiency of power plants. Both 1st and 2nd generations involved very large and material-intensive network components. In the 1970s, the oil crises led to significant rises in energy prices and severe shortages of supply across the globe. This critical scenario caused fuel rationing in many countries and demonstrated the need to enhance energy security, ultimately setting a propitious environment for the emergence of a 3rd Generation of District Heating (3GDH), focused on alternative fuels to oil and the use of CHP systems to improve energy efficiency. The third generation is characterised by prefabricated network components, which include pre-insulated pipes and compact heat exchangers, as well as by operating with pressurised water at lower distribution temperatures, typically under 100°C.

Lund et al. (2014) defined the concept of 4th Generation District Heating (4GDH) by addressing the need to integrate district energy systems with the electricity grid to form future smart energy systems; such integration demands a combined operation of both thermal and electrical grids, identifying synergies to enable an optimum operation in terms of overall energy efficiency. These smart energy systems are able to balance the fluctuating generation of renewable power by coordinating heating, cooling and electricity demands through different technologies such as HPs, chillers and thermal storage, which enable the use of renewable and waste heat. Some examples are the 4GDH network utilising industrial waste heat that was analysed by Ziemele et al. (2018), and the case studies reported by Schmidt et al. (2017), which included a low-temperature network using a ground-source heat pump (GSHP). Fourth generation networks can be categorised by even lower operating temperatures and consequently greater efficiencies than previous generations.

Another novel approach to heat networks, which follows this pattern, has been identified as a new generation of district heating. Buffa et al. (2019) reviewed 40 different district energy systems that can provide both heating and cooling and proposed an appropriate nomenclature to define this new type of network: 5th Generation District Heating and Cooling (5GDHC). A similar concept has been investigated by other authors, who used different terminologies when defining this new network topology, such as seen in the works of Bünning et al. (2018), Pellegrini and Bianchini (2018), Pattijn and Baumans (2017), and Ruesch and Haller (2017). These studies highlighted how different technologies such as HPs, WHR and TES can be used to balance heating and cooling demands through a district energy network whilst also enabling sector coupling. The 5th generation concept is characterised by operation at ultra-low temperatures, leading to negligible thermal losses and a high network efficiency, even discarding the need for pipework insulation in some cases. This enables heat and coolth to be shared between end users, with any required upgrades (or downgrades) taking place closer to consumers. The evolution of district heating, from the 1st to its 5th generation, is illustrated in Figure 2.5.

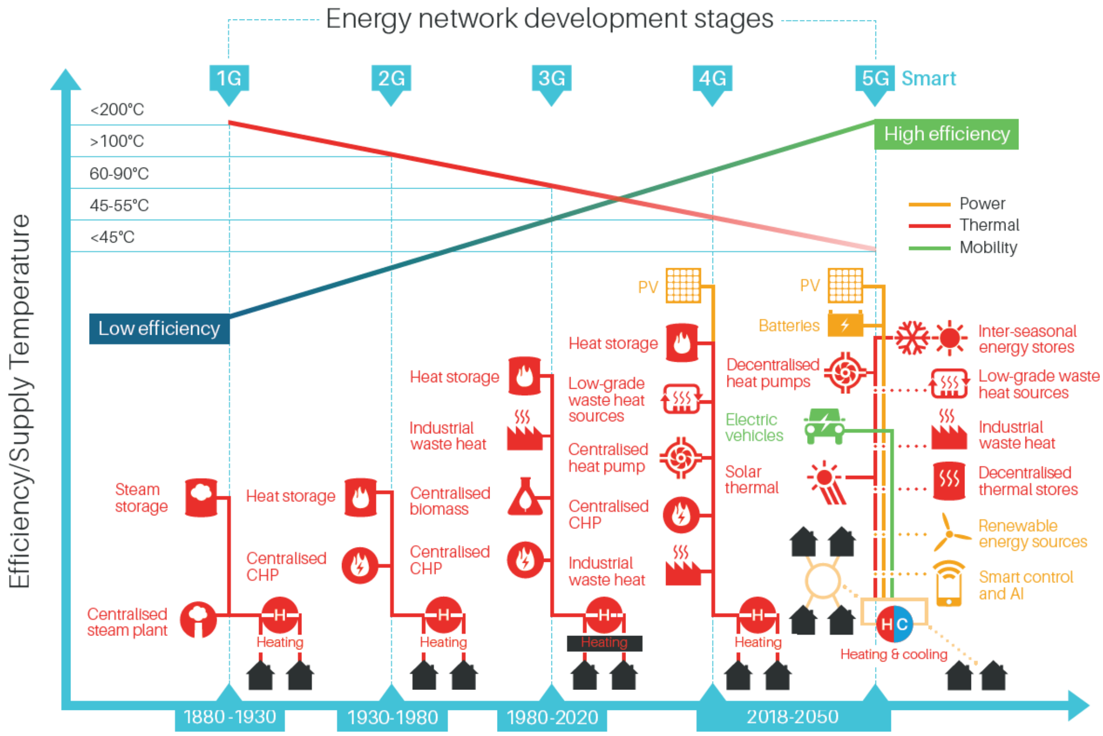

Figure 2.5 – Representation of the evolution of district heating, from 1GDH to 5GDHC (Revesz et al., 2020).

The GreenSCIES project (Revesz et al., 2020) is a London based example of the capabilities of 5GDHC. The project involves the design of an ambient temperature loop connected to locally available urban waste heat sources such as data centres and URs. End users can either consume heat or reject it into the system using reversible HPs and thermal stores distributed across decentralised energy centres, which also act as hubs for renewable electricity generation by using photovoltaic (PV) panels and charging/storage points for electric vehicles (EVs), combining renewable power and mobility with the DHC network. The integrated approach of this 5GDHC system, illustrated in Figure 2.6, is expected to involve 6.8 MW of HP capacity, 740 m^3 of thermal storage, 611 kW of PV and 49 EV charge points. This would deliver low carbon heat, mobility and power to more than 10,000 urban residents, reducing carbon emissions by 80% (over existing gas-fired systems), improving local air quality, and addressing fuel poverty by providing a 25% reduction on consumer bills.

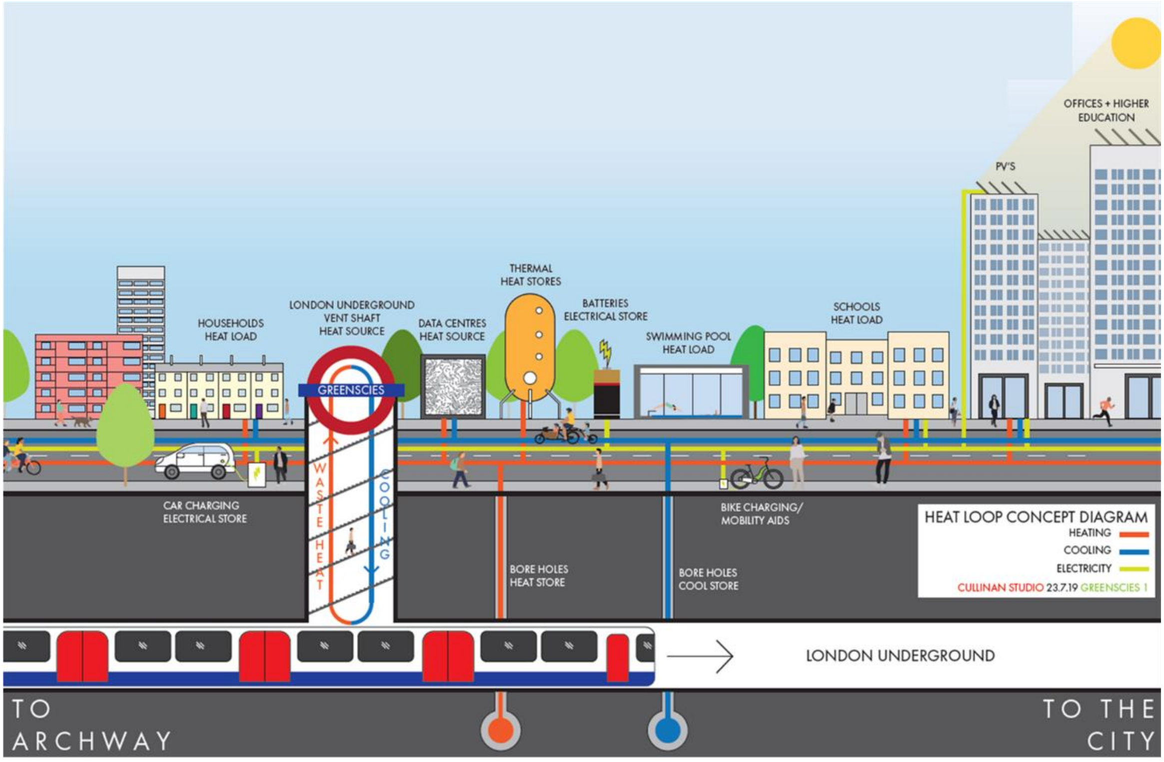

Figure 2.6 – Conceptual schematic of the GreenSCIES project (GreenSCIES, 2020).

As 4GDH and 5GDHC are contemporaneous technologies, deciding which to apply will mostly depend on whether there is a balance between the cooling and heating loads that could be met via district energy, with 5GDHC being suitable for places where there is a synergy between heating and cooling demands (Lund et al., 2021). Therefore, energy planners must consider if there is a significant cooling load when designing a 5GDHC; if the local energy demands are mainly associated with heating, then 4GDH represents the most appropriate solution (Jones et al., 2019). Table 2.1 categorises the different generations of district heating according to their main features, including periods of greater deployment, type of energy provided, medium used to transport the heat, typical operating temperatures, heat sources commonly used, network components and the main motivation for their development, as well as references to the authors reporting each generation.

Table 2.1 – The generations of district heating and their features.

Generation	1st (1GDH)	2nd (2GDH)	3rd (3GDH)	4th (4GDH)	5th (5GDHC)
Period of Greater Deployment	1880s to 1930s	1920s to 1970s	1970s to 2010s	From 2010s	From 2010s
Energy Provision	Only Heating				Heating and Cooling
Heat Carrier	Steam	Water			Water or Brine
Typical Distribution Temperatures	Very high, below 200°C	High, above 100°C	Medium, below 100°C	Low, 30 to 70°C	Ultra-low, below 30°C (near ground temperature)
Efficiency	Very low	Low	Medium	High	High
Heat Sources	Main coal steam boilers	Coal and oil boilers and CHP plants	Mainly CHP plants, as well as some biomass, waste, and fossil fuel boilers	Waste heat and renewable sources, with HPs and thermal stores	Waste heat and renewable sources, with chillers, HPs and thermal store
Network Components	in-situ insulated steel pipes within concrete ducts, very large components	In-situ insulated steel pipes within concrete ducts, very large components	Pre-insulated steel pipes with lean network components	Flexible pre-insulated pipes with smaller size and improved insulation	Pipes are larger, can often be uninsulated and made of polymeric materials
Motivation	Comfort and reduced risks	Fuel savings and reduced operational costs	Enhancing energy security	Transformation towards a smart low carbon energy system	Bidirectional energy flow (prosumers) and enhanced integration with smart energy systems
References	Werner (2017) Lund et al. (2014)	Werner (2017) Lund et al. (2014)	Werner (2017) Lund et al. (2014)	Werner (2017) Lund et al. (2014) Ziemele et al. (2018) Schmidt et al. (2017)	Buffa et al. (2019) Pattijn & Baumans (2017) Pellegrini & Bianchini (2018) Revesz et al. (2020)

2.6. Heat Pumps and Waste Heat Recovery

HPs are devices that use electrical energy to transport heat from a low-grade (i.e. low temperature) heat source, to a higher-grade heat sink. The efficiency of the process is expressed by its coefficient of performance (COP), which relates the necessary electrical input with the total heat output. Typically, the COP is a function of the temperature difference between the heat source and heat sink, meaning that exploiting high temperature sources can lead to significant benefits in terms of reducing the energy input required to reach the necessary temperature for supply. In 5GDHC and 4GDH networks, which are characterised by low distribution temperatures, HPs can operate with even higher efficiencies, particularly when coupled with heat sources of higher temperature, as the temperature difference between source and sink is further reduced. By achieving high COPs, HPs can operate with low electricity inputs, leading to low carbon intensities per unit of delivered heat as the electricity grid decarbonises. This is illustrated in Figure 2.7, which shows how HPs can lead to much lower emissions per kilowatt-hour (kWh) when compared to typical counterfactuals, such as natural gas boilers and electric space heaters, as well as against hydrogen boilers.

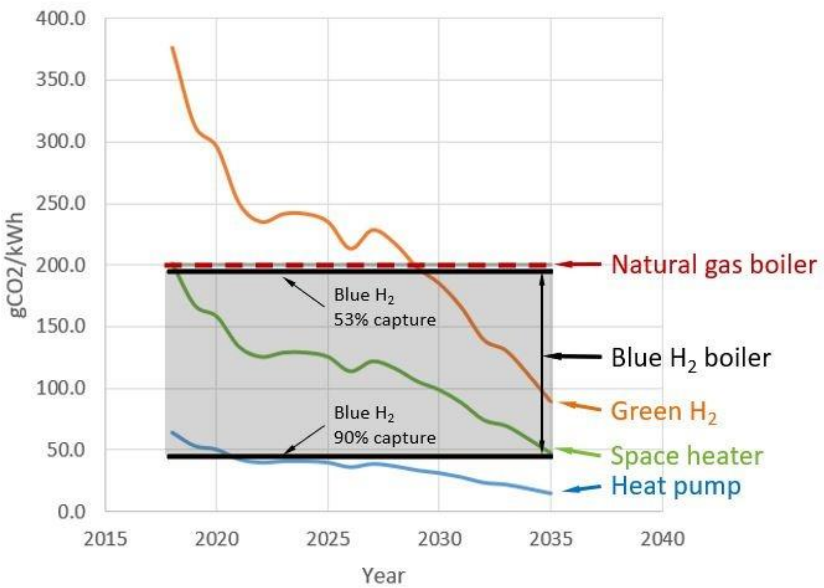

Figure 2.7 – Emission intensity of heat produced by different technologies based on carbon intensity of the grid projected by BEIS (Cebon, 2020).

Cebon assumed a HP COP of 3.0, an efficiency of 95% for electric space heaters, and typical efficiencies for both green and blue hydrogen production processes. Another study by UKERC (2020) demonstrated how even a lower seasonal COP of 2.5 could lead to carbon intensities as low as 16 gCO_2e per kWh of heat delivered by HPs in 2035. By exploiting waste heat, much higher COPs can be achieved, reducing the carbon intensity even further. This makes waste heat a valuable resource that is widely available in urban areas, as commercial/industrial activities release significant amounts of thermal energy in their day-to-day operation.

2.7. Urban Waste Heat Sources

Waste heat can be defined as heat rejected from commercial/industrial activities because its temperature is too low for direct use (ASHRAE, 2020). Urban WHR offers a wide range of possibilities as heat can be reclaimed from several sources. Due to its typical low grade, waste heat found in cities can be well integrated into DHNs, connectable with or without upgrade by a HP. This depends on the temperature of the heat source, as well as on the generation of the connecting heat network and its operating temperatures. Many authors have investigated the potential of harnessing urban waste heat from a variety of sources, some of which are compared in Table 2.2 based on a review of related studies in current literature. Each source is summarised according to its typical temperatures, availability in the urban environment, seasonal variation as well as its potential advantages and restrictions as a waste heat source. The following subsections describe each of the analysed heat sources in more detail.

2.7.1. Data Centres

The potential of recovering waste heat from data centres has been investigated by Ebrahimi et al. (2014), Davies et al. (2016) and Wahlroos (2018). The proposed methods involve reclaiming heat from either the hot air exiting the racks, typically from 25 to 45°C, or the chilled water system commonly used to provide cooling to the computer rooms, leading to lower heat recovery temperatures that can vary from around 10 to 20°C. If direct liquid cooling is applied, waste heat is then available at higher temperatures (50 to 60°C), as shown in Table 2.2.

2.7.2. Electricity Distribution Systems

Electricity distribution systems provide a good opportunity for heat recovery as electrical losses associated with resistive heating can generate significant amounts of waste heat. The potential to recover waste heat from cable tunnels in London has been investigated by Davies et al. (2019a), who proposed a system that can either cool cable tunnels (cold-led) while recovering heat from ambient air (6 to 19°C) or recover heat from exhaust ventilation air (heat-led) at higher temperatures (27 to 32°C). Other waste heat sources of great potential are electrical substations, which are used throughout the electricity grid for stepping up and down voltages for the transmission and distribution of electricity, a process with inherent energy losses in the form of heat. This potential has been investigated by Imperial College London & Sohn Associates (2014) and Hazi et al. (2013), who demonstrated how different transformer cooling systems have varying potentials for WHR. Generally, waste heat can be reclaimed from electricity substations at temperatures that vary from 30 to 70°C. Amongst the different cooling methods, pumped oil circulation through the transformer core, with the heat absorbed by the oil then transferred to a pumped water loop represents an interesting technology for heat recovery, as a heat exchanger could be easily retrofitted into the water loop.

2.7.3. Industrial Plants

WHR can also be achieved in industrial sites (e.g. metallurgical, glass, cement, ceramics, and paper), which involve many energy intensive processes that generate substantial amounts of recoverable surplus heat. This potential has been investigated in the works of Hammond and Norman (2014), Law et al. (2013) and Fang et al. (2015), which highlight how industrial waste heat can be exploited in different ways, such as to generate electricity, heating or cooling, as temperatures can vary from 40 to over 550°C. According to Hammond and Norman (2014), low-grade industrial waste heat could be exploited by HPs, whilst absorption chillers were identified as an efficient use for excess heat at temperatures from 100 to 300°C, with higher temperature heat being suitable for generating electricity. One challenge associated with industrial plants is that they are often located far away from densely populated areas, whereas heat networks tend to be more economical in urban areas.

2.7.4. Wastewater

Wastewater offers the potential of a widespread resource for low temperature waste heat, with wastewater in sewers normally at temperatures greater than ambient, as most of the water comes from buildings, where it has been heated. Wastewater can be used at different stages of the sewage system, so WHR can be implemented within households, on sewer lines, or at treatment plants. These possibilities were investigated by Cipolla and Maglionico (2014) in Italy, whilst Culha et al. (2015) reported on case studies from Germany, Japan, and Switzerland. The authors highlighted that although recovering waste heat from treatment plants is efficient and technically feasible, the distances between treatment plants and consumers often pose a challenge. Although wastewater temperatures vary seasonally and are sensitive to local weather, the reported studies show that temperatures typically rise from around 10°C during the winter to up to 30°C during the summer.

2.7.5. Supermarkets

Other potential secondary energy sources in urban areas are supermarkets. As food storage requires low temperatures, vapour compression refrigeration systems must be deployed which, in turn, reject waste heat through condensers and desuperheaters. Ge and Tassou (2014) presented a case study for the refrigeration system of a supermarket in northern UK from which heat could be recovered at a maximum temperature of 35°C. Polzot et al. (2017) reported that a CO_2 refrigeration system with heat recovery could be used to meet the heat demands of a supermarket, leading to energy savings of up to 6.5%. One challenge with heat recovery from supermarkets is that although high condensing pressures lead to a greater opportunity for heat recovery, this comes at the cost of increasing compressor power consumption and can ultimately reduce the cost effectiveness of WHR.

Table 2.2 – Potential urban waste heat sources for district energy and their characteristics.

Waste Heat Source	Typical Temperatures	Availability	Seasonality	Advantages	Restrictions	References
Data Centres	10 to 20°C (chilled water) 25 to 45°C (air) 50 to 60°C (liquid)	Can be located in urban centres or remote areas	Operates constantly throughout the year	The heat recovery system can add resilience to the standard cooling system	As operation is constant, heat recovery needs to be included early in design stage	Ebrahimi et al. (2014) Davies et al. (2016) Wahlroos et al. (2018)
Electrical Cable Tunnels	6 to 19°C (cold-led) 27 to 32°C (heat-led)	Available in cities with underground power cables	Operates constantly throughout the year	Can also provide cooling to the tunnels depending on method	Temperature variation for cold led systems can affect efficiency	Davies et al. (2019a)
Electrical Substations	40 to 70°C (oil) 30 to 42°C (water)	Available in urban areas, but not widely	Operates constantly throughout the year	Depending on cooling method, can be easily connected to heat recovery system	Retrofitting is likely to be a challenge as transformers need constant cooling; access an issue for security	Imperial College London & Sohn Associates (2014) Hazi et al. (2013)
Industrial Plants	30 to 100°C (heating) 100 to 300°C (cooling)	Usually located in outskirts of cities, in areas not so densely populated	Operates constantly throughout the year	Heat can be available at much higher grades, being able to supply cooling via absorption chillers	Disruption in production or site closure can affect the heat supply; distance from cities might pose a challenge	Hammond & Norman (2014) Law et al. (2013) Fang et al. (2015)
Wastewater	10 to 30°C	Sewers widely available in cities, treatment plants usually in outskirts	Operates constantly throughout the year	It is a relatively stable heat source, proving to be more reliable than ambient air	Biofilm can accumulate on the heat exchanger, reducing its efficiency	Cipolla & Maglionico (2014) Culha et al. (2015)
Supermarkets	<35°C	Widely available in cities, especially in central areas	Operates constantly throughout the year	Overall energy efficiency of supermarket is increased, particularly in mild climates	Higher heat recovery rates increase power consumption; Mismatch between peak heat generation and demand	Ge & Tassou (2014) Polzot et al. (2017)
Underground Railways	15 to 18°C (Glasgow) 20 to 32°C (London)	Limited to cities with UR systems	Operates constantly throughout the year	Can also provide cooling to the tunnels depending on method	Mismatch between peak heat generation and consumer demand	Ninikas et al. (2016) Gilbey et al. (2011)

2.7.6. Underground Railways

Railway tunnels represent a great opportunity for WHR in cities where public transport heavily relies on UR systems. The potential to recover waste heat from URs in the UK has been investigated by Ninikas et al. (2016) and Gilbey et al. (2011), who analysed the environment of the subway systems of Glasgow and London, respectively. Ninikas et al. (2016) measured the annual temperatures in a station of the Glasgow subway and reported annual variations between 15 and 18°C while the outside average temperature ranged from 4 to 16°C, indicating how HPs can operate more efficiently using the underground air (rather than ambient air) as a heat source. The London study showed that average platform temperatures could be as high as 20°C on a cold winter's day and reach up to 32°C during summer. The authors also analysed different design options for placing a heat recovery heat exchanger, either at stations or in the network's ventilation system, and highlighted how solutions that lead to train service disruptions are unlikely to be considered by LU operators.

As discussed by the CCC (2020) and the IEA (2021), electrifying the heating sector using HPs is a key step in the road towards net zero and should, therefore, become a priority. Amongst all the urban heat sources analysed, URs are particularly interesting for cities such as London, which relies on fossil fuels to meet its high heat demands (GLA, 2018a) whilst having an extensive underground transport network that covers a considerable area of the city. However, many challenges are involved in exploiting waste heat from URs and it is important to select carefully the most suitable technology to recover waste heat from tunnels, maximising energy efficiency without posing any risks to the safe and reliable operation of these rapid transit systems.

2.7.7. Recent Projects on Urban Waste Heat Recovery

Recent nationwide and international projects have focused on the potential of waste heat as a resource for decarbonising heat supply. The second National Comprehensive Assessment (NCA) (BEIS, 2021e) looked at opportunity areas for DHNs in the UK, forming the basis for heat network zoning across the country. The NCA estimated that 61.1 TWh per annum of waste heat could be reclaimed from a number of urban and industrial heat sources. Although this potential is similar to what was estimated for London by the GLA and Buro Happold (2013), the latter study also considered natural sources of heat (e.g. rivers, geothermal and air) and estimated the total potential assuming that HPs would be used to upgrade the heat where applicable. Furthermore, the NCA estimated a total output of 311.3 TWh per year for the UK if other sites such as power plants, CHP systems and incineration processes are considered.

The ReUseHeat project (2020) investigated the potential of urban WHR across Europe; this involved four different demonstrations aimed at recovering waste heat from a data centre, a hospital's cooling system, a wastewater treatment site, and an underground railway station. Furthermore, the project also estimated how much thermal energy could be recovered annually in Europe from data centres, food production and retail, UR stations, wastewater treatment plants, and cooling systems of buildings. The total waste heat available in Europe was estimated at 1842.3 petajoules (PJ) or 511.75 TWh per annum; for the UK, the estimate was of 178.5 PJ or 49.6 TWh of waste heat annually. The annual waste heat output from URs in Europe was estimated by considering monthly average temperature and relative humidity (RH) values for cities containing a total of 37 metro systems across 18 countries. The calculations considered that waste heat would be recovered from stations, assumed an average air flow rate of 30 m^3/s and that station temperatures would vary from 15 to 30°C depending on the location, with heat being recovered by reducing air temperatures to a lower limit of 5°C. The total waste heat output estimated for railway tunnels in Europe was of 35.3 PJ or 9.81 TWh per annum, of which around 2.2 PJ or 611 gigawatt-hour (GWh) account for the UK's contribution, considering the UR systems of Glasgow, Newcastle, and London.

2.8. Waste Heat Recovery from Railway Tunnels

According to the UITP (2018), at the end of 2017, 178 cities in 56 countries worldwide had UR systems, carrying an approximate average of 168 million passengers per day. From 2012 to 2017, annual ridership of urban railway systems grew by 19.5%. These transport networks are likely to grow further in the future, as urban population increases worldwide, particularly in metropolises of developing countries. This expected growth enhances the case for UR networks becoming a significant source of waste heat in urban areas across the world. Energy can be reclaimed from underground trains in different ways; for instance, regenerative braking can convert the kinetic energy of a moving train into electricity that can be reused by the network, thereby slowing the vehicle down while also reducing the heat generated when braking. However, as the current research focuses on waste heat from URs and its potential as a low-carbon source for heating, only technologies that could be applied to reclaim dissipated energy in the form of heat during the operation of the trains are discussed.

A range of investigations into WHR from URs have been reported by different authors. These studies are summarised in Table 2.3 and further described in the following subsections. Table 2.3 also indicates the location where the technology was implemented/simulated; the temperatures and media considered for the heat source; the estimated heat extraction rates; and if it would be possible to retrofit each of the technologies onto an existing network. The heat extraction rates presented by each author are used to calculate how much heat each technology could yield per kilometre of tunnel, considering the typical geometry of the LU deep tube tunnels. The potential for retrofitting depends on the type of technology; for those that involve installing heat recovery elements within the structure of the tunnel, it was considered that they would only be applicable to new tunnel segments. Retrofit was deemed to be possible for solutions that would not affect the tunnel structure and that could be installed without posing any risk to the reliable operation of the trains. As urban transport systems are at the core of most modern cities, any service disruption should be avoided as much as possible, so as to minimise impacts on the urban economy and quality of life.

Table 2.3 – Potential technologies for WHR from railway tunnels.

Technology	Location	Heat Source Medium	Heat Source Temperature	Heat Extraction Rate	Retrofit Potential	References
Energy pile walls and diaphragm walls	Vienna, Austria	Air & Ground	>20°C	30 W/m^2 of earth-contact area	No	Brandl (2006) Adam et al. (2001)
Energy foundation slabs	Vienna, Austria	Ground	>20°C	10 to 30 W/m^2 of earth-contact area	No	Brandl (2006) Adam & Markiewicz (2009)
Absorber pipes attached to geotextile between tunnel linings	Stuttgart, Germany	Air	7 to 9°C	20 W/m^2 of tunnel surface area	No	Buhmann et al. (2016)
Embedded absorber pipes in tunnel segments	London, UK	Air	17 to 36°C	Up to 30 W/m^2 of tunnel surface area	No	Nicholson et al. (2014)
	Jenbach, Austria	Air & Ground	15°C	10 to 20 W/m^2 of tunnel surface area	No	Franzius & Pralle (2011)
	Turin, Italy	Ground	14°C	53 W/m^2 of tunnel surface area	No	Barla et al. (2016)
Geothermal heat exchangers next to tunnels	London, UK	Ground	20 to 30°C	20 to 29 W/m of borehole length	Yes	Revesz et al. (2016), (2019)
	London, UK	Ground	17 to 29°C	18 W/m of borehole length	Yes	Mortada et al. (2018)
Heat exchangers within vent shafts	London, UK	Air	16 to 27°C	12 kW per m^3/s of air flow rate	Yes	Davies et al. (2017, 2019b)

2.8.1. Thermo-active Bearing Structures: Cut and Cover Method

Many of the solutions listed in Table 2.3 are based upon technologies that have been implemented to harvest geothermal energy from the soil. The use of such technologies for recovering waste heat from underground rail networks have resulted in innovative solutions that are both environmentally friendly and cost-effective. Brandl (2006) and Adam et al. (2001) have investigated how foundations and underground structures, including tunnels, can be designed as thermo-active elements able to capture heat from the surrounding environment. Brandl (2006) researched how absorber pipes could be applied to reinforcement cages of bearing structures, such as bored piles, diaphragm walls, and foundation slabs, to capture waste heat from cut-and-cover railway tunnels and stations in Vienna. A case study on a Vienna UR station was provided, where diaphragm walls and slabs were thermally activated. Brandl suggested that small temperature differences of 2 K for the heat carrier fluid could be enough to make the technology economic. Both Brandl (2006) and Adam et al. (2001) reported on a case study that involved recovering 150 kW of heat from a 100 m tunnel section with thermo-activated pile walls connected to a HP serving an adjacent school building, as shown in Figure 2.8. Based on these case studies, Brandl (2006) also provided general heat extraction benchmarks to be used in feasibility studies of 30 W/m^2 for bearing walls and 10 to 30 W/m^2 for foundation slabs.

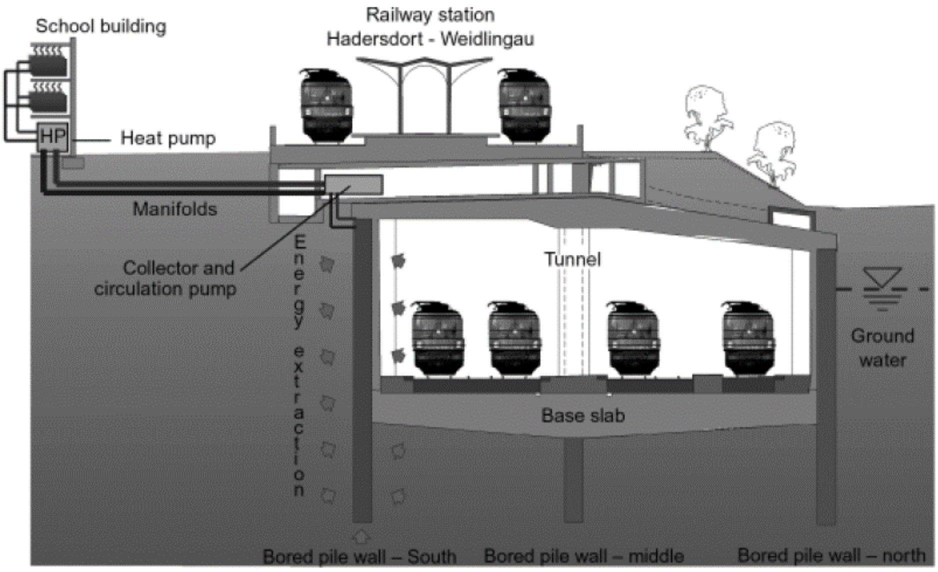

Figure 2.8 – Thermo-active pile walls used for heat recovery from cut-and-cover railway tunnels (Brandl, 2006).

2.8.2. Absorber Pipes Attached to Geotextiles

Brandl (2006) and Adam and Markiewicz (2009) highlighted the potential of heat extraction based on absorber pipes attached to an energy geocomposite placed between the outer and inner linings of a tunnel, with absorber fluid temperatures varying from 10 to 28°C depending on heat source conditions. This technology was applied to tunnels built in the New Austrian Tunnelling Method, which consists of a primary support of reinforced sprayed concrete, rockbolts and anchors, and a secondary lining of reinforced concrete.

(a) **(b)**

Figure 2.9 – Absorber pipes installed within tunnel linings in (a) Vienna (Brandl, 2006) and (b) Stuttgart (Buhmann et al., 2016).

In Stuttgart, Germany, a similar heat recovery trial was conducted on the city's UR system, where absorber pipes were attached to a geotextile and placed between the tunnel linings, covering a total area of 360 m^2 over a 20 m long section of the UR. Based on temperature data from the surrounding soil, tunnel linings, and tunnel air, the authors calculated that heat could be extracted from the tunnels at a rate of 20 W/m^2 (Buhmann et al., 2016). This was calculated based upon tunnel air temperatures that varied from 7 to 9°C during the heating season, with a fixed flow rate of 500 litres per hour for the absorber fluid, an ethylene glycol/water mixture. The fluid temperatures ranged between 0.5 and 1.5°C at the inlet of the pipes and between 6 and 7.5°C at the outlet. Figure 2.9 shows absorber pipes attached to geotextiles from the case studies in Vienna, Austria, and Stuttgart, Germany.

2.8.3. Absorber Pipes within Pre-cast Tunnel Linings

A different design approach is necessary for UR systems built with mechanised tunnelling. A design of railway tunnels with absorber pipes embedded within segments of the tunnel lining is illustrated in Figure 2.10. This technology was reported by Nicholson et al. (2014), who proposed a system able to recover waste heat from the Elizabeth Line (Crossrail) in London, whilst providing cooling to the network. A finite element model was developed to simulate the performance of the thermo-active tunnel segments by analysing how different heat extraction rates would affect the temperature of the heat carrier fluid. The results showed that heat extraction rates are limited by the risk of fluid freezing and can reach up to 30 W/m^2 for a flow rate of 0.12 l/s, with absorber fluid temperatures varying from around 3 to 30°C throughout the year due to the variation of tunnel temperatures between winter and summer.

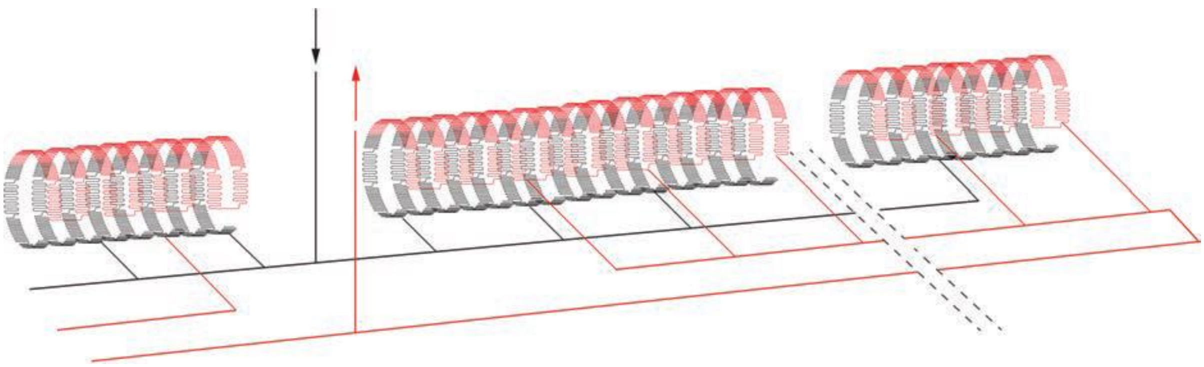

Figure 2.10 – A diagram of the pipework connections of the absorber pipes within pre-cast tunnel linings (Nicholson et al., 2014).

A case study reported by Franzius and Pralle (2011) looked at the same technology for high-speed railway tunnels. Based on field trials carried out in Germany, as shown in Figure 2.11, the authors showed how the heat flux for the analysed heat recovery system would vary from 10 to 20 W/m^2. Prior to the trials, tunnel temperatures of around 15°C were recorded, with heat being recovered at fluid temperatures well above 0°C (specific values were not provided).

The field trials then led to the development of a demonstration project in Austria, where 30 kW could be captured from a 54 m long tunnel section before being upgraded to 40 kW and supplied to a local building in the town of Jenbach.

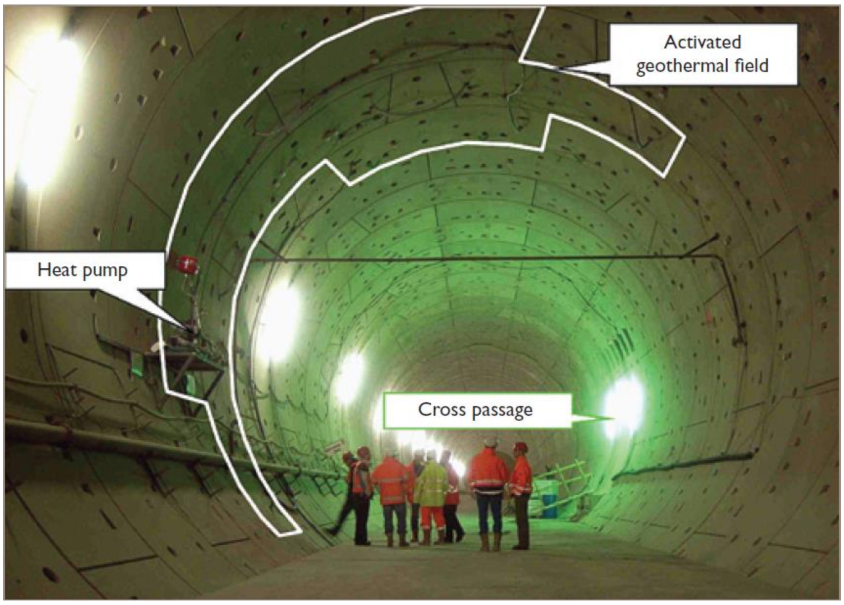

Figure 2.11 – A photograph from field trials for a heat recovery system based on absorber pipes within pre-cast tunnel linings (Franzius and Pralle, 2011).

A similar system was proposed by Barla et al. (2016), who analysed the feasibility of developing an energy tunnel in Turin. The analysis was based on the development of a finite element thermo-hydro model to simulate the heat transfer between absorber pipes within tunnel linings and its surrounding environment, considering that heat would mainly be recovered from the soil. In this case, a heat extraction rate of 53 W/m^2 was estimated, which is considerably higher than the values observed in the investigations reported by Nicholson et al. (2014) and Franzius and Pralle (2011). This was due to groundwater velocity, as the lower heat fluxes of around 10 W/m^2 were previously achieved in simulations without groundwater movement. In this case, the heat carrier fluid (propylene glycol/water mixture) was modelled with a constant inlet temperature of 4°C, reaching approximately 7°C at the outlet of the absorber pipes for a flow rate of 0.6 m^3 per hour. Thermo-active tunnels and bearing structures can achieve high heat extraction rates, although these technologies can only be applied to new UR developments and are not suitable to recover heat from existing tunnels. Other technologies, which could be retrofitted into existing URs, are explored next.

2.8.4. Geothermal Heat Exchangers next to Tunnels

A different approach to recover the excess heat that is generated in railway tunnels was proposed by Revesz et al. (2019). The technology involves utilising geothermal heat exchangers (GHEs) to collect the heat conducted into the surrounding soil during the operation of trains due to the heat sink effect. A finite element model was developed to analyse how GHEs can have their performance enhanced by up to 43% when placed near railway tunnels and how different configurations of GHEs – with varying numbers of rows and loops, sizes, and proximity to tunnels – could affect their heat extraction rate. This was modelled with fixed values for flow rate (0.1 l/s) and inlet fluid temperature (5°C), and the heat extraction rate was assessed in terms of the outlet temperature of the absorber fluid, which could vary from approximately 7 to 15°C depending on the year of operation, converging towards the lowest value over the years. Figure 2.12 demonstrates the interactions between the GHEs and the thermal energy stored in the soil surrounding railway tunnels. Revesz et al. (2016) reported a heat extraction rate of 20 W/m of GHE length from an existing system in central London, which agrees well with values reported by Mortada et al. (2018). By assuming that this could be enhanced by 43%, a heat extraction rate of about 29 W/m could be obtained.

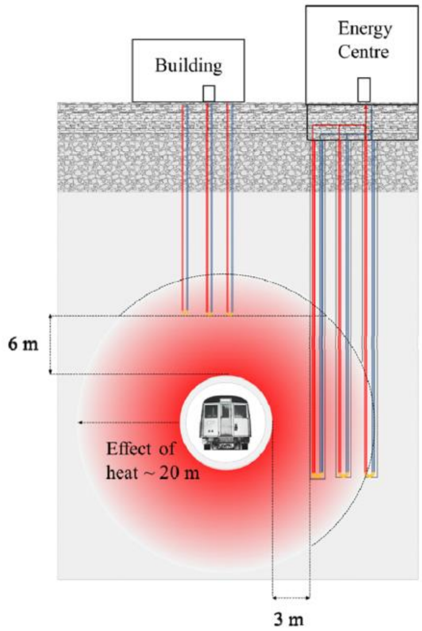

Figure 2.12 – Conceptual schematic of heat recovery from the soil surrounding the tunnels (Revesz et al., 2016).

Mortada et al. (2018) also simulated the interactions between GHEs and URs by coupling a 3D finite element (FE) model of the GHEs with a 1D model of the LU's Central Line. The investigation analysed how the extracted heat could be supplied to local buildings and estimated the cooling effect GHEs would have on the tunnels. The simulation results showed that GHEs could reach an extraction rate of about 18 W/m of borehole length, based on a borehole temperature of 0°C. Overall, this technology is able to recover waste heat from existing URs as it can be deployed independently from the tunnel structural elements. The high capital costs related to the excavation of boreholes represent, however, a significant drawback. Another challenge to its development relates to land ownership, as energy plants would have to be installed along the tunnels, in what could be privately owned areas.

2.8.5. Heat Exchangers within Ventilation Shafts

An alternative heat extraction technology was proposed by Davies et al. (2017), who investigated the potential to recover waste heat from ventilation shafts of the LU network by deploying an air-to-water heat exchanger connected to a HP, a scheme similar to the Bunhill WHR System. The concept of the proposed system is further detailed in (Davies et al., 2019b) and shown in Figure 2.13. The case study was based upon the recovery of 900 kW of heat from a vent shaft with an air flow rate of 75 m^3/s, equivalent to a benchmark of 12 kW per m^3/s of air flow rate. Vent shaft air temperatures were reported to vary between 16 and 27°C, with a 5 K temperature difference modelled for the heat recovery fluid (water), which would operate at different temperatures depending on heat source conditions. Recovering heat from vent shafts represents a great opportunity, as heat can be extracted while keeping service disruptions to a minimum. However, there are still some constraints to this technology regarding the existing LU ventilation infrastructure, namely the usual limited space within existing vent shafts and the low capacity of the fans used for ventilation purposes.

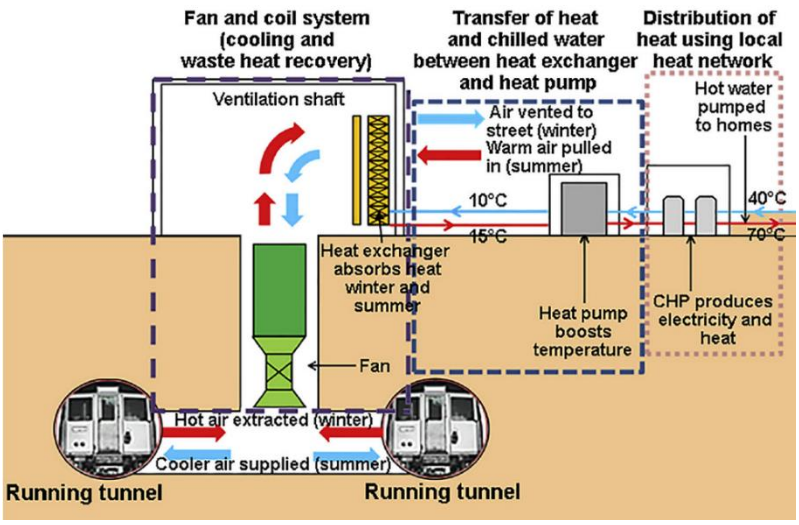

Figure 2.13 – A schematic of the WHR system proposed by Davies et al. (2019b), based on recovering waste heat from a LU ventilation shaft.

2.8.6. Technology Comparison

The literature review on technologies for heat recovery from URs showed that many different solutions have been applied to reclaim waste heat that is generated by underground trains, as summarised in Table 2.3. These technologies have different characteristics and applications that are difficult to compare in quantitative terms, as the potential to recover waste heat would vary according to factors such as typical tunnel air temperatures, type and size of tunnel, as well as absorber fluid temperatures and flow rates. However, an effort to compare these technologies in terms of their published heat extraction potentials was made, and this is shown in Table 2.4. In this case, the technologies were grouped according to their principle of operation, which relates to how the WHR process would take place (e.g. through absorber pipes within tunnel elements, GHEs next to tunnels, or heat exchangers installed within ventilation shafts). The range of heat extraction rates from Table 2.3 was used to provide an indication of how much heat each technology could potentially yield per kilometre of tunnel if applied to the LU deep tube tunnels, considering minimum, average and maximum estimates.

Table 2.4 – A quantitative comparison on the heat recovery potential for different technologies, in kW/km, considering the LU deep tube tunnels geometry.

Technology	Heat Extraction Rate	Calculation Assumptions	Heat Recovery Potential (kW/km)		
			Minimum	Average	Maximum
Absorber pipes within tunnel linings/segments	10 to 30 W/m^2 of tunnel surface or earth-contact area	3.8 m tunnel diameter	119	239	358
Geothermal heat exchangers next to tunnels	18 to 29 W/m of borehole length	8000 m total borehole length installed along 234 m of tunnel	615	803	991
Heat exchangers within ventilation shafts	12 kW per m^3/s of air flow rate	113 ventilation shafts 40 to 75 m^3/s of flow rate 402 km network (45% underground)	300	431	562

The technologies that involved utilising absorber pipes within the tunnel structure were grouped together as their typical extraction rates varied between 10 and 30 W/m^2 of tunnel surface or earth-contact area. The only exception was observed for the work presented by Barla et al. (2016), where a heat flux of 53 W/m^2 was reported due to the presence of groundwater, which would lead to a much higher heat yield. This value was not considered in the analysis as the LU deep tube tunnels are predominantly surrounded by London Clay, a soil of very low permeability (Revesz, 2017). As seen in Table 2.4, when the deep tube tunnel geometry is considered, absorber pipes would lead to heat recovery potentials from 119 to 358 kW/km, the lowest values amongst the analysed technologies. Furthermore, these intrusive technologies are not feasible to be retrofitted into existing tunnels.

Other solutions such as GHEs placed next to railway tunnels offer an opportunity for WHR to take place without affecting structural elements or disrupting train services. The works of Mortada et al. (2018) and Revesz et al. (2019) reported a range of potential configurations for GHEs near tunnels, which could potentially achieve high heat yields varying between 615 and 991 kW/km. These calculations considered the GHE array reported by Revesz et al. (2019), where 8000 m of boreholes would be installed along a 234 m tunnel section. As previously mentioned, however, high capital costs might pose a challenge to the adoption of this technology. This makes WHR from ventilation shafts particularly attractive, as they could be retrofitted and reach significant heat recovery potentials, without causing any service disruption or requiring expensive drilling. Overall, potential heat outputs between 300 and 562 kW/km were estimated for WHR from vent shafts. These values were obtained based on the total length of the underground part of the LU network (45% of 402 km = 180.9 km), and by considering that there are 113 vent shafts spread across London, with an average air flow rate of 40 m^3/s (Gilbey et al., 2011). As fans would likely need to be upgraded to enable heat recovery, a range of air flow rates was included in the analysis, varying from the existing average of 40 m^3/s to a maximum of 75 m^3/s, a design value reported by Davies et al. (2019b).

2.9. The London Underground as a Heat Source

2.9.1. The History of the London Underground

The LU was the first UR system in the world, dating back to 1863, when the Metropolitan Railway was inaugurated to connect what are today's Paddington and Farringdon stations (TfL, 2020a). The first UR line would later become part of the Circle Line, which was completed in 1884 and consisted of sub-surface tunnels built using the cut and cover technique. The first deep tube line would only be introduced 27 years later, when the world's first deep-level electric railway was opened, connecting the City of London to Stockwell, with trains running under the River Thames. This section of the Underground is now part of the Bank branch of the Northern Line, connecting Camden Town to Kennington, which happens to be where the City Road ventilation shaft is located. The term "tube" refers to the construction technique utilised to build the tunnels; at that time, pneumatic tunnelling cut through the earth and cast-iron line segments were used to bear the weight of the surrounding soil, creating a cylindrical structure (History House, 2020). Figure 2.14 shows two photographs highlighting both the cut and cover (a) and tube (b) construction techniques.

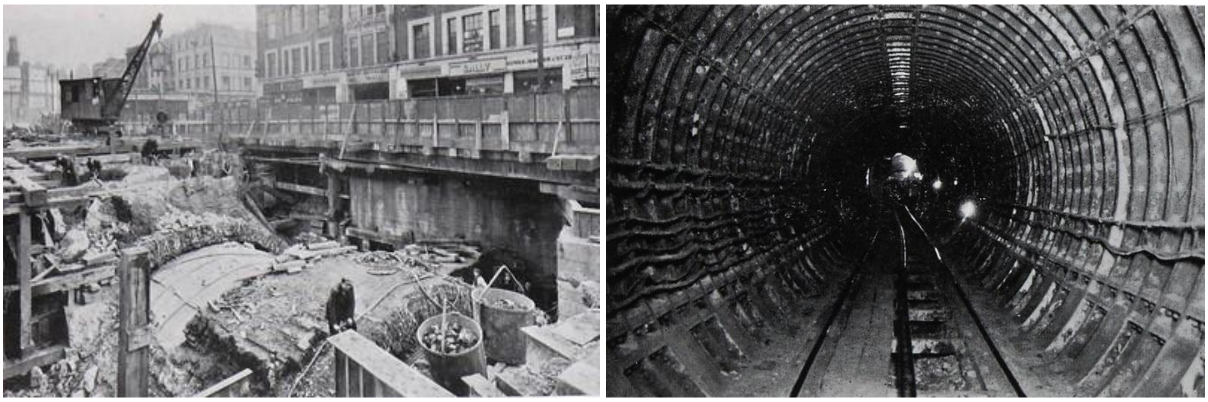

(a) (b)

Figure 2.14 – (a) Demolition of an old sub-surface Circle Line tunnel and (b) a photograph of an original tube tunnel (The National Archives, 1946).

In 1902, the Underground Electric Railway Company of London, commonly known as "the Underground Group" was formed and three deep tube lines were opened. These were the precursors of today's Bakerloo and Piccadilly Lines, as well as the Charing Cross Branch of the Northern Line. By the start of World War I, the Underground Group had merged many lines together into a single administration (TfL, 2020a), in a similar format to what is today the LU network. Figure 2.15 shows the development of the Underground over time, highlighting all the lines inaugurated to date and the decades in which they were opened.

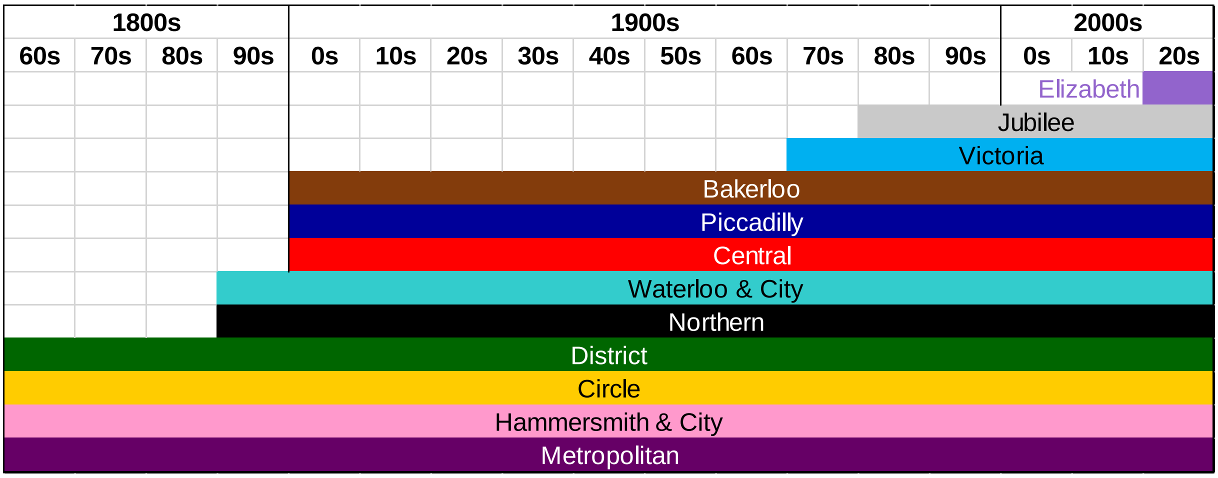

Figure 2.15 – The Underground Lines and their decades of inauguration.

2.9.2. The Current London Underground Network

Since its inauguration in 1863, the LU has grown to a network length of 402 km (45% in tunnels), the fourth longest in the world (UITP, 2018), carrying around 1.35 billion passengers per year. The rolling stock consists of electric trains that achieve an average speed of 33 km/h (TfL, 2019a). The Metropolitan, Hammersmith & City, Circle and District Lines were built via the cut and cover method and are therefore subsurface lines. They typically consist of bi-directional tunnels and have a peak hour train frequency of 30 trains per hour (TPH). The trains are the tallest in the network, with a height of approximately 3.7 m and a width of around 2.9 m. Most trains consist of six carriages with a total length of 91 m. When fully occupied, trains can carry 870 passengers, weighing approximately 160 tons (Revesz, 2017).

The deep tube network is located well below the surface, with its deepest station at Hampstead, on the Northern Line, being 58.5 metres below ground level (TfL, 2019a). The tube tunnelled lines have a typical diameter of 3.8 m and a free cross-section area of 10.2 m^2, operating with train frequencies that vary from 19 to 30 TPH. As the tunnels are narrower, deep tube line trains are smaller, with a height and width of about 2.9 and 2.6 metres, respectively. They vary between six and eight carriages, with a six-carriage train being 106 metres long, carrying up to 800 passengers and weighing ca. 157 tons (Revesz, 2017).

2.9.3. The Thermal Environment of the London Underground

The LU environment has changed significantly since its first years of operation in the 1860s. Back then, tunnel temperatures were mild and much lower than ambient temperatures. In the early 1900s, records show that station temperatures were approximately 15°C during summer, when outside temperatures would reach nearly 29°C. During winter, station temperatures would remain fairly consistent, providing some relief from the cold weather (TfL, 2019b). With the increase in train service and associated energy use, station and tunnel temperatures rose over the years. In 2016/2017, the Underground consumed over 1,700 GWh of electricity, resulting in over 2 million tonnes of CO_2 emissions annually with around 500 GWh of the input energy ending up degraded and released as waste heat (Duffy, 2018). The increase in energy consumption and dissipation from the Underground has led to thermal saturation of the surrounding soil, causing tunnel temperatures to reach above 30°C during the summer.

Figure 2.16 – Recorded temperatures on the LU network for peak-hours in August 2015 (TfL, 2017).

Figure 2.16 shows how network temperatures reached between 26 and 32°C in August 2015. The Central and Bakerloo lines appear to be the hottest, with average temperatures above 30°C for some sections. The high temperatures recorded over the years have led researchers to investigate the main causes behind LU's heat generation. Ampofo et al. (2004) developed a model which calculated that over 80% of the heat load within the LU tunnels came from the braking mechanism of the trains. Similar results were reported by Botelle et al. (2010), who estimated that over 80% of the heat introduced into the network can be traced back to mechanical losses related to the running of the trains; mainly braking friction and resistive losses in the traction-control system. Figure 2.17 illustrates a schematic of the heat loads within a tunnel (a) as reported by Ampofo et al. (2004), as well as a graph with the results from their heat load model (b).

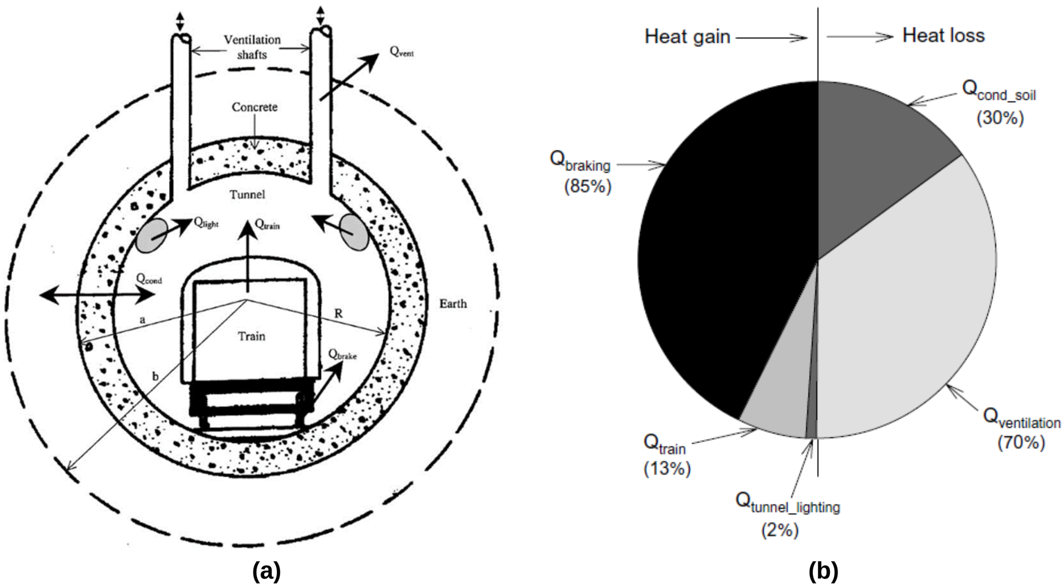

Figure 2.17 – The heat loads within a LU tunnel (a) and their contributions to the overall heat gain, as well as the main causes of heat loss (b) (Ampofo et al., 2004).

As can be seen in Figure 2.17, nearly 70% of the heat removed from the LU environment is through its ventilation system; over the years, ventilation has been essential to reduce tunnel temperatures and guarantee the supply of fresh air to the deep tube network. The ventilation infrastructure mainly consists of station and mid-tunnel ventilation shafts. According to Gilbey et al. (2011), there are 58 station shafts, with flow rates varying from 10 to 60 m^3/s and an average of around 28 m^3/s. As for mid-tunnel shafts, they amount to 55 units, with flow rates between 12 and 90 m^3/s and an average of about 53 m^3/s. These shafts can operate in either (or both) Extract and Supply modes. Davies et al. (2017) proposed that, by recovering waste heat from ventilation shafts, it would also be possible to deliver cooling to the tunnels when required by switching the direction of the fan within the shaft, which represents a unique opportunity to reduce tunnel temperatures or at least diminish the thermal impacts caused by climate change and future increases in train service levels.

2.9.4. Future Perspectives on Waste Heat from the London Underground

Following the official launch of Bunhill 2 in March 2020, Transport for London (TfL) released a prior information notice aimed at engaging with the market on future opportunities for utilising waste heat from LU vent shafts (TfL, 2020b). This followed a project carried out in collaboration with consultancy firm Ove Arup & Partners Ltd, which identified 55 ventilation shafts from which it would be feasible to recover waste heat. These sites were ranked according to criteria such as accessibility, space, nearby waste heat receptors, and possible DHN routes. The most promising sites were shortlisted, and detailed feasibility assessments were carried out for each of them using the Bunhill WHR system as a design reference. The study estimated the capital and operational costs for developing WHR systems at the shortlisted locations, focusing on the amount of heat the system would deliver throughout its lifetime. Other benefits such as cooling, flexibility and particulate emission reductions were not included in the investigation. The main outcomes of the feasibility studies are summarised in Table 2.5.

Table 2.5 – Summary of results from feasibility study on WHR from LU vent shafts (Adapted from TfL, 2020b).

Ventilation shaft flow rate	47 – 100 m^3/s
Nominal HP output capacity	0.6 – 1.5 MW
Primary water circuit (cold loop) flow/return temperatures	11/6°C
HP output temperatures	60 – 85°C
Seasonal COP	2.8 – 3.6
HP annual energy output (depends on development consumption/demand profile)	5 – 10 GWh/annum
System capital cost (excluding pipe network costs)	£2.5 – 4.5 million
Pipe network cost (assuming plastic pipe, distributed at primary water circuit temps)	£960 – 1,600/m

2.10. Cooling the London Underground

As this project also aims to investigate the cooling benefit potentially achieved by WHR systems, the technologies that have been applied to cool the LU will also be reviewed. Conventional cooling technologies such as train air-conditioning might not be suitable for the LU due to the narrow deep tube tunnels; furthermore, air-conditioners would pump heat from the trains into the tunnels, increasing network temperatures (Ampofo et al., 2011). With that in mind, a number of different technologies have been investigated and trialled, including platform air-handling units (PAHUs), ventilation shaft cooling, and heat pipes installed at tunnel walls. The PAHU concept would be supplied with cold water that could be obtained using mechanical chillers or from sustainable sources, such as aquifers and seepage water sumps (Botelle et al., 2010). Seepage groundwater is particularly interesting as over 30 million litres of water already need to be pumped out of the LU network every day. This opportunity has been investigated by Ampofo et al. (2011), who reported on a pilot project based on three fan coil units at Victoria station. The PAHUs were supplied with seepage groundwater and were able to deliver 150 kW of cooling. The concept of the system is illustrated in Figure 2.18. This successful trial led to the development of similar projects at the LU stations of Oxford Circus and Green Park, which utilised mechanical chillers and aquifer boreholes for cold water provision, respectively.

Rowe and Paul (2022) investigated the potential of utilising aquifer groundwater and underground rivers for cooling LU stations. The authors considered the distances between subterranean rivers and London Basin's chalk aquifer to the stations to estimate the costs associated with the proposed systems. The results showed how underground rivers could be particularly interesting, providing up to 19 MW of natural cooling, which could reduce costs over a 10-year period by 3.6 times against vapour compression refrigeration. However, this was only an initial feasibility analysis, and the pumping power requirements to circulate river water through stations were not considered. Another technology that has been successfully implemented is the use of cooling coils within a ventilation shaft. This system was installed at the Forest Road vent shaft on the Victoria Line, and follows a concept similar to the Bunhill WHR system, but using a chiller, with a 920 kW cooling capacity, connected to the coils instead of a HP (TfL, 2019b).

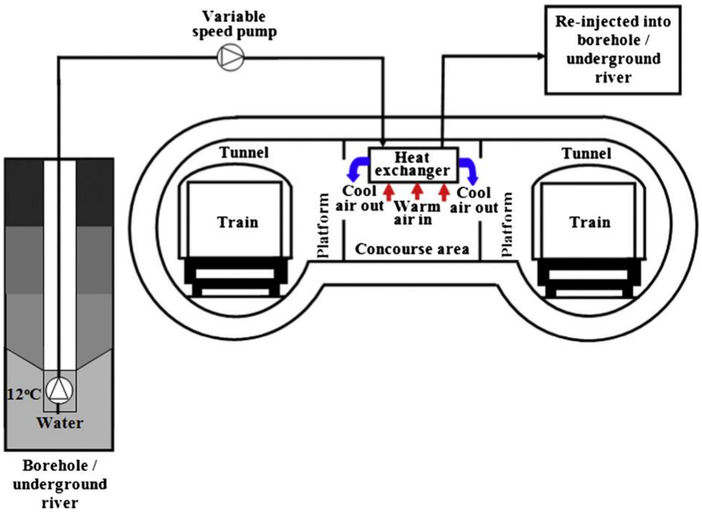

Figure 2.18 – The concept of a groundwater PAHU system trialled at Victoria Station (Ampofo, et al., 2011).

Both PAHUs and vent shaft chiller technologies generate waste heat that could potentially be exploited for heating purposes. Another sustainable yet more intrusive cooling technology was proposed by Thompson et al. (2006b), who looked at inserting heat pipes in the soil surrounding the tunnels to enhance the heat sink effect, thus reducing tunnel temperatures. Overall, cooling solutions are expected to gain importance as air temperatures rise in the future due to climate change, which is likely to increase train service delays (Greenham et al., 2020) and the risk of incidents related to heat stress (Wen et al., 2020). Therefore, the cooling potential of WHR systems will be increasingly valuable, particularly as the integration with heating benefits can help reduce the costs of cooling URs.

2.11. Additional Benefits of WHR from Underground Railways

Recovering waste heat from URs with HPs leads to benefits that go beyond heating and cooling. HPs are expected to replace fossil fuel heating, which is a major contributor to air pollution in cities. Furthermore, the decarbonisation of the UK economy, driven by the national net zero target, will require large-scale electrification of the heating sector. The rise in electricity demand associated with this process will mean that WHR will be increasingly relevant in the future, particularly if coupled with TES, as together they can achieve higher heating efficiencies and alleviate stress on the electricity grid by decoupling heat production and demand. A review of recent studies shows how these benefits have been analysed in terms of their economic impacts, and this will be further discussed in this section.

2.11.1. Thermal Energy Storage and Flexibility

Thermal energy can be stored by different means; the most commonly used being in the form of sensible heat storage in hot water tanks. However, other infrastructures such as pits, aquifers and boreholes can also be applied, particularly when storage is used to overcome seasonal mismatch between demand and supply. Other forms of thermal energy storage (TES) include latent heat thermal storage in the form of phase-change materials (PCMs), which are able to absorb and release significant quantities of energy during a phase change process, as well as thermochemical energy storage (TCES), which utilises reversible endothermic/exothermic chemical reactions to store energy for later use. Although investment costs are high, PCMs offer the advantages of higher energy densities and smaller space requirements, whilst TCES is still at an early stage of development (ESC, 2020b).

Many authors have investigated the role that HPs coupled with TES can play in future energy systems dominated by fluctuating renewable energy generation. Østergaard and Andersen (2021) investigated how the adoption of a variable electricity tax that follows spot market prices, as opposed to a fixed tax structure, could lead to investments in larger volumes of TES and incentivise the flexible operation of HPs. Vijay and Hawkes (2019) analysed how electric heating systems with thermal stores can be used to reduce the curtailment of renewable energy generation by setting the electricity price to zero when generation is excessive, highlighting the importance of time-of-use tariffs to make electric heating systems cost effective and avoid curtailing renewable power generation. Another interesting study was carried out by Patteeuw et al. (2015), who introduced the concept of carbon abatement costs (CAC) to analyse the benefits of introducing HPs with active demand response in Belgium. The study also considered the cost savings that could be achieved by displacing higher cost peak generation plants through flexibility. By combining a HP with TES, it is possible to take advantage of time-of-use tariffs to lower the costs of heat production whist still meeting network demands at all times. Furthermore, with the increasing share of intermittent renewables in the electricity generation mix, the flexibility provided by TES becomes critical, as HPs can be utilised when renewable energy supply is at its peak, enabling heat production to achieve low or even zero carbon intensity.

2.11.2. Flexibility and Electrification Costs

Another important benefit associated with WHR relates to the wider energy system and the upgrades required to enable the electrification of relevant fields within the energy sector, such as transport and heating. Element Energy and Imperial College (2014) estimated that investments of up to £53.4 billion would be required to upgrade transmission and distribution networks to a level compatible with an emission reduction target of 60% by 2030. By utilising waste heat, HPs can operate with higher efficiencies and require less power from the grid. Furthermore, if coupled with TES, WHR systems could shift heat generation away from peak periods, when stress on the electricity grid and heat production costs are higher.

Other studies have looked at the potential of flexibility as a tool for reducing costs associated with electrification. A recent report by the Carbon Trust (2021) has estimated that investing in flexibility across the entire energy system in Great Britain (GB) could lead to savings of up to £16.7 billion per year, which would be associated with a reduction in peak electricity demand of around 25% or 61 GW achieved through a combination of flexibility technologies, such as vehicle-to-grid, batteries, pumped hydro, and thermal storage, in a future scenario where all heat demand would be met with low-carbon district heating and individual air-source heat pumps (ASHPs). In this case, TES could deliver 211 GW of flexibility, which would represent 55% of the predicted flexible capacity for the GB energy system in 2050. An investigation by Piclo Energy (2020) projected that flexibility from demand-side response, which includes smart heating and EV charging, could lead to a 50% reduction in necessary network investments by 2050, reaching annual savings of £4.55 billion, around 60% of which would be associated with network reinforcement costs. The potential benefits of flexibility have been investigated by several authors, but the energy efficiency gains that could be achieved with a WHR system operating flexibly have not been investigated in detail, and this additional benefit of waste heat will be analysed as part of this investigation.

2.11.3. Air Pollution and Emission Savings

The use of fossil fuels for heating represents a significant source of air pollutants that can be harmful to human health. The most common pollutants are particulate matter, nitrogen oxides (NO_x), sulphur dioxide (SO_2), and carbon monoxide (DEFRA, 2021a), with different compounds being released depending on the fuel that is used. As mentioned in section 2.2.3, natural gas boilers represent the dominant heating technology in the UK. The London Environment Strategy shows that commercial and domestic boilers accounted for around a fifth of NO_x emissions in London in 2013 (GLA, 2018a). A report by think tank ECIU (2020) estimated damage costs of around £190 million due to an increase in NO_x emissions from gas boilers in England during the COVID-19 lockdown over the winter of 2020. This was based upon DEFRA's air quality appraisal guidelines (2021b), which provide a methodology for assessing the damage costs of air pollution for different emitting sectors and pollutants. For nitrogen oxides, the economic impacts are derived from health issues related mainly to chronic illnesses (e.g. asthma, diabetes, and lung cancer). NO_x pollution is also a concern for some low-carbon heating technologies, such as biomass and hydrogen, since the pollutant would still be formed as a product of the combustion process of both fuels (BEIS, 2021b). This highlights another advantage of HPs that is often overlooked when compared to other decarbonisation alternatives.

2.12. The Bunhill Waste Heat Recovery System

Within the context of fuel poverty and carbon intensive heating in London, the Bunhill Heat Network was an initiative from Islington Council to supply low-carbon heat to nearby housing estates and service buildings at a lower cost (Islington Council, 2021). The network began operating in 2012 through its first phase, also referred to as Bunhill 1, which was based upon a gas-fired CHP system. This technology was seen as a low-carbon alternative due to its high efficiency and the high carbon intensity of the electricity grid at that time. In an effort to further expand the supply of low cost and low carbon heat to its residents, Islington Council started to research potential extensions to the Bunhill Scheme, which led to the opportunity of developing a WHR system based on heat capture from the LU, in partnership with TfL and the GLA. This project was the first of its kind in Europe and was part of the EU CELSIUS Project. The decision to use waste heat is also related to the decreasing carbon savings now being obtained with CHP systems as a result of the decarbonisation of electricity in the UK.

The Bunhill Heat Network is illustrated in Figure 2.19, which shows its energy centres and connected buildings. The Bunhill 1 Energy Centre comprises a 1.9 MW_e/2.3 MW_{th} CHP unit and a 115 m^3 thermal store. Initially, the network operated with flow and return temperatures of respectively 95 and 75°C. After Bunhill 1 and 2 were connected, the operating temperatures were lowered to 75°C and 55°C in order to accommodate the WHR system. Its main components are a reversible fan, heat recovery coils (HRC) with a nominal capacity of 780 kW, a 1 MW_{th} two-stage ammonia HP, and a coolant loop that connects the coils to the HP. The WHR system was constructed within a new energy centre, which also houses two 237kW_e/372kW_{th} CHP units, with a combined energy efficiency of 91%. A thermal store of 50 m^3 was also installed to provide flexibility and help with managing network demands. As the air flowing through the ventilation shaft has varying temperatures, the coolant loop, which transports the heat from the HRC to the HP, also works with temperatures that float based on the conditions of the vent shaft air. The impacts of these varying coolant temperatures to the system's cooling and heating duties are addressed in Chapter 8. As this project aims to research the novelty related to the system, only the Bunhill 2 network will be investigated in detail, focusing on the first trial to recover waste heat from the LU.

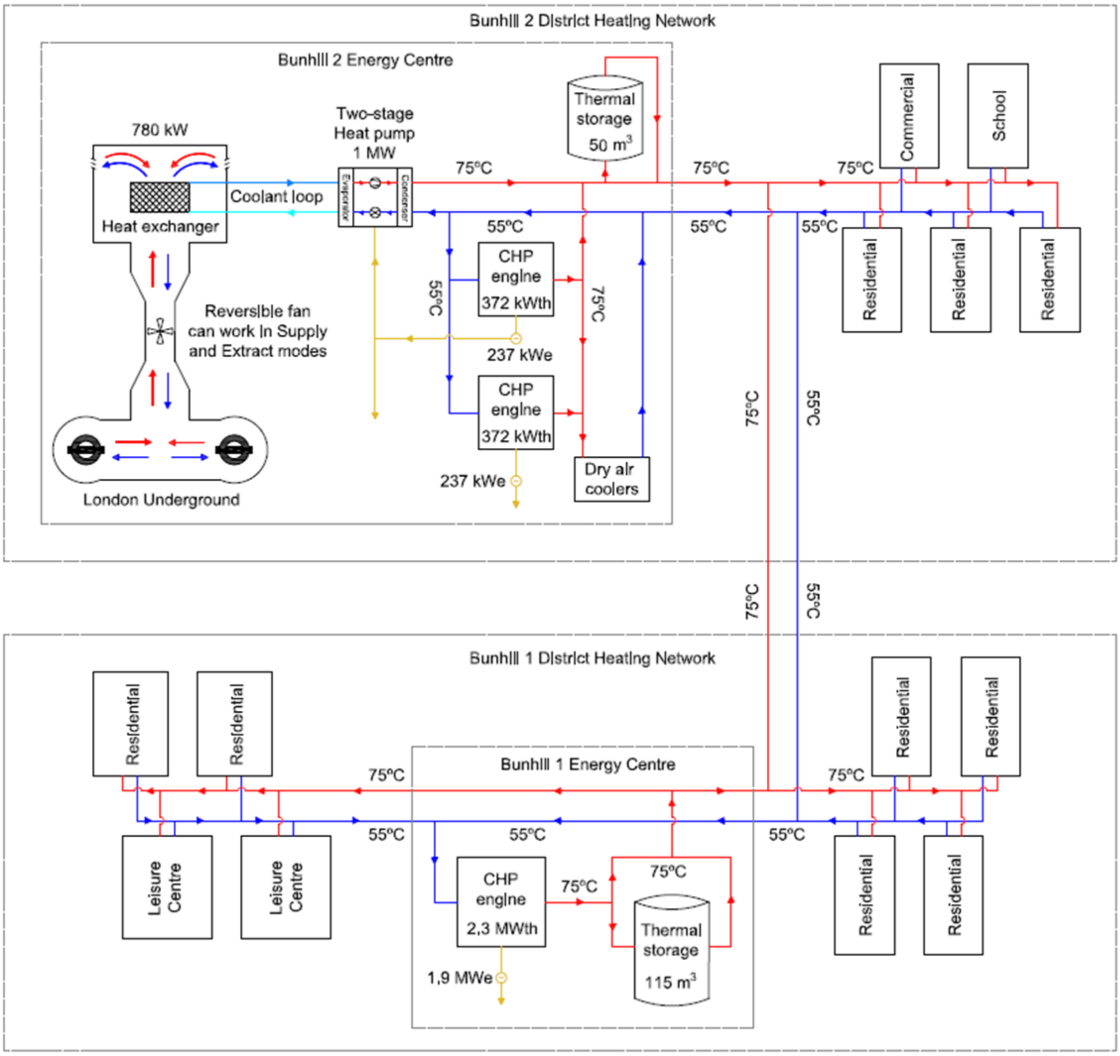

Figure 2.19 – Schematic of the Bunhill Heat Network, including both networks, Bunhill 1 and 2.

2.13. Monitoring the Performance of WHR Systems

As discussed in 2.8, recovering waste heat from URs is still very much at an incipient stage, with only small scale demonstrations having been developed to this date. Therefore, there are limited reports in current literature about monitoring the performance of such systems. The works of Franzius and Pralle (2011) and Buhmann et al. (2016) involved analysing the heat recovery potential of thermally activated tunnels by modulating inlet conditions and measuring outlet temperatures for the heat recovery fluid. Both studies also monitored tunnel air and soil temperatures, which were used to analyse how local conditions affect performance.

Ninikas et al. (2019) and Vasilyev et al. (2019) reported on case studies of HP systems installed at platform level in UR stations in Glasgow and Moscow, respectively. The former study monitored the performance of a 9 kW ASHP system based on electricity consumption and heat meter readings over 9 months of operation. Heat source temperatures were not monitored but the accumulation of dust was found to impact performance markedly, indicating the relevance of monitoring pressure loss across the heat recovery heat exchanger. The study by Vasilyev et al. (2019) provided a similar monitoring approach for a HP connected to absorber pipes, with instruments installed at the inlet and outlet of the HP to monitor how much heating and cooling are being delivered. In the aforementioned studies, the heat recovery potential was estimated from temperature and flow rate measurements for the heat carrier, with the impacts of WHR on the UR environment often being neglected.

Furthermore, other studies have investigated the operation of system components separately, which can be used as references for performance monitoring. For example, Naphon and Wongwises (2005) investigated humid air cooling coils and emphasised the need to measure moisture contents in order to account for the occurrence of condensation when estimating heat transfer coefficients. Several studies have also looked at how to measure the performance of HPs accurately. Tran et al. (2012) proposed a metering strategy to determine heat output from an ASHP based on measurements on the refrigerant side. The authors showed how this approach can provide greater accuracy when compared to common meters which are placed on the heat source/sink side. Kwon et al. (2013) investigated how critical parameters such as heat source/sink flow rates and temperatures, as well as compressor speed, may affect the performance of a two-stage HP using waste heat. The results indicated the need to monitor pressure lifts, superheats and suction/discharge pressures when analysing the behaviour of HP systems. The findings reported in the aforementioned studies, together with the monitoring strategy in place for the Bunhill WHR system, have been used to develop a data collection plan for this project, which is described in detailed in Chapter 6.

2.14. Modelling the Performance and Impacts of WHR Systems

Mathematical modelling consists of representing a system in terms of the mathematical relations and physical concepts that define its operation, simplifying its components and enabling the prediction of its behaviour under different circumstances. To analyse the potential benefits of WHR from the LU, a mathematical model was developed based on the design specifications of the Bunhill WHR system, allowing its performance to be investigated under different heat source conditions and operation modes. This model of the WHR system was then coupled with a DHN model to evaluate the potential carbon and cost savings achieved through waste heat against conventional technologies, considering the secondary benefits of cooling and flexibility. In terms of cooling, additional modelling was carried out to investigate how the coolth delivered by the WHR system would impact the LU tunnelled environment. The model of the WHR system will hereinafter be defined as the WHR model, whilst the model that analyses the impact of cooling to the URs will be referred to as the UR model. The objective behind this section is to review adequate tools for modelling the performance of the Bunhill WHR system and its implications to the LU environment. One key aspect of modelling energy systems is to find the right balance between complexity and accuracy. Reasonable simplifications must be sought whilst keeping the model detailed enough to capture the behaviour of the system with sufficient accuracy. With that in mind, different tools were compared in order to identify the most suitable for the development of the aforementioned models. The following sections describe the main tools reviewed and their capabilities.

2.14.1. The WHR Model

The model of the WHR system forms the core of this investigation and can determine the system's energy efficiency as well as its heating and cooling outputs for different operating conditions throughout the year. The efficiency of the WHR system can be expressed in terms of modelled COP values which are used as inputs for the heat network model in order to compare the benefits of recovering waste heat from URs against the performance of typical technologies used to provide heating. The cooling output calculated using the WHR model also serves as an input for the UR model simulations, which should indicate how tunnel temperatures are affected when cooling is delivered by the WHR system. There are many modelling tools reported in current literature that have been used to analyse the performance of HP based heat networks, and a table summary of these can be found in Appendix A.

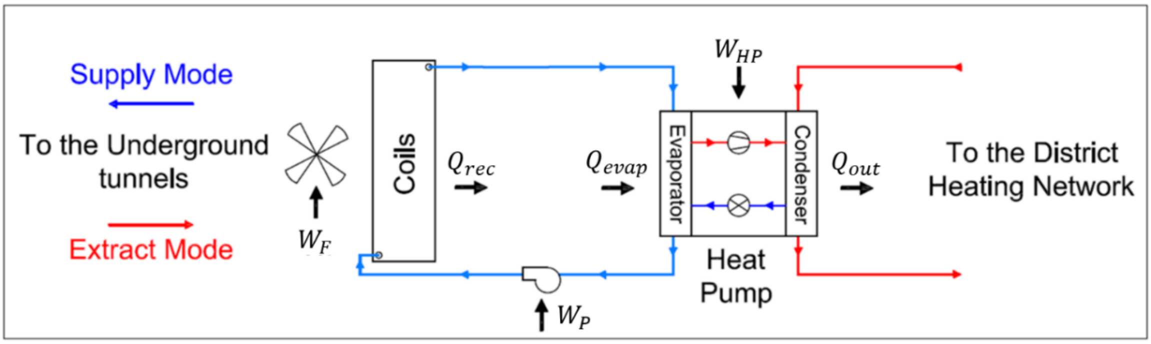

Figure 2.20 – Schematic highlighting energy inputs and outputs associated with the WHR model.

The analysis of such complex energy systems, involving heat generation, distribution, and demand, requires the deployment of different tools, capable of simulating specific parts of the system in detail. The first step in this process involves modelling the WHR system, which consists mainly of the HP, the HRC, and the reversible fan. The components of the system are described in more detail in Chapter 4 and a simplified schematic of its operation is provided in Figure 2.20, highlighting the main energy outputs to be calculated by the model. These refer to the electricity used to run the fan (W_F), the coolant circulation pump (W_P), and the HP (W_{HP}) as well as the heat delivered (Q_{out}) and recovered (Q_{rec}) by the system. The WHR model should be able to iteratively solve thermodynamic balance equations across the system, considering the heat transfer regimes that characterise heat recovery and HPs. The main tools that have been identified as suitable for this purpose are listed in the following subsections.

2.12.1.1. Coolpack

Coolpack is a tool that comprises a number of simulation models for refrigeration systems which can be applied for specific purposes such as cycle analysis, component sizing, energy analysis and optimisation (IPU, 2019). Coolpack offers a user-friendly interface through which users can input parameters and calculate specific values related to cycles and components of refrigeration systems (e.g. COP of HP cycles and UA values for heat exchangers). The software can be useful in terms of simulating the operation of specific components, but it is not suitable for systemic analyses and is not suitable for temporal analysis as the input parameters are not time dependent. Furthermore, it focuses on refrigeration systems and it is unable to model heat recovery with air-to-water heat exchangers. In terms of environmental and economic benefits, the software has a simplified life cycle cost functionality based on fixed annual values that must be inserted by the user. Therefore, Coolpack is not suitable for modelling the WHR system according to the objectives of this project.

2.12.1.2. TRNSYS

TRNSYS is defined as a platform for the analysis of transient systems, being applicable not only to thermal and electrical energy systems, but also to other dynamic systems such as traffic flow and biological processes (TRNSYS, 2019). The tool consists of two parts, an engine that performs calculations to determine the flows within the system concerned and a library of components that can be used in modelling. The tool also allows users to modify components or even write their own in programming languages such as Fortran, C and C++, providing valuable flexibility. According to Allegrini et al. (2015), TRNSYS can be applied for detailed thermal and electrical modelling, being suitable for simulating HPs, DHNs and seasonal storage systems. Allegrini et al. (2015) also stated that TRNSYS is not suitable for modelling air flows or district heating applications, even though the authors reported some papers in which TRNSYS was used for such purposes. Safa et al. (2015) used TRNSYS to simulate the heating and cooling demands of a building and the performance of a two-stage ASHP based on experimental data. Overall, TRNSYS is a powerful and flexible tool, able to provide detailed simulations of energy systems. However, some limitations were reported in the reviewed literature, particularly regarding air flow simulations, which could represent a challenge when modelling the air-to-water heat exchangers such as the HRC.

2.12.1.3. Engineering Equation Solver (EES)

EES is a steady state equation-solving program that numerically solves coupled non-linear algebraic and differential equations; it is also used to solve integral equations, carry out optimisations, provide uncertainty analyses and perform linear or non-linear regressions (F-Chart Software, 2019). The software also has an extensive thermodynamic database, providing the properties of hundreds of substances, including air, ammonia, brines, and water. EES is a highly flexible tool, as it allows the user to apply its built-in functions as well as introduce their own equations. Ghoubali et al. (2014) used EES to model a HP that delivered heating and cooling simultaneously and analysed its seasonal COP based on a TRNSYS-EES interface; the model was validated by an experiment and discrepancy was lower than 5%. Madani et al. (2011) also applied a combination of TRNSYS and EES to analyse potential capacity control methods for GSHPs (e.g. using variable speed compressors and pumps). Once again, EES was used to develop a HP model, whilst TRNSYS was used to develop the other components of the heating system. The experimental validation showed that the model achieved less than 15% deviation from the measurements. EES is ideally suited for modelling small energy systems (e.g. single energy source), although it may be less suitable for district level models as these may become too complex and require significant computational effort.

2.14.2. The Heat Network Model

The WHR model was coupled with a heat network model to analyse the holistic efficiency of the system, considering energy losses and pumping power required to distribute heat to end users. This enabled comparing the WHR system against conventional heating technologies, indicating the carbon and cost savings potentially achieved with waste heat. The study of thermodynamic principles combined with economic analyses is defined as thermoeconomics and it is critical for the analysis of energy systems, as the flow, conservation, and conversion of energy have significant economic and environmental implications (Demirel and Gerbaud, 2018). Therefore, the coupling of both WHR and DHN models served as the basis for a thermoeconomic analysis, which was used to investigate the efficiency of the WHR scheme as a source for district heating from economic and environmental perspectives. The following subsections describe a couple of tools that could be applied for this purpose.

2.12.2.1. Termis

Termis is a hydraulic modelling platform that simulates the flow, pressure, and thermal behaviour of district energy networks (AVEVA, 2019). Termis focuses on using real-time data to help DHN operators streamline production and enhance the system’s economic performance. The tool aims to deliver savings in operating costs and carbon emissions by optimising operating parameters (e.g. temperature, flow rates, and pressures) and system components (e.g. pumps, heat sources, and thermal stores) (Allegrini et al., 2015). Gabrielaitiene et al. (2007) compared a custom-built model to a TERMIS model to analyse if these tools can be used to effectively predict the dynamic performance of heat networks; they reported pronounced discrepancies between modelled and measured data for the supply temperatures of consumers located at greater distances from the heat source, but satisfactory results when analysing return temperatures at the heat source. Termis is focused on offering intelligence to assist the operation of DHNs, being unfit for scenario analyses.

2.12.2.2. Thermos

Thermos is a Geographic Information System (GIS) based tool designed to assist energy planners in feasibility studies on heat networks. Based on GIS shapefiles, the software estimates annual and peak demands for heating in a selected area while also providing the optimum route for a DHN based on identified anchor heat loads. After heat loads are calculated and a route is established, the tool allows the user to choose a heat source and, based on fixed predetermined values, yields performance indicators for the network, such as emissions produced, net present value, internal rate of return and payback period of the project (THERMOS Project, 2019). One potential limitation of Thermos is its inability to account for time-of-use tariffs, which are essential when modelling the operation of TES technologies.

2.12.2.3. energyPRO

energyPRO is a simulation tool that enables the techno-economic modelling of complex energy systems, which may involve different energy vectors and technologies. It is ideally suited to perform optimisations of DHNs that operate with HPs and TES under different electricity market conditions (EMD, 2014). The software can model district heating systems and include several energy sources, including CHP engines, HPs, and renewables (Allegrini et al., 2015). As reported in the work of Østergaard and Andersen (2021), energyPRO is based upon a cost optimisation approach which follows a non-chronological order, ensuring timesteps with the highest priorities in terms of the cost of heat production are solved first. Østergaard and Andersen (2016) used energyPRO to compare different district heating configurations and identify how decentralised booster HPs could increase the overall efficiency of the network. The authors reported that the tool can model energy systems at a user-defined level of aggregation, being able to adjust the COP of a HP, for instance, according to other parameters such as heat source temperature.

The software has also been applied in other studies, such as the work of Revesz et al. (2020), who modelled a 5GDHC smart energy network involving the provision of heating, cooling, mobility, and power in London. Another investigation carried out with the tool was reported by

Marques et al. (2021), who used it to assess the feasibility of connecting the same 5GDHC network to the Bunhill Heat Network, which is described in this investigation. Hinojosa et al. (2007) compared energyPRO to other tools that can be used for feasibility studies of CHP projects and reported that it is suitable for simulating the operation of flexible energy systems. energyPRO was reported as being particularly interesting for a systemic analysis, meaning it could be used to model a waste heat based DHN, considering important aspects such as flexibility and the variation of COP with time.

2.14.3. The UR Model

Many authors have reported the deployment of mathematical models that simulate the environment of URs. These models are either custom built to simulate a specific section of the tunnel or developed to provide a thorough thermal analysis of the UR environment (Revesz, 2017). The modelling method can be either analytical or numerical. Analytical models yield an exact solution to the problem at hand, based on algebraic equations. This solution is often provided rapidly and with a reasonable degree of accuracy within certain constraining limits defined by the modelling functions. In the case of numerical models, they transform the partial differential conditions of a system into a set of ordinary differential equations or algebraic equations that are easier to solve, providing an approximate solution that is within acceptable limits. Numerical modelling is particularly useful when dealing with complex problems with unusual geometry or thermal interactions. When analysing transient systems, numerical models that deploy different solving techniques, e.g. finite difference (FD) and finite element (FE) methods, can be applied to approach a problem, providing solutions that can integrate models with different dimensions (1D, 2D and 3D) and timescales. Although 3D modelling tends to lead to more accurate solutions, 1D can still be applied to reduce computational complexity without compromising accuracy. This is commonly the case for heat transfer applications in URs, where the entire cross section of a tunnel can be represented by a single one-dimensional point. The FD method, often used in 1D modelling, consists of breaking down the geometry of the studied environment into discrete nodal points at which energy balances and rate equations are solved. As for FE, the differential equations are transformed into an integral form which is then solved for specific subdomains that are typically 2D or 3D.

According to Mortada (2016), the modelling of heat transfer through tunnel walls and in specific sections of tunnels requires applying conduction and convection heat equations through FE methods. However, as stated before, these models demand considerable computation effort and simplification should be sought as long as it does not affect reliability. Thompson et al. (2006a) stated that using a numerical method is necessary when dealing with the heat sink and thermal storage effects of URs due to validation restrictions of analytical models. The authors also highlighted that FD methods, despite being less accurate, provide faster solutions than FE and that both techniques can be combined depending on the desired performance of the model. Potential tools that could be applied to model the UR environment were analysed and the following subsections describe their features and limitations in detail.

2.14.3.1. COMSOL Multiphysics

COMSOL Multiphysics is a simulation software for numerical modelling of designs, devices and processes that can be applied to a wide number of fields within engineering. The platform can be used on its own or expanded to incorporate add-on modules, which include computational fluid dynamics for the analysis of systems containing fluid flows and a heat transfer module for the analysis of conduction, convection or radiation phenomena within a system (COMSOL, 2019). This tool was used by Revesz et al. (2019), who analysed the potential of extracting heat by placing vertical GHEs near LU tunnels, as introduced in section 2.8.4. According to Revesz (2017), COMSOL can create geometries using either a 1D, 2D or 3D modelling domain, simplifying the reproduction of the complex format of railway tunnels. Additionally, results can be exported in different formats for use in further analyses. COMSOL also provides a user-programmable interface for equation editing and can be linked to other software such as computer-aided design (CAD) tools and MATLAB, providing valuable flexibility. Its high sophistication makes COMSOL Multiphysics suitable for modelling railway tunnels in a great level of detail, which can, however, be computationally expensive.

2.14.3.2. Dynamo

Dynamo is a 1D tool developed by engineering consultancy WSP (2018) that allows performing a fully transient, multi-year, long-term simulation of a tunnel. Dynamo can forecast tunnel air and wall temperatures over long time periods, accounting for both variations in air flow and heat loads. However, Dynamo was initially developed for use in cable tunnel thermal analysis and for that reason is unable to directly simulate the movements of trains in tunnels. Therefore, in order to perform thermal analyses of URs, the effects of train movement in terms of heat dissipation and air displacement must be incorporated into the model by the user.

2.14.3.3. Subway Environment Simulation (SES)

According to Thompson et al. (2006a), SES is the most commonly used tool in the field of UR assessment and design. The software provides 1D simulations of the operation of trains in tunnels, allowing the modelling of different aspects of a subway environment, such as air flows, temperatures and humidity levels in stations, tunnels, and ventilation shafts. The simulation considers aspects of train movement, including propulsion and braking systems, as well as environmental aspects such as air conditioning systems and natural/forced ventilation in tunnels and stations. The model provides maximum, minimum and average readings of the aforementioned parameters along the tunnels and can be used to estimate heating or cooling requirements for stations (Thompson et al., 2006a). The tool has been validated in field tests on railway systems in Montreal, Pittsburgh, San Francisco, Toronto and Washington (Thompson, 2006). The tool consists of four interdependent subprograms: performance, aerodynamics, temperature and humidity, and a heat-sink package. This makes SES suitable for a comprehensive analysis of the heat generation within railway tunnels and their cooling requirements. Furthermore, SES is the basis of the bespoke modelling tool used by TfL to simulate the LU tunnelled environment for a range of studies and investigations. This SES based tool was applied during the “Cooling the Tube” project, which looked at different cooling solutions that could be used to mitigate overheating in LU tunnels.

2.14.3.4. Thermotun

Thermotun is a 1D tool that can be deployed to simulate pressures, velocities and temperatures in UR tunnels or stations based on train movements and the operation of fans (Dundee Tunnel Research, 2019). The software can handle complex systems with several tunnel elements, being able to incorporate different elevations, temperatures and geometries. 1D models provide simplicity of use and enable reliable solutions to be reached with relatively high computational speed. However, the main disadvantage of such models is their lack of details on the 3D effects, assuming uniform flows in each cross section (Dundee Tunnel Research, 2019). Thermotun has been validated with experimental data from the Grauholtz tunnel and the LU, with a high degree of accuracy obtained for pressure fluctuations if the correct tunnel and train parameters are considered (Revesz, 2017). According to Mortada (2016), Thermotun is frequently used as a pre-processing step for thermal analyses, in which air flows are simulated and used as an input to calculate thermal properties, such as temperatures, heat transfer rates and moisture contents, using other software tools. Additionally, the tool is unable to calculate the effects of soil thermal storage and capacitance accurately (Thompson et al., 2006a).

2.15. Conclusion

This chapter has provided a critical review of state-of-the-art research on WHR from URs. The reviewed studies involve both experimental work from case studies and theoretical investigations using numerical modelling, which serve as a basis for determining how to model and monitor the operation of a WHR system. Furthermore, this chapter has also explored the current context of the energy market and its policy landscape, helping to understand how waste heat, from URs and other urban infrastructure, can be coupled with DHNs to help reducing the costs of decarbonising buildings in densely populated urban settings. At first, a review of the current energy sector was undertaken, in the UK and abroad, which showed how the electrification of heat represents one of the main challenges on the path towards net zero. DHNs and HPs have been highlighted as key technologies in this process, as announced in the UK's Heat and Buildings Strategy, which includes policies such as the GHNF, heat network zoning, and the Boiler Upgrade Scheme. A comprehensive review of current research on district energy, with focus on recent 4th and 5th generations, has highlighted how waste heat can be recovered from several different sources to help enhance the efficiency of low-carbon DHNs that operate with HPs as their main energy source. The use of HPs also enables sector coupling between electrical and thermal grids, acting as flexibility assets that can help with managing the fluctuating nature of renewable power generation.

Based on studies reported in current literature, URs were compared to other commercial and industrial applications in terms of the potential to recover the excess heat generated as a by-product of their operation. Different technologies that can be used to reclaim waste heat from URs were then discussed and compared, with the installation of air-to-water heat exchangers within ventilation shafts being emphasised as particularly promising due to their low impact on the transport system and relatively high heat recovery potential. The opportunities for WHR from railway tunnels have been explored in different studies. Most of these studies were either focused on feasibility analyses through numerical modelling or performance investigation of small-scale trials. This indicates how the potential of recovering waste heat from URs still needs to be examined from a large-scale operational perspective.

Investigating the performance of a practical example of WHR from URs represents an opportunity to further understand the behaviour of such systems, as the review has shown that there is still a gap in the literature when it comes to monitoring and modelling their operation as a source of energy for district heating. With that in mind, a number of tools that could be applied to model heat recovery and distribution systems have been identified and reviewed. The literature also lacks exploration of the cooling potential behind systems that recover waste heat from URs. Most investigations reviewed in this chapter have focused either on the benefits of utilising waste heat or on how to sustainably cool URs. Therefore, better understanding of the impacts of WHR on the tunnelled environment would be beneficial, and this can be achieved through the FE and FD numerical modelling techniques discussed in this chapter. Furthermore, other advantages of supplying HPs with waste heat from URs should be investigated in greater detail. These include, for example, improvements to local air quality and power demand reductions for HPs, which are triggered by a flexible and more efficient operation enabled through the use of waste heat and TES. The benefits resulting from WHR are still diffuse and this thesis aims to investigate how they can be quantified, combined and applied to demonstrate how waste heat can become a key resource for minimising the costs of decarbonisation as the UK moves towards a clean energy future.

3. Research Methodology

3.1. Contribution to Knowledge

The critical literature review highlighted how district heating can play an important role in the decarbonisation of the heating sector in the UK, particularly if waste heat sources are incorporated into these energy distribution networks. Chapter 2 also reviewed how underground railways (URs) generate significant amounts of heat in their day-to-day operation, with data recorded in the London Underground (LU) showing how temperatures are often above 30°C during peak summer conditions (TfL, 2017) and can even reach 20°C during winter (Gilbey et al., 2011). Waste heat recovery (WHR) from UR systems can not only increase the efficiency of district energy networks, but also provide much valuable cooling to railway tunnels.

A number of studies have investigated the thermal environment of URs in different countries. Most of the reviewed studies were either focused on determining heat extraction rates from railway tunnels or were aimed at proposing cooling solutions for tunnels and stations. Furthermore, the review showed how research on WHR from URs is still at an early stage, particularly as the analysed studies consisted of conceptual/feasibility investigations and small-scale trials. Therefore, there is scope for new research that can provide evidence of how WHR systems would operate at a larger, district scale. In addition, exploring the combination between heating, cooling and other secondary benefits of the WHR system would be a novelty that this thesis aims to address. These secondary benefits include air quality improvements and mitigating the impacts of decarbonisation on the wider energy system through flexibility and higher energy efficiencies. An integrated approach able to combine these different benefits would represent a means of demonstrating the full potential of waste heat from URs, highlighting its advantages to all stakeholders involved, which include end users of heat, network operators, transport providers, the local community, and the wider energy system.

Therefore, this project's original contribution to knowledge consists of developing a methodology for evaluating the benefits that can be obtained by recovering waste heat from URs, based upon the design of the Bunhill WHR system. The work described in this thesis is mainly based upon mathematical modelling and the collection of experimental data. The experimental work provides evidence on how the WHR system is performing, as well as validation for the mathematical models, which are used to compare the carbon emissions and costs of the system against typical heating and cooling technologies. Furthermore, the models are used to investigate how the system behaves under different conditions, as well as its implications to the LU tunnelled environment and the wider energy system. This work should inform how a first-of-its-kind system that recovers waste heat from railway tunnels would perform at a district level, as well as how it could be operated to enhance its efficiency as a heat source, its cooling outputs, and other secondary benefits.

3.2. Methodology

The methodology developed for this research project is illustrated in Figure 3.1. One of the main pillars of the proposed methodology is mathematical modelling, and three different models are utilised to investigate the potential benefits of the WHR system. Firstly, a model of the WHR system was developed in order to evaluate its heating and cooling outputs as well as its energy consumption when supplying heat to the local district heating network (DHN). This involves calculating thermodynamic balances and deploying heat transfer equations for both convection and conduction in order to model the different heat exchangers that comprise the WHR system. Furthermore, specific equations are applied to model the energy efficiency of other mechanical components, such as the HP's compressors, the reversible fan and the pumps that circulate coolant between the heat recovery coils (HRC) and the heat pump (HP). Amongst the reviewed software tools, Engineering Equation Solver (EES) was identified as the most suitable for analysing the performance of the WHR system due to its high flexibility, equation-based coding and built-in thermodynamic properties for different working fluids. The WHR model involves calculating energy balances at key points of the system, and the reviewed studies have shown that EES has been applied successfully to perform such tasks.

Analysing the impacts of the WHR system on the LU network requires a different type of model that is able to account for the complex thermal interactions that are typical to URs. Factors such as train movement, soil thermal capacitance and ventilation systems have significant impacts on the heat transfer regimes within the UR environment. Therefore, a number of specialised tools were reviewed, as described in section 2.14.3, and the Subway Environment Simulation (SES) platform was chosen as the most appropriate for the simulation of the LU environment. This was due to the fact that SES has been utilised for design, analysis and optimisation of several URs around the world, including the LU. SES has been extensively applied by Transport for London (TfL) when investigating the feasibility of cooling projects for their network and has been validated with temperature measurements from LU stations.

In addition to the modelling work, experimental data was collected in order to investigate how the Bunhill WHR system is performing, as well as to validate the main mathematical model developed as part of this investigation. The monitoring system of the Bunhill 2 energy centre collects operational data from different system components. The instruments used, as well as the data collected are discussed in Chapter 6. Following validation, the developed models are used to compare the performance of the WHR system against conventional technologies and to analyse system behaviour in different scenarios. For this purpose, an energyPRO model is applied, as this tool enables incorporating flexibility elements and time-of-use tariffs into the analysis, which are essential when modelling the operation of a DHN.

3.3. Research Questions

The literature review presented in Chapter 2 and the proposed contribution to knowledge underpin the development of specific research questions that this thesis aims to answer. These relate to the investigation of the actual performance of the Bunhill WHR system, as well as the evaluation of its potential in terms of different benefits that could be achieved through WHR from URs. This led to the development of six research questions, which are addressed throughout the thesis and linked to specific research objectives, as described in Table 3.1.

Table 3.1 – Research questions and objectives for the Heat FUEL Project.

Research Questions	Corresponding Objectives
How does the Bunhill WHR system perform?	To set up an instrumentation strategy, collect operational data and measure system performance.
How can the efficiency of WHR from URs be compared to conventional and low-carbon heating technologies?	To develop an integrated approach that combines WHR and heat network models in order to compare the WHR system's performance against other heating technologies.
How can the secondary benefits of WHR from URs be evaluated?	To incorporate additional value streams such as cooling and flexibility into the developed models and investigate their implications to the overall costs and carbon emissions associated with the WHR system.
What are the expected impacts of the WHR system on the LU environment?	To combine the developed WHR model with a model of the UR environment to investigate how the cooling delivered by the WHR system would affect tunnel temperatures.
What is the potential for replication of this technology?	To extrapolate model results in order to evaluate the overall benefit achieved through the replication of WHR from URs across the UK.
How could the Bunhill WHR system be optimised and what are the lessons learned from this project?	To apply the developed mathematical models to assess optimisation opportunities and provide recommendations for future WHR systems and related research projects.

3.4. Thesis Framework

Figure 3.2 provides the framework for this thesis, illustrating the steps undertaken as part of this investigation. The framework highlights the four main activities that were carried out, namely: Literature Review, Modelling the WHR System, Investigating Impacts on the LU, as well as Results and Discussion. Each main activity is also divided in terms of their contents and corresponding chapters. The Literature Review provided an overview of state-of-the-art research in WHR from railway tunnels and highlighted how it fits into a wider context of heat decarbonisation, and this was used to identify the project's contribution to knowledge. Modelling the WHR System refers to the development of the WHR model and its validation process. The Investigation of Impacts on the LU is based upon the UR model, whilst the final activity, Results and Discussion, focuses on analysing outputs from the modelling work. This includes comparing system performance against counterfactuals, analysing possible improvements to design and operation, as well as investigating the potential for replication.

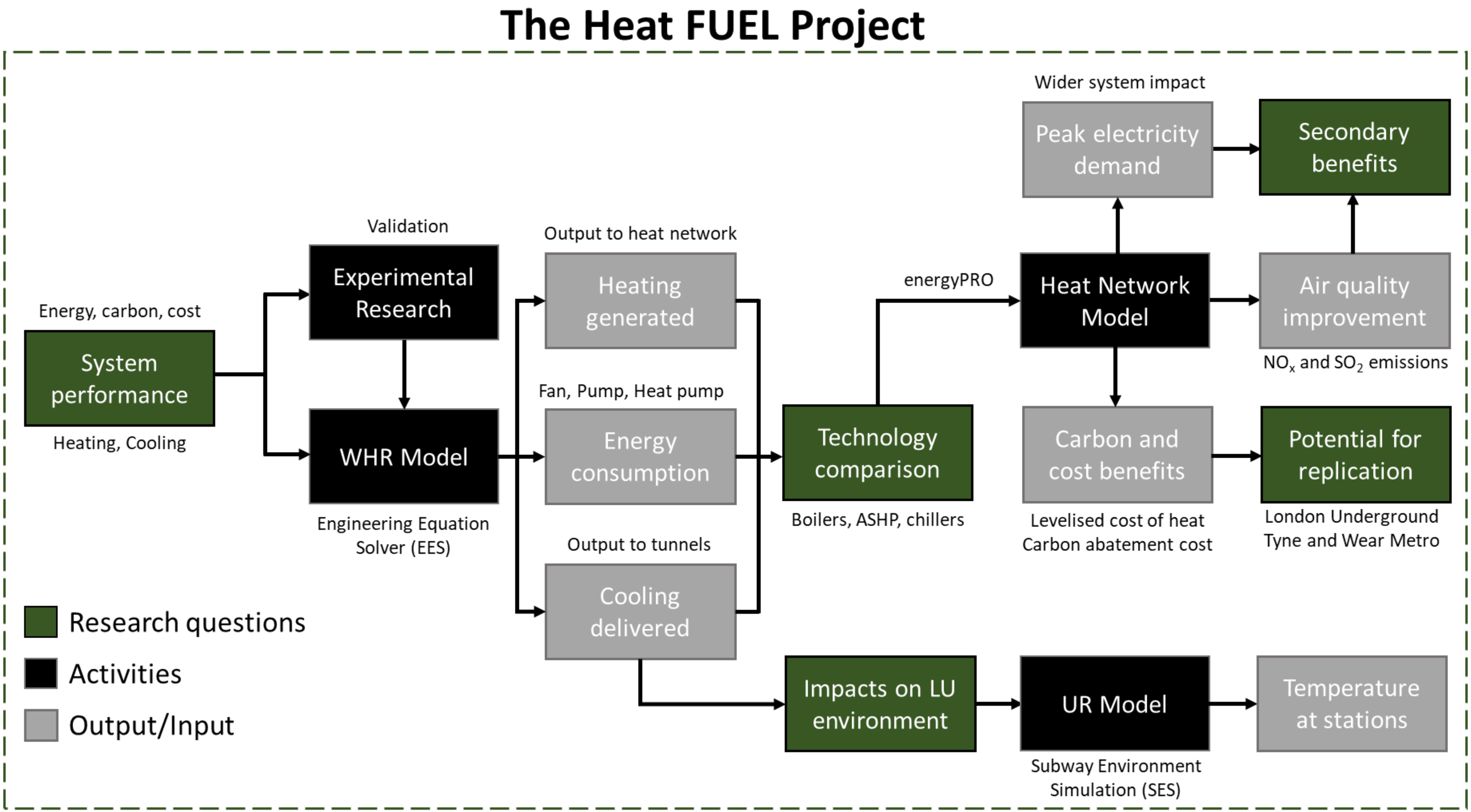

Figure 3.1 – Research methodology for the Heat FUEL Project.

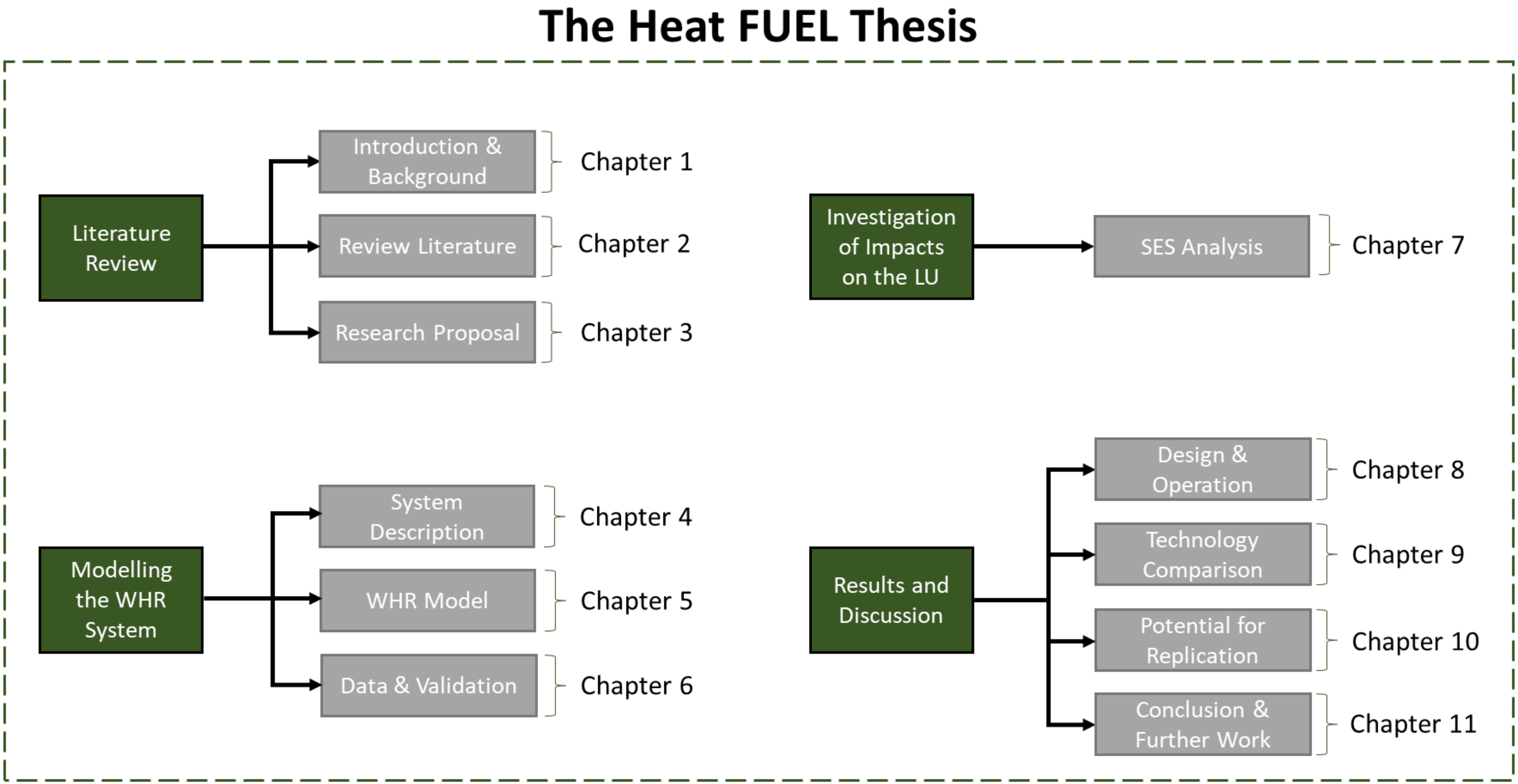

Figure 3.2 – Thesis framework for the Heat FUEL Project.

4. The Bunhill Waste Heat Recovery System

4.1. Introduction

As introduced in Chapter 1 and emphasised through the research questions presented in Chapter 3, the overarching aim of this research project is to investigate the performance and potential of waste heat recovery (WHR) from underground railways (URs) based on the concept of the Bunhill WHR system. Therefore, this chapter is aimed at describing the main components that comprise the system in greater detail, which is then used as a basis for the modelling and experimental works described in Chapters 5 and 6, respectively.

4.2. WHR System Overview

As described in section 2.12, the Bunhill Heat Network is supplied with two energy centres that were developed during different stages of the project. While Bunhill 1 is based on a 1.9 MW_e/2.3 MW_{th} gas-fired combined heat and power (CHP) engine, Bunhill 2 aimed to decarbonise the heating supply in Islington through the development of a novel HP based system operating with waste heat from a London Underground (LU) ventilation shaft. The WHR system is based upon the installation of a heat recovery heat exchanger with a nominal capacity of 780 kW, which consists of cooling coils and a reversible fan. The coils are connected to a 1 MW heat pump (HP) that supplies low carbon thermal energy to local buildings in Islington. The energy centre for Bunhill 2 also houses a 50 m^3 thermal store and two 237kW_e/372kW_{th} CHP units, supplying the district heating network (DHN) which operates with flow and return temperatures of 75 and 55°C. Figure 4.1 provides a schematic of the Bunhill 2 energy centre. As this research project focuses on waste heat from URs, the following sections describe only the components associated with the WHR system.

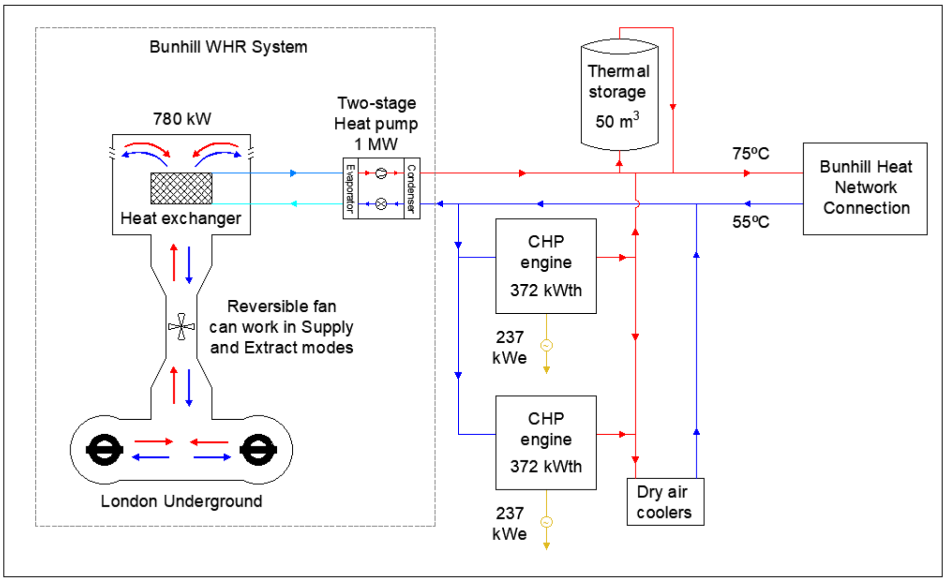

Figure 4.1 – The energy centre for Bunhill 2, highlighting the WHR system and its main components.

4.3. Heat Recovery Heat Exchanger

The first stage of the system involves capturing the waste heat through a fan coil unit installed within the City Road ventilation shaft. The ventilation shaft had to be adapted in order to accommodate the heat recovery heat exchanger. This involved building a head house where the coils were installed, and replacing the existing fan for a reversible one, which enables the system to work in both Extract and Supply modes. The benefits of operating in these two modes have been previously investigated by Davies et al. (2017), and consists of reversing the flow direction of the fan. By doing so, the system is capable of operating by either extracting hot air from the LU tunnels, which can then be used to warm the water in the coils, or using ambient air, which would be cooled by the coils and then supplied to the Underground, with the captured heat being delivered to the HP. Extract Mode would be used during the colder months of the year, when the heat demand is at its peak and heat can be collected from the ventilation shaft at higher temperatures. When in Supply Mode, the cooled air would be used to provide cooling to the Underground, with ambient air as the heat source. Figure 4.2 illustrates the operation of the WHR system under both Extract and Supply modes.

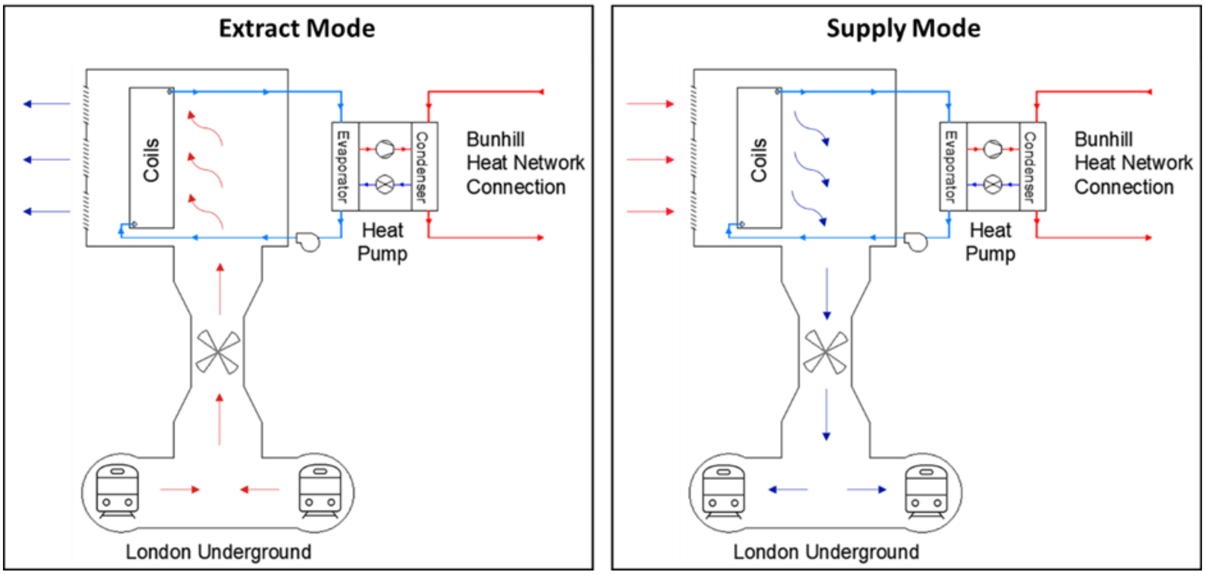

Figure 4.2 – Conceptual schematics of the WHR system operating in Extract and Supply modes.

The heat recovery coils (HRC) have a nominal operating cooling duty of approximately 780 kW under its design condition, and consists of 6 modules with 6 rows of copper tubes, resulting in a total of 36 rows of tubes comprising the coil heat exchanger. The coils were built up in modules to make maintenance simpler and minimise downtime for cleaning. The tubes are 12 mm diameter, with a fin spacing of ¼ inch (approximately 6 mm), and a thickness of 0.18 mm. The fins were designed to provide adequate spacing in order to avoid the use of filters, which can be applied to prevent fouling, but still require regular cleaning and represent a potential fire hazard. Dragoni et al. (2016) have reported that fouling effects can be minimised and filters avoided as long as the coil has a wide fin spacing of at least ¼ inch. Figure 4.3 provides photographs of the enclosed reversible fan and the HRC.

(a) **(b)** **(c)**

Figure 4.3 – Pictures of the enclosed reversible fan (a) and HRC (b; c) of the Bunhill WHR system.

4.4. Heat Pump

Following heat capture at the ventilation shaft, the coolant loop transports the recovered heat to a two-stage ammonia (R717) HP, which was designed based on the flow and return DHN temperatures of 75°C and 55°C, respectively. For district heating purposes, as the evaporator and the condenser operate with a large temperature difference, deploying single-stage HPs could lead to lower compression efficiency and decrease the overall system performance (Kwon, et al., 2013). Two-stage compression should provide a more flexible system, being able to operate at different capacities, and with greater efficiency. The main components of the low stage are two plate-and-shell heat exchangers (PSHEs), namely a desuperheater and a flooded evaporator that is connected to a small separator vessel, as well as a V1100 Grasso reciprocating compressor with 6 cylinders and nominal motor power of 280 kW. The low-stage compressor can run at different capacities in order to accommodate the variation in ventilation temperatures exhausted from the LU shaft, with higher heat source temperatures increasing the cooling duty of the coils and the coefficient of performance (COP) of the HP.

As for the high stage, its main components include two parallel reciprocating compressors, both model 45HP Grasso, with 4 cylinders and a nominal motor power of 90 kW each, as well as three PSHEs that act as a desuperheater, a condenser and a subcooler. The two compressors can also accommodate varying capacities, while maintaining the desired outlet water temperature at 75°C. The two cycles are connected by a separator tank, where saturated ammonia is kept at constant pressure. Figure 4.4 shows a schematic of the two-stage HP installed at the Energy Centre of the Bunhill 2 heat network, whilst Figure 4.5 provides a photograph of the plant room where the HP was installed.

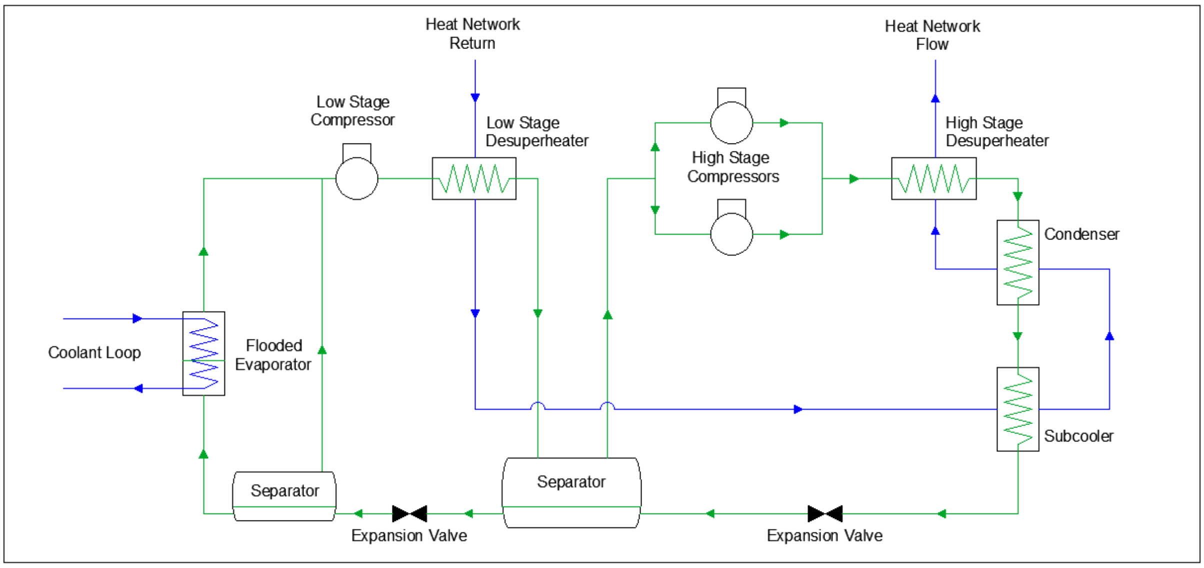

Figure 4.4 – Schematic of the two-stage HP of the Bunhill WHR system.

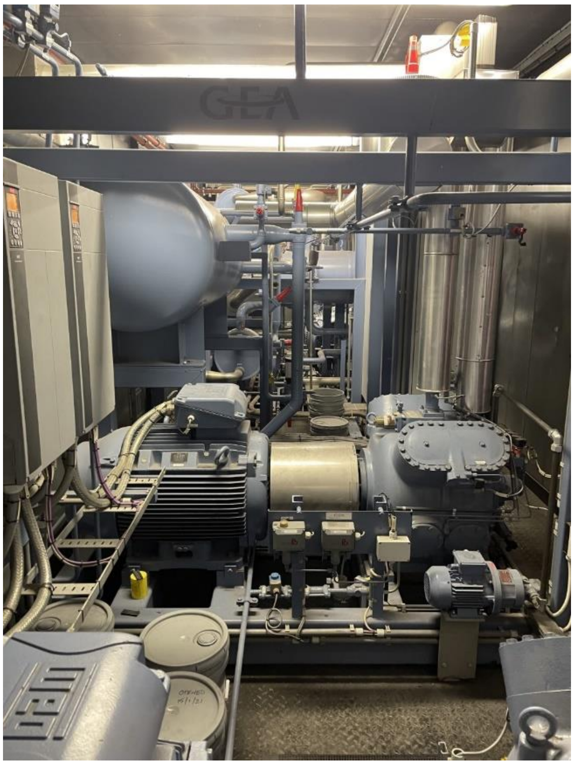

Figure 4.5 – Photograph of the two-stage HP installed at the Bunhill 2 energy centre.

4.5. Thermal Energy Storage (TES)

TES represents an important feature of district heating, as these systems enable a flexible operation of heat sources, which can be used to produce heat at times of lower energy costs. These economic benefits were discussed in 2.11.2, which focused on HPs, but CHP systems can also be operated, when needed, to exploit the fluctuating prices of electricity. Furthermore, storing thermal energy is crucial to manage peak demands, securing the reliability of the system when it is most required. With these benefits in mind, a 50 m^3 water tank was also installed at the energy centre, allowing the WHR system to operate flexibly when meeting the heat demands of the network throughout the year.

4.6. Heat Distribution Pipework

The heat distribution pipework has an approximate length of 2.4 km and utilises two parallel insulated thermoplastic pipes, for the flow, i.e. heat delivery, and return water streams. The design flow and return temperatures are 75°C and 55°C, respectively. The network has different pipe diameters, varying from DN 80 for local building connections to DN 250 for the main flow/return pipes, which distribute the heated water from the heat sources to local circuits, which feed one or more buildings connected to the network. Figure 4.6 shows an overview map of the existing Bunhill 1 and 2 networks, including the heat distribution pipework, heat sources and connected buildings. The building codes adopted in Table 4.1 will be used to identify each of the connected buildings on the map. Energy centre 1 (EC1) corresponds to the Bunhill 1 CHP unit, whilst the energy centre 2 (EC2) represents the site where heat will be captured from the City Road vent shaft, and also includes the HP and two other CHP units.

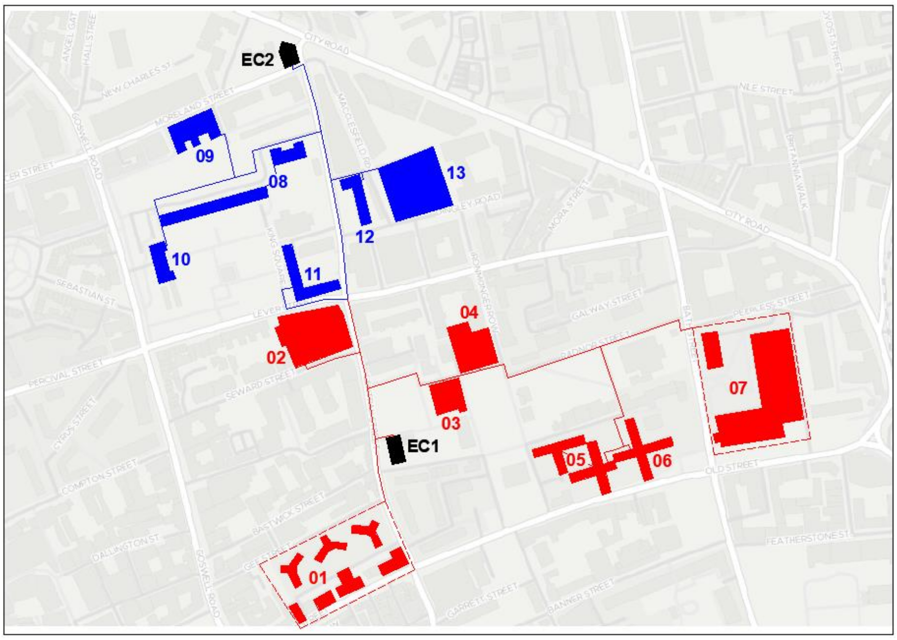

Figure 4.6 – The heat networks for Bunhill 1 (red) and Bunhill 2 (blue) (adapted from Islington Council, 2018).

4.7. Connected Buildings and Heat Demands

The Bunhill Heat Network represents a landmark project for Islington Council, having paved the way for a net zero plan that is largely grounded on the development of low-carbon heat networks across the borough (Islington Council, 2020). Overall, the council has identified 15 clusters for DHNs in Islington, with an initial potential to connect to 8,000 properties. Currently, the Bunhill Heat Network serves a range of domestic, mixed-use and commercial buildings. At first, Bunhill 1 connected to over 800 homes within five housing estates, as well as four office buildings and two leisure centres. The Bunhill 2 extension project added five more estates to the network, comprising 550 dwellings, as well as a local primary school. There are plans to further expand the network and connect to a newly developed mixed-use building complex, which includes 720 residential units, a 160-bed student accommodation and a 125-bed hotel, as well as areas for offices, retail and restaurants. Table 4.1 provides annual heat demands and types for all the existing and planned connections related to Bunhill 1 and 2.

Table 4.1 – Details of all connections to the Bunhill Heat Network.

Network Connection	Building Code	Type of Building	Annual Heat Consumption (MWh)
Bunhill 1 (EC 1)	01	Residential/commercial	3,044
	02	Residential	876
	03	Leisure	82
	04	Leisure	1,352
	05	Residential	837
	06	Residential	1,184
	07	Residential	5,478
	Total		**12,853**
Bunhill 2 (EC 2)	08	Residential	2,527
	09	School	169
	10	Residential	1,497
	11	Residential	468
	12	Residential	919
	13	Mixed Use	5,783
	Total		**11,363**
Whole Network	**Total**		**24,216**

4.8. Conclusion

This chapter introduced the principles of operation and the main components of the Bunhill WHR system. The technical specifications hereby presented were used as references for the development of a mathematical model of the WHR system. The scientific principles and thermodynamic relations that underpin this model are described in Chapter 5, whilst model results and discussion are presented in Chapter 8. Understanding the principles of operation of the WHR system was also key for developing a data collection strategy, which is introduced in Chapter 6. Furthermore, the topology of the Bunhill Heat Network and the heat demand data associated with the connected buildings were used to investigate the operation of a heat network that utilises waste heat from URs, which is discussed in Chapter 9.

5. Modelling of the Waste Heat Recovery System

5.1. Introduction

This chapter describes the development of a mathematical model that investigates the performance of the Bunhill Waste Heat Recovery (WHR) system based on its design specifications, both in terms of the cooling it provides to the Underground tunnels, as well as the heat it produces for the local heat network. The development of the WHR model was based upon the simulation of the main system components, consisting of a fan coil heat exchanger and a two-stage heat pump (HP), which are connected by pipework hereon referred to as the coolant loop. The heat exchanger modelling combines models for both the reversible fan and the heat recovery coils (HRC). The HP was modelled based on its design specifications and its circuit of five plate-and-shell heat exchangers, whereas the coolant loop was modelled considering the energy required for pumping. The WHR model simulates each of these components and its outputs are calculated by solving mass and energy balances between the coils and the HP. These outputs are illustrated in Figure 5.1, together with the main inputs and connections between the different model components, which are detailed in the next sections.

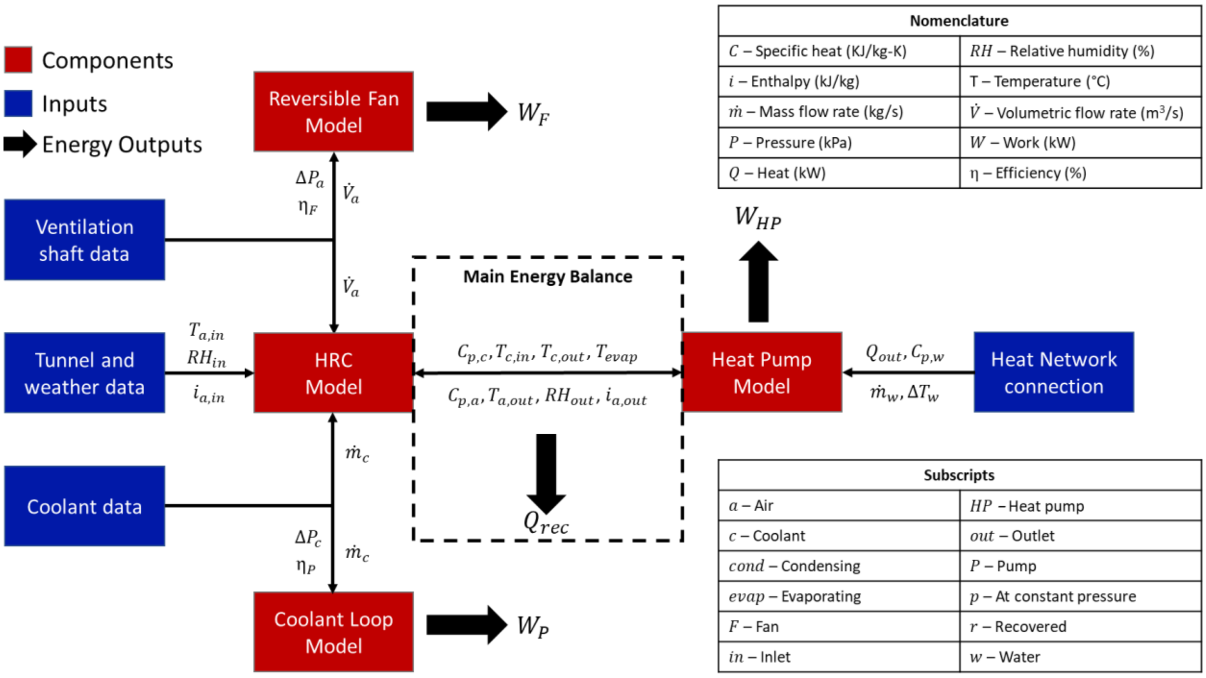

Figure 5.1 – Framework for the WHR model, highlighting components, inputs and outputs.

5.2. Energy Efficiency of the Waste Heat Recovery System

The performance of an energy system is based upon the ratio between its useful energy outputs and its energy inputs. The energy outputs can be for both heating and cooling, being equivalent, respectively, to the total heat output of the HP (Q_{out}) or the cooling delivered to the air stream, which corresponds to the heat recovered by the coolant side of the heat exchanger (Q_{rec}). As for the energy inputs to the system, they consist of the power input to the HP (W_{HP}), the power input to the coolant circulation pumps (W_P), as well as the power demand of the reversible fan (W_F) within the ventilation shaft. Based on these values, the overall energy efficiency of the system can be expressed in terms of a coefficient of system performance (COSP). The COSP can be calculated either for system operation in heating (COSP_H) or cooling (COSP_C) modes, as shown in Equations 5.1 and 5.2, respectively.

$$\mathrm{COSP}_H = \frac{Q_{out}}{\Sigma W} = \frac{Q_{out}}{W_F + W_P + W_{HP}} \tag{5.1}$$

$$\mathrm{COSP}_C = \frac{Q_{rec}}{\Sigma W} = \frac{Q_{rec}}{W_F + W_P + W_{HP}} \tag{5.2}$$

The calculation method for the parameters listed in Equations 5.1 and 5.2 and described above will be listed in the following subsections. The physical and thermodynamic principles hereafter described form the basis for the mathematical model of the WHR system developed using the EES platform, a tool selected based on the review described in section 2.14.1.

5.3. Reversible Fan

One of the main energy inputs to the WHR system is the electricity used to power the reversible fan, which allows the system to operate in either Extract or Supply Mode. Each mode is associated with a specific flow direction of the fan, as described in section 4.3. Figure 5.2 illustrates how the reversible fan model is related to the other model components.

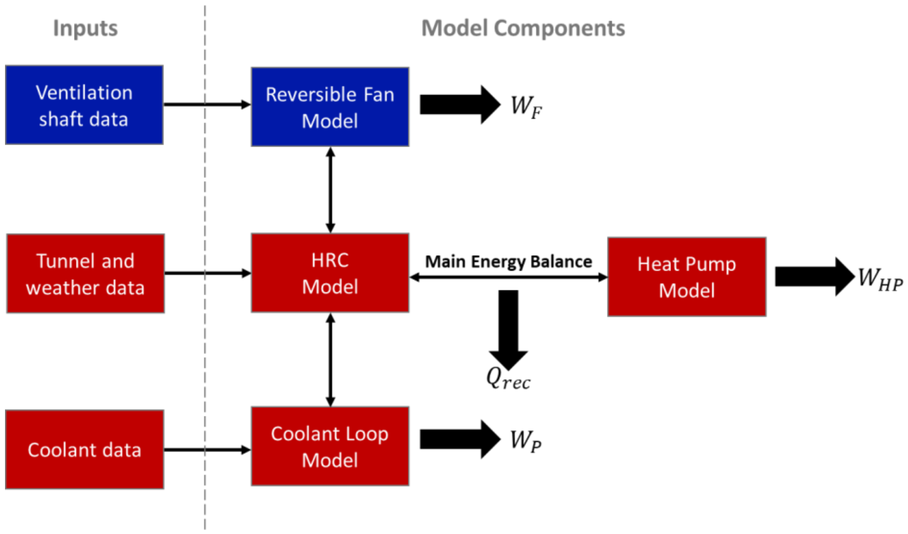

Figure 5.2 – The WHR model framework, with the components and inputs associated with the reversible fan highlighted in blue.

For the purpose of modelling the energy consumption of the WHR system, only the additional power required to overcome the pressure drop directly associated with the heat recovery equipment is considered. The components linked to the WHR system are the HRC, dampers, louvres and cladding, as well as the newly built headhouse. The design pressure drops associated with each of these components, in both Extract and Supply modes, are provided in Table 5.1. The pressure drop calculations also include a safety margin of 15%, as considered in the fan design sheet shared by Transport for London (TfL, 2019b).

Table 5.1 – Air side pressure losses associated with different components of the newly installed WHR system.

Component	Pressure Drop (Pa)	
	Extract Mode	Supply Mode
Louvre and cladding	10.00	10.01
Dampers	20.40	20.40
Coils	58.01	58.01
New headhouse	3.67	3.93
15% Margin	13.82	13.85
Total	105.90	106.20

Based on the values shown in Table 5.1, the additional power required to run the reversible fan (W_F), in kW, can be calculated as shown in Equation 5.3 (Jones, 1973). The calculations are based upon the volumetric air flow in the shaft ($\dot{V}_a = 70\ m^3/s$) the pressure drop (ΔP_a), as calculated in Table 5.1, in Pa, and the fan efficiency (η_F) of 59.5%, which was obtained from fan design specifications as provided by TfL (2019b).

$$\mathrm{W}_F = \frac{\Delta P_a * \dot{V}_a}{\eta_F} \tag{5.3}$$

It is noteworthy that fouling can have a considerable impact on the pressure drop that has to be overcome by the fan. According to Dragoni et al. (2016), who conducted an analysis of the fouling effect on different types of air-handling units (AHUs) in the London Underground (LU) environment, a wider fin spacing is able to avoid particle build up on the coils as they appear to "air wash" or self-clean once a certain thickness of particles is achieved. Results indicated that there was no increase in pressure drop over a four-month period for a spacing of 4 fins per inch, or every 6.35 mm, which was also adopted for the Bunhill HRC, and therefore this analysis neglected the long-term effects of fouling and only considered the design values with a 15% safety margin when calculating fan energy consumption.

5.4. Heat Recovery Coils

The process of heat recovery takes place at the air-to-water heat exchanger placed within the City Road ventilation shaft. The heat exchanger consists of two main components, the copper coils through which heat is recovered and a fan that blows air onto those coils. When the system is operating in Extract Mode, the heat source used is tunnel air, whilst when operating in Supply, it recovers heat from ambient air and simultaneously supplies cooled air to the LU tunnels. These operation modes are illustrated in Figure 4.2 and the following sections will describe the scientific principles and relations used to derive a functional model of the heat transfer process that occurs between the air and coolant streams. The model components and inputs discussed in this section are indicated by Figure 5.3.

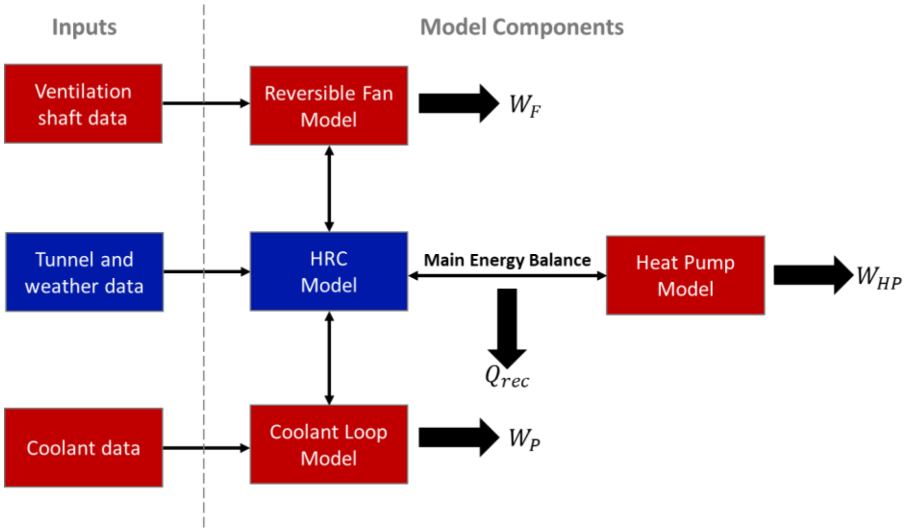

Figure 5.3 – The WHR model framework, with the components and inputs associated with the HRC highlighted in blue.

Table 5.2 – Geometric parameters values for the HRC.

Parameter	Description	Unit	Value
d_{ext}	Tube external diameter	mm	12
t_{tube}	Tube thickness	mm	0.4
ε_{tube}	Tube roughness (drawn copper)	μm	1.5
d_{int}	Tube internal diameter	mm	11.2
r_{out}	Tube external radius	mm	6
r_{in}	Tube internal radius	mm	5.6
N_{rows}	Number of rows	N/A	12
N_{tubes}	Number of tubes high	N/A	158
$N_{circuits}$	Number of circuits	N/A	$1.5 \times N_{tubes}$
S_L	Longitudinal tube pitch	mm	33
S_T	Transversal tube pitch	mm	38.1
S_D	Diagonal tube pitch	mm	38.1
L_{coil}	Coil length	m	4.75
H_{coil}	Coil height	m	6.04
D_{coil}	Coil depth	m	0.29
A_{face}	Coil face area (L_{coil} x H_{coil})	m^2	28.69
A_{out}	Total external tube area	m^2	339.5
A_{in}	Total internal tube area	m^2	316.9
A_{tubes}	Total tube cross section area	m^2	0.2144
s_{fin}	Spacing gap between fins	mm	6.35
t_{fin}	Fin thickness	mm	0.15
N_{fins}	Total number of fins	N/A	748
A_{fin}	Single fin area (excluding tubes)	m^2	3.289
A_{coil}	Total coil external area	m^2	2800

5.4.1. Coil Geometry

The HRC consist of two banks with three modules with 6 rows of copper finned tubes each. The tubes have a 12 mm diameter, a thickness of 0.40 mm, whilst the fins have a spacing of

6.35 mm and a thickness of 0.15 mm. In order to simplify the model and reduce computational effort, the coils were considered as a single bank with 12 rows with 158 tubes each, totalling a length of 4.75 m, a height of 6.04 m and a depth of 0.29 m. A list of coil geometric parameters, with their units and values, is provided in Table 5.2.

5.4.2. Energy Balance at the Heat Recovery Coils

The energy balance at the HRC is determined by calculating the heat transfer rate (Q_{rec}) through a number of different equations. These equations consist of the sensible heat transfer on the coolant side (Equation 5.4), the enthalpy change across the air stream (Equation 5.5), as well as an additional equation able to calculate the overall heat transfer rate of the heat exchanger. Equation 5.4 is calculated based on the coolant mass flow rate ($\dot{m}_c$), the specific heat of the coolant ($C_{p,c}$), evaluated at the average coolant temperature, and the difference between the outlet ($T_{c,out}$) and inlet ($T_{c,in}$) temperatures. As for the air side heat transfer, it is calculated based on the mass flow rate of air ($\dot{m}_a$) and the variation of specific enthalpy (Δi_a) across the airstream from the inlet to the outlet of the heat exchanger.

$$Q_{rec} = \dot{m}_c C_{p,c}(T_{c,out} - T_{c,in}) \tag{5.4}$$

$$Q_{rec} = \dot{m}_a(i_{a,in} - i_{a,out}) \tag{5.5}$$

In order to calculate the heat recovered (Q_{rec}) with the aforementioned equations, the conditions of the fluids involved must be known. However, the only known conditions are for the air entering the coils, which is either exhaust air from the ventilation shaft (Extract Mode) or ambient air from the external environment (Supply Mode). These known conditions relate to temperature and relative humidity (RH) data recorded for a one-year period, between 24/01/2013 and 24/01/2014. The vent shaft air data set was provided by TfL (2019b), whilst the ambient weather data were provided by the UK Meteorological Office (Met Office, 2019) using the closest weather station to the ventilation shaft with data recordings available (either from St. James's Park, Kew Gardens or Heathrow Airport).

Knowledge of outlet air conditions is essential for determining the cooling being generated by the system, whilst coolant temperatures can affect the efficiency of the HP, and these parameters can be determined by calculating an energy balance between the HRC and the HP. In this case, the heat absorbed at the HP's evaporator (Q_{evap}) is considered to be equal to the heat recovered at the HRC. This is based on the assumption that the coolant loop, which connects the coils to the HP, is well insulated and short in length, meaning that its heat losses can be neglected. Considering full-load heat output (Q_{out}), Equation 5.6 can be introduced into the energy balance, relating the cooling and heating duties of the HP with its coefficient of performance (COP). The variables shown in Equation 5.6 are a function of the operating conditions of the HP and will be determined based upon the mathematical model of the WHR system, as described later in this chapter.

$$Q_{evap} = Q_{rec} = Q_{out} - \frac{Q_{out}}{COP} \tag{5.6}$$

The combination of Equations 5.4, 5.5 and 5.6 leads to a system of 3 equations with 4 unknown variables (Q_{rec}, $i_{a,out}$, $T_{c,in}$ and $T_{c,out}$). Therefore, another heat transfer equation, based on the overall heat transfer coefficient of the coils (U value), must be introduced when calculating the energy balance. However, there are different methods of calculating the U value and they are dependent upon the coil surface conditions, which can be either fully dry, fully wet or partially wet. These conditions will change if moisture condenses from the air stream onto the coils, and the model must be able to differentiate between the possible surface conditions and apply the correct method to calculate the overall heat transfer coefficient according to the inlet air temperature and humidity.

5.4.3. Coil Surface Conditions

Modelling HRC often requires complex simulations as cooling humid air involves not only heat but also mass transfer from the air stream as condensate is formed. Mitchell and Braun (2013) proposed a methodology for modelling cooling coils that relies on an analogy of sensible heat transfer that simplifies calculations whilst determining coil performance accurately. The methodology is based upon different heat transfer coefficient calculations for both fully dry and fully wet conditions, whilst a partial configuration can be represented by a combination of both dry and wet models, whereby the coil is divided into “dry” and “wet” sections. The “dry” section corresponds to the initial fraction of the heat exchanger, where the coil surface temperature is above the dew point and the air does not condense, causing the heat transfer to be entirely sensible. As for the “wet” section, it is characterised by the point beyond which the coil surface temperature is below the dew point, leading to the transfer of both heat and mass from the air stream and a different heat transfer coefficient, as a wetted surface alters the heat transfer process between both fluids. The process of cooling humid air can be best represented by psychrometric charts, as discussed by Nellis and Klein (2008).

Figure 5.4 shows an ideal representation of the process associated with moist air going through cooling coils in a partially wet condition. The idealised representation assumes that the bulk of air is always at the same conditions i.e. temperature and humidity ratio. This would mean that condensation would only start to take place when the whole mass of air reaches the saturation point (point 2 in Figure 5.4). Therefore, the coil surface is assumed to be dry from points 1 to 2 and wet from points 2 to 3. In the wet region, the whole mass of air would be saturated at all times, with air leaving the coils with a RH of 100% at point 3. A more accurate representation of the dehumidification process can be seen in Figure 5.5. In this case, the cooling process can also be separated into dry and wet sections. In the dry section, from points 1 to 2, the coil surface temperature is above the dew point of air, therefore no condensation occurs and the humidity ratio of air remains constant as only sensible cooling is taking place. This process is similar to the dry section represented in Figure 5.4.

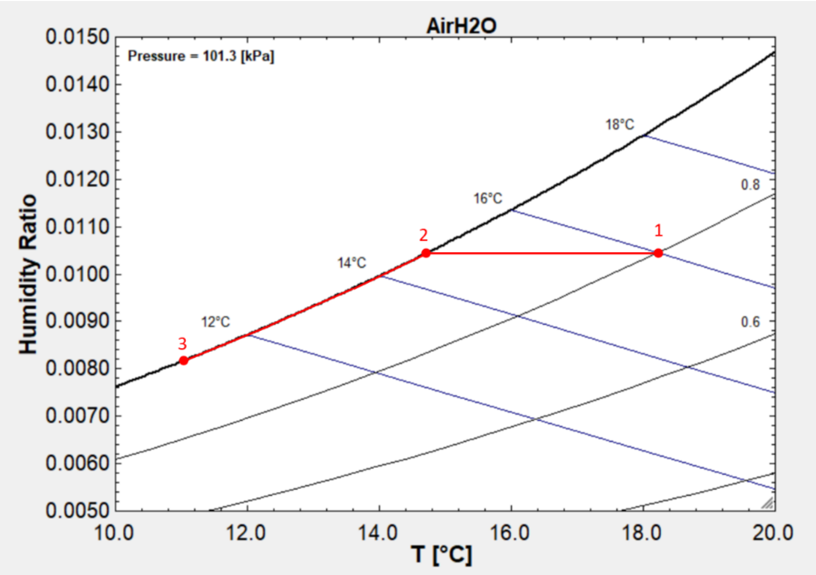

Figure 5.4 – A psychrometric chart with an idealised representation of the process of cooling moist air.

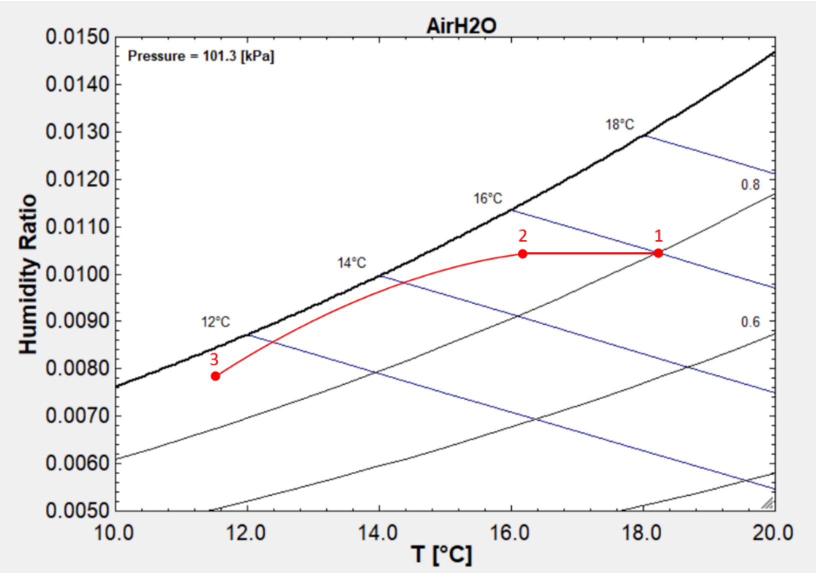

Figure 5.5 – A psychrometric chart with an accurate representation of the process of cooling moist air.

The wet section of the coil is where the inaccuracies from the idealised process stem from. In reality, there is a temperature gradient in the bulk of air progressing through the cooling coils, with the air closer to the coil surface experiencing lower temperatures than the air travelling further from the coils. This means that condensation can occur even though the mean air temperature is above the dew point. As the air travels through the coils, it encounters lower surface temperatures, which cause the change in humidity ratio to become higher as the air approaches the outlet of the coil. The curve connecting points 2 and 3 in Figure 5.5 represents this phenomenon, once it becomes steeper as it approaches point 3. Another important aspect of the actual process is that the air will not necessarily leave the coils saturated, as represented by point 3, since the mean air temperature might be above the dew point even when dehumidification takes place. The following sections explore the appropriate methodologies to be used when calculating heat transfer coefficients for both fully dry and fully wet coil surfaces, as well as how these methods can be combined when dealing with a partially wet condition.

5.4.3.1. Fully Dry Coil Surface

In a fully dry coil condition, the energy transfer is entirely sensible, with the moisture content of air remaining unaltered. In such conditions, the energy balance at the heat exchanger can be calculated based upon the log-mean temperature difference (LMTD) method (Incropera, et al., 2002), as shown in Equation 5.7. The variable U_d represents the overall dry heat transfer coefficient, whilst A is the total outside finned area of the coils, as shown in Table 5.2, and the $LMTD$ can be calculated utilising Equation 5.8, which combines inlet and outlet temperature for both coolant and air streams, respectively.

$$\mathrm{Q}_{rec} = U_d * A * LMTD \tag{5.7}$$

$$LMTD = \frac{\Delta T_2 - \Delta T_1}{\ln(\frac{\Delta T_2}{\Delta T_1})} \text{ ; where: } \Delta T_2 = T_{c,out} - T_{a,in} \text{ and } \Delta T_1 = T_{a,out} - T_{c,in} \tag{5.8}$$

5.4.3.2. Fully Wet Coil Surface

The calculation of heat transfer on wet coils and the impacts of mass transfer through condensation have been investigated by several authors, as shown by Kastl (2012) in a review of different methods for simulating and designing cooling coils. The methods presented in (Mitchell and Braun, 2013), (Elmahdy and Mitalas, 1977) and (Threlkeld, 1962) rely on the concepts of fictitious enthalpy and enthalpy potentials, whilst Wang and Hihara (2003) reported a method that analyses the psychrometric process of a wet coil and derives an equivalent dry process that can be used in simulations. The successful application of enthalpy potentials to describe heat and mass transfer phenomena associated with cooling coils has been reported by the aforementioned authors and will therefore form the basis of the heat recovery model developed as part of this investigation.

According to Kastl (2012), the concept of a fictitious air enthalpy corresponds to the saturated air enthalpy calculated for a temperature other than that of the air stream. This concept is utilised by Mitchell and Braun (2013) when describing the heat and mass transfers that take place in a cooling coil with a wet surface. Figure 5.6 illustrates the temperature (T), moisture content (ω), the enthalpy (i) and the RH profiles within the boundary layer of the air stream, as well as the temperature profiles through the coil walls and into the coolant stream. On the air side, the driving potential for heat transfer is a difference in temperature, whilst a difference in moisture content is what drives the mass transfer. The combination of the two, which corresponds to the total energy transfer, is driven by a difference in enthalpy.

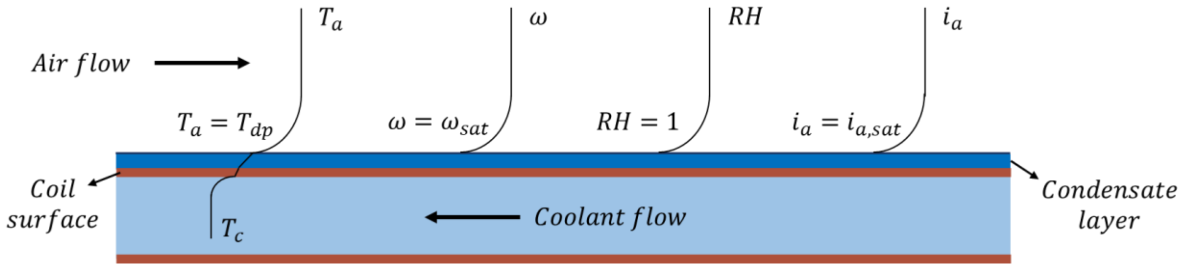

Figure 5.6 – Property profiles associated with a wet cooling coil (adapted from Mitchell and Braun, 2013).

The profiles observed in Figure 5.6 describe the air cooling process for a wet surface condition. The temperature difference between the air and coolant streams is what drives the heat transfer process. At the furthest point from the coil surface, the air temperature is at its highest, decreasing towards its dew point (T_{dp}) at the top of the condensate layer, where condensation starts to occur. The temperature profile is linear through the coil wall and condensate layer as heat is transferred by conduction in those regions, and a convective thermal boundary layer is formed within the coolant stream.

The mass transfer is driven by a difference in air moisture content (ω). The moisture content decreases towards the boundary layer, where condensation takes place. The condensation phenomenon is associated with the dehumidification of air and, in order for a condensate film to form, its moisture content must be lower near the surface than in the air stream. This is also represented by the RH profile, which shows that RH reaches unity at the top of the condensate layer. The enthalpy potential profile follows that of moisture content, with its highest value out in the air stream and its lowest at the edge of the condensate layer. The value of enthalpy at the condensate layer represents the saturation enthalpy evaluated at the condensate temperature. This change in enthalpy can be used to represent the energy flow in the air stream, combining both heat and mass flows from the bulk of air towards the boundary layer.

Overall, the energy balance from Figure 5.6 can be summarised as an energy transfer (ΔE) – including both heat and mass – from the air stream to the condensate layer, beyond which there is only heat transfer (ΔQ); through the condensate film and the coil wall into the coolant stream. In order for the energy balance to be satisfied, the mass of condensate flowing out of the coils should also be accounted for, but this is often neglected as the energy flow associated with condensate drainage is small compared to the other terms in the energy balance (Mitchell and Braun, 2013). By neglecting the condensate energy flow, the energy balance can be represented by the schematic in Figure 5.7, which illustrates a counterflow configuration.

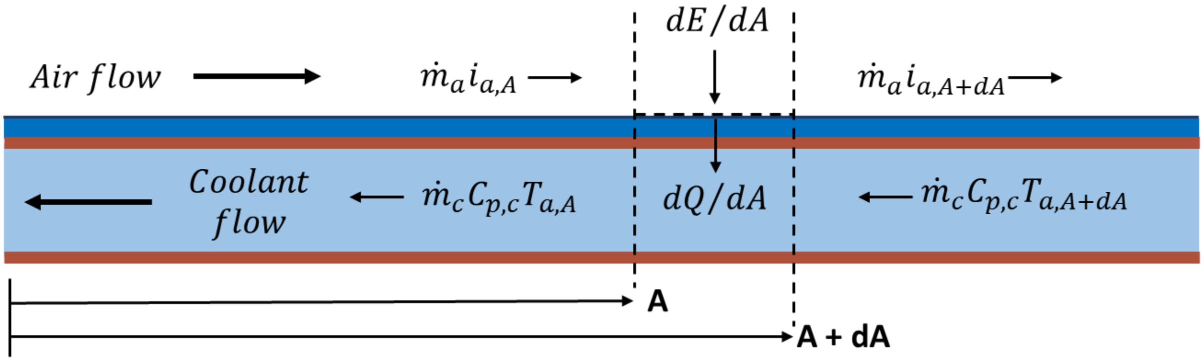

Figure 5.7 – Energy balance for a wet cooling coil (adapted from Mitchell and Braun, 2013).

The energy balance shown in Figure 5.7 can be translated into Equations 5.4 and 5.5 if integrated for the total coil surface area (A) and considering that the energy transfer on the air side is equal to the energy transfer on the coolant side ($\Delta E = \Delta Q$). Therefore, an equivalent form of Equation 5.5, for a differential coil area dA, can be expressed as in Equation 5.9.

$$\frac{dE}{dA} = \frac{dQ}{dA} = \dot{m}_a \frac{di_a}{dA} \tag{5.9}$$

As discussed in this section, the energy transfer expressed by an enthalpy potential relates to the combination of sensible heat transfer and the energy flow associated with condensation. The heat transfer can be expressed in terms of a convective heat transfer coefficient (h_a) and the temperature difference between the air stream (T_a) and the condensate surface (T_s). The mass transfer can be calculated based upon a convective mass transfer coefficient (h_m), as well as the moisture content potential between the air stream and the edge of the condensate layer ($\Delta\omega = \omega - \omega_{sat}$). By utilising the enthalpy of vaporisation (i_{vap}), the mass transfer can be expressed in terms of an energy transfer, leading to Equation 5.10.

$$\frac{dE}{dA} = \frac{dQ}{dA} = h_a(T_a - T_s) + h_m(\omega - \omega_{sat})i_{vap} \tag{5.10}$$

The Lewis Number (Le) provides a relationship between the convective heat and mass transfer coefficients (Kastl, 2012), as shown in Equation 5.11, where $C_{p,a}$ represents the specific heat of humid air. According to the ASHRAE Handbook of Fundamentals (2017), the Lewis Number for air and water vapour mixtures is 0.845. However, Mitchell and Braun (2013), Elmahdy and Mitalas (1977), and Threlkeld (1962) assumed a Le of unity for simplification purposes. Kastl (2012) compared the effects of utilising variable Lewis Numbers for different cooling coil models and found that the difference in latent capacity obtained by applying a Lewis Number of 0.845 was below 3% for all the models analysed. Therefore, a Lewis Number equal to unity will also be used in this investigation, yielding Equation 5.12.

$$Le^{2/3} = \frac{h_a}{C_{p,a} h_m} \tag{5.11}$$

$$h_m = \frac{h_a}{C_{p,a}} \tag{5.12}$$

The relationship between mass and heat convective transfer coefficients, given by Equation 5.12, was applied by Kastl (2012) to derive a method for calculating the air side energy transfer. This method is based upon the difference between the enthalpy of air at the bulk conditions (i_a) and the enthalpy of saturated air at the condensate surface temperature ($i_{s,sat}$), as shown in Equation 5.13, which defines the concept of enthalpy potential.

$$\frac{d\mathrm{E}}{d\mathrm{A}} = \frac{d\mathrm{Q}}{d\mathrm{A}} \approx h_m\left(i_a - i_{s,sat}\right) = \frac{h_a}{C_{p,a}}\left(i_a - i_{s,sat}\right) \tag{5.13}$$

The energy balance on the coolant side involves only the transfer of heat, which occurs between the air/condensate interface and the coolant stream, going through the coil walls. As this process is related to sensible heat transfer, the energy balance on the coolant side can be expressed as in Equation 5.14.

$$\frac{d\mathrm{Q}}{d\mathrm{A}} = \dot{m}_c C_{p,c} \frac{dT_c}{dA} \tag{5.14}$$

The energy balance shown in Figure 5.7 is therefore expressed as a function of both enthalpies and temperatures. The fictitious enthalpy method allows the coolant condition to be expressed in terms of an enthalpy value by utilising an effective specific heat (C_{ef}), yielding the enthalpy of saturated air at the coolant temperature ($i_{c,sat}$). The effective specific heat C_{ef} equates a change in coolant temperature to a change of saturated air at the coolant temperature, as shown in Equation 5.15.

$$C_{ef} \frac{d\mathrm{T}_c}{d\mathrm{A}} = \frac{d\mathrm{i}_{c,sat}}{d\mathrm{A}} \tag{5.15}$$

The integration of Equation 5.15 for the coil external area (A), from the coil inlet to its outlet, allows the effective specific heat (C_{ef}) to be evaluated based upon the inlet ($T_{c,in}$) and outlet ($T_{c,out}$) coolant temperatures, as shown in Equation 5.16.

$$C_{ef} = \int \frac{\mathrm{i}_{c,sat}}{\mathrm{T}_c} d\mathrm{A} = \frac{i_{c,sat,in} - i_{c,sat,out}}{T_{c,in} - T_{c,out}} \tag{5.16}$$

By assuming a negligible thermal resistance between the inner tube wall and the outer condensate layer surface, the saturated enthalpy at the surface ($i_{s,sat}$) can be evaluated at its corresponding coolant temperature ($i_{c,sat}$) for a specific coil location (Kastl, 2012), as shown in Equation 5.17. In this case, an overall wet heat transfer coefficient (U_w) must be applied, accounting for both convective and conductive heat transfer across the coils.

$$\frac{d\mathrm{Q}}{d\mathrm{A}} = U_w\left(i_a - i_{c,sat}\right) \tag{5.17}$$

Equation 5.17 can be integrated for the external coil area (A) to yield the total heat transfer for the coils. Since the enthalpy of the air stream and the enthalpy of saturated air at coolant temperatures are not constant across the coils, they must be expressed by a log-mean enthalpy difference (LMED), which is calculated in the same way as the LMTD, as shown in Equation 5.8, but now using enthalpy values instead of temperatures. This yields Equation 5.18, which can be used to calculate the overall heat transfer of cooling coils with wet surfaces.

$$Q_{rec} = U_w * A * LMED \tag{5.18}$$

5.4.3.3. Partially Wet Coil Surface

A partially wet condition is observed when condensation occurs at a specific point along the coils, with only a fraction of the coils being wet. Mitchell and Braun (2013) proposed a method for calculating the point where condensation starts to occur based on coil surface temperatures. The method considers that condensate starts forming when the surface temperature on the air side is equal to the dew point of the entering air, as shown in Figure 5.8 for a counterflow condition. According to the authors, this method can also be applied to crossflow heat exchangers, as they have a similar performance to a counterflow configuration.

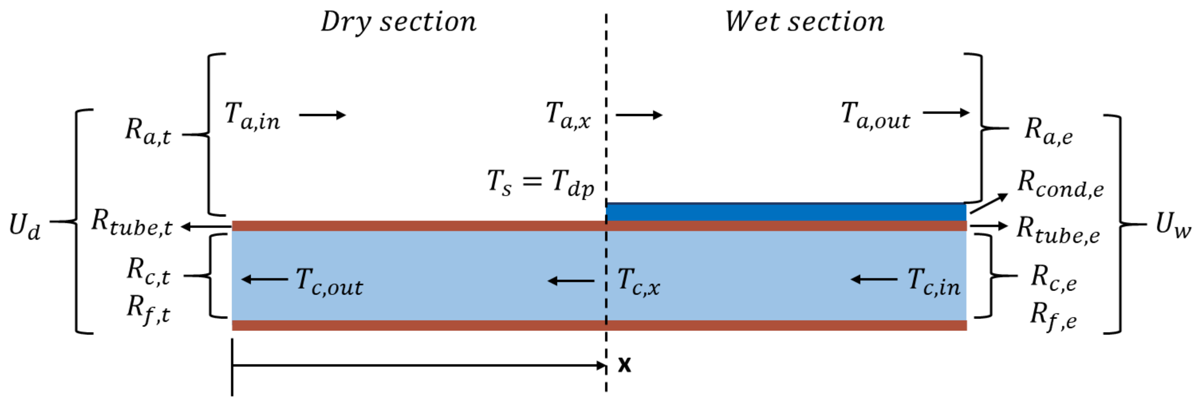

Figure 5.8 – A schematic illustrating a counterflow HRC with a partially wet surface.

As Figure 5.8 illustrates, the air side of the coil is dry until point X, where the coil surface temperature (T_s) becomes equal to the dew point (T_{dp}) of the air stream that entered the coils with a temperature of $T_{a,in}$. Up until this point, the heat transfer is entirely sensible and an overall dry heat transfer coefficient (U_d) is calculated based on thermal resistances of the air ($R_{a,t}$), the tube wall ($R_{t,t}$) and the coolant stream ($R_{c,t}$), as well as any resistance associated with fouling ($R_{f,t}$). The temperatures of both air ($T_{a,x}$) and coolant ($T_{c,x}$) streams at point X can be calculated based on the sum of thermal resistances on both the air ($\Sigma R_{a,t}$) and coolant ($\Sigma R_{c,t}$) sides, as well as the surface temperature ($T_s = T_{dp}$), as shown in Equation 5.19.

$$\frac{(T_{a,x} - T_{dp})}{\Sigma R_{a,t}} = \frac{(T_{dp} - T_{c,x})}{\Sigma R_{c,t}} \tag{5.19}$$

Beyond point X, the coil surface becomes wet and the heat transfer is both latent and sensible. In this case, the overall wet heat transfer coefficient (U_w) can be calculated based on enthalpic resistances of the air ($R_{a,e}$), the condensate layer ($R_{cond,e}$), the tube wall ($R_{tube,e}$) and the coolant stream ($R_{c,e}$). Based on Equation 5.19, air and coolant temperatures can be determined at the exact point where condensation starts to occur. This enables the heat transfer to be calculated for both dry (Q_d) and wet (Q_w) sections separately by using Equations 5.7 and 5.18 and applying the fraction coefficient X that represents the proportion of the coil that is dry. This leads to Equations 5.20 and 5.21, which can be used to calculate the energy balance for a partially wet coil surface that has fraction X of its surface in a dry condition. The sum of the heat transferred on both dry (Q_d) and wet (Q_w) sections is equal to the total amount of heat being recovered from the air stream (Q_{rec}), as given by Equation 5.22.

$$\mathrm{Q}_d = X * U_d * A * LMTD \tag{5.20}$$

$$\mathrm{Q}_w = (1 - X) * U_w * A * LMED \tag{5.21}$$

$$Q_{rec} = \mathrm{Q}_d + \mathrm{Q}_w \tag{5.22}$$

The model is bound by X values between 0 and 1, which correspond, respectively, to fully wet and fully dry surface conditions. The calculation of both dry and wet heat transfer coefficients U_d and U_w, respectively, as well as their associated resistances, are described in the following sections.

5.4.4. Internal Convection in Circular Tubes

The phenomenon of forced convection in circular tubes has been discussed by many authors, such as Nellis and Klein (2008), Incropera et al. (2002) and Holman (2010). The calculation of convective heat transfer coefficients is typically based upon empirically derived equations that cover a range of flow conditions. For that reason, different relations must be used when dealing with laminar and turbulent flows, which are dependent upon the coolant's Reynolds Number (Re_c), which can be calculated as shown in Equation 5.23.

$$Re_c = \frac{\rho_c v_c d_{int}}{\mu_c} \tag{5.23}$$

A laminar flow condition is defined by a Reynolds number lower than 2300. For values between 2300 and 3000, the flow is at a transitional stage, between laminar and turbulent regimes. For Reynolds numbers above 3000, the flow is defined as fully turbulent. The calculation of convective heat transfer for the coolant flow depends upon the average Nusselt number (Nu_c), which is essentially the ratio between convective (h_c) and conductive heat transfer (k_c) at the boundary of a fluid. Equation 5.24 provides the relation between Nusselt number and the convective heat transfer coefficient (Incropera, et al., 2002).

$$Nu_c = \frac{h_c d_{int}}{k_c} \tag{5.24}$$

For heat transfer purposes, a turbulent flow configuration would be preferred as it leads to much greater Nusselt numbers and, consequently, greater heat transfer coefficients. One particular challenge associated with this system is the recovery of heat from ambient air when operating in Supply Mode. As temperatures in winter are often near or even below 0°C, this would require very low coolant temperatures for heat recovery, which might lead to high viscosity values that characterise a laminar flow regime if a glycol mixture is used. If only water is used as the coolant, the low temperatures might lead to the risk of freezing, which could damage components and compromise operation in Supply Mode.

In reality, recovering heat from such low temperature air might not be feasible, or engineers would have to adjust other parameters, such as the coolant mass flow rate or the HP load, in order to avoid very low coolant temperatures. For the purpose of this model, the coolant mass flow rate and the HP loads were kept constant, forcing convergence using laminar flow correlations for such conditions. This configuration was modelled in order to understand what would be the value, in terms of energy efficiency, of recovering heat at lower temperatures. The benefits of operating with an antifreeze mixture against a water counterfactual, as well as a strategy for dealing with the risk of freezing, are discussed in section 8.6.

5.4.4.1. Laminar Flow

The average Nusselt number for laminar flow depends upon the shape of the pipe or duct, as well as upon the entrance conditions and the development of the flow (Nellis and Klein, 2008). The Graetz number (Gz) is a dimensionless parameter that can be used to determine the flow development, which affects the Nusselt number. Equation 5.25 provides the formula to determine Gz, based on the total tube length L and the Prandtl number for the coolant flow Pr_c. The coolant Nusselt number for a laminar flow ($Nu_{c,l}$) can be calculated assuming a constant tube wall temperature or a constant heat flux. As wall temperatures vary significantly across the coil, the constant heat flux assumption has been used. This assumption yields Equation 5.26, which provides a correlation for calculating $Nu_{c,l}$ for a circular tube. It is important to notice that the fully developed value of Nusselt number (4.36) is reached when Gz approaches 0, i.e. when L becomes very large. This correlation is based on the works of Hornbeck (1965) and Shah and London (1978), as reported in (Nellis and Klein, 2008).

$$Gz = \frac{d_{int} Re_c Pr_c}{L} \tag{5.25}$$

$$Nu_{c,l} = 4.36 + \frac{\left[0.1156 + \frac{0.08569}{Pr_c^{0.4}}\right] Gz}{[1 + 0.1158 Gz^{0.6}]} \tag{5.26}$$

5.4.4.2. Turbulent Flow

In turbulent flow regimes, the Nusselt number is affected by the roughness of the coils internal surface (ε_c) and is not dependent upon the shape of the pipe (Nellis and Klein, 2008). Equation 5.27 provides a correlation for calculating the fully developed Nusselt number ($Nu_{c,tb,fd}$) for Prandtl (Pr_c) numbers between 0.5 and 2000 and Reynolds numbers (Re_c) from 2300 to 5 x 10^6 (Gnielinski, 1976). Equation 5.28 can be used to account for the developing regions (Kakaç et al., 1987) and yields an average Nusselt number ($Nu_{c,tb}$) that should be applied to calculate the convective heat transfer coefficient.

$$Nu_{c,tb,fd} = \frac{(\frac{f_{fd}}{8})(Re_c - 1000)Pr_c}{1 + 12.7(Pr_c^{2/3} - 1)\sqrt{\frac{f_{fd}}{8}}} \tag{5.27}$$

$$Nu_{c,tb} \cong Nu_{c,tb,fd}[1 + \left(\frac{d_{int}}{L}\right)^{0.7}] \tag{5.28}$$

The friction factor for a fully developed flow (f_{fd}) can be determined as shown in Equation 5.29 (Offor and Alabi, 2016). The average friction factor (ƒ) must account for the developing region and can be calculated for the entire tube length (L) in a similar manner as for the average Nusselt number ($Nu_{c,t}$), as shown in Equation 5.30 (Nellis and Klein, 2008).

$$\mathrm{f}_{fd} = \left(-2log_{10}\left[\frac{\varepsilon_c/d_{int}}{3.71} - \frac{1.975}{Re_c}\left(\ln\left[\left(\frac{\varepsilon_c/d_{int}}{3.93}\right)^{1.092} + \left(\frac{7.627}{Re_c + 395.9}\right)\right]\right)\right]\right)^{-2} \tag{5.29}$$

$$\mathrm{f} \cong \mathrm{f}_{fd}[1 + \left(\frac{d_{int}}{L}\right)^{0.7}] \tag{5.30}$$

5.4.4.3. Transitional Flow

Engineering Equation Solver (EES) determines the transitional Nusselt number ($Nu_{c,tr}$) based on a weighted average between the laminar ($Nu_{c,l}$) and turbulent ($Nu_{c,tb}$) values, as shown in Equation 5.31. This is achieved by considering the upper Reynolds number limit for laminar flow (2300) and the lower limit for a turbulent regime (3000), as well as the calculated Reynolds number (Re_c), which lies within these limits.

$$Nu_{c,tr} = Nu_{c,l} + \frac{Re_c - 2300}{3000 - 2300}(Nu_{c,tb} - Nu_{c,l}) \tag{5.31}$$

5.4.4.4. Thermal Resistance

After calculating the coolant's Nusselt number (Nu_c) for the HRC, the convective heat transfer coefficient for the coolant (h_c) can be determined as shown in Equation 5.24. The convective heat transfer can be also expressed in terms of a convective thermal resistance on the coolant side ($R_{c,t}$), which can be calculated as shown in Equation 5.32, based upon the heat transfer coefficient (h_c) and the total inside coil area (A_{in}) (Holman, 2010).

$$R_{c,t} = \frac{1}{h_c A_{int}} \tag{5.32}$$

5.4.5. Conduction through Tube Walls

The heat transfer through the wall of the metallic tubes carrying the coolant is driven by conduction. The conductive thermal resistance through the tubes ($R_{tube,t}$) is calculated as shown in Equation 5.33 (Holman, 2010). The calculations are based upon the external (r_{ext}) and internal (r_{int}) radii of the copper tubes, their length (L), conductivity (k_{tube}), as well as the total number of rows (N_{rows}) of the heat exchanger and the number of tubes per row (N_{tubes}).

$$R_{tube,t} = \frac{\ln(r_{ext}/r_{int})}{2\pi L k_{tube} N_{rows} N_{tubes}} \tag{5.33}$$

5.4.6. External Convection across a Bank of Tubes

In a fan coil heat exchanger, such as the one utilised in the WHR system, the air side heat transfer is dominated by forced convection across a bank of tubes. In this case, the Reynolds number for the air stream (Re_a) can be calculated with a formula analogous to Equation 5.23, but now with viscosity (μ_a) and density (ρ_a) values for air. The hydraulic diameter should now be computed as the tube external diameter (d_{ext}) and the maximum velocity (v_{max}) across the bundle of tubes should be used, as shown in Equation 5.34.

$$Re_a = \frac{\rho_a v_{max} d_{ext}}{\mu_a} \tag{5.34}$$

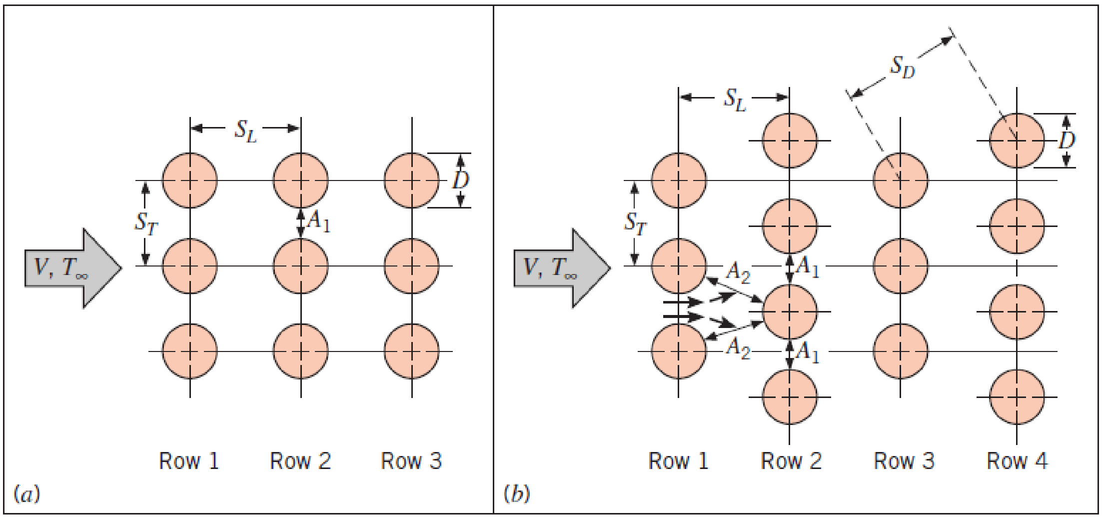

Figure 5.9 – Tube arrangements for a coil bank, which can be either: aligned (a); or staggered (b) (Incropera et al., 2002).

The maximum velocity depends on the configuration of the tubes, which is defined by the transverse pitch (S_T), the longitudinal pitch (S_L) and the tube external diameter, as shown in Figure 5.9. Tube configurations can be either aligned or staggered. The maximum velocity for a staggered coil arrangement may occur either on the transverse plane A_1 or the diagonal plane A_2, meaning that the velocities at both planes must be compared. The maximum velocity will be observed in A_2 if Equation 5.35 is satisfied. Since this is not the case for the WHR coils, as can be seen from Table 5.2, the maximum velocity will occur in plane A_1 and can be calculated by the correlation provided in Equation 5.36.

$$S_D < \frac{S_T + d_{ext}}{2} \tag{5.35}$$

$$v_{max} = \frac{S_T}{S_T - d_{ext}} v \tag{5.36}$$

Žukauskas (1972) developed a correlation for calculating the Nusselt number for air flowing across a bank of tubes (Nu_a), which can be determined as a function of the airstream Reynolds number, its Prandtl number (Pr_a) and the air Prandtl number at the coil surface temperature ($Pr_{a,s}$). This correlation is provided in Equation 5.37 and is valid for Prandtl numbers from 0.7 to 500 and Reynolds numbers from 10 to 2 x 10^6, covering the range of operation of the HRC.

$$Nu_a = C_1 C_2 Re_a^m Pr_a^{0.36} (\frac{Pr_a}{Pr_{a,s}})^{\frac{1}{4}} \tag{5.37}$$

The coefficients C_1, C_2 and m represent constants that are used to adjust the equation to the correct type of heat exchanger. The coefficients C_1 and m are dependent upon the maximum airstream Reynolds number (Re_a) and the coil arrangement. As for coefficient C_2, it is used as a correction factor for heat exchangers with a number of rows (N_{rows}) lower than 20. Both coefficients can be determined as detailed in the work of Incropera et al. (2002). Since the airstream Reynolds number for the HRC always sits between 2000 and 3000 as a result of its design volumetric flow rate ($V_a = 70\, m^3/s$), and also due to the coil configuration, C_1 is calculated as a function of the tube pitches ($C_1 = 0.35(S_T/S_L)^{1/5} \approx 0.36$), whilst m has a fixed value of 0.60. As for C_2, its value for a 12-row heat exchanger is 0.976.

5.4.6.1. Thermal Resistance

The convective heat transfer coefficient for the airstream (h_a) can be determined by utilising a correlation analogous to Equation 5.24, but now considering parameters relative to the flow or air across the coils, as shown in Equation 5.38 (Incropera et al., 2002). Based on the air heat transfer coefficient (h_a), the airside thermal resistance ($R_{a,t}$) can then be determined, as shown in Equation 5.39, where A_{coil} represents the total outside coil surface area, including fins, and η_o represents the global fin efficiency associated with the WHR coils. The fin efficiency calculations will be detailed in section 5.4.6.2.

$$Nu_a = \frac{h_a d_{ext}}{k_a} \tag{5.38}$$

$$R_{a,t} = \frac{1}{\eta_o h_a A_{coil}} \tag{5.39}$$

5.4.6.2. Fin Efficiency

There are different ways to enhance the heat transfer between two fluids. As shown in Equations 5.7 and 5.18, the heat transfer is a function of the overall heat transfer coefficient, the coil surface area, as well as the fluid temperatures and their specific enthalpies. One widely used method for enhancing heat transfer is by increasing the coil surface area with fins. According to Incropera et al. (2002), fins can be modelled accurately by assuming an adiabatic tip and a corrected fin length L_{fin}, which yields a correlation for calculating the efficiency of a single fin (η_{fin}) based on L_{fin} and a coefficient m_{fin}, as shown in Equation 5.40. The coefficient m_{fin} for a dry fin surface ($m_{fin,d}$) can be derived utilising Equation 5.41, based upon the air convective heat transfer coefficient (h_a), as well as the fin thickness (t_{fin}), and its conductivity, which in this case is equal to the tube conductivity (k_{tube}).

$$\eta_{fin} = \frac{\tanh(m_{fin}L_{fin})}{m_{fin}L_{fin}} \tag{5.40}$$

$$m_{fin,d} = \sqrt{\frac{2h_a}{k_{tube}t_{fin}}} \tag{5.41}$$

Equation 5.41 can be corrected to account for a wet surface condition by introducing the effective specific heat (C_{ef}), as shown in Equation 5.16, and replacing the convective heat transfer coefficient (h_a) for the convective mass transfer coefficient (h_m) utilising Equation 5.12 (Mitchell and Braun, 2013). The wet fin efficiency can then be calculated as shown in Equation 5.42. The correct coefficient m_{fin} must then be used depending on the coil surface conditions to derive the fin efficiency as presented in Equation 5.40.

$$m_{fin,w} = \sqrt{\frac{2h_a}{k_{tube}t_{fin}}\frac{C_{ef}}{C_{p,a}}} \tag{5.42}$$

A method for calculating the fin efficiency of straight fins was reported by Maidment (1998), where rectangular plate type fins were expressed in terms of a flat circular plate fin. Equations 5.43 and 5.44 show, respectively, the formulas used to determine the fin length L_{fin} and its equivalent plate fin diameter d_{fin}.

$$L_{fin} = \frac{d_{fin}}{2} - \frac{d_{ext}}{2} \tag{5.43}$$

$$d_{fin} = 2\sqrt{\frac{S_T S_L}{\pi}} \tag{5.44}$$

The global fin efficiency (η_o), which represents the efficiency of all the fins that comprise an extended surface, can be determined based on the number of fins (N_{fins}), the area of a single fin (A_{fin}), as well as the total outside coil surface area (A_{coil}), as shown in Equation 5.45. The global fin efficiency value can then be used to determine the overall airside thermal resistance by applying Equation 5.39.

$$\eta_o = 1 - \frac{N_{fins} A_{fin}}{A_{coil}} (1 - \eta_f) \tag{5.45}$$

5.4.7. Fouling

Another important aspect to consider in the modelling of heat exchangers is fouling, which is associated with the build-up of deposits on the heat transfer surface, possibly affecting both air and coolant streams. It has been reported that the LU air has higher mass concentrations of particulate matter when compared to ambient air (COMEAP, 2019), which could increase the risk of fouling when the system is operating in Extract Mode. However, different coil configurations were tested in the LU environment and no coil capacity reduction was noticed over a period of three months with a wide fin spacing similar to the one adopted for the HRC analysed in this study (Dragoni et al., 2016). Therefore, no capacity reduction associated with air side fouling will be regarded in this model.

As for the coolant side, EES provides fouling factors for a variety of fluids. The fouling factor (ξ_f) for closed-loop treated water is equal to $0.000175\, m^2K/W$ (Rohsenow et al., 1998) and has been utilised in the WHR model. It is assumed that the fouling factor would remain the same for a glycol mixture. The fouling factor can then be applied to the total internal coil area (A_{int}) to yield its associated thermal resistance ($R_{f,t}$), as shown in Equation 5.46.

$$R_{f,t} = \frac{\xi_f}{A_{int}} \tag{5.46}$$

5.4.8. Conduction through the Condensate Layer

As shown in Figure 5.6, the occurrence of condensation can lead to the formation of a layer of water between the coil surface and the air stream. The small thickness of this layer means that only conductive heat transfer takes place through the condensate film (Mitchell and Braun, 2013). Therefore, the thermal resistance associated with the condensate layer can be calculated by applying Equation 5.33 for a new ratio between the external and internal radii and considering the conductivity of water at atmospheric pressure. The ratio between radii would depend upon the thickness of the condensate layer, which requires complex modelling to be determined. Therefore, an analysis was carried out to identify the impact of the thickness of the condensate layer (t_{cond}) on the overall thermal resistance (ΣR_t), as shown in Table 5.3. The analysis considered a typical fully wet coil condition, with an air inlet temperature ($T_{a,in}$) of 18°C and relative humidity (RH_{in}) of 90%, to represent the most critical scenario in terms of condensate formation, where a water film would be present for the entire length of the coil.

Table 5.3 – Thermal resistances for the condensate layer (R_{cond}) and the overall coil (ΣR_t), for different layer thicknesses (t_{cond}).

t_{cond} (mm)	R_{cond} (K/W)	ΣR_t (K/W)	%
0	0	8.030×10^{-6}	0.00
0.4	2.868×10^{-9}	8.033×10^{-6}	0.04
3.3	1.948×10^{-8}	8.049×10^{-6}	0.24
6.2	3.154×10^{-8}	8.061×10^{-6}	0.39
9.1	4.102×10^{-8}	8.071×10^{-6}	0.51
12	4.882×10^{-8}	8.079×10^{-6}	0.60

Table 5.3 shows the condensate thermal resistance (R_{cond}) for different values of layer thickness, as well as how the overall thermal resistance for the wet surface is impacted by condensate formation. The last column provides the percentage of the thermal resistance that is associated with the condensate film. The thickness of the layer was assumed as five different values from 0.4 mm (equal to the tube thickness) to 12mm (equal to the tube external diameter), as well as a value of 0 mm, in order to illustrate the impact of the condensate film on heat transfer. As it can be seen from Table 5.3, even for values as high as 12 mm, the impact on the overall thermal resistance is below 1%. Therefore, due to the complexity of determining the condensate layer thickness and its low impact, the associated film conductive resistance will be neglected in the WHR model.

5.4.9. Overall Heat Transfer Coefficient

A dry coil condition means that the energy transfer can be expressed solely in terms of a transfer of heat, for which the driving potential is a difference in temperature. In this case, the overall dry heat transfer coefficient (U_d) is a function of the thermal resistances across the coil, which are expressed in $W/(m^2K)$. As for a wet condition, the energy balance involves both heat and mass transfer, with the process being driven by an enthalpy potential. In this case, the heat transfer must be calculated as a function of enthalpic resistances across the coil, which are expressed in $W/(m^2J\ kg^{-1})$. Therefore, the dry heat transfer coefficient (U_d), based on the external coil area (A_{coil}), is a function of the total thermal resistances (ΣR_t). As explained in section 5.4.8, the thermal resistance associated with the condensate layer ($R_{cond,t}$) is complex to model and has a minor impact on heat transfer and is thus neglected. Equation 5.47 provides a formula for calculating the overall dry heat transfer coefficient (U_d).

$$U_d = \frac{1}{A_{coil}\Sigma R_t} = \frac{1}{A_{coil}(R_{c,t}+R_{f,t}+R_{tube,t}+R_{a,t})} \tag{5.47}$$

The calculation of the wet heat transfer coefficient (U_w) must utilise enthalpic resistances across the coils. Therefore, the thermal resistances described in this investigation must be translated into enthalpic values. On the air side, this can be achieved by combining Equations 5.12 and 5.39, whereby the convective mass transfer coefficient is used to yield an enthalpic resistance. In this case, the fin efficiency must be calculated considering a wet surface and the resulting air enthalpic resistance ($R_{a,e}$) can be obtained using Equation 5.48.

$$R_{a,e} = C_{p,a} R_{a,t} \tag{5.48}$$

The remaining enthalpic resistances relate to coolant convection ($R_{c,e}$), fouling ($R_{f,e}$) and conduction through the tube walls ($R_{tube,e}$). These resistances are calculated based upon the coolant conditions and therefore the effective specific heat (C_{ef}) must be applied to the thermal resistances in order to express them in enthalpic terms, as shown in Equations 5.49 to 5.51.

$$R_{c,e} = C_{ef} R_{c,t} \tag{5.49}$$

$$R_{f,e} = C_{ef} R_{f,t} \tag{5.50}$$

$$R_{tube,e} = C_{ef} R_{tube,t} \tag{5.51}$$

After all the enthalpic resistances (ΣR_e) are determined, the wet heat transfer coefficient (U_w) can be calculated in an analogous manner to the thermal coefficient, as shown in Equation 5.52. The heat transfer coefficients for both dry (U_d) and wet (U_w) sections can then be applied to calculate the energy balance at the HRC using Equations 5.20 to 5.22.

$$U_w = \frac{1}{A_{coil} \Sigma R_e} = \frac{1}{A_{coil}(R_{c,e} + R_{f,e} + R_{tube,e} + R_{a,e})} \tag{5.52}$$

5.4.10. Condensation

After the heat transfer process is correctly defined based on the coil surface condition, it is necessary to introduce correlations into the model that enable the determination of the air outlet conditions, which relates to the sensible and latent cooling loads of the HRC. As seen in Figure 5.5, the process of cooling humid air can be best represented by a straight line for the dry section and a curve for the wet section of a given coil. One method that can be used to calculate the change in moisture content ($\Delta\omega$) as humid air travels through HRC is called the enthalpy-based effectiveness method (Nellis and Klein, 2008). This method works by defining a wet effectiveness (ϵ_w), which is based upon the air stream enthalpies and moisture contents for the wet section of the coil. Considering that the air stream enters the wet section at point X, as shown in Figure 5.8, the inlet enthalpy ($i_{a,x}$) and moisture content (ω_x) would be evaluated also at point X, as shown in Equation 5.53.

$$\epsilon_w = \frac{i_{a,x} - i_{a,out}}{i_{a,x} - i_{c,sat,in}} = \frac{\Delta\omega}{\Delta\omega_{max}} = \frac{\omega_x - \omega_{out}}{\omega_x - \omega_{min}} \tag{5.53}$$

In this case, as can be observed from Equation 5.53, the heat exchanger would be 100% effective if the air stream was able to leave the coils saturated and at the coolant inlet temperature, which corresponds to an enthalpy equal to $i_{c,sat,in}$, as described in section

5.4.3.2. The minimum air enthalpy at the coil outlet ($i_{c,sat,in}$) is associated with the minimum achievable saturated moisture content (ω_{min}). By relating the actual ($\Delta\omega$) and maximum ($\Delta\omega_{max}$) changes in moisture content to the coil wet effectiveness (ϵ_w), the outlet air moisture content (ω_{out}) can then be determined. This process is illustrated in Figure 5.10, with the wet section being represented by the line connecting points 2 and 3.

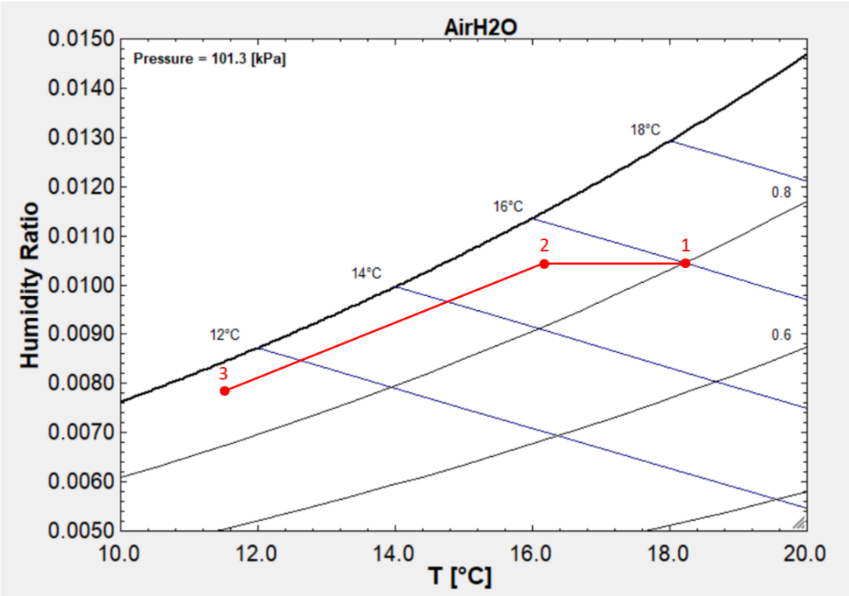

Figure 5.10 – A psychrometric chart with a representation of the process of cooling moist air using the enthalpy-based effectiveness method.

After the outlet air conditions and the moisture content change are determined as part of the energy balance, the mass of water condensed from the air stream (m_{cond}) as well as the sensible heat load (Q_{sen}) can be determined. The mass of condensate is determined based on Equation 5.54, which involves the humidity ratio change ($\Delta\omega = \omega_{in} - \omega_{out}$) and the mass flow rate of dry air ($\dot{m}_{a,d}$) and the period analysed (Δt). The mass flow rate of dry air can be calculated using the inlet mass flow rate of air ($\dot{m}_a$) and the inlet moisuture content (ω_{in}), as shown in Equation 5.55. The sensible heat load can be determined using Equation 5.56. This is then used to determine the Sensible Heat Ratio (SHR), as shown in Equation 5.57.

$$m_{cond} = \dot{m}_{a,d}(\omega_{in} - \omega_{out})\Delta t \tag{5.54}$$

$$\dot{m}_{a,d} = \frac{\dot{m}_a}{1+\omega_{in}} \tag{5.55}$$

$$Q_{sen} = \dot{m}_a C_{p,a}(T_{a,in} - T_{a,out}) \tag{5.56}$$

$$SHR = \frac{Q_{sen}}{Q_{rec}} \tag{5.57}$$

5.4.11. Risk of Frost Accumulation

When cold air is used for heat recovery, which can occur particularly when operating in Supply Mode, condensation can lead to the build-up of frost on the HRC. Frosting is a complex phenomenon that could either reduce or enhance the heat transfer coefficient, depending on fluid flow, geometry and type of frost that forms on a given heat exchanger. This phenomenon was analysed by Maidment (1998), who investigated the performance of an evaporator used in a supermarket refrigeration system and found that frost was able to improve heat transfer. The enhancement reported was, however, below 5%, showing that frosting had little impact on the performance of the evaporator. The HRC operate at much higher temperatures than the heat exchanger reported in the aforementioned study, and frost accumulation would be more likely to occur if the system were operating in Supply Mode on particularly cold days, which is unlikely to take place, as this would have a negative impact on HP performance. For those reasons, the risk of frosting will be disregarded in the WHR model.

5.5. The Coolant Loop

The coolant loop consists of the pipework carrying the heat recovery fluid from the coils to the HP's evaporator. It was simulated solely to account for pumping energy, as heat losses across the loop are neglected in the WHR model due to its short length and low temperatures. Another important aspect for simulating the WHR system is defining the correct fluid to be considered as coolant. The WHR system was designed to utilise water, but initial model calculations indicate that the coolant could reach negative temperatures, particularly when running at night-time in Supply Mode during the winter season. The use of an antifreeze mixture could help in reducing system downtime, but it would result in lower energy efficiency. An analysis of the running hours and performance implications associated with utilising different coolants is discussed in Chapter 8, whereas this section focuses on the modelling of the pumping requirements for the coolant loop. Figure 5.11 highlights the model components and inputs associated with the coolant loop, and how they are linked to the other elements of the model.

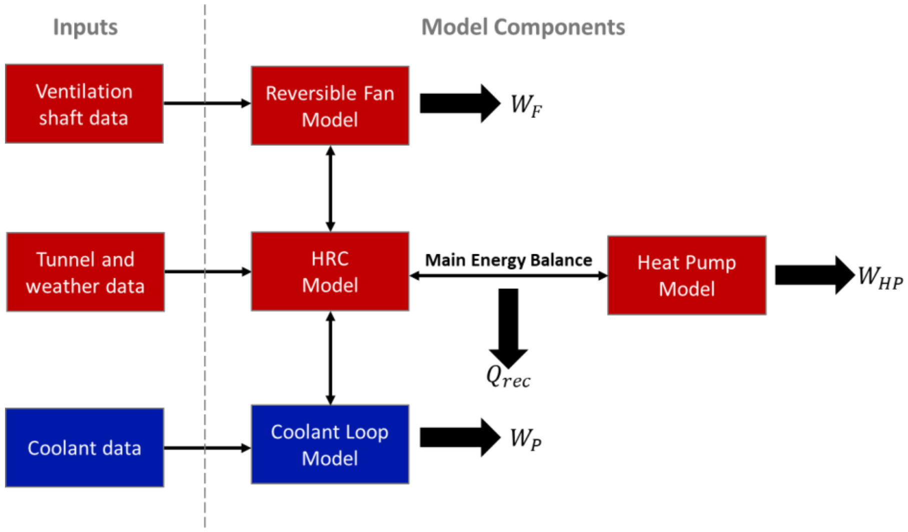

Figure 5.11 – The WHR model framework, with the components and inputs associated with the coolant loop highlighted in blue.

5.5.1. Pumping Power

The role of a pump in a hydraulic system is to provide sufficient pressure to overcome any head losses and move a working fluid at a desirable flow rate. The operating pressure of a pumping system can be expressed in the SI unit of meters (m), being also known as pressure head. For the WHR system, the total system head can be expressed as in Equation 5.58.

$$H_{total} = H_{static} + H_{dynamic} + H_{components} \tag{5.58}$$

Where the static head represents any difference in elevation that must be overcome by the pumps and the dynamic head is associated with friction. The last term in Equation 5.58 accounts for the head loss related to the components of the WHR system that are connected by the coolant loop, namely the HRC and the evaporator of the HP. As the detailed hydraulic design of the system was not available, a static head of 5.00 m was assumed and the dynamic head was calculated as shown in Equation 5.59 (Milnes, 2010).

$$H_{dynamic} = \frac{K * v^2}{2 * g} \tag{5.59}$$

Where K is the head loss coefficient, v is the coolant velocity in the pipe, in m/s, and g is the acceleration due to gravity, in m/s^2. The velocity for the coolant loop (v_{loop}) can be calculated as shown in Equation 5.60 (Milnes, 2010), which involves the pipe cross sectional area (A_{loop}), in m^2, and the coolant volumetric flow rate ($\dot{V}_c$) through the pipe, given in m^3/s.

$$v_{loop} = \frac{\dot{V}_c}{A_{loop}} = \frac{4 * \dot{V}_c}{\pi * d_{loop}} \tag{5.60}$$

The coolant volumetric flow rate ($\dot{V}_c$) is calculated based upon the design mass flow rate ($\dot{m}_c$) of 37.6 kg/s and the density of the fluid (ρ_c). Assuming a DN 150 mm stainless steel pipe for the loop, with a hydraulic diameter (d_{loop}) of 154.1 mm, the velocity can then be calculated. The head loss coefficient (K) is able to represent both friction and pipework fitting losses in terms of an equivalent pipe length and therefore consists of two elements, the loss coefficient associated with the fittings (K_{fit}) and the loss coefficient related to the friction of the straight pipe lengths (K_{pipe}). This relationship is expressed in Equation 5.61 (Milnes, 2010).

$$K = K_{fit} + K_{pipe} \tag{5.61}$$

As the detailed hydraulic design of the coolant loop was not available when developing this model, some assumptions had to be used to calculate the head loss coefficients. Table 5.4 lists the items considered to calculate the fittings loss coefficient of the coolant loop. The table also provides the location where these items should be installed, as well as the number of items and their associated K values. A total head loss coefficient factor of 12.40 was calculated for the pipework fittings (K_{fit}). As for the loss coefficient of the straight lengths of the pipework (K_{pipe}), it can be obtained by applying Equation 5.62 (Milnes, 2010).

Table 5.4 – Total loss coefficients from fittings of the coolant pipework, based on values from Milnes (2010).

Fitting item	Location	No. of items	K value	Item total
Inlet pipe (Bellmouth)	HRC and evaporator	2	0.05	0.1
90° Bend (short radius)	Assuming 10	10	0.75	7.5
45° Bend (short radius)	Assuming 6	6	0.3	1.8
Butterfly valve (fully open)	Before HRC and evaporator	2	0.3	0.6
Non-return valve	After HRC and evaporator	2	1	2
Outlet pipe (Bellmouth)	HRC and evaporator	2	0.2	0.4

$$K_{pipe} = \frac{f * L_{loop}}{d_{loop}} \tag{5.62}$$

Where L_{loop} is the pipework length, assumed to be equal to 20 meters in the model, and D_{loop} is the pipe hydraulic diameter. The friction coefficient f is a dimensionless parameter that can be calculated for the coolant loop parameters using Equations 5.29 and 5.30, whereby the loop diameter (d_{loop}), in metres, and its Reynolds number (Re_{loop}) have to be applied, as well as the loop roughness factor (ε_{loop}), which is equal to 0.000046 m for commercial steel (Stoecker and Jones, 1982). The Reynolds number was calculated for each time step, since it varies at different temperatures. After both K_{fit} and K_{pipe} are calculated, the dynamic head can be determined applying Equations 5.59, 5.60 and 5.61.

In order to calculate the total head (H_{total}), as shown in Equation 5.58, the head loss associated with system components must also be determined. The main components for this circuit are the HRC and the HP evaporator. Their associated head losses can be calculated as a function of the pressure drop on the coolant side of each component (ΔP_c), in Pa, and the acceleration due to gravity (g), as shown in Equation 5.63. The design values for the pressure drops of the HRC and the evaporator are of 134 kPa and 20 kPa, respectively. After the total head loss (H_{total}) is calculated, the pumping power required to overcome this head loss (W_P), in kW, can be found, as shown in Equation 5.64 (Milnes, 2010). The calculations assumed a pump efficiency (η_P) of 50%. As the model is based upon hourly time steps, the pumping energy consumption, in kWh, can also be determined by Equation 5.64.

$$H_{components} = \frac{\Delta P_c}{g} \tag{5.63}$$

$$W_P = \frac{H_{total} * g * \dot{m}_c}{\eta_P * 10} \tag{5.64}$$

5.6. Two-stage Heat Pump

The HP is used to upgrade the recovered heat to suitable temperatures for distribution via the district heating network (DHN). The framework for the WHR model, highlighting the HP model component is shown in Figure 5.12. A HP is a device capable of moving heat from a source at lower temperature to a sink at higher temperature through the input of energy. This process can be described as in Equation 5.65, in which Q_{evap} represents the heat being absorbed at the evaporator, whilst Q_{out} and W_{HP} are the HP's heat output and work input, respectively.

$$Q_{out} = Q_{evap} + W_{HP} \tag{5.65}$$

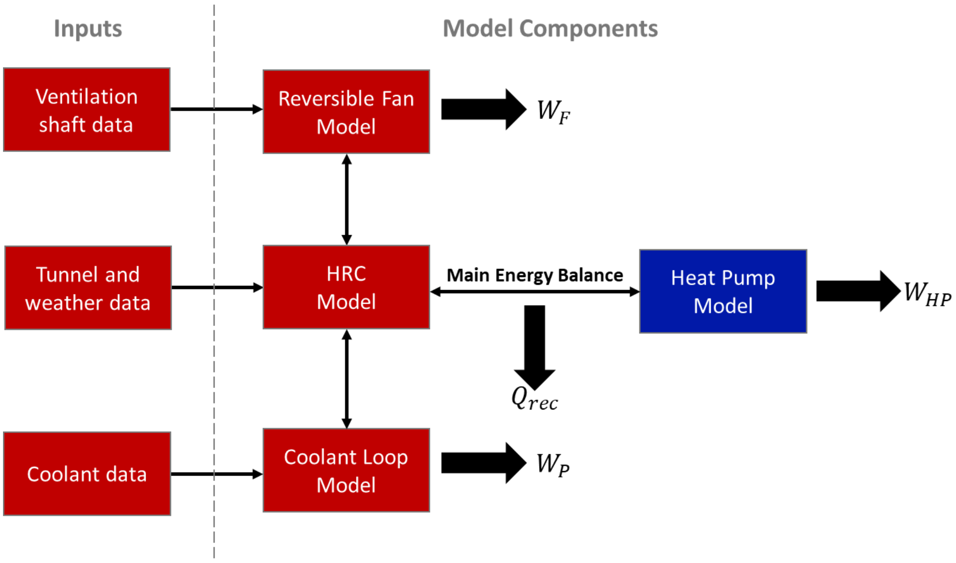

Figure 5.12 – The WHR model framework, with the components and inputs associated with the HP highlighted in blue.

The Bunhill WHR system utilises a two-stage ammonia (NH_3/R717) electric HP, designed by GEA Refrigeration based upon the flow and return DHN temperatures of, respectively, 75°C and 55°C. As mentioned in 4.4, two-stage cycles can increase the efficiency of HPs that operate with large temperature differences between heat source and sink. The two-stage HP can be divided into low and high-pressure stages, which are connected by a separator tank, where saturated NH_3 is kept at constant pressure. The compressors for both stages have inverters that enable them to operate at variable speeds, and the capacity of the HP can be adjusted in the model by modulating its heat output. The COP of the HP can then be determined based on the power demand for the low-stage ($W_{comp,ls}$) and high-stage ($W_{comp,hs}$) compressors, as shown in Equations 5.66 and 5.67.

$$COP_h = \frac{Q_{out}}{W_{HP}} \tag{5.66}$$

$$W_{HP} = W_{comp,ls} + W_{comp,hs} \tag{5.67}$$

The HP was modelled based on full-load design specifications provided by Islington Council (2019). A schematic of the HP is provided in Figure 4.4, whist Table 5.5 shows the inlet (T_{in}) and outlet (T_{out}) temperatures, as well as the pressure drops (ΔP) for each of the aforementioned heat exchangers. These values were provided for an operation where the coolant used is water, with an inlet temperature of 6°C and a ΔT of 5 K. In order to reduce computational effort, the two-stage refrigeration cycle shown in Figure 4.4 has been adapted to the cycle shown in Figure 5.13.

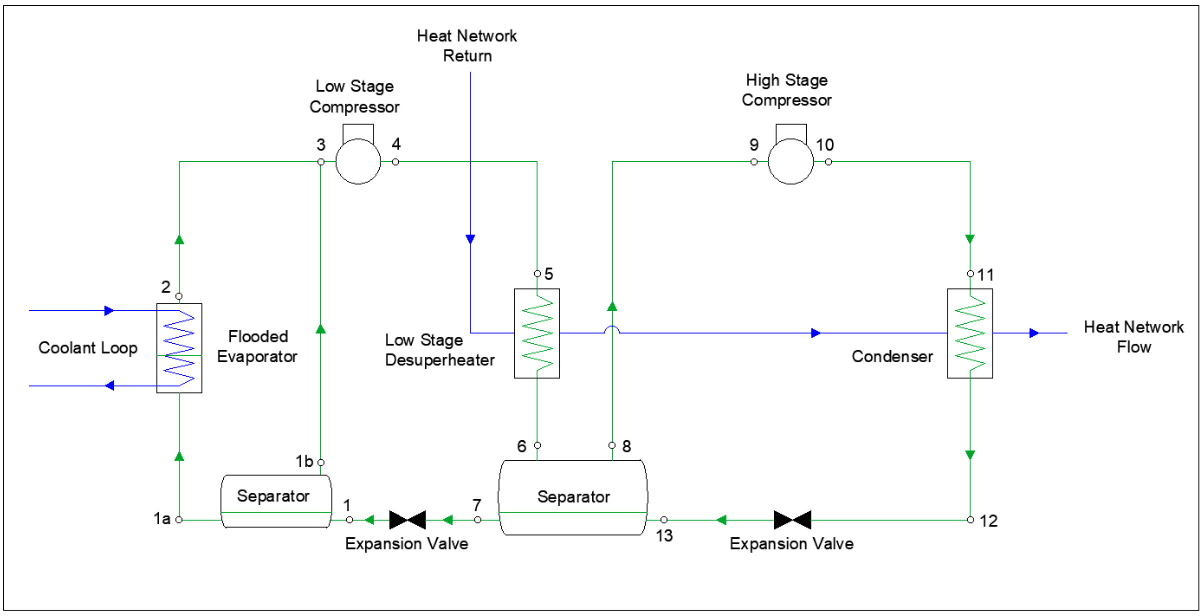

Figure 5.13 – Schematic of the adapted two-stage ammonia HP of the WHR system.

Table 5.5 – List of heat exchangers for the HP and their design pressure drops and temperatures (Islington Council, 2019).

Stage	Heat Exchanger	Coolant (water)			Refrigerant (NH_3/R717)		
		T_{in} (°C)	T_{out} (°C)	ΔP (kPa)	T_{in} (°C)	T_{out} (°C)	ΔP (kPa)
Low	**Evaporator**	11	6	30	4	4	1
	Desuperheater	55	56.7	22.7	103	60	0.7
High	**Desuperheater**	72.9	75	28.3	113	78	1.2
	Condenser	58	72.9	27	78	75	0.6
	Subcooler	56.7	58	50.5	75	58.8	0.3

The main simplifications are associated with the high stage. The parallel compressors were modelled as a single compressor with twice the capacity of the former, considering the same pressure lift and double the refrigerant mass flow rate. The other significant adaptation has been the high-stage heat exchangers, which were modelled as a single condenser, with the overall temperature and pressure differentials being calculated as the sum of those associated with each separate heat exchanger. The main reason behind the latter simplification is associated with the controls of the HP, which is based on its compressors. The low-stage compressor speed is adjusted to make sure the intermediate saturation temperature is always 42°C, whilst the high-stage compressors are controlled to guarantee that the water leaves the

HP at the DHN set point of 75°C. Since the WHR model is based on a full-load operation with a fixed water temperature difference (ΔT_w), the high-stage heat exchangers would be operating in the same temperature range, so they can be modelled as a single unit. Table 5.6 provides an overview of the operating parameters that were used to model the HP, based upon the data from Table 5.5.

Table 5.6 – List of heat exchangers for the adapted two-stage HP and their operating parameters.

Stage	Heat Exchanger	Coolant (brine or water)			Refrigerant (NH_3/R717)		
		T_{in} (°C)	T_{out} (°C)	ΔP (kPa)	T_{in} (°C)	T_{out} (°C)	ΔP (kPa)
Low	**Evaporator**	Variable		30	Variable		0
	Desuperheater	55	Variable	22.7	Variable		0.7
High	**Condenser**	Variable	75	105.8	113	58.8	2.1

The heat output from the HP (Q_{out}) therefore consists of both the heat being delivered at the desuperheater ($Q_{ds,ls}$) and the condenser (Q_{cond}), as shown in Equation 5.68.

$$Q_{out} = Q_{ds,ls} + Q_{cond} \tag{5.68}$$

In a full-load operation, the model assumes that the HP delivers a constant heating duty of 1038 kW, which is the load necessary to heat up water from 55 to 75°C with the design flow rate of 12.4 kg/s. It must be highlighted that the evaporator and the low-stage desuperheater were modelled with varying temperatures. The evaporating temperature depends on the coolant temperatures calculated at the HRC energy balance, which vary according to the air conditions at the ventilation shaft. As for the desuperheater, its temperatures float according to the refrigerant mass flow rate calculated for the energy balance at the evaporator. The pressure drop across the desuperheater was assumed constant and the pressure drop across the evaporator was assumed negligible for simplification. The detailed modelling of each component shown in Figure 5.13 is described in the following sections.

5.6.1. Evaporator

The evaporator, as well as the other heat exchangers in the HP circuit, are plate-and-shell heat exchangers (PSHEs), which consist of a welded plate pack that is covered by a metallic shell. The plate pack is assembled in a way that forms two separate fluid streams without the need for gaskets. One fluid flows within the plate pack, whilst the other flows between the shell and the external surface of the plates. PSHEs can have different arrangements, as the cold and hot fluids can either flow through the plate pack or the shell, having one or more passes through the heat exchanger. Figure 5.14 provides a schematic of a typical PSHE, obtained from the manufacturer of the heat exchangers used for the two-stage HP installed at Bunhill.

PSHEs combine the robustness of shell-and-tube heat exchangers with the high thermal performance of plate heat exchangers (PHEs) (Ayub, 2003). They work in a similar manner to other PHEs and can be modelled as such. The evaporator is the most complex heat exchanger to be modelled within the HP circuit, as it involves variable operating temperatures and combines both single phase and two-phase heat transfer regimes. Therefore, the evaporator model must be able to calculate an energy balance for different coolant temperatures, considering the sensible heat transfer on the coolant stream and the boiling heat transfer on the refrigerant side. The modelling of the evaporator is described in the following subsections.

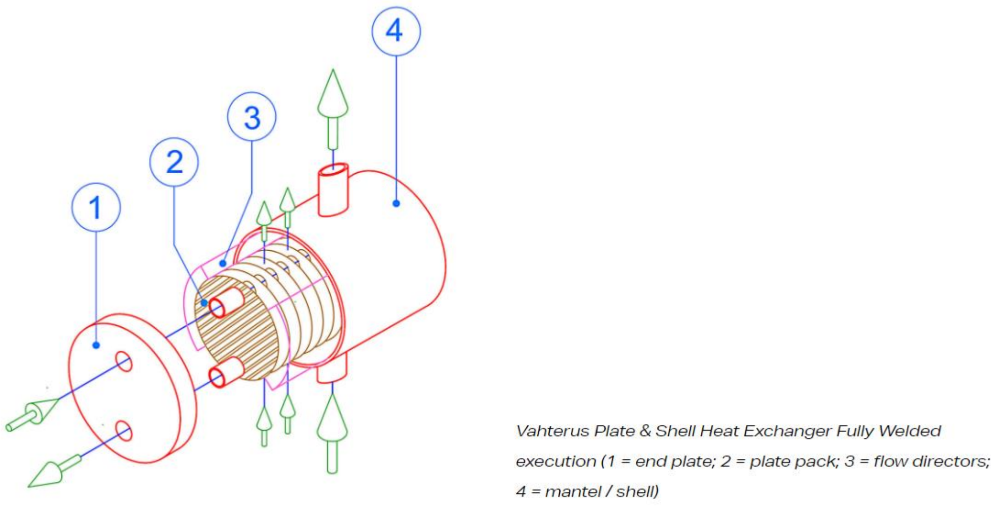

Figure 5.14 – A schematic of a typical plate-and-shell heat exchanger (Vahterus, 2020).

5.6.1.1. Geometry

In the evaporator, the coolant flows through the plate stack and the refrigerant flows between the shell and the plate surface, with both fluids passing a single time through the heat exchanger. The plate pack consists of 342 plates with a diameter (d_{plate}) of 556 mm and thickness (t_{plate}) of 0.8 mm. The shell has a diameter of 850 mm and a total length (L_{evap}) of 1015 mm. The refrigerant enters the shell through a single nozzle on the end plate of the shell, leaving the evaporator through two nozzles at the top of the shell.

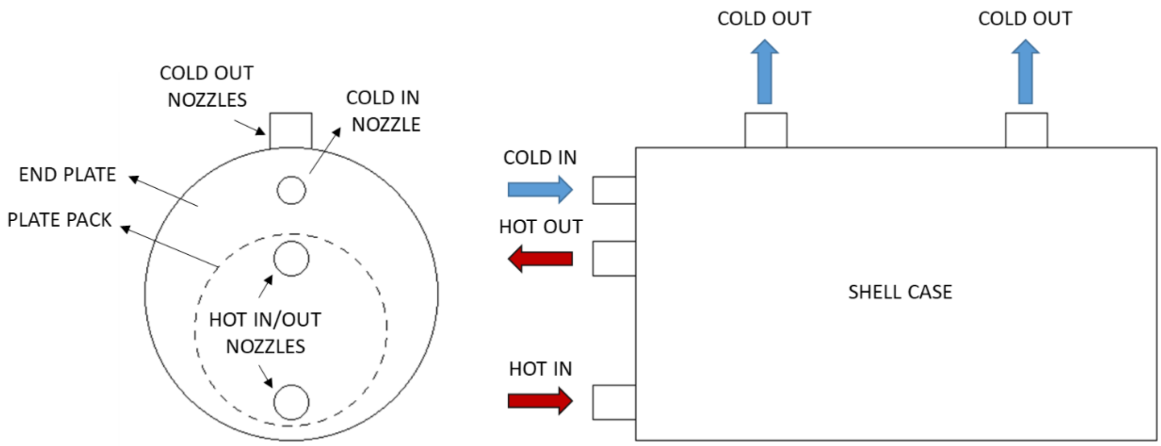

Figure 5.15 – Schematic highlighting the components, and fluid inlets and outlets for the evaporator.

The coolant enters and leaves the evaporator through the end plate of the shell, entering at the bottom and leaving at the middle of the end plate. Figure 5.15 shows a schematic of the fluid flows through the evaporator, whilst Table 5.7 provides a list of its geometric parameter values.

Table 5.7 – Plate-and-shell evaporator geometric parameter values.

Parameter	Description	Unit	Value
N_{plates}	Number of plates	N/A	342
d_{plate}	Plate diameter	mm	556
t_{plate}	Plate thickness	mm	0.8
A_{plate}	Plate area	m^2	0.26
A_{evap}	Evaporator surface area	m^2	88.92
L_{evap}	Length of plate pack	m	1.015
d_{nozzle}	Hot fluid nozzle diameter	mm	102.3
A_{nozzle}	Total nozzle area for plate pack	cm^2	82.13
A_{proj}	Projected plate area	m^2	0.2264
ϕ_{evap}	Evaporator surface enlargement factor	N/A	1.149
w_{plate}	Equivalent plate width	mm	436.7
p_{plate}	Plate pitch	mm	2.968
b_{plate}	Plate channel spacing	mm	2.168
d_{evap}	Evaporator hydraulic diameter	mm	3.775
β_{plate}	Plate Chevron angle	Degrees	60

Some of the parameter values listed above were obtained from design specifications provided by Islington Council (2019), whilst others were derived from data provided by the manufacturer. Kakaç et al. (2012) reported a method for designing PHEs that has been applied in this investigation. This method is based on a rectangular gasketed PHE, however, as reported by Ayub (2003), it can be adjusted and used for PSHEs with circular plates. Kakaç et al. (2012) demonstrated how to calculate the hydraulic diameter and the channel spacing of a PHE based upon its geometry. Initially, the surface enlargement factor for the evaporator (ϕ_{evap}) must be determined, as shown in Equation 5.69, which relates the actual and projected plate areas. The actual plate area (A_{plate}) was obtained from the manufacturer and accounts for the enlargement associated with plate corrugation, whilst the projected area (A_{proj}) represents the original flat area of the plate, which can be calculated as shown in Equation 5.70.

$$\phi_{evap} = \frac{A_{plate}}{A_{proj}} \quad (5.69)$$

$$A_{proj} = \frac{\pi d_{evap}^2}{4} - 2 * A_{nozzle} \quad (5.70)$$

The surface enlargement factor should be used to determine the hydraulic diameter of the evaporator (d_{evap}), as shown in Equation 5.71. This means that the plate channel spacing

(b_{evap}) must also be calculated by applying Equation 5.72. The channel spacing is a function of the plate thickness (t_{plate}) and pitch (p_{plate}). The former was obtained from the PSHE manufacturer and the latter can be calculated by dividing the total plate pack length (L_{evap}) by the total number of plates (N_{plate}), as shown in Equation 5.73.

$$d_{evap} = \frac{2b_{evap}}{\phi_{evap}} \tag{5.71}$$

$$b_{evap} = p_{plate} - t_{plate} \tag{5.72}$$

$$p_{plate} = \frac{L_{evap}}{N_{plates}} \tag{5.73}$$

Other geometric parameters used to calculate the heat transfer at the evaporator include the plate Chevron angle (β_{plate}) and the plate width, as well as the number of flow channels per pass (N_{cp}) for each fluid in the PHE. The number of flow channels per pass can be calculated based on the total number of plates (N_{plates}) in the heat exchanger and the number of passes (N_{pass}) for the fluid being analysed, as shown in Equation 5.74. The Chevron angle was assumed as 60° and an equivalent plate width (w_{plate}) was calculated to represent the circular plates as rectangles, as shown in Equation 5.75, where the plate diameter was considered as the plate length, so that the method reported by Kakaç et al. (2012) could be used.

$$N_{cp} = \frac{N_{plates} - 1}{2N_{pass}} \tag{5.74}$$

$$w_{plate} = \frac{\pi d_{plate}^2}{4} * \frac{1}{d_{plate}} \tag{5.75}$$

5.6.1.2. Single Phase Heat Transfer

The phenomenon of single phase heat transfer in PHEs has been investigated by several authors. Similarly to the calculation method for the HRC, described in section 5.4, heat transfer regimes in PHEs can also be calculated using empirical correlations. Some examples of developed correlations can be found in the works of Khan et al. (2010), Muley and Manglik (1999), Wanniarchchi et al. (1995), Thonon (1995) and Kumar (1984). Amongst these, the correlations developed by Khan et al. (2010) and Muley and Manglik (1999) are not applicable to the evaporator, as they have only been tested for a limited range of Prandtl and Reynolds numbers. The remaining correlations are described in this section and were tested together with two-phase heat transfer correlations to assess their applicability in the HP model.

Before each correlation is introduced, two flow parameters that form the basis for single phase heat transfer calculations must be determined. The first one is the coolant mass flux or velocity through the evaporator ($G_{c,evap}$), which is detailed in Equation 5.76 and provides a figure for the coolant mass flow rate ($\dot{m}_c$) per surface area for a given PHE. The other parameter is the Reynolds number, which was introduced in section 5.4.4 and can be determined for coolant flow in the evaporator using Equation 5.77.

$$G_{c,evap} = \frac{\dot{m}_c}{N_{cp} b_{evap} w_{plate}} \tag{5.76}$$

$$Re_{c,evap} = \frac{G_{c,evap} d_{evap}}{\mu_c} \tag{5.77}$$

Based upon these parameters, the Nusselt number for single phase coolant flow in the evaporator ($Nu_{c,evap}$) can be calculated, and different correlations for doing so are introduced in the following subsections. The Nusselt number can then be used to yield the convective heat transfer coefficient for coolant flow in the evaporator ($h_{c,evap}$), as shown in Equation 5.78.

$$h_{c,evap} = \frac{Nu_{c,evap} k_c}{d_{evap}} \tag{5.78}$$

5.6.1.2.1. The Wanniarchchi Correlation

The correlation developed by Wanniarchchi et al. (1995) can be utilised to determine the coolant side Nusselt number for the evaporator ($Nu_{c,evap}$) based on a combination of turbulent ($Nu_{c,tb,evap}$) and laminar ($Nu_{c,l,evap}$) conditions. These parameters can be calculated as shown in Equations 5.79 to 5.82, where Pr_c represents the Prandtl number for the coolant and $\mu_{c,s}$ is the coolant viscosity at the plate surface temperature. This correlation is valid for Reynolds numbers up to 10000 and for Chevron angles above 22°, being applicable to the evaporator.

$$Nu_{c,evap} = \sqrt[3]{Nu_{c,l,evap}^3 + Nu_{c,tb,evap}^3} Pr_c^{1/3} \left(\frac{\mu_c}{\mu_{c,s}}\right)^{0.17} \tag{5.79}$$

$$Nu_{c,l,evap} = 3.65 \beta_{evap}^{-0.455} \phi_{evap}^{0.661} Re_{c,evap}^{0.339} \tag{5.80}$$

$$Nu_{c,tb,evap} = 12.6 \beta_{evap}^{-1.142} \phi_{evap}^{1-m} Re_{c,evap}^{m} \tag{5.81}$$

$$m = 0.646 + 0.0011 \beta_{evap} \tag{5.82}$$

5.6.1.2.2. The Thonon Correlation

Another method for calculating the coolant side Nusselt number for the evaporator ($Nu_{c,evap}$) is the correlation developed by Thonon (1995). This correlation can be applied for Reynolds numbers between 50 and 15,000, and for Chevron angles varying from 30° to 75°. The correlation is based upon the Reynolds ($Re_{c,evap}$) and Prandtl (Pr_c) numbers for the coolant flow and can be calculated as shown in Equation 5.83. The empirical coefficients C_1 and m are dependent upon the plate Chevron angle of the PSHE plates. In the case of the evaporator, where the Chevron angle is assumed as 60°, C_1 is 0.2267 and m is 0.631.

$$Nu_{c,evap} = C_1 Re_{c,evap}^{m} Pr_c^{1/3} \tag{5.83}$$

5.6.1.2.3. The Kumar Correlation

The correlation proposed by Kumar (1984) has been developed for water and has a similar format to Thonon's correlation. It is also based upon the Reynolds ($Re_{c,evap}$) and Prandtl (Pr_c) numbers for the coolant, as well as on its viscosity, both at fluid (μ_c) and plate surface ($\mu_{c,s}$) temperatures, as shown in Equation 5.84. For this correlation, coefficients C_1 and m are dependent upon the Chevron angle and the Reynolds number. For an angle of 60° and Reynolds numbers above 400, C_1 is 0.108 and m is 0.703.

$$Nu_{c,evap} = C_1 Re_{c,evap}^{m} Pr_c^{1/3} (\frac{\mu_c}{\mu_{c,s}})^{0.17} \tag{5.84}$$

5.6.1.3. Two-phase Heat Transfer

Two-phase heat transfer is a more complex phenomenon as it involves both forced convection and phase change. When it comes to PHEs, two-phase heat transfer is not as well reported in literature as single phase regimes, and the correlation adopted must be applicable to evaporators that use ammonia as the working fluid. The work of Ayub (2003) involved the development of a correlation for calculating two-phase heat transfer coefficients in PHEs, based upon a survey of 38 industrial evaporators, of which 30 were flooded and utilised ammonia as the refrigerant. Khan et al. (2014) proposed another correlation for NH_3 two-phase flow, which was developed for a counterflow PHE with ammonia saturation temperatures from -25 to -2°C. Both these correlations will be described in the following subsections and compared against available manufacturer data (Islington Council, 2019).

5.6.1.3.1. The Ayub Correlation

The correlation proposed by Ayub (2003) was developed based on refrigeration systems with evaporating temperatures from -18 to 10°C and varying capacities. The correlation can be applied to calculate the two-phase refrigerant heat transfer coefficient ($h_{r,evap}$) considering the Reynolds number ($Re_{r,liq,evap}$) and the conductivity ($k_{r,liq}$) of liquid refrigerant at evaporating pressure, as well as the plate diameter (d_{plate}), the evaporator hydraulic diameter (d_{evap}), the heat of vaporisation for ammonia (i_{vap}), the evaporating pressure (P_{evap}), the critical pressure for ammonia (P_{crit}), and the plate Chevron angle (β_{evap}). The correlation, shown in Equation 5.85, yields $h_{r,evap}$ in imperial units and must be converted for use in SI units.

$$h_{r,evap} = C \frac{k_{r,liq}}{d_{evap}} \left(\frac{Re_{r,liq,evap}^2 i_{vap}}{d_{plate}}\right)^{0.4124} \left(\frac{P_{evap}}{P_{crit}}\right)^{0.12} \left(\frac{65}{\beta_{evap}}\right)^{0.35} \tag{5.85}$$

The correlation is applicable for both direct expansion and flooded evaporators, and the empirical coefficient C is used to specify the evaporator's type. In the case of flooded evaporators as in the HP, C is 0.1121. The statistical error reported for the proposed correlation is of ±8%.

5.6.1.3.2. The Khan Correlation

The correlation proposed by Khan et al. (2014) was developed with low evaporating temperatures, heat fluxes from 21 to 44 kW/m^2, and Reynolds numbers from 1,225 to 3,000. The Reynolds number calculated for the manufacturer data available was within that range, which was not the case for the heat flux ($q"_{evap}$) and the evaporating temperature. The proposed correlation calculates the Nusselt number for two-phase refrigerant flow ($Nu_{r,evap}$) based upon an equivalent Reynolds number ($Re_{r,eq}$) and an equivalent Boiling number ($Bo_{r,eq}$), which can be calculated as demonstrated in Equations 5.86 and 5.87, respectively.

$$Re_{r,eq} = \frac{G_{r,eq} d_{evap}}{\mu_r} \tag{5.86}$$

$$Bo_{r,eq} = \frac{q"_{evap}}{G_{r,eq} i_{vap}} \tag{5.87}$$

The term μ_r represents the average refrigerant viscosity at the evaporating temperature and $G_{r,eq}$ is the equivalent mass flux, which can be calculated based upon refrigerant mass flux ($G_{r,evap}$) and average quality (x_r) through the evaporator, as well as its liquid (ρ_{liq}) and gaseous (ρ_{gas}) densities at the evaporating temperature. Equations 5.88 and 5.89 demonstrate how to determine both $G_{r,evap}$ and $G_{r,eq}$, respectively.

$$G_{r,evap} = \frac{\dot{m}_r}{N_{cp} b_{evap} w_{plate}} \tag{5.88}$$

$$G_{r,eq} = G_{r,evap} \sqrt{1 - x_r + x_r \left(\frac{\rho_{liq}}{\rho_{gas}}\right)} \tag{5.89}$$

The average quality was assumed to be 50% for the flooded evaporator. After the equivalent Reynolds and Boiling numbers are determined, the refrigerant Nusselt number ($Nu_{r,evap}$) can be calculated as shown in Equation 5.90. The coefficient m and j are functions of the plate Chevron angle (β_{evap}) and can be determined as in Equations 5.91 and 5.92, respectively.

$$Nu_{r,evap} = (-173.52 \frac{\beta_{evap}}{60} + 257.12)(Re_{r,eq} Bo_{r,eq})^m (\frac{P_{evap}}{P_{crit}})^j \tag{5.90}$$

$$m = 0.0005 - 0.09 \frac{\beta_{evap}}{60} \tag{5.91}$$

$$j = 0.624 \frac{\beta_{evap}}{60} - 0.822 \tag{5.92}$$

The correlation shown in 5.90 was able to predict the Nusselt number with an accuracy of ±10% when compared to the experimental data used in the study. The convective heat transfer coefficient associated with the two-phase flow ($h_{r,evap}$) can then be determined based on Equation 5.93, which is analogous to Equation 5.78, but now calculated for refrigerant flow.

$$h_{r,evap} = \frac{Nu_{r,evap} k_r}{d_{evap}} \tag{5.93}$$

5.6.1.4. Plate Thermal Resistance

Along with the convective heat transfer coefficients for both coolant and refrigerant, which can be calculated by means of different correlations, as shown in sections 5.6.1.2 and 5.6.1.3, the conductive thermal resistance across evaporator plates ($R_{plate,t}$) must be determined. Equation 5.94 shows the formula for plate resistance (Holman, 2010), based upon the plate conductivity (k_{plate}) and its thickness (t_{plate}). A value of 14 $W/(K * m)$ has been used in the model for the conductivity of the 254SMO stainless steel plates (AZO Materials, 2013).

$$R_{plate,t} = \frac{t_{plate}}{k_{plate}} \tag{5.94}$$

5.6.1.5. Overall Heat Transfer Coefficient

The overall heat transfer coefficient combines the thermal resistances associated with convection within both fluid streams, as well as with conduction through the PSHE plates. Similarly to the method described in section 5.4.9, the overall heat transfer coefficient for the evaporator (U_{evap}) can be calculated as shown in Equation 5.95.

$$U_{evap} = \frac{1}{R_{plate,t} + R_{c,t} + R_{r,t}} \tag{5.95}$$

The thermal resistances associated with the coolant ($R_{c,t}$) and refrigerant ($R_{r,t}$) convection can be determined based on the convective heat transfer coefficient for single ($h_{c,evap}$) and two-phase ($h_{r,evap}$) flows, respectively. In both cases, the thermal resistance is inversely proportional to the convective heat transfer coefficient, as shown in Equations 5.96 and 5.97.

$$R_{c,t} = \frac{1}{h_{c,evap}} \tag{5.96}$$

$$R_{r,t} = \frac{1}{h_{r,evap}} \tag{5.97}$$

5.6.1.6. Correlation Comparison

As there are different correlations that could be used to model the single and two-phase heat transfers of a PSHE, it is important to understand their limitations and to select the most appropriate, considering their applicability, complexity and accuracy. For that matter, the design heat transfer coefficient for the evaporator was compared to the overall coefficients obtained from the combination of different single and two-phase correlations. The manufacturer data for the evaporator is provided in Table 5.8. Based upon the inlet (T_{in}) and outlet (T_{out}) temperatures of the working fluids, as well as on the capacity of the evaporator (Q_{evap}) and its overall heat transfer area (A_{evap}), the LMTD method was used to obtain its overall heat transfer coefficient (U_{evap}), or U value. The coolant considered for this analysis was pure water, as manufacturer data was only available for that fluid.

Table 5.8 – List of operating parameters for the plate-and-shell evaporator based on manufacturer data (Islington Council, 2019).

Capacity	Surface Area	U value	Coolant (water)			Refrigerant (NH_3/R717)		
Q_e (kW)	A_{evap} (m^2)	U_{evap} (W/m^{2}K)	T_{in} (°C)	T_{out} (°C)	$\dot{m}$ (kg/s)	T_{in} (°C)	T_{out} (°C)	$\dot{m}$ (kg/s)
779	88.92	2195	11	6	37.6	4	4	0.7

The temperatures and mass flow rates ($\dot{m}$) for both coolant and refrigerant, also shown in Table 5.8, were used for calculating the heat transfer coefficients with each of the correlations presented in this investigation. The geometric parameters shown in Table 5.7 and the correlations presented in sections 5.6.1.2 and 5.6.1.3 formed the basis for the comparison, which is shown in Table 5.9. The correlations were combined based on Equation 5.95 to yield values for the overall heat transfer coefficient of the evaporator (U_{evap}).

Table 5.9 – Comparison of overall heat transfer coefficients for the evaporator using different correlations.

Manufacturer data (Islington Council, 2019): U_{evap} = 2195 W/m^{2}K		Two-phase heat transfer correlations	
		Ayub (2003)	**Khan et al.** (2014)
Single phase heat transfer correlations	**Wanniarachchi et al.** (1995)	2104 W/m^{2}K (-4%)	1754 W/m^{2}K (-20%)
	Thonon (1995)	2199 W/m^{2}K (+0.2%)	1821 W/m^{2}K (-17%)
	Kumar (1984)	1864 W/m^{2}K (-15%)	1585 W/m^{2}K (-28%)

The values indicated in brackets in Table 5.9 represent the deviation between the design heat transfer coefficient and the values calculated for each combination of single and two-phase heat transfer correlations. For single phase heat transfer, the correlation proposed by Kumar (1984) had the highest difference compared with manufacturer data, in both combinations with the correlations from Ayub (2003) and Khan et al. (2014). When comparing the correlations from Wanniarachchi et al. (1995) and Thonon (1995), the lower deviation from the manufacturer data benchmarked was obtained using the latter. Therefore, the correlation proposed by Thonon (1995) will be used in the WHR model.

With regard to two-phase heat transfer, the results obtained by applying Ayub's correlation (2003) were closer to the design value for every combination. On average, the correlation proposed by Khan et al. (2014) underestimated the U-value by 16% when compared to Ayub's formula. Furthermore, Ayub's correlation has been developed based on a variety of industrial refrigeration systems, and was also used in a recent model of a two-stage ammonia HP for district heating (Meesenburg et al., 2020), in a similar configuration to the HP used for the WHR system. Therefore, for the purpose of this investigation, the correlation proposed by Ayub (2003) will be used to model the refrigerant heat transfer in the evaporator, whilst Thonon's correlation (1995) will be applied to the coolant stream.

5.6.1.7. Energy Balance

After the U-value is determined, the energy balance at the evaporator must be calculated. The fundamental assumption for the evaporator energy balance is that the heat recovered at the HRC (Q_{rec}), calculated as shown in Equation 5.22, is equal to the heat being absorbed by the evaporator (Q_{evap}). The evaporator is combined with a separator vessel, meaning that refrigerant will enter point 1a in Figure 5.13 as a saturated liquid. As the evaporator is flooded, it is assumed that refrigerant will always leave the heat exchanger, at point 2 in Figure 5.13, as a saturated gas. Therefore, the heat absorbed by the refrigerant stream must be calculated based upon its mass flow rate through the evaporator ($\dot{m}_{r,2} = \dot{m}_{r,1a}$), as well as the difference between its inlet ($i_{r,1a}$) and outlet ($i_{r,2}$) enthalpies, as shown in Equation 5.98. The LMTD method is also introduced to satisfy the energy balance, based upon the calculated evaporator heat transfer coefficient (U_{evap}), its surface area (A_{evap}) and the evaporating temperature (T_{evap}), as well as coolant temperatures at the inlet ($T_{c,in,evap}$) and outlet ($T_{c,out,evap}$) of the evaporator, as shown in Equations 5.99 and 5.100.

$$Q_{evap} = \dot{m}_{r,2}(i_{r,2} - i_{r,1a}) \tag{5.98}$$

$$\mathrm{Q}_{evap} = U_{evap} A_{evap} LMTD_{evap} \tag{5.99}$$

$$LMTD_{evap} = \frac{\Delta T_2 - \Delta T_1}{\ln(\frac{\Delta T_2}{\Delta T_1})} \text{ ; where: } \Delta T_2 = T_{c,in,evap} - T_{evap} \text{ and } \Delta T_1 = T_{c,out,evap} - T_{evap} \tag{5.100}$$

As the refrigerant enthalpies at the inlet and outlet of the evaporator have known qualities, they can be represented as a function of the evaporating temperature (T_{evap}). The energy balance can therefore be used to determine the evaporating temperature and its associated pressure (P_{evap}), as well as the mass flow rate of refrigerant for the evaporator ($\dot{m}_{r,2} = \dot{m}_{r,1a}$).

5.6.2. Compressors

The work input to a specific compressor (W_{comp}) can be calculated as a function of its isentropic efficiency (η_{comp}) and mass flow rate ($\dot{m}_{r,comp}$), as well as the difference in fluid enthalpy between suction ($i_{r,suc}$) and discharge lines ($i_{r,dis}$) (Çengel and Boles, 2011). The isentropic efficiency is applied to compare the actual compression to an isentropic process where the discharge enthalpy would be $i_{r,is,dis}$. The calculation used to determine compressor work based on isentropic efficiency is detailed in Equations 5.101 and 5.102.

$$W_{comp} = \eta_{comp}(i_{r,dis} - i_{r,suc}) \tag{5.101}$$

$$\eta_{comp} = \frac{i_{r,is,dis} - i_{r,suc}}{i_{r,dis} - i_{r,suc}} \tag{5.102}$$

$$W_{HP} = \frac{W_{comp,ls} + W_{comp,hs}}{\eta_{motor}} \tag{5.103}$$

Design specifications for different HP operating conditions were also provided by Islington Council (2019) and are listed in Table 5.10. These values are for water being used as the coolant. The energy losses associated with the motor must be considered when calculating the overall HP work input and the motor efficiency (η_{motor}) of 92% was applied to calculate the HP power demand (W_{HP}), adapting Equation 5.67 to Equation 5.103.

Table 5.10 – HP COPs and operating pressures for different water temperatures.

Description	Operation 1	Operation 2	Operation 3
Evaporator outlet water temperature (°C)	6	8	13
Heating COP w/out motor losses	3.95	4.09	4.44
Heating COP with motor losses	3.64	3.76	4.08
Evaporating pressure (kPa)	492.6	530.5	634.9
Intermediate pressure (kPa)		1643	
Condensing pressure (kPa)		3792	
Low-stage pressure ratio	3.34	3.10	2.59
High-stage pressure ratio		2.31	

5.6.2.1. Low-stage Compressor

Following evaporation, the refrigerant then flows into the low-stage compressor, which must be able to respond to the varying evaporating pressures that result from the fluctuating coolant temperatures approaching the evaporator. As it can be noted from Table 5.10, the low-stage compressor is controlled to maintain the separator saturation pressure at 1643 kPa, which corresponds to a saturation temperature of 42°C. Therefore, the low-stage compressor requires less work when the HP is operating with higher coolant temperatures and thus higher evaporating temperatures. The model has been calibrated according to the operating conditions in Table 5.10, with a correlation being developed to determine the isentropic efficiency of the low-stage compressor ($\eta_{comp,ls}$) from the low-stage pressure ratio (P_{ls}^*) between the evaporating (P_{evap}) and intermediate pressures (P_{int}), as shown in Equation 5.104.

$$\eta_{comp,ls} = -0.0383{P_{ls}^*}^2 + 0.2287P_{ls}^* + 0.5448;\ \text{where: } P_{ls}^* = \frac{P_{int}}{P_{evap}} \tag{5.104}$$

The difference in refrigerant enthalpy is calculated between points 3 ($i_{r,3}$) and 4 ($i_{r,4}$) in Figure 5.13. The mass flow rate is the sum of mass flows coming from the evaporator ($\dot{m}_{r,2}$) and directly from the low-stage separator vessel ($\dot{m}_{r,1b}$). The compressor work input for the low stage ($W_{comp,ls}$) can then be determined using Equations 5.101 and 5.102. A superheat of 1 K is assumed for the suction pressure to help ensure that only vapour enters the compressor.

5.6.2.2. High-stage Compressor

The high-stage compressor is controlled in relation to the supply temperature required for the heat network. Therefore, if the same delivery temperature is assumed throughout the year, it should always operate under the same set of conditions, as shown in Table 5.10. Therefore, the isentropic efficiency for the high-stage compressor was simulated assuming a fixed value of 88%. This was based upon the refrigerant temperature entering the condenser, as shown in Table 5.6, on the pressure drops of the high stage, as indicated in Table 5.11, as well as on a condensing temperature of 76°C. These conditions reflect a full-load operation and were also validated for a part-load condition. The work input to the high-stage compressor ($W_{comp,hs}$) can also be obtained from Equations 5.101 and 5.102.

5.6.3. Low-stage Desuperheater

The low-stage desuperheater preheats the water coming from the heat network before most of the heat is delivered by the high-stage PSHEs. The heat transfer at the low-stage desuperheater ($Q_{ds,ls}$) is represented by points 5 and 6 in Figure 5.13, being calculated based on the energy balance between refrigerant and coolant streams, as shown in Equations 5.105, 5.106 and 5.107. For Equation 5.107, a design UA value of 4.796 kW/K and the LMTD across the desuperheater are considered, as shown in Equation 5.108. The refrigerant pressure loss through the low-stage desuperheater was assumed as 0.7 kPa, as shown in Table 5.6.

$$Q_{ds,ls} = \dot{m}_{r,5}(i_{r,5} - i_{r,6}) \tag{5.105}$$

$$Q_{ds,ls} = \dot{m}_w C_{p,w}(T_{w,6} - T_{w,5}) \tag{5.106}$$

$$\mathrm{Q}_{ds,ls} = UA_{ds,ls} LMTD_{ds,ls} \tag{5.107}$$

$$LMTD_{ds,ls} = \frac{\Delta T_2 - \Delta T_1}{\ln(\frac{\Delta T_2}{\Delta T_1})}; \text{ where: } \Delta T_2 = T_{r,5} - T_{w,6} \text{ and } \Delta T_1 = T_{r,6} - T_{w,5} \tag{5.108}$$

5.6.4. Separator

The HP modelled as part of the WHR system has two separators. The main separator tank connects the low and high stages, whilst a small separator vessel is connected to the flooded evaporator, as shown in Figure 5.13. The modelling of both separators will be based on mass and energy balances, as shown in Equations 5.109 and 5.110, respectively. The main separator tank was modelled as an individual component and computes balances between points 6, 7, 8 and 13, whilst the smaller vessel was modelled along with the low-stage thermal expansion valve (TEV) and calculates mass and energy flows between points 1, 1a and 1b. The separator tanks and vessel were assumed to have negligible pressure losses.

$$\sum \dot{m}_{in} = \sum \dot{m}_{out} \quad (5.109)$$

$$\sum(\dot{m}_{in} i_{in}) = \sum(\dot{m}_{out} i_{out}) \quad (5.110)$$

5.6.5. Condenser

The high-stage PSHEs are modelled as a single condenser for simplicity, as they are assumed to operate at a constant pressure and deliver the same supply temperature for every time step throughout the year. The model assumes that refrigerant leaves the high-stage compressor and enters the combined condenser with 37 K of superheat, condensing at 76°C and leaving the heat exchanger subcooled by approximately 17 K. Similarly as for the evaporator and the low-stage desuperheater, the energy balance at the condenser is calculated based upon heat transfer equations for both fluids and the LMTD method. Equation 5.111 can be used to calculate the heat transfer on the refrigerant side, considering points 11 and 12 in Figure 5.13, whilst Equation 5.112 can be used to calculate the sensible heat transfer across the water stream. The energy balance determines the mass flow rate through the condenser, which is assumed constant as refrigerant flows through the high-stage compressors and TEV.

$$\mathrm{Q}_{cond} = \dot{m}_{r,12}(i_{r,11} - i_{r,12}) \quad (5.111)$$

$$\mathrm{Q}_{cond} = \dot{m}_{w} C_{p,w}(T_{w,12} - T_{w,11}) \quad (5.112)$$

Lastly, the LMTD method must be introduced to satisfy the energy balance, as shown in Equations 5.113 and 5.114. Since the condenser is modelled as operating at fixed conditions, it is reasonable to assume its heat transfer coefficient (U_{cond}) will remain constant. Although the three high-stage PSHEs have different surface areas and heat transfer coefficients, a combined condenser model simulation was carried out using an overall UA value (UA_{cond}). The UA value combines the total heat transfer coefficient (U_{cond}) and the total heat transfer area (A_{cond}). Its value for the combined condenser was 76.55 kW/K, which was determined based upon the design water and refrigerant temperatures shown in Table 5.6. As previously mentioned, the 2.1 kPa pressure drop across the condenser was assumed to be constant and equal to the sum of pressure drops for each of the high-stage PSHEs, as shown in Table 5.6.

$$\mathrm{Q}_{cond} = UA_{cond} LMTD_{cond} \quad (5.113)$$

$$LMTD_{cond} = \frac{\Delta T_2 - \Delta T_1}{\ln(\frac{\Delta T_2}{\Delta T_1})}; \text{ where: } \Delta T_2 = T_{r,11} - T_{w,11} \text{ and } \Delta T_1 = T_{r,12} - T_{w,12} \quad (5.114)$$

5.6.6. Thermal Expansion Valves

Thermal expansion valves, which are also known as throttle valves, are devices used to reduce the pressure of a given refrigerant flow, causing a considerable drop in temperature.

According to Çengel and Boles (2011), TEVs can be modelled assuming a conservation of enthalpy and by calculating the fluid conditions for inlet and outlet pressures.

5.6.6.1. Low-stage Expansion Valve

The low-stage expansion valve operates between the intermediate and low-stage pressures, and will be modelled in conjunction with the separator vessel that is connected to the evaporator. In this case, saturated liquid refrigerant leaves the main separator tank at point 7 in Figure 5.13 ($x_{r,7} = 0$). The isenthalpic expansion then takes place from point 7 to point 1, as shown in Equation 5.115. EES built-in functions are then used to determine the quality of the vapour that is leaving the low-stage TEV ($x_{r,1}$). This allows the mass and energy balances to be determined for the separator, as shown in Equations 5.116 to 5.118. The vapour refrigerant goes to point 1b, whilst only liquid goes to point 1a towards the evaporator.

$$i_{r,7} = i_{r,1} \tag{5.115}$$

$$\dot{m}_{r,1b} = x_{r,1}\dot{m}_{r,1} \tag{5.116}$$

$$\dot{m}_{r,1a} = (1 - x_{r,1})\dot{m}_{r,1} \tag{5.117}$$

$$\dot{m}_{r,1}i_{r,1} = \dot{m}_{r,1a}i_{r,1a} + \dot{m}_{r,1b}i_{r,1b} \tag{5.118}$$

5.6.6.2. High-stage Expansion Valve

The high-stage TEV operates between the high and intermediate pressures, linking the discharge line to the separator tank. In this case, the energy and mass balances at the separator were carried out separately as it involved several in and out flows. Therefore, simple mass balance and enthalpy conservation equations were used between points 12 and 13 (see Figure 5.13) for the high-stage TEV, as shown in Equations 5.119 and 5.120, respectively.

$$\dot{m}_{r,12} = \dot{m}_{r,13} \tag{5.119}$$

$$i_{r,12} = i_{r,13} \tag{5.120}$$

5.6.7. Line Pressure Drops

For the purpose of simplification, the pressure drops across the suction and discharge lines connecting the components of the HP were assumed as constant. These values were based upon design specifications (Islington Council, 2019) and used to model the appropriate pressure lifts and associated work inputs for the compressors. A list of pressure drop (ΔP) values assumed for each line for both low and high stages is provided in Table 5.11.

Table 5.11 – List of pressure drops across the pipeline of the HP for both low and high stages.

Stage	Line	Points in Figure 5.13	ΔP (kPa)
Low	Suction	2 to 3	1.3
	Discharge	4 to 5	25.3
High	Suction	8 to 9	5.9
	Discharge	10 to 11	16.05

5.7. Modelling the Part-load Operation of the Heat Pump

The WHR model has been calibrated based on full-load operation data, as shown in Table 5.10. However, in reality, the loading/unloading of pistons and the variable speed drive used to achieve part-load conditions may affect the COP of the HP. The HP manufacturer provided part-load design performance parameters for the same water temperatures as in Table 5.10, and these are shown in Table 5.12 (GEA Refrigeration, 2021).

Table 5.12 – HP design performance parameters for different water temperatures at part-load condition.

Parameter	Operation 1	Operation 2	Operation 3
Evaporator inlet water temperature (°C)	11	13	18
Evaporator outlet water temperature (°C)	6	8	13
Cooling duty (kW)	391	391	393
Heating duty (kW)	518	517	510
Hot water supply temperature (°C)	75	75	75
Hot water return temperature (°C)	55	55	55
Electrical demand (kW)	138	138	128
Heating COP	3.75	3.75	3.98

The conditions shown in Table 5.12 were replicated with the WHR model in order to analyse how outputs such as heating duty and COP would vary for a part-load condition and how the modelled figures compare to the design values established by GEA Refrigeration. This was achieved by adjusting the HP model to the cooling duty and inlet temperatures from Table 5.12. The mass flow rates for both hot and cold sides were also reduced to 50% of its design value to represent the part-load condition whilst still maintaining the required supply temperature for the DHN. The results from the simulations are shown in Table 5.13, together with the deviation between design and modelled values.

Table 5.13 – WHR model inputs and outputs for the part-load conditions from Table 5.12.

	Parameter	Operation 1	Operation 2	Operation 3
Inputs	**Evaporator inlet water temperature (°C)**	11	13	18
	Cold side mass flow rate (kg/s)	18.8	18.8	18.8
	Hot side mass flow rate (kg/s)	6.2	6.2	6.2
	Cooling duty (kW)	391	391	393
	Hot water supply temperature (°C)	75	75	75
	Hot water return temperature (°C)	55	55	55
Outputs	**Evaporator outlet water temperature (°C)**	6.04 (+0.73%)	8.04 (+0.50%)	13.01 (+0.08%)
	Heating duty (kW)	519.9 (+0.37%)	514.7 (-0.44%)	505.9 (-0.80%)
	Electrical demand (kW)	140.2 (+1.59%)	134.4 (-2.61%)	122.7 (-4.14%)
	Heating COP	3.71 (-1.07%)	3.83 (+2.08%)	4.12 (+3.62%)

As it can be observed, all the parameters calculated using the WHR model, including the COP, are within ±5% of the design values provided by the manufacturer. Although the low-stage compressor model is based on a correlation between pressure ratio and isentropic efficiency for full-load conditions, the results shown in Table 5.13 demonstrate how the WHR model is able to represent part-load COPs with only slight deviations.

5.8. Conclusion

This chapter described the scientific principles behind the development of a mathematical model of the WHR system. The model was developed using the commercial software tool Engineering Equation Solver (EES), which is able to iteratively solve thermodynamic balance equations across the system, and is used to determine its energy consumption, as well as heating and cooling outputs. The model is built around design specifications for the Bunhill WHR System, utilising heat transfer equations and temperature and humidity data to investigate performance for different heat source and operating conditions. The EES code developed for the WHR model is provided in Appendix B, considering water as the coolant, whilst Appendix C provides detailed model results based on average monthly conditions for both Supply and Extract modes in a full-load operation.

The main novelties behind the approach described in this chapter are around a detailed model of HRC and its combination with a model of a two-stage ammonia HP. The HRC were modelled to account for the phenomenon of condensation and the different coil surface conditions that may occur depending on temperature and RH inputs for the heat source. This enables calculating sensible and latent heat loads associated with the heat recovery process, which are essential for simulating coil performance and its cooling effect accurately. As for the HP model, it combines both single and two-phase heat transfer correlations for the evaporator, allowing the energy balance between HP and coils to be calculated considering the fluctuating coolant temperatures, which are a function of air conditions at the heat source (either ambient or tunnel air). Additionally, design specifications provided by the HP manufacturer have been applied to model the HP compressors and remaining plate-and-shell heat exchangers.

The WHR model is used throughout this investigation as the basis for analysing the potential benefits and challenges associated with heat recovery from underground railways (URs). The validation approach is described in Chapter 6, whilst Chapter 7 explains how the WHR model has been coupled with a model of the LU network in order to assess the impacts of WHR in terms of station temperatures. Chapter 8 provides an overview of the results from both WHR and UR models, and Chapters 9 and 10 explore the economic and environmental benefits that could be achieved by recovering waste heat from railway tunnels, utilising the results from the WHR model as inputs for further simulations.

6. Data Collection and Model Validation

6.1. Introduction

Since this project aims to analyse the efficiency and potential of recovering waste heat from underground railways (URs), collecting operational data from the Bunhill Waste Heat Recovery (WHR) system is an important step of the investigation, as it enables assessing the performance of the WHR system as well as validating the model developed as part of this project. At first, this chapter provides a review of the instrumentation used for collecting experimental data from the WHR plant. The experimental data collected was utilised to validate the heat pump (HP) model, and the validation approach is also described in this chapter, along with the method adopted for validating the heat recovery coils (HRC) model, which is based on data obtained from the coil manufacturer. Due to project delays and the impacts of the COVID-19 pandemic, the WHR system is still under commissioning at the time of writing, and the challenges encountered to date are also discussed in this chapter.

6.2. Instrumentation and Data Collection Plan

6.2.1. Data Collection Objectives

The purpose of data collection was to enable the operational performance assessment for the Bunhill WHR system and to serve as a means of validation for the mathematical model described in Chapter 5. The collected data should allow the evaluation of the WHR system's heating efficiency and the quantification of how much cooling the system delivers when operating in Supply Mode. The following objectives summarise the purpose of data collection for the Heat FUEL Project.

- To provide a means of validation for the WHR model;
- To analyse the performance of the WHR system in terms of its heating output and energy consumption;
- To quantify how much cooling the system delivers to the LU tunnels when operating in Supply Mode;
- To identify any anomalies and issues associated with the operation of the WHR plant.

6.2.2. Data Collection Plan

Figure 6.1 shows a schematic of the WHR system, highlighting the key points (1, 2 and 3) where a heat transfer process occurs, namely the HRC (1), the evaporator (2) and the high-stage heat exchanger circuit (3), as well as all the energy inputs to the system. The energy balances at these points were described in Chapter 5 and enable the identification of the key parameters that should be monitored to calculate the efficiency of the WHR system.

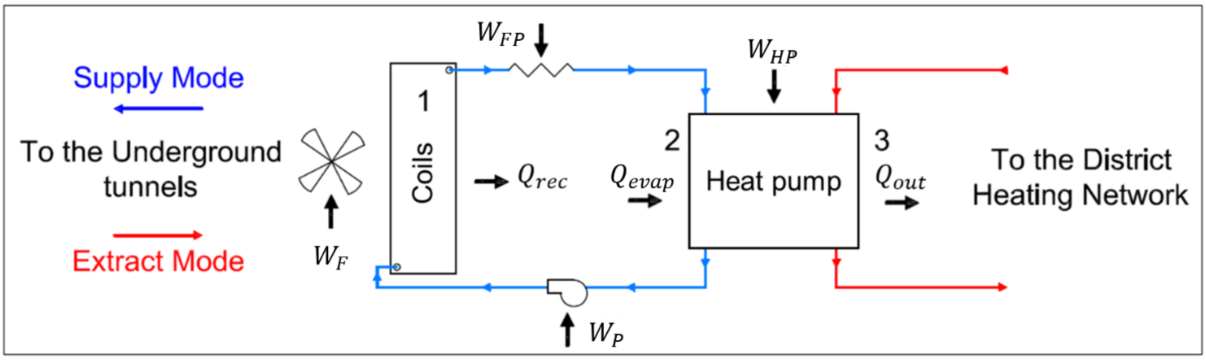

Figure 6.1 – Schematic highlighting energy inputs and outputs associated with the WHR system.

Table 6.1 – List of parameters to be monitored to analyse the performance of the WHR System.

Location	Medium	Parameter	Unit	Instrument
Heat recovery heat exchanger	Air	Fan power and energy consumption	kW, kWh	EM-1
		Inlet and outlet temperatures	°C	TA-1, TA-2
		Differential pressure	Pa	DP-F
	Water	Inlet and outlet temperatures	°C	TW-1, TW-2
		Differential pressure	kPa or bar	DP-C
Coolant loop	Water	Flow rate	kg/s or m^3/s	FR-1
		Frost protection power and consumption	kW, kWh	EM-2
		Pumping power and consumption	kW, kWh	EM-3
Evaporator/ Separator	Ammonia	Evaporating temperature	°C	TE-1
	Water	Inlet and outlet temperatures	°C	TW-3, TW-4
		Differential pressure	kPa or bar	DP-E
Compressor 1 (Low stage)	Ammonia	Power demand and energy consumption	kW, kWh	EM-4
		Suction and discharge pressures	kPa or bar	PS-1, PD-1
		Suction and discharge temperatures	°C	TS-1, TD-1
Low stage desuperheater	Water	Inlet and outlet temperatures	°C	TW-5, TW-6
		Flow rate	kg/s or m^3/s	FR-2
Separator	Ammonia	Intermediate pressure	kPa or bar	PI-1
		Inlet and outlet temperatures	°C	TI-1, TI-2
Subcooler	Water	Outlet temperature	°C	TW-7
Condenser	Ammonia	Condensing temperature	°C	TC-1
	Water	Outlet temperature	°C	TW-8
High stage desuperheater	Ammonia	Inlet pressure	kPa or bar	PH-1
	Water	Outlet temperature	°C	TW-9
Compressor 2 (High stage)	Ammonia	Power demand and energy consumption	kW, kWh	EM-5
		Suction and discharge pressures	kPa or bar	PS-2, PD-2
		Suction and discharge temperatures	°C	TS-2, TD-2
Compressor 3 (High stage)	Ammonia	Power demand and energy consumption	kW, kWh	EM-6
		Suction and discharge pressures	kPa or bar	PS-3, PD-3
		Suction and discharge temperatures	°C	TS-3, TD-3

Different operating parameters must be monitored at each of the highlighted points. These include flow rates, temperatures and pressures for air, water, and refrigerant streams as well as the electricity consumption for different devices within the system, i.e. the fan (W_F), pumps (W_P), HP (W_{HP}) and the electric immersion heater used for frost protection (W_{FP}). As part of the control strategy for the energy centre, the WHR system was fitted with several instruments that allow monitoring system performance. Table 6.1 summarises all the key parameters to be monitored, along with the location where the meters are installed and through which medium the parameters will be measured, as well as their related units of measurement. The locations for each meter are also illustrated in Figure 6.2 for the entire WHR system except the HP, whose instruments are shown in detail in Figure 6.3.

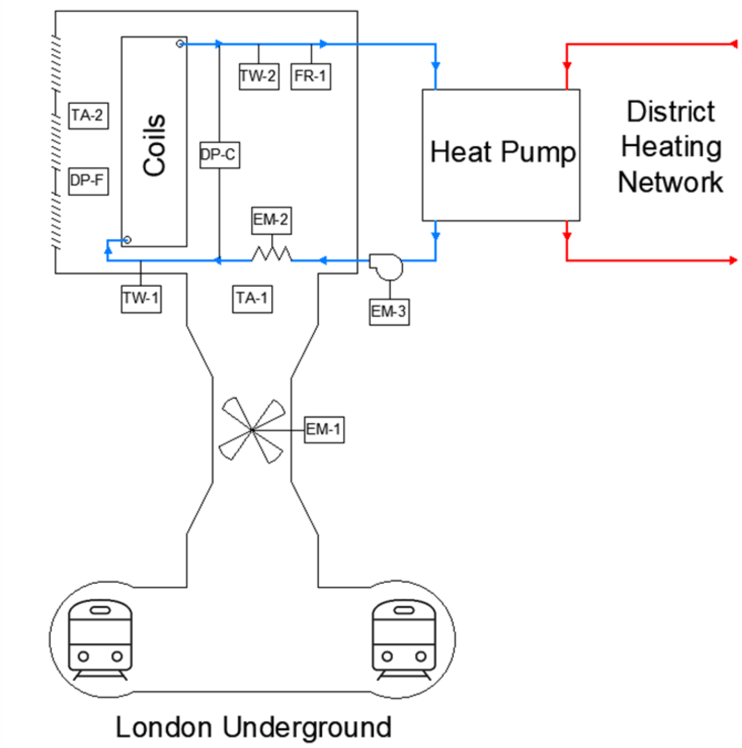

Figure 6.2 – Schematic illustrating instrument locations for monitoring the performance of the WHR system.

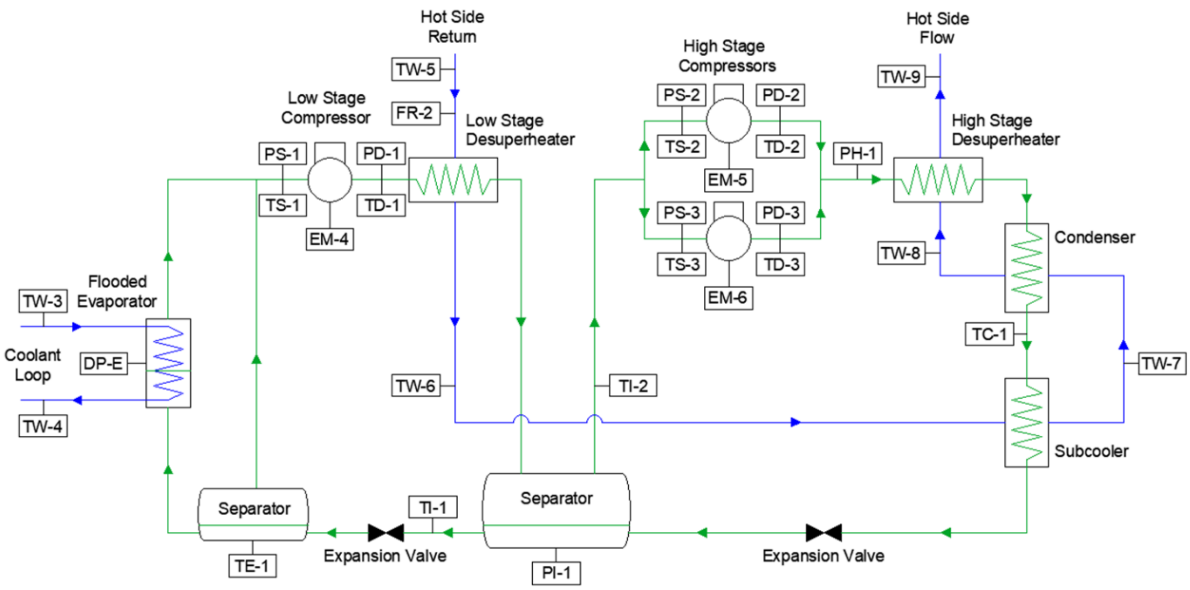

Figure 6.3 – Schematic illustrating instrument locations for monitoring the performance of the HP.

6.2.3. Instruments and Uncertainties

The instrumentation for the Bunhill WHR system enables the data collection objectives for this investigation to be addressed. In terms of monitoring system performance ($COSP_h$), as defined by Equation 5.1, all HP compressors (EM-4, EM-5 and EM-6) as well the vent shaft fan (EM-

1) and coolant pumps (EM-3) are fitted with electricity meters, whilst the heat output can be measured based on water temperatures (TW-5 to TW-9) and flow rate (FR-2) across the high-stage heat exchangers. The cooling benefit can be determined by considering the temperature probes installed at the HRC (TW-1 and TW-2) and evaporator (TW-3 and TW-4) as well as the flow rate meter installed at the coolant loop (FR-1), and calculated using Equation 5.4. This can be compared to the temperature reduction measured through sensors TA-1 and TA-2, yielding the sensible cooling effect on the air stream (see Equation 5.56). All temperature sensors are Sontay platinum resistance thermometers with an accuracy of ±0.5°C. Water flow rates are measured via Endress & Hauser heat meters, with class 2 accuracy as per EN1434-1 standards, which is associated with a maximum permissible error of ±5% (BEIS, 2016). The electricity meters are Socomec E53 Series, with an accuracy of ±0.5%.

The flow rate of air across the coils is not monitored by the plant operators, but can be provided by Transport for London (TfL). In terms of model validation, the main limitation of the monitoring system is the lack of relative humidity (RH) instruments, which could be used to measure the latent cooling effect. However, the amount of latent cooling can still be calculated based on the total heat recovered and the sensible cooling on the air side. Furthermore, measuring the mass flow rate of refrigerant across the HP would be beneficial, as it could be used to calculate energy balances for the different heat exchangers that comprise the HP, serving as a means of cross-checking the measurements taken from the water streams.

6.3. Model Validation

6.3.1. Introduction

The data and methods used for validation of the WHR model are described in this section. The validation approach has been based on experimental data for the HP model and on manufacturer's data for the HRC model, as operational data for the HRC were initially not available from the monitoring system. The validation procedure was carried out for both the HP and HRC model components, as these represent the main parts of the WHR model, which were simulated to calculate thermodynamic balances based on heat transfer principles and correlations.

6.3.2. Heat Recovery Coils

The HRC model has been validated with data from the coil manufacturer for the Bunhill WHR system, SPC Coils. The company offers an online coil selection software (SPC Coils, 2020) that has been used to validate the model under different conditions, namely fully dry, partially wet and fully wet. As mentioned in section 5.4.1, the Bunhill 2 coils consist of 6 modules divided into two banks. Since the design specifications of a single module only were provided by Islington Council (2019), the HRC model was validated based on temperatures predicted by the coil selection software for a single module, with 6 rows of 25 tubes high, and the same set of inputs. The inputs were the module capacity, the coolant mass flow rate, the air volumetric flow rate, the air inlet temperature, and RH. The coolant inlet temperature predicted by the HRC model had to be used as an input to the coil selection software, since it does not calculate an energy balance and solely provides outlet conditions based on fixed inlet parameters. The coolant assumed during the validation process was water. Table 6.2 summarises the design specs used as inputs for the analysis.

Table 6.2 – Design specs used as inputs for the validation of the HRC model.

Parameter	Unit	Value
Coil module duty	kW	70.94
Coolant used	N/A	Water
Coolant mass flow rate	kg/s	5.647
Air volumetric flow rate	m^3/s	11.08
Finned height	m	0.956
Finned length	m	4.75
Tubes high	N/A	25
Number of rows	N/A	6

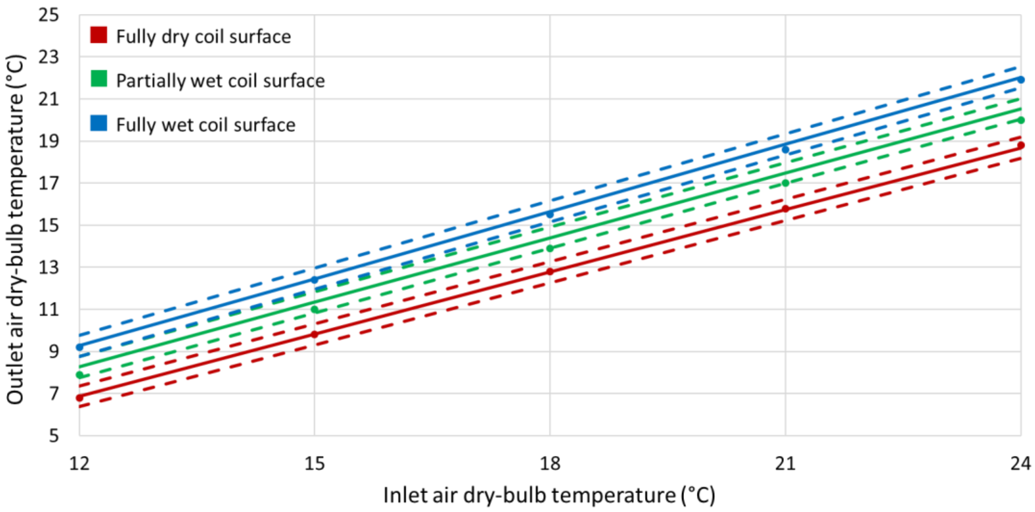

Figure 6.4 – Outlet air dry-bulb temperatures predicted by the HRC model and according to manufacturer data for different air inlet dry-bulb temperatures.

Figures 6.4, 6.5 and 6.6 provide an overview of the validation results based upon outlet air dry-bulb and wet-bulb temperatures, as well as outlet coolant temperatures, respectively. The different colours represent different surface conditions, as described in Section 5.4.3. Fully dry conditions were simulated with a RH of 40%, whilst partially and fully wet were simulated with RHs of 70% and 90%, respectively. In all figures, the solid lines represent the HRC model results, whilst the dashed lines represent upper and lower limits of 0.5°C. These limits are used to highlight how the outputs calculated by the coil selection software, represented by the rounded markers, are within a range of ±0.5°C of the HRC model results, which is equal to the accuracy of the water and air temperature measuring devices installed at the WHR plant. This demonstrates that the WHR model is able to predict the performance of the HRC within the level of uncertainty of a typical temperature sensor.

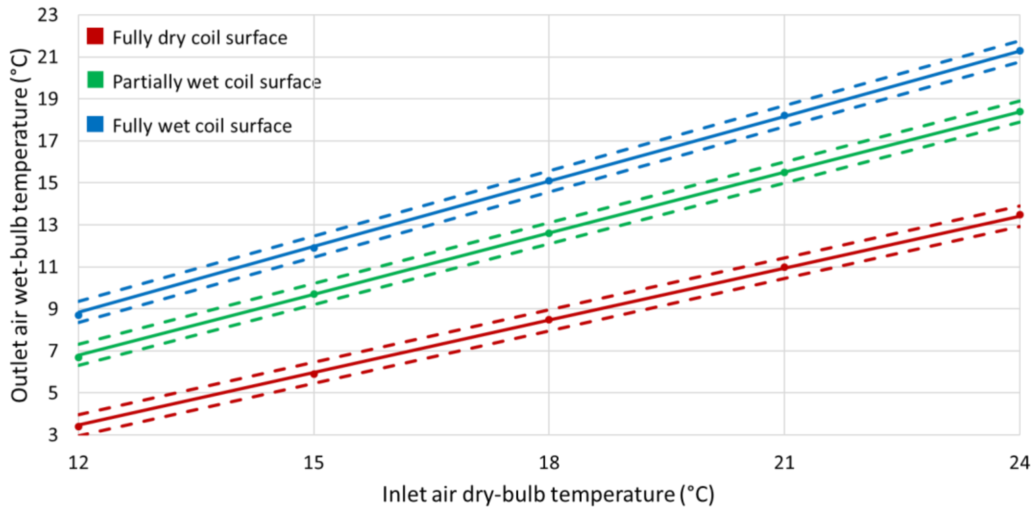

Figure 6.5 – Outlet air wet-bulb temperatures predicted by the HRC model and according to manufacturer data for different air inlet dry-bulb temperatures.

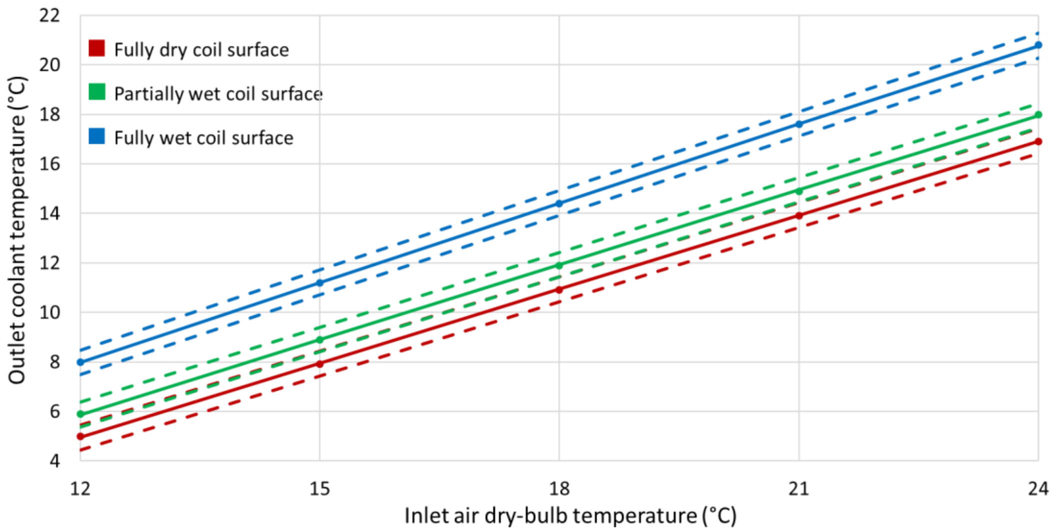

Figure 6.6 – Outlet coolant temperatures predicted by the HRC model and according to manufacturer data for different air inlet dry-bulb temperatures.

6.3.3. Heat Pump

The HP model was validated utilising experimental data from Bunhill 2. The data collected refers to a part-load test carried out 30 November 2021, which involved monitoring the heat delivered (Q_{out}) and absorbed (Q_{evap}) by the HP, as well as its heating coefficient of performance (COP), for different flow rates and temperatures on both hot and cold sides. In this case, the inputs for the test were measured at the inlets of the evaporator and the high-stage desuperheater, which represents the first heat exchanger of the hot-side circuit. The flow rate and temperature inputs were then used to simulate the testing conditions using the HP model, with an additional input for the outlet temperature on the hot side, as the heat delivered by the HP is also an input for the WHR model. The monitoring system records operational data on a second-by-second basis, with some parameters being measured in subsecond intervals, meaning that measurements are not necessarily simultaneous. For validation purposes, the steady-state operation of the HP over a 10-minute period was analysed, when 15 simultaneous measurements of all parameters of interest where taken, and these are summarised in Figure 6.7.

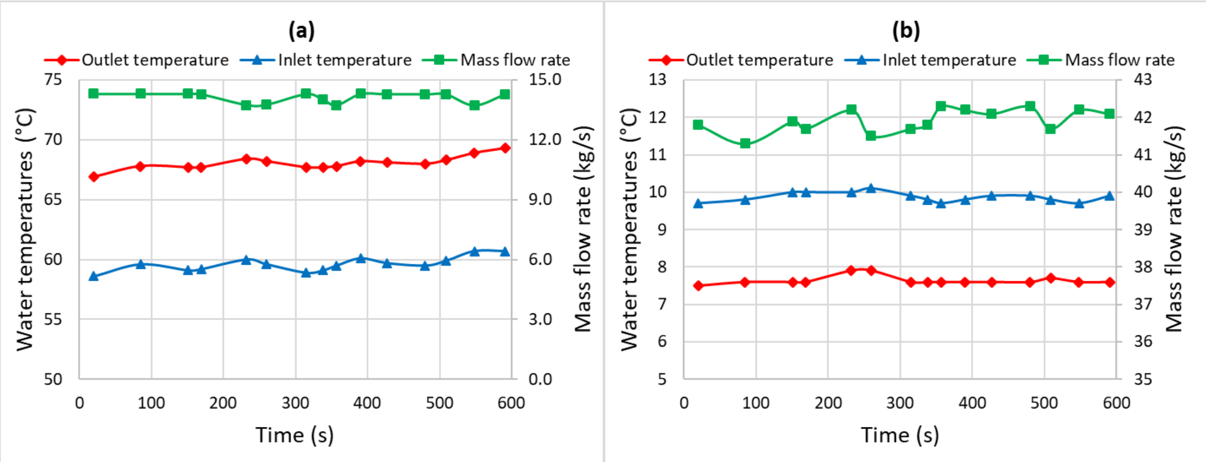

Figure 6.7 – Flow rate and temperature measurements from the Bunhill HP for both hot (a) and cold (b) sides.

The validation results are shown in Figures 6.8, 6.9 and 6.10. The uncertainties of the instruments utilised are also considered, providing maximum and minimum boundaries for the readings obtained from the SCADA system. As it can be observed, the model results are within the uncertainty margins for all the parameters analysed. The average deviation between measured and modelled COP was 5.9%, with a maximum of 12.5% being observed for t=480s in Figure 6.8, showing close agreement between the model predicted and measured data.

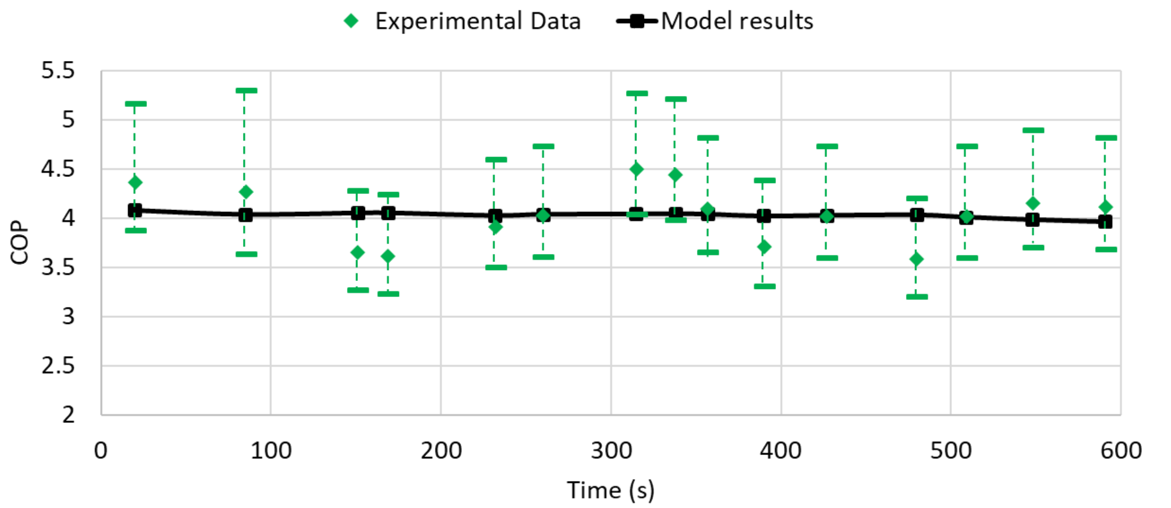

Figure 6.8 – Experimental data and WHR model results for HP COP.

The outlet water temperatures for the HP evaporator were also measured and compared to model results. As shown in Figure 6.9, the modelled values agree well with the data collected from the plant. In this case, an uncertainty in the measured values of ±0.5°C was assumed, based on instrument accuracy. The HP cooling duty, indicated by Figure 6.10, was calculated from the flow rate and temperature measurements, which leads to a higher uncertainty. Due to the low water temperature differences observed at the evaporator, the accuracy of the thermometers leads to a significant degree of uncertainty for the calculated cooling duty, of the order of ±50%. However, the model was also able to replicate the experimental data accurately, with average and maximum deviations of 2.7% and 6.5%, respectively.

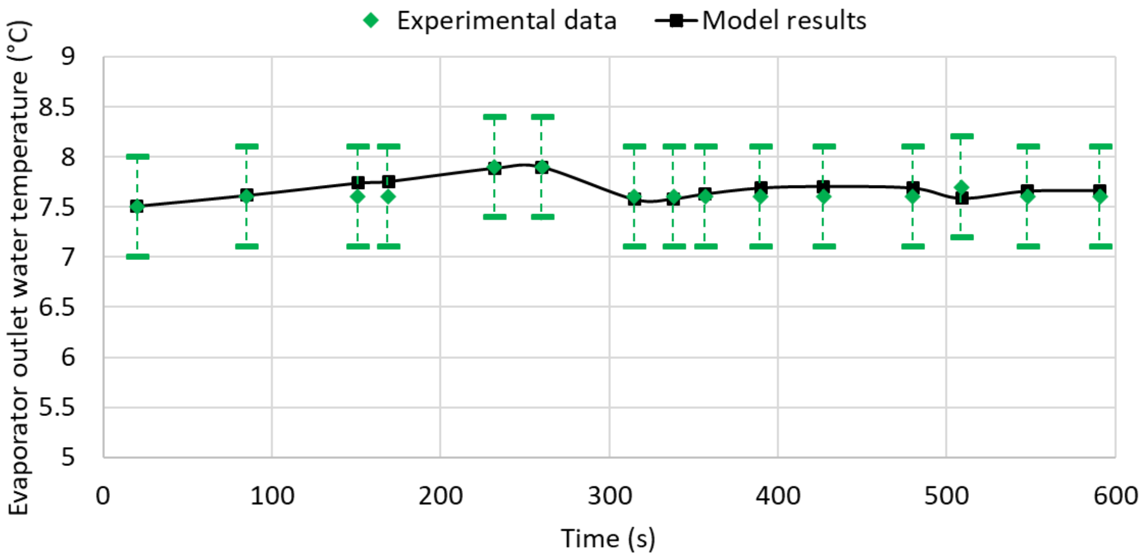

Figure 6.9 – Experimental data and WHR model results for water temperatures at evaporator outlet.

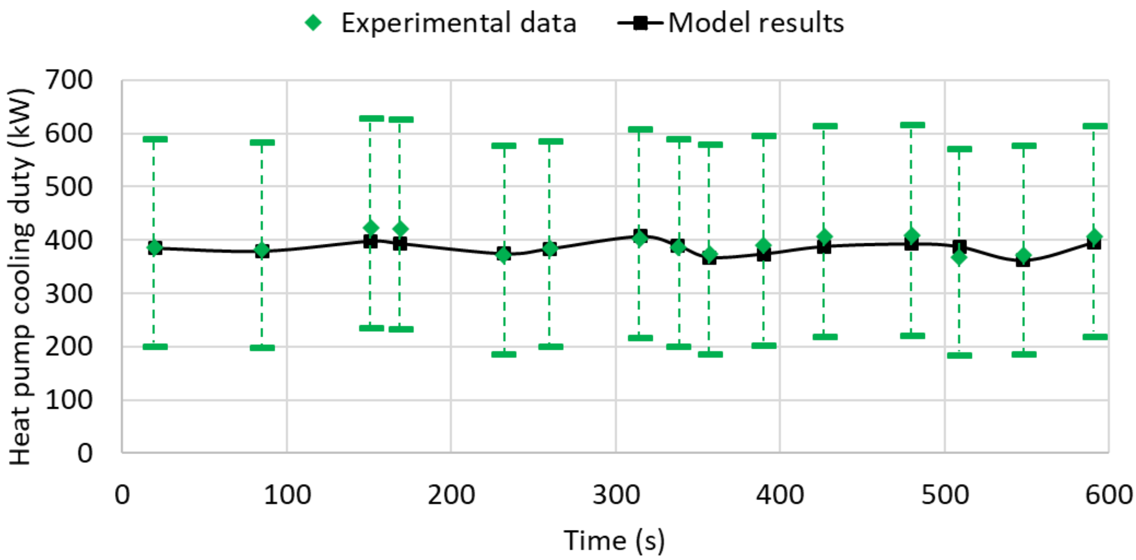

Figure 6.10 – Experimental data and WHR model results for HP cooling duty.

6.4. Data Collection Challenges

6.4.1. Challenge Description

The commissioning of the Bunhill WHR System was delayed due to operational issues with the HP, which failed to run continuously during tests carried out from July to August 2021. This is highlighted in Figure 6.11, which illustrates the fluctuation of heat output from the HP in that period. The two-stage HP was designed to accommodate the temperature variation from the City Road vent shaft (heat source) and deliver a water flow temperature of 75°C. Up to this date, the WHR system has only been commissioned to operate in Extract Mode, leading to higher heat source temperatures than originally anticipated being recorded during testing periods. These conditions may go beyond the operating limits of the HP, which resulted in triggering of the control system to bring the operation of the heat pump to a halt.

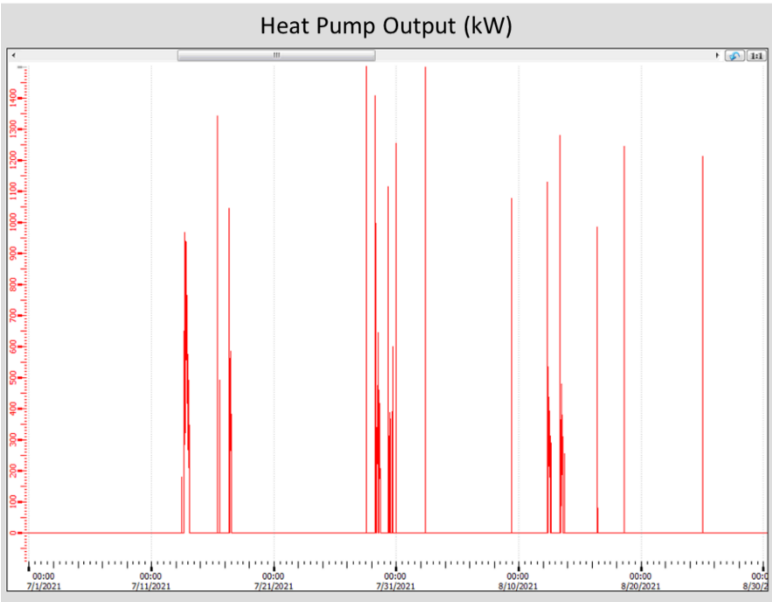

Figure 6.11 – Recorded HP output for tests run from July to August 2021.

The operating limits of the HP can be analysed by replicating typical operating conditions with the WHR model and comparing those to the envelope of the low-stage compressor, which works with varying suction pressures due to the fluctuating evaporating temperature. These typical conditions are based upon the design specifications listed in Table 5.10 and an additional scenario for a particularly high coolant temperature (condition D). Each condition was replicated with the WHR model, and the results are provided in Table 6.3. Based on the energy balance generated by the model, it is possible to calculate the HP's evaporating temperature for each of the operating conditions described in Table 6.3. The WHR model can also be used to indicate what vent shaft air temperatures would lead to each condition, and this is also highlighted in Table 6.3, together with the calculated evaporating temperatures and heating COP for each scenario. The calculations assumed a RH of 50% and a flow rate of 70 m³/s for vent shaft air, whilst cold and hot sides of the HP were modelled with constant flow rates of 37.6 and 12.4 kg/s, respectively. As seen, the evaporating temperatures would vary significantly depending on coolant temperatures, which in turn are a function of the air temperatures from the vent shaft. High evaporating temperatures and associated pressures might interfere with the normal operation of the HP – particularly of the low-stage compressor, which must operate within the limits set by its envelope, as shown in Figure 6.12.

Table 6.3 – Modelled vent shaft air and evaporating temperatures for different operating conditions.

Parameter	Condition A	Condition B	Condition C	Condition D
Coil inlet water temperature (°C)	6	8	13	19
Modelled Heating COP	3.63	3.75	4.05	4.40
Vent Shaft Air Temperature (°C)	18.1	20.3	25.7	32.1
Evaporating temperature (°C)	3.7	5.8	10.9	17.1

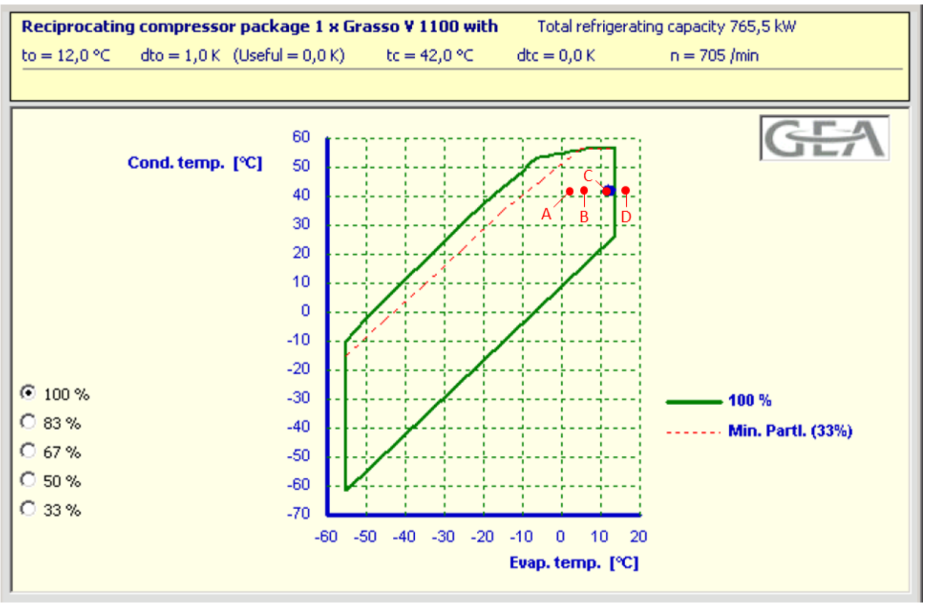

Figure 6.12 – Low-stage compressor envelope, highlighting its limits of operation (GEA Refrigeration, 2021).

The operating conditions from Table 6.3 are also highlighted in Figure 6.12 and assume that the low-stage compressor would deliver a constant discharge pressure equal to its set point of 42°C (16.43 bar). As demonstrated, the compressor would operate close to its upper limit in terms of the evaporating temperature. For condition D, when the vent shaft air temperatures are around 32°C, the required evaporating temperature to satisfy the energy balance would be outside the operating limits of the low-stage compressor. According to the manufacturer, the HP is controlled to ensure that evaporating temperatures do not rise above a maximum set point of 10°C. As seen in Table 6.3, evaporating temperatures may go beyond those limits for particularly high heat source temperatures (>25°C), and the control limits might be impeding the HP from operating under those circumstances. The following sections discuss some of the different factors that might contribute to high evaporating temperatures and lead to undesired conditions for the system.

6.4.2. Contributing Factors

6.4.2.1. Small Load on the Network

One issue that can affect the HP operation is a lower load on the network than designed. This would lead to a part-load operation of the HP, which would affect its COP and evaporating temperature as less heat would need to be removed from the cold water stream. The manufacturer has also provided indicative performance data for part-load operation (GEA Refrigeration, 2021), and these values were replicated using the WHR model to analyse their impact in terms of changes in evaporating temperature and COP. This comparison is presented in Table 6.3, considering only the conditions that are within the compressor envelope (A, B and C), as illustrated in Figure 6.12. In this case, the chilled water temperatures and the cooling duty were used as inputs for the simulations, and the hot side was modelled with a constant flow rate of 6.2 kg/s.

By comparing Tables 6.2 and 6.3, it is possible to see that the evaporating temperatures simulated for part-load conditions would be higher than those for full-load operation, considering the same chilled water temperatures. Therefore, part-load operation might contribute to higher evaporating temperatures, which could trigger HP alarms more frequently and hinder a continuous operation of the system, which has been observed to happen during the commissioning trials.

Table 6.4 – Modelled and design values for HP part-load performance and evaporating temperatures.

Parameter		Condition A	Condition B	Condition C
Design Specifications	Evaporator inlet water temperature (°C)	11	13	18
	Cooling Duty (kW)	391	391	393
	Heating Duty (kW)	518	517	510
	Indicative Heating COP	3.75	3.75	3.98
WHR Model Results	Modelled Heating Duty (kW)	520	515	506
	Modelled Heating COP	3.71	3.83	4.12
	Evaporating temperature (°C)	4.6	6.6	11.7

6.4.2.2. Extract Mode in Summer

The original design of the WHR system considered that the fan would operate in Supply Mode for 6 months, from May to October. However, the initial testing phase took place with the fan running in Extract Mode, meaning that the HP had to deal with much higher temperatures than it would if the fan was operating in Supply Mode, as discussed in section 8.2. This resulted in an increased risk of evaporating temperatures reaching values that were outside the operating range of the low-stage compressor.

6.5. Conclusion

This chapter reviewed the monitoring strategy for the Bunhill WHR system; described the methodology used to validate the WHR model; and presented the main challenges faced during commissioning of the WHR system. As discussed, the HP was unable to operate steadily during early testing stages. This was due to the tests having been carried out in Extract Mode during summer, which is the period of highest vent shaft temperatures and lowest heat demand on the district heating network (DHN), and which can lead to high evaporating temperatures and unstable operating conditions. It is expected that higher loads on the heat network and Supply Mode operation during warmer months will allow the HP to operate in accordance with its design conditions.

As the system is still in its commissioning phase at the time of writing, the HP has not been operating continuously and testing data for part-load operation had to be used for the validation purposes of this thesis. Furthermore, only data pertaining to the operation of the HP were available, so the HRC model had to be validated with data from the manufacturer of the coils. Despite these challenges, both HP and HRC models were able to replicate typical operating conditions to the degree of accuracy of typical sensors, as generally used in energy applications. When compared to experimental data, the HP model achieved maximum deviations of 12.5% for COP and 6.5% for cooling duty, with modelled outlet water temperatures at the evaporator being within ±0.5°C of the measured data. The validation of the HRC model also proved its reliability, with outlet temperatures for both air and water simulated by the coil selection software being within ±0.5°C of the temperatures predicted by the WHR model.

7. Modelling of the Underground Railway Environment

7.1. Introduction

This chapter describes the principles behind an investigation of the cooling implications of the waste heat recovery (WHR) system to the London Underground (LU) environment, focusing on a tunnel section that is adjacent to the City Road ventilation shaft, where the heat recovery coils (HRC) were installed. The objective of this investigation is to evaluate how the cooling output calculated with the WHR model, which was described in Chapter 5, would affect tunnel temperatures. The model utilised for this investigation is a bespoke tool developed by Transport for London (TfL) based upon the Subway Environment Simulation (SES) platform. As described in section 2.14.3.3, SES is an analytical design tool that provides estimates of air flows, temperatures, and humidity, as well as air conditioning requirements, based upon rail system characteristics such as train performance and operation, tunnel geometry and ventilation, as well as any sensible and latent heat exchanges within the network.

The SES platform consists of four interdependent subprogrammes covering specific aspects of the system (U.S. Department of Transportation, 2002). The train performance subprogramme is used to determine the speed, acceleration, position of trains and their associated heat rejection. The aerodynamic subprogramme utilises these train parameters, combined with tunnel geometry and ventilation system data, to yield air velocities and flow rates in stations, tunnels and ventilation shafts. The combination of the aerodynamic and train performance subprogrammes can also be used to calculate train aerodynamic drag and pressure variations associated with the piston effect. The temperature/humidity subprogramme computes air flow parameters and train heat release data from the aforementioned subprogrammes to provide an estimation of sensible and latent heat exchange throughout the system, which enables determining temperature and humidity data at all locations. Lastly, the ventilation and heat load data from these subprogrammes, together with climate projections and ambient temperature data, are used to determine the long-term transfer of heat between tunnel air, the structure and the surrounding soil.

Together, these subprogrammes combine several operating parameters in order to simulate the interdependent multi-factor phenomena that characterise the dynamics of an underground railway (UR). An overview of the modelling framework of SES is provided in Figure 7.1. This chapter presents the principles of the temperature/humidity subprogramme, with the other subprogrammes described in Appendices D, E, F and G. This chapter also describes the methodology developed to evaluate the impacts of the WHR system on the adjacent stations to the City Road ventilation shaft, based on a novel approach that combines the WHR model, which is able to accurately represent the cooling process, with LU's SES model.

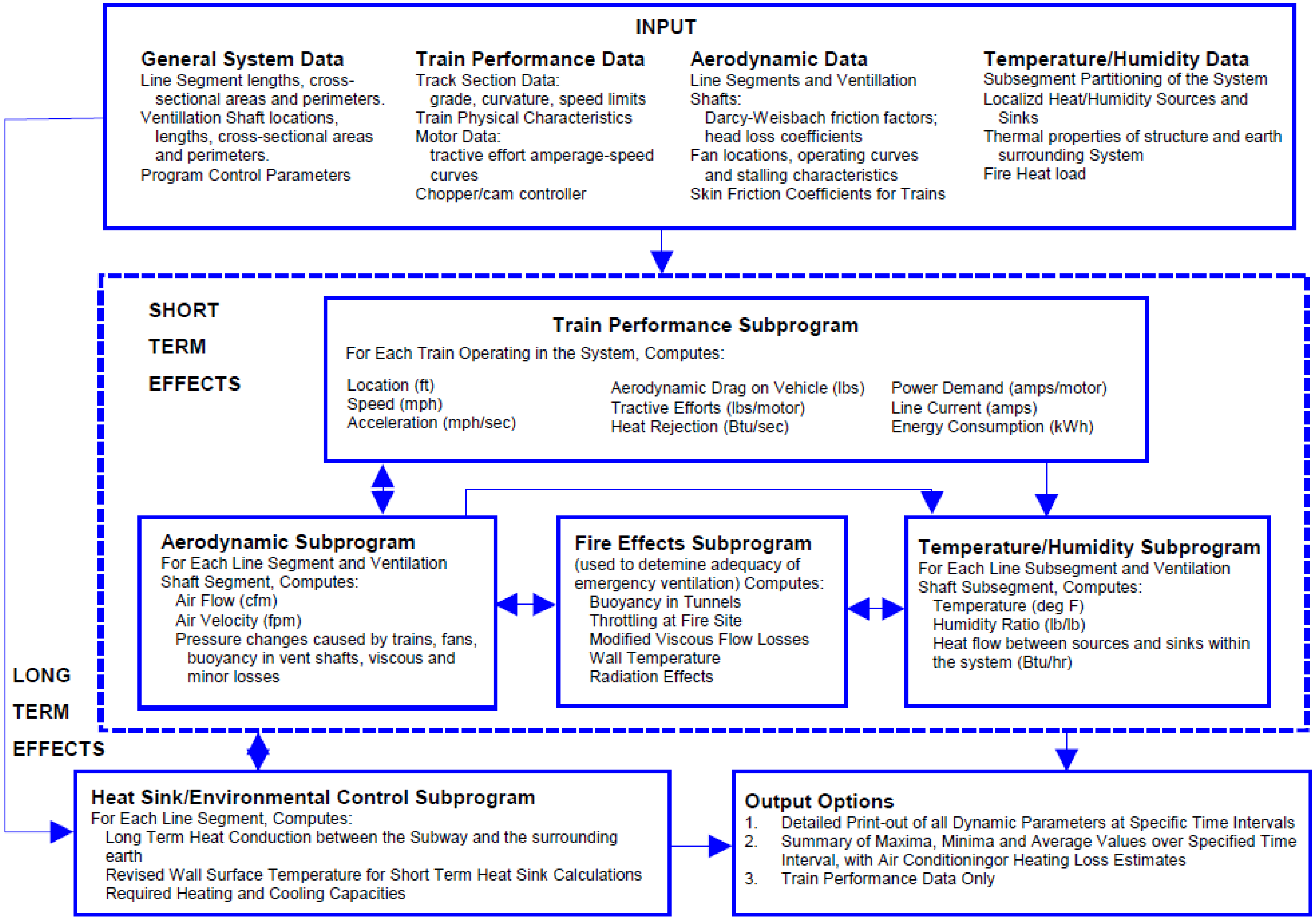

Figure 7.1 – SES modelling framework, including its inputs and outputs for each stage and subprogramme (U.S. Department of Transportation, 2002).

7.2. Thermodynamic Phenomena in Underground Railways

The thermal interactions within the UR environment are simulated using the temperature/humidity subprogramme of SES. These simulations consist of breaking down the network into smaller discrete components of constant temperature and humidity named subsegments. The heat generated within each component over time, based upon train profiles and airflow patterns, is then used to calculate energy and mass balances at nodes connecting subsequent components, whilst also considering the conductive heat transfer between tunnel walls and the surrounding soil. In SES, the heat transfer regimes within tunnels are simulated as one-dimensional, meaning that the air temperature and humidity is considered as uniform in a given tunnel cross section. As in typical duct flows, heat transfer by axial conduction is assumed negligible when compared to the convective heat transfer caused by air movement.

During simulations, each tunnel subsegment is analysed separately and their net difference of thermal energy is calculated. This net difference is based upon the conditions of the air flowing into the tunnel subsegment. The heat added/removed by sources and sinks within the subsegment is then calculated, yielding an outlet condition which is used as input for the analysis of the adjacent subsegment through thermodynamic nodes. The temperature/humidity subprogramme therefore utilises airflow estimates produced by the aerodynamic subprogramme and heat loads calculated by the train performance simulations. The energy balance across each tunnel subsegment forms separate differential equations that characterise the rate of change in sensible and latent heat in each subsegment. When analysing the entire network, the differential equations for each tunnel subsegment form a system of equations that are then integrated to yield time-dependent values for temperature and humidity throughout the UR network.

7.2.1. Outside Ambient Conditions and Climate Change

The thermal environment of a UR network is affected by outside ambient conditions, which provide boundaries for simulations. The user must supply dry and wet-bulb ambient temperatures as inputs, as well as values for ambient barometric pressure. It is common for a UR system to be analysed for the most extreme weather conditions, which represent the temperatures that are only likely to be exceeded for 1% of a one-year period. As simulations are aimed at analysing future network conditions, the effects of a warming climate must be accounted for when supplying weather data. For the purpose of this investigation, simulations were carried out to analyse the thermal environment of the LU for the years of 2030 and 2050. The SES model used by TfL is calibrated to utilise 2006 weather data, which is then projected to the target years based on the UK Climate Projections from 2009 (UKCP09), as provided by the Met Office (2018). The UKCP09 provides predictions for several climate variables, including ambient temperatures, between the years of 2006 and 2050, considering probability levels of 10, 50 and 90%, which correspond to scenarios of low, medium and high future emission levels, respectively. Although the latest climate projections available are from 2018, TfL uses 2009 data as they predict higher temperatures and therefore represent a more conservative approach when analysing the risk of heat stress across the network. Based upon a probability of occurrence of 50% and a medium emission scenario, the average temperature increase in the London area is calculated for the target years of 2030 and 2050. These represent increases of 0.5 and 1.3°C respectively from the benchmark year of 2006.

7.2.2. Heat Sources

The heat sources within a specific tunnel segment can be categorised as steady-state or unsteady heat sources. This will depend upon the variation of the heat output from a given source over the entire simulation. Steady-state heat sources consist of any positive or negative heat source that remains constant over the span of a simulation. Positive heat sources are associated with the addition of heat to the tunnelled network, whilst negative heat sources represent heat removal from the system. Examples of positive steady-state heat sources include tunnel lighting, third rail losses and passenger heat, whilst negative sources are generally associated with heat removed by cooling equipment when applicable. In contrast to steady-state heat sources, unsteady sources can be positive or negative and may vary during the simulation period. These sources are mainly the heat dissipation associated with trains, as discussed in Appendix E, as well as tunnel wall surface evaporation and trackway exhaust systems. The calculation procedures for both steady-state and unsteady heat sources can be found in the SES manual (U.S. Department of Transportation, 2002).

7.2.3. Energy Balances

The variation of temperature and humidity as air flows through the tunnels is calculated from the energy and mass balances between subsegments. This involves accounting for the net heat gains across each subsegment and performing calculations to guarantee continuity at thermodynamic nodes, which connect different subsegments. A representation of a node between subsegments 1 and 2 is shown in Figure 7.2.

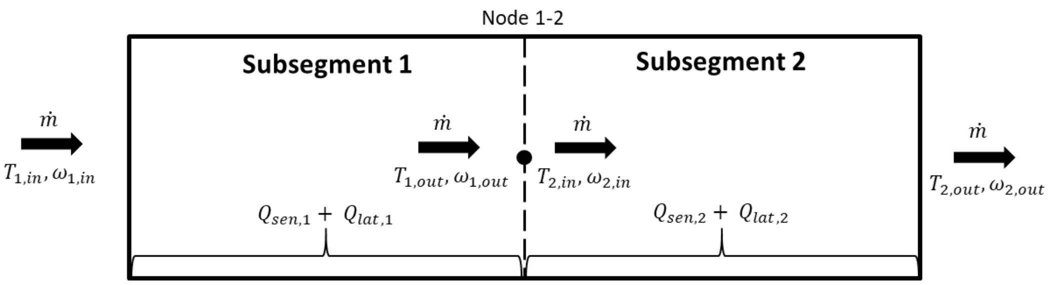

Figure 7.2 – A representation of the parameters utilised to calculate temperature and humidity for subsegments.

SES calculates the net sensible (Q_{sen}) and latent (Q_{lat}) heat gains separately, and these are used in its temperature and humidity models, respectively, to yield air conditions for each subsegment of the UR network. The principles behind these models are described in the following subsections.

7.2.3.1. Temperature Model

The finite difference method is utilised to calculate energy balances at the thermodynamic nodes connecting two subsegments. The temperature model computes only sensible heat gains/losses across a given segment, which are then added to the energy balance to yield the temperature for the following subsegment. This applies to the subsegments shown in Figure 7.2, and their energy balances can be calculated for each differential timestep dt, which corresponds to the time necessary for tunnel air to travel across a subsegment. The air temperature change can be calculated by the integrals shown in Equations 7.1 and 7.2 for subsegments 1 and 2, respectively, where C_p represents the specific heat for tunnel air, which is assumed to be constant across the subsegments, as reported in the work of Mortada (2016).

$$\dot{m}C_p \int T_1 \, dt = \int Q_{sen,1} \, dt \tag{7.1}$$

$$\dot{m}C_p \int T_2 \, dt = \int Q_{sen,2} \, dt \tag{7.2}$$

The mass flow rate across both subsegments is constant as they belong to the same tunnel section (see Appendix D). The temperatures T_1 and T_2 represent the air temperature as it travels from the inlet to the outlet of their respective subsegment. For a given moment in time, the energy balance for node 1-2, shown in Figure 7.2, would be calculated based upon the principle of continuity, as shown in Equation 7.3, since the mass flow rate and specific heat of air remain constant between two successive subsegments.

$$T_{1,out} = T_{2,in} \tag{7.3}$$

However, when more than two subsegments meet at the same node, which is often the case for UR systems, SES computes the energy balance depending on the type of node that is encountered. The different node types according to SES classifications are described in section 7.2.4.

7.2.3.2. Humidity Model

Similarly to the temperature model, the humidity model is also based upon the energy balance across subsegments, but these are now associated with a change in air moisture content (ω) due to the gain or loss of latent heat (Q_{lat}), as shown in Figure 7.2. In this case, the average moisture content for subsegments 1 and 2 are calculated based upon the change in latent heat across each subsegment, as shown in Equations 7.4 and 7.5, respectively, where i_{vap} is the heat of vaporisation for water at the average temperature of the subsegment.

$$\dot{m}i_{vap} \int \omega_1 \, dt = \int Q_{lat,1} \, dt \quad (7.4)$$

$$\dot{m}i_{vap} \int \omega_2 \, dt = \int Q_{lat,2} \, dt \quad (7.5)$$

The moisture contents for subsegments 1 (ω_1) and 2 (ω_2) represent the change in humidity from inlet to outlet points over time. The continuity principle also applies in this case and, assuming a constant heat of vaporisation, Equation 7.6 can be used to calculate the latent energy balance at node 1-2. The latent energy balance for nodes connecting more than two segments depends upon the type of node being evaluated, which is detailed in section 7.2.4.

$$\omega_{1,out} = \omega_{2,in} \quad (7.6)$$

7.2.4. Thermodynamic Nodes

Similarly to the aerodynamic nodes described in Appendix F, which connect tunnel sections, the thermodynamic nodes represent the connections between tunnel subsegments and are used for the calculation of energy and mass balances between them. Thermodynamic nodes can be assigned as one of three different types depending on their configuration. These different types are referred to as either mixing, partially mixing or boundary nodes (U.S. Department of Transportation, 2002), and must be assigned depending on the actual geometry and air flow behaviour at different network junctions.

7.2.4.1. Type 1 – Mixing Nodes

At any particular thermodynamic node, the continuity of flow must be observed, meaning that the mass flow rate of air approaching a node is always equal to the mass flow rate leaving it. For type 1 nodes, it is assumed that complete thermodynamic mixing takes place, so temperatures and specific humidities can be determined as the energy-based average of the temperatures and moisture contents of the air flows approaching the node (U.S. Department of Transportation, 2002). Type 1 nodes can be assigned to any junction with up to five subsegments. A representation of a node connecting three subsegments is shown in Figure 7.3. In this case, as complete mixing is considered, the temperature and humidity leaving the node to subsegment 3, as shown respectively in Equations 7.7 and 7.8, can be calculated based on the conditions of the air streams approaching the node from subsegments 1 and 2.

$$\dot{m}_1 T_1 + \dot{m}_2 T_2 = \dot{m}_3 T_3 \quad (7.7)$$

$$\dot{m}_1 \omega_1 + \dot{m}_2 \omega_2 = \dot{m}_3 \omega_3 \quad (7.8)$$

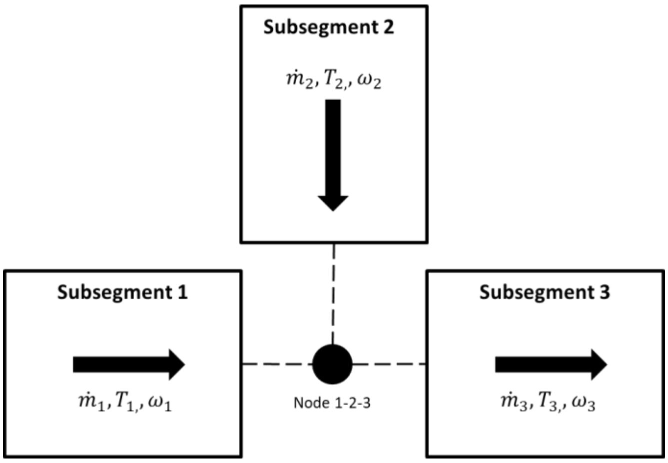

Figure 7.3 – A representation of a type 1 node connecting three subsegments (adapted from Mortada, 2006).

7.2.4.2. Type 2 – Partially Mixing Nodes

When four or more subsegments meet, it is possible that air inflowing from a given subsegment does not mix completely with other inflows before leaving the node. This can be used to model tunnel-to-tunnel crossovers and junctions where a ventilation shaft is connected to two separate tunnels (U.S. Department of Transportation, 2002). In these cases, the node has to be divided into subnodes that connect three different subsegments and behave as a Type 1 fully mixing node. Figure 7.4 shows how SES deals with a junction between five tunnel sections, with their connecting node being divided into subnodes A, B and C.

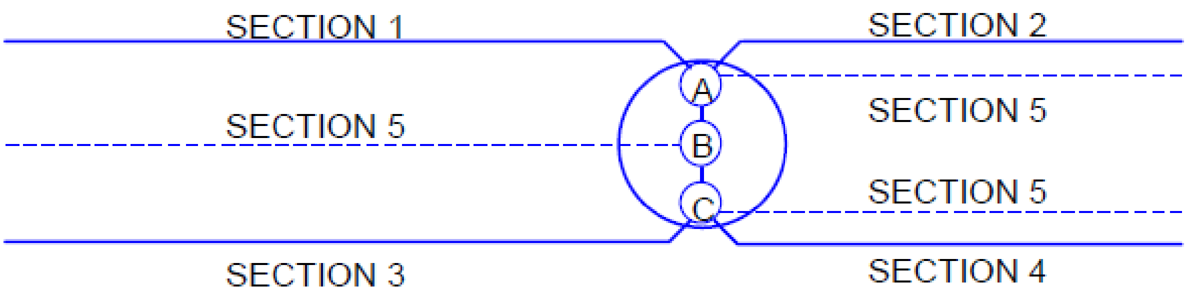

Figure 7.4 – Typical subdivision of a node connecting five different tunnel sections (U.S. Department of Transportation, 2002).

7.2.4.3. Type 3 – Boundary Nodes

At last, the Type 3 nodes are utilised at the boundaries of the UR system. These boundaries are represented by points at which the user defines the temperature and humidity of the air flow approaching the node. Type 3 nodes are commonly applied to openings to the atmosphere and portals, where the air entering the subsegment is at ambient conditions.

7.3. Simulation Procedure for the UR Model of the London Underground

After describing the thermodynamic principles behind the SES based UR Model, it is important to define how its functionalities are used to simulate the impacts of the WHR system on the UR environment. As mentioned in the introduction to this chapter, the cooling potential of the

WHR system is assessed in terms of the change in tunnel temperature that is caused by the system's cooling output, focusing on the Northern Line section where the City Road ventilation shaft is located. TfL typically analyses the impacts of cooling projects on SES by modelling the temperature reduction achievable at stations. For that reason, this investigation will focus on the temperature change the WHR system could achieve at the stations of Angel, Old Street, Moorgate and King's Cross. Angel and Old Street represent the adjacent stations to the City Road shaft and should benefit the most from the cooling delivered, whilst King's Cross and Moorgate will be included in order to evaluate if a cooling benefit can be achieved beyond the immediate surroundings of the WHR system.

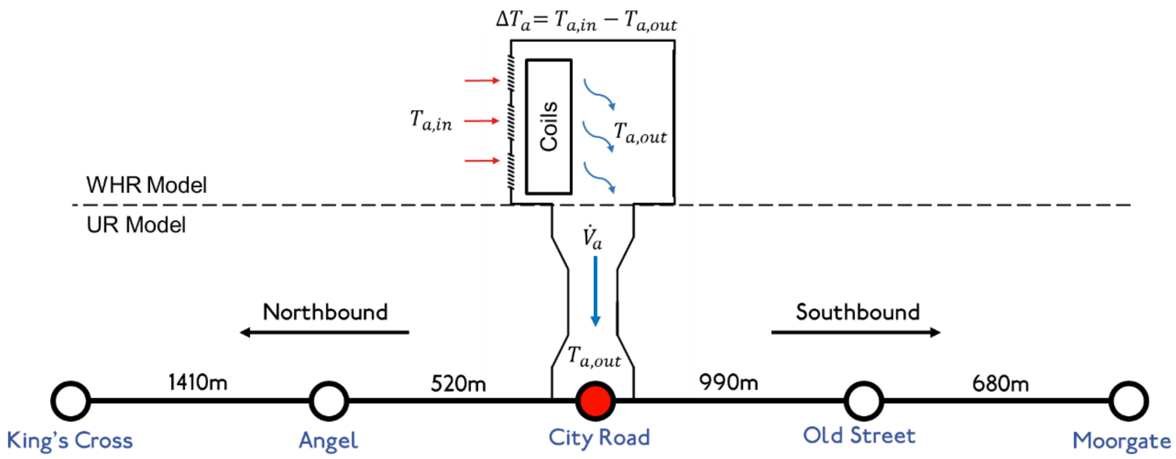

Figure 7.5 – Schematic highlighting the temperature input from the WHR model to the SES simulations.

The vent shaft is modelled in SES based upon the fan performance curves and its design volumetric flow rate ($\dot{V}_a$ = 70 m^3/s). The air temperatures for a Supply ventilation shaft are generally based upon the ambient air conditions, as the end node of a vent shaft structure represents an opening to the atmosphere. The cooling output from the WHR system can therefore be represented by changing the temperature of the air that is supplied through the ventilation shaft according to the air outlet temperatures obtained with the WHR model, considering the volumetric flow rate of the shaft as well as the shares of latent and sensible cooling associated with the heat recovery process. In this case, the air supplied to the tunnels would be at the coil outlet temperature ($T_{a,out}$), as opposed to the ambient air temperature, which is observed at the coil inlet ($T_{a,in}$). This process is illustrated in Figure 7.5, which shows how the WHR model outputs are used to simulate the cooling effect on the UR network, highlighting the nearest stations to the City Road vent shaft and the distances between them. As SES simulations involve both long-term and short-term analyses, certain adaptations must be made before the WHR model results can be used as inputs to the SES investigation.

7.4. Adapting the Results from the WHR Model

The analysis of the UR environment on SES is based upon short-term and long-term simulations. Long-term simulations are used as part of the heat sink analysis to predict the variation of tunnel wall temperatures throughout the year, whereas short-term simulations are used to represent the direct impacts of a cooling supply over a given period within that year. Therefore, the long-term heat sink analysis yields tunnel wall temperature values, which can then be used in the short-term simulations to represent the tunnel air temperature reduction during any year of interest. The WHR model results must then be treated differently for long and short term simulations, and this process is described in the following sections.

7.4.1. Short-term Simulations

The procedure adopted by TfL to simulate the short-term impacts of cooling systems is based upon the worst-case scenario, which corresponds to the hottest temperatures the UR system could be exposed to. These conditions typically correspond to the service peak hours for the hottest week of the hottest month within a year. Therefore, short-term simulations are run only for that week, based upon the 1% exceedance criteria introduced in section 7.2.1. Initially, the hottest week of the hottest month, from 17 to 21 July, was identified based upon the original 2006 temperature data set. The average ambient air temperature for that week was then calculated and the temperature rise predicted from UKCP09, as described in 7.2.1, was applied to yield the average ambient air temperature for the evening service peak period for the target year. The average morning peak temperature for the short-term simulations ($T_{mor,st}$) was then calculated considering the average evening peak temperature in the short-term ($T_{eve,st}$) and the daily temperature amplitude for the base year ($T_{amp,day}$ = 7.8°C), as shown in Equation 7.9 (U.S. Department of Transportation, 2002). The average relative humidity (RH) of ambient air for the same peak periods also needed to be provided based on the base year data. The ambient temperature and RH data used for the short-term simulations, considering the temperature rise for the years of 2030 (0.5°C) and 2050 (1.3°C), are provided in Table 7.1.

$$T_{mor,st} = T_{eve,st} - \frac{T_{amp,day}}{2} \tag{7.9}$$

Table 7.1 – Average morning and evening peak ambient air conditions for the hottest weeks of 2030 and 2050.

Period	Average RH (%)	Average Ambient Temperatures (°C)	
		2030 Projection	2050 Projection
Evening Peak	38%	27.3	28.1
Morning Peak	55%	23.4	24.2

Based upon the ambient air conditions shown in Table 7.1, the supply temperatures from the WHR system were then determined by subtracting an average coil air temperature reduction

(ΔT_a), calculated for 2006 data, from the average ambient temperatures for the peak periods of the hottest week of the target year. The average coil ΔT_a for peak conditions was obtained directly from the WHR model described in Chapter 5, utilising ambient air data from the 2006 data set, which is discussed further in Chapter 8. The air temperature reduction, calculated for both the morning and evening service peaks, as well as the associated sensible cooling ratios and supply temperatures are provided in Table 7.2. The difference in ΔT_a between morning and evening peaks is affected by the different shares of sensible and latent cooling calculated for both periods. The conditions of the air that is supplied at the City Road ventilation shaft node were then adjusted to the dry and wet-bulb temperatures predicted by the WHR model. This enabled analysing the implications of the cooling output from the WHR system for the UR network during the warmest periods of the year.

Table 7.2 – Average air supply temperatures for service peaks during the hottest weeks of 2030 and 2050.

Period	Coil Temperature Reduction ΔT_a (°C)	Sensible Cooling Ratio (%)	Average Supply Temperatures (°C)	
			2030 Projection	2050 Projection
Evening Peak	8.2	87.5%	19.1	19.9
Morning Peak	6.6	73.1%	16.8	17.6

7.4.2. Long-term Simulations

The long-term simulations are applied to represent long-term variations in tunnel temperatures, which are mainly associated with the heat sink effect and its effects on tunnel wall temperatures throughout the target year. In order to represent the impacts of the WHR system over the year, long-term simulations must consider the annual average supply temperature ($\bar{T}_{a,out}$), based upon coil outlet temperatures, and the annual ambient temperature amplitude ($T_{amp,year}$), as described in Appendix G. The value of $\bar{T}_{a,out}$ depends upon the amount of time the coil operates in Supply Mode during the year and can be obtained from the WHR model results for the base year. The long-term simulation inputs are also based upon the evening and morning service peaks, which are now calculated for the summer period as opposed to a single week. Based upon the estimated summer peaks, SES takes into account daily and annual amplitudes to determine network temperatures throughout the year. The equivalent summer morning peak temperature ($T_{mor,lt}$), used for the long-term simulations, is a function of the average vent shaft supply temperature and the annual amplitude, as shown in Equation 7.10. The long-term summer evening peak temperature ($T_{eve,lt}$) was then determined based upon the morning peak temperature and the daily temperature amplitude ($T_{amp,day}$), as shown in Equation 7.11.

$$T_{mor,lt} = \bar{T}_{a,out} + T_{amp,year} \tag{7.10}$$

$$T_{eve,lt} = T_{mor,lt} + \frac{T_{amp,day}}{2} \quad (7.11)$$

In contrast with the short-term simulations, where the supply temperature is always calculated for the same 1% exceedance temperature values, corresponding to the hottest week of the hottest month, the supply temperatures in the long-term simulations vary depending on the annual operating schedule of the WHR system, which combines both Extract and Supply modes. An increase in operation in Supply Mode means cooled air is provided to tunnels for longer periods, which reduces the annual average temperature and, consequently, the peak tunnel temperatures used in simulations. Different options of operation in both Extract and Supply modes are introduced and analysed in Chapter 8.

7.5. Main Limitations of the SES UR Model

The main limitation of SES is its inability to model a combined fan operation for a given simulation, i.e. SES requires the vent shaft fan to be set either in Supply or Extract Mode for the entire simulation. Therefore, a mixed Extract and Supply operation will be analysed by combining the SES results obtained from simulations that consider the WHR system to be operating entirely either in Extract or Supply Mode. The approach typically adopted by TfL to represent a mixed operation is by calculating a weighted average of the results based on the running times for both Extract and Supply modes over the year. This consists of applying weighting factors that vary from zero to unity for the temperatures predicted in Extract ($T_{extract}$) and Supply (T_{supply}) operations, as shown in Equation 7.12, which provides the formula for estimating platform temperatures ($T_{platform}$) for a weighting factor α.

$$T_{platform} = \alpha T_{extract} + (1-\alpha) T_{supply}; \text{ where: } 0 \leq \alpha \leq 1 \quad (7.12)$$

7.6. Conclusion

This chapter described a novel methodology for analysing the impacts of the WHR system on the LU environment. The novelty behind this approach is enabling the use of an accurate representation of the cooling process, which is achieved with the WHR model, to investigate the impacts of cooling coils through SES simulations. The methodology developed can be used to analyse how different operation regimes, which involve both Extract and Supply Modes, could potentially affect peak temperatures at adjacent LU stations, which is discussed in Chapter 8. One potential limitation associated with SES is its inability to run in a combined operation mode. However, the method for representing a mixed fan operation has been used by TfL for other cooling projects and provides a good indication of station temperatures as results are bound by the conditions for year-round operations in Extract and Supply modes. Furthermore, SES is a widely validated tool that was custom-made for the LU and calibrated against tunnel temperature measurements.

8. Heat Recovery Analysis – Design and Operation

8.1. Introduction

This chapter aims to analyse the technical performance of the waste heat recovery (WHR) system based on the results from the model described in Chapter 5. This involves assessing system behaviour when subject to different operating modes, i.e. Extract and Supply, as well as varying heat source conditions, as temperature and relative humidity (RH) have significant effects on heat transfer. In this case, the efficiency of the WHR system is evaluated according to its energy consumption, as well as heating and cooling outputs. Furthermore, this chapter also investigates the thermal interactions between the WHR system and the underground railway (UR) utilising the UR model described in Chapter 7. The WHR model can predict coil surface conditions according to air inlet parameters, and this is used to calculate latent and sensible cooling loads, which are applied to simulate how the system impacts the nearby stations. Lastly, the implications on system performance of operating for longer periods in Supply Mode are discussed, with focus on coolant choice and the occurrence of condensation.

8.2. Temperature and Humidity Data

The main inputs to the WHR Model are hourly temperature and RH data for both tunnel and ambient air. The tunnel air temperature and RH measurements were provided by Transport for London (TfL, 2019b) and recorded at the City Road ventilation shaft from January 2013 to January 2014. These are used as the basis for calculations in simulations representing system operation in Extract Mode. In order to represent Supply Mode operation, weather data for the same one-year period were utilised, obtained from the nearest available weather station belonging to the Meteorological Office (Met Office, 2019). Figure 8.1 and 8.2 summarise daily average dry and wet-bulb temperatures for the tunnel and ambient air data sets, respectively.

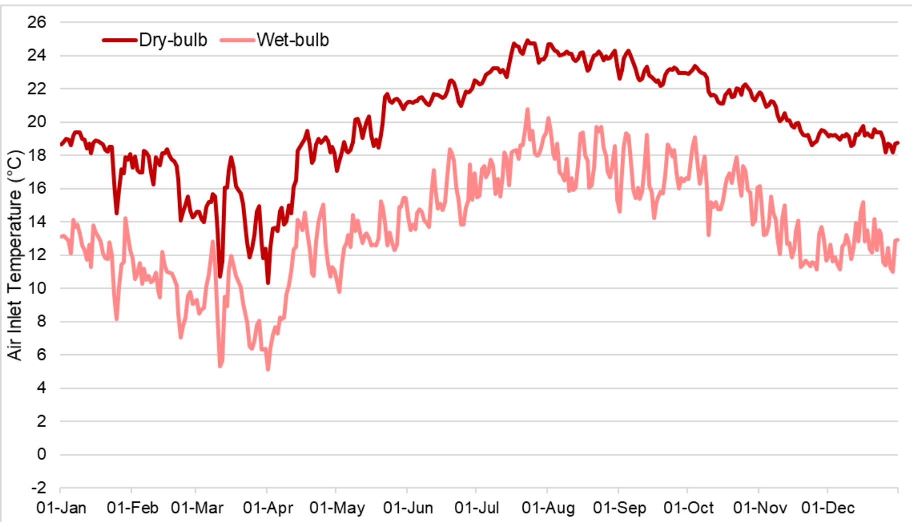

Figure 8.1 – Daily averages of dry and wet-bulb temperatures for tunnel air used in this investigation.

As it can be seen from Figure 8.1 and Figure 8.2, the temperatures recorded for the ventilation shaft were generally higher than ambient temperatures throughout the year. However, the highest hourly value recorded was for ambient air in July (32.8°C), as opposed to an hourly maximum of 25.6°C registered for tunnel air. The minimum hourly temperature measured for the vent shaft was 7.8°C, whilst ambient air had a lowest value of -1.4°C. The standard deviation (SD) recorded for tunnel air dry-bulb temperature was of 3.2°C, whilst ambient air had a SD of 6.2°C. This indicates the significant variation of ambient air temperature across the year, highlighting how URs represent a more stable source of heat than the ambient.

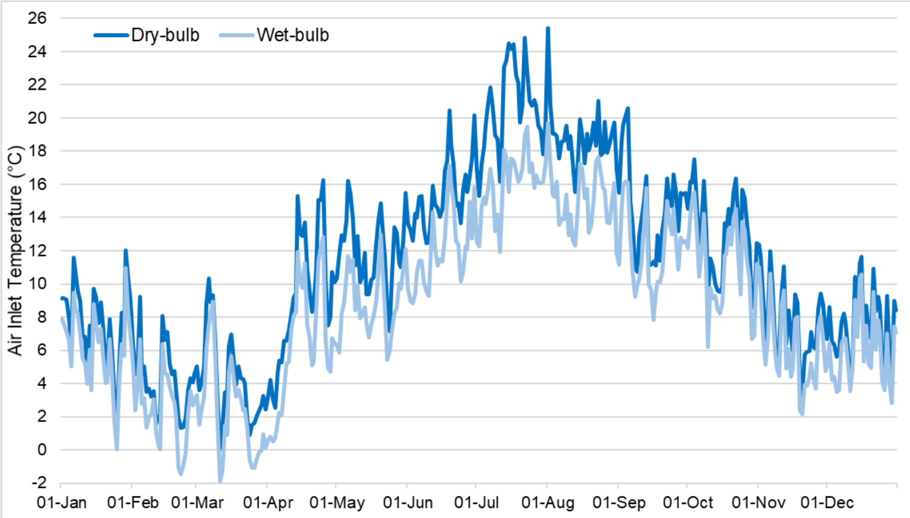

Figure 8.2 – Daily averages of dry and wet-bulb temperatures for ambient air used in this investigation.

The analysis of humidity involves both dry and wet-bulb temperatures. The difference between daily dry and wet-bulb temperatures is much lower for ambient air, meaning that it is generally much closer to saturation. Overall, the average difference between the two temperatures was 6°C for tunnel air and 2°C for ambient air. In terms of RH, the annual average calculated for tunnel and ambient air were of approximately 50% and 75%, respectively. The presence of moisture in the air stream affects the condition of the coil surface and may change the calculation procedure for the energy balance at the heat recovery coils (HRC) (see section 5.4.3). Lower dry and wet-bulb differences, or higher RHs, result in higher rates of condensation as air travels across the coils, which is discussed in detail in section 8.4.2.

8.3. System Performance Overview

The performance of the WHR system has been analysed based upon the energy consumption of its main components, namely the two-stage heat pump (HP), the coolant pump, and the reversible fan, as described in Chapter 5. The results presented in this chapter are based on the full-load operation of the HP, while delivering enough heat to increase the district heating water temperature by 20 K. Based upon this heating duty, as well as on the air inlet conditions described in section 8.2, the efficiency of the system is represented and assessed in terms of the coefficient of system performance (COSP), introduced in section 5.2. The heating performance will be analysed by comparing different operating conditions throughout the year, which are based upon fan operation in Extract and Supply modes. These operating conditions are reflected in the five modelling scenarios shown in Table 8.1. The modelling scenarios were chosen in order to represent a diverse number of operating conditions for the WHR system, as this enables a comparison of how the system would behave when operating in Extract and Supply modes for different periods of the year.

Table 8.1 – Different modelling scenarios for the WHR model, based upon fan operation mode.

Scenario	Operating Condition	Description
1	12E/0S	Fan operating in Extract Mode for the entire year (12 months).
2	9E/3S	Fan operating in Supply Mode during meteorological summer (Jun/Jul/Aug), and in Extract for the rest of the year.
3	6E/6S	Fan operating in Supply Mode for half the year, from May to October, and in Extract for the remaining 6 months.
4	3E/9S	Fan operating in Extract Mode only during meteorological winter (Dec/Jan/Feb), and in Supply for the rest of the year.
5	0E/12S	Fan operating in Supply Mode for the entire year (12 months).

The average $COSP_H$ was analysed for the five different scenarios, as shown in Figure 8.3. Since Supply Mode operation is severely limited when utilising water as the coolant, the analysis assumed that a mixture with 30% mass concentration of propylene glycol (PG) would be utilised (see section 8.6). If operating in Extract Mode, water can be used as coolant without additional downtime, achieving an annual $COSP_H$ of 3.38. By using a PG mixture, the $COSP_H$ would be reduced by 3%, assuming that pressure drops across the evaporator and the HRC remain constant. Therefore, utilising a PG mixture would have a minor effect on efficiency, whilst also allowing the WHR system to operate in full-load even in colder conditions, something that cannot be achieved with water. Therefore, this investigation compares Extract and Supply modes considering a 30% PG/water mixture as the coolant for both modes.

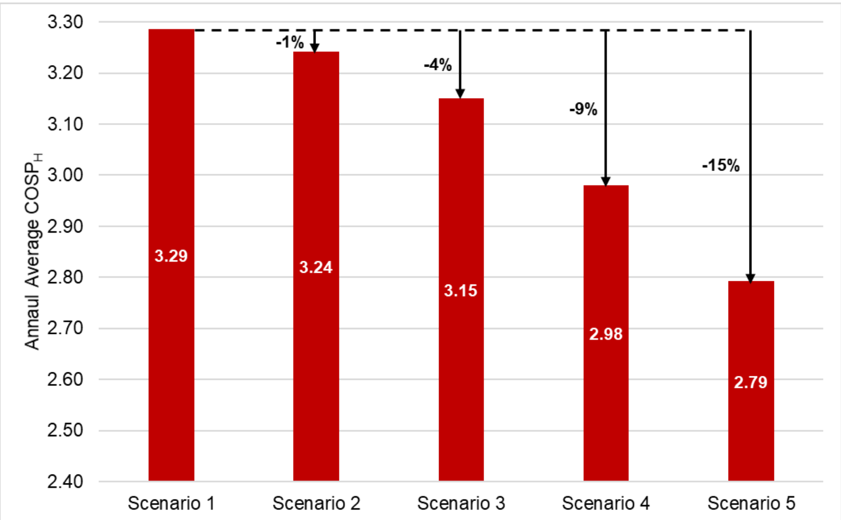

Figure 8.3 – Annual average heating COSP for the different modelling scenarios from Table 8.1.

As seen from Figure 8.3, the annual $COSP_H$ reduces as the period of operation in Supply Mode increases, falling from 3.29 for scenario 1 down to 2.79 for scenario 5, a decrease of 15%. However, operating for longer periods in Supply Mode has the advantage of providing cooling to the LU tunnels. This is highlighted in Figure 8.4, which shows the annual sum of heat energy recovered, cooling delivered and electrical energy consumed by the WHR system, assuming a continuous operation with an annual downtime of 5%.

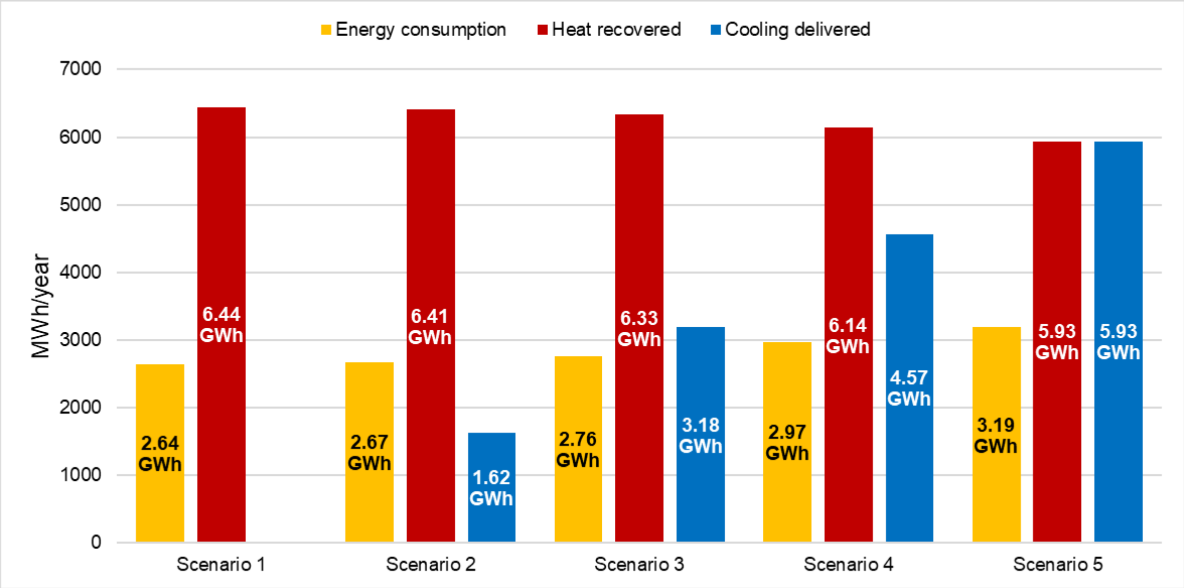

Figure 8.4 – Energy consumption, heat recovered and cooling delivered for the five modelling scenarios.

As it can be noted from Figure 8.4, the total heat recovered is reduced slightly as the period operating in Supply Mode increases, which is due to the lower heat transfer coefficients that are experienced at lower temperatures (see section 8.4.1). In terms of energy consumption, there is a gradual increase for higher ratios of operation in Supply Mode, which is expected due to the differences in COSP between the analysed scenarios. Overall, a 20.9% increase from scenario 1 to scenario 5 was observed. As for the cooling output, it is equivalent to the heat recovered when the system operates in Supply, so is not applicable to scenario 1. The total cooling delivered for scenario 2 was 1,621 megawatt-hour (MWh) per annum, whilst scenario 5 led to a total of 5,934 MWh per year. Although Supply Mode operation reduces $COSP_H$, it can provide significant benefits in terms of cooling. If scenarios 2 and 5 are compared, an increase of 19.3% in energy consumption could lead to an increase of around 366% in the amount of cooling delivered. The cooling potential estimated utilising the WHR model serves as an input for the SES simulations, which show how the cooling output during Supply Mode operation affects the UR environment (see section 8.5). The detailed analysis of annual energy consumption and system performance are provided in the following subsections, whilst the impacts of sensible and latent heat loads on system capacity and efficiency are discussed later in this chapter.

8.3.1. Monthly Heating COSP of the WHR System

The performance of the WHR System can be further analysed based upon monthly averages of $COSP_H$ for both Extract and Supply modes, as illustrated in Figure 8.5. This enables a detailed performance comparison between Extract and Supply modes throughout the year, highlighting the percentage difference in $COSP_H$ between the two modes for each month.

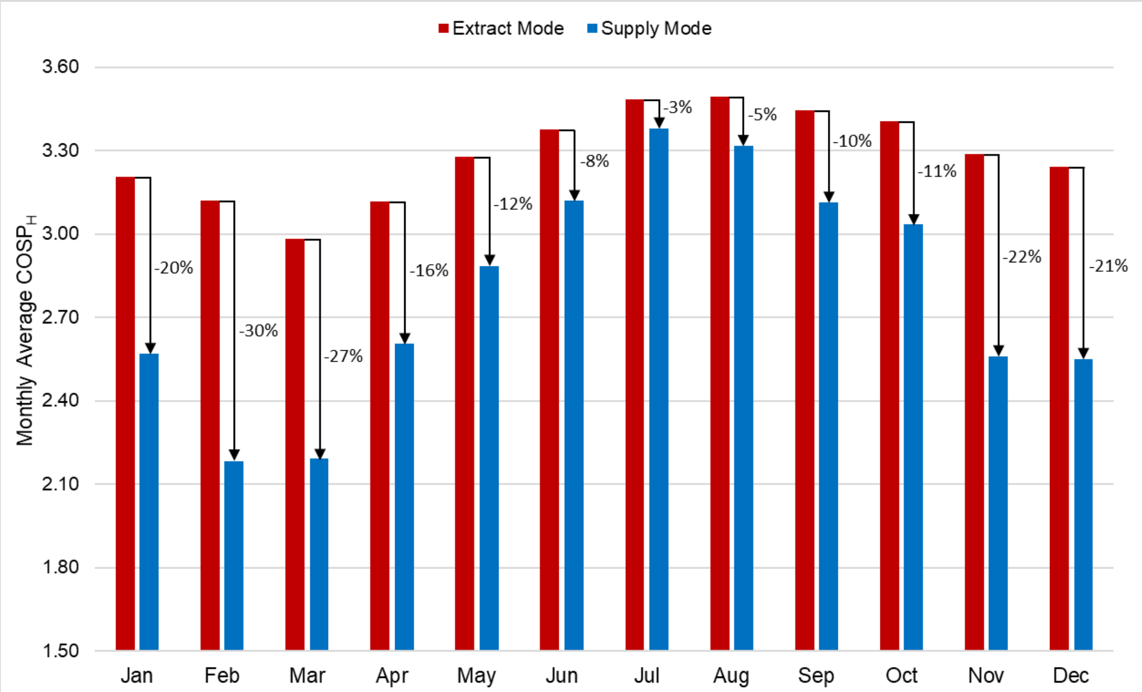

Figure 8.5 – Monthly average heating COSP and its percentage differences for Supply and Extract modes.

It can be seen from Figure 8.5 that the difference between Supply and Extract Mode varies widely throughout the year. During colder months, the difference in performance was substantially higher, reaching up to 30% in February. On the other hand, the summer months (June to August) showed smaller differences, meaning that the heating performance of the system ($COSP_H$) would be less affected if operating in Supply Mode for that period. This is particularly useful as the summer months represent the period when LU temperatures are at their peak and cooling supply would be most valuable.

8.3.2. Energy Consumption

The energy consumption of the WHR system can be further analysed by comparing the work inputs predicted by the model for each of the system components, namely the two-stage HP, the coolant pump, and the reversible fan. The total energy consumptions for the scenarios described in Table 8.1, broken down by system component, are provided in Figure 8.6. The energy consumption associated with the pump and the reversible fan is approximately constant, as the model assumed that the system would operate with the same flow rates for both the coolant and air streams, and the air pressure losses across the WHR system were similar for Extract and Supply modes (see Table 5.1). Overall, the energy consumption variation between the different scenarios is due to the different work inputs required for the HP when operating in different conditions. Compared to scenario 5, equivalent to a year-round operation in Supply, scenario 1, which corresponds to year-round operation in Extract, would reduce energy consumption by 17%.

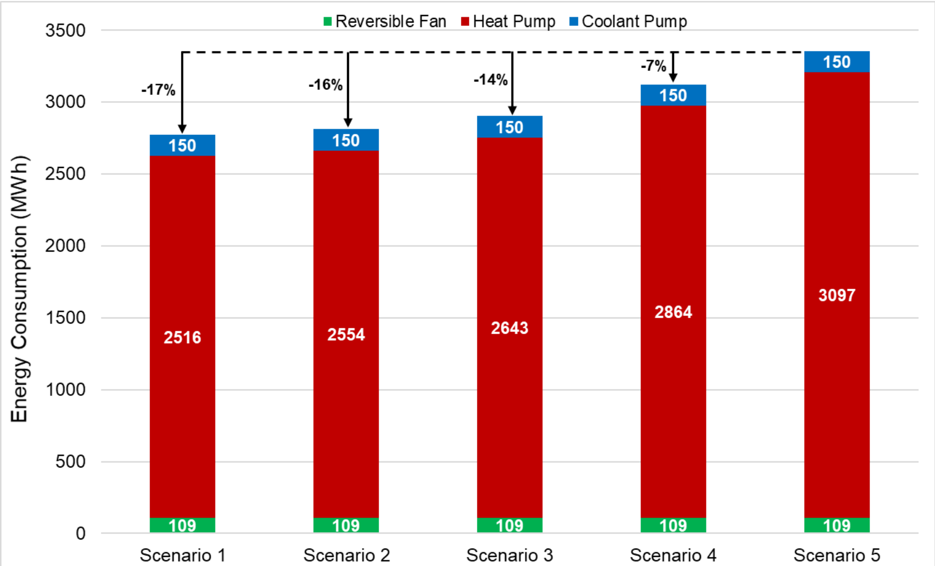

Figure 8.6 – Energy consumption breakdown per system component for each modelling scenario.

8.3.3. Heat Pump Performance

As described in section 8.3.2, the variations in energy consumption and hence system performance between the different scenarios are directly associated with the efficiency of the two-stage ammonia HP. Therefore, it is important to understand how the HP performs under different conditions, which is discussed in the following subsections.

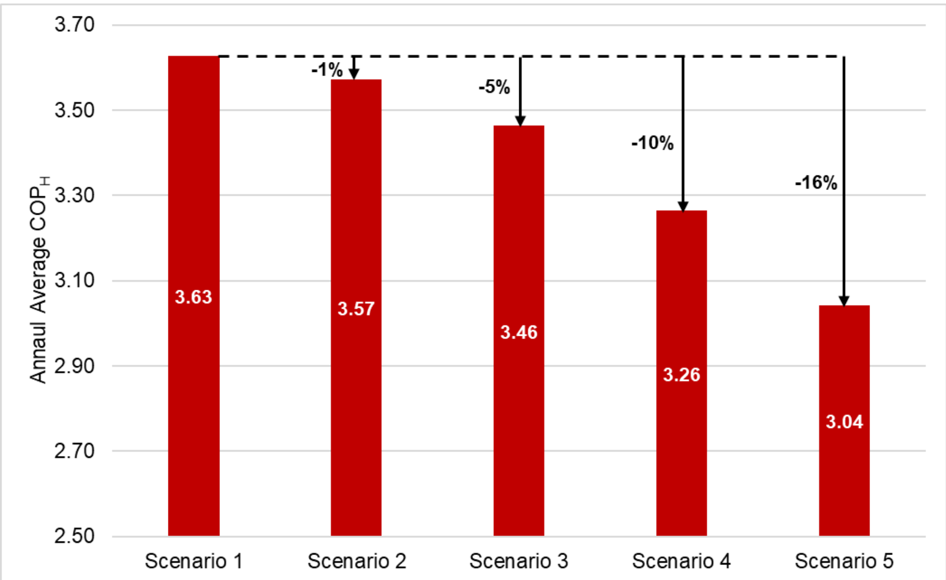

Figure 8.7 – Annual average heating COP for the different modelling scenarios from Table 8.1.

8.3.3.1. Coefficient of Performance

The energy efficiency of a HP can be expressed in terms of its coefficient of performance (COP). As introduced in section 2.6, the COP is the ratio between the useful energy output and energy input of a refrigeration system, with the useful energy being associated with the heating output in this case. As in the analysis of the $COSP_H$, the annual average COP_H is also compared for the five modelling scenarios from Table 8.1, as shown in Figure 8.7. The annual average COP_H reduces as the period of operation in Supply Mode increases, going from 3.63 for Scenario 1 down to 3.04 for Scenario 5, a reduction of 16%. If water is used as the coolant, Scenario 1 would reach a COP_H of 3.75. Therefore, the trade-off between operating with higher efficiencies and the cooling benefit only achievable in Supply Mode must be investigated to determine the optimum operation for the WHR system, which is discussed in Chapter 9.

8.3.3.2. Pressure-Enthalpy Chart

The HP behaviour under different operating conditions can also be visualised by means of a pressure-enthalpy chart, which is shown in Figure 8.8 and was plotted for the modelled pressures and enthalpies at the points highlighted in the schematic from Figure 5.13. The refrigeration cycles shown in Figure 8.8 have been plotted based upon the annual average air conditions for both Extract and Supply modes, as discussed in section 8.2. This approach highlights the gains of efficiency that can be obtained when operating with a higher evaporating temperature, which in this case corresponds to Extract Mode. It is important to note that the high stage is the same for both cycles, as the heat output and intermediate pressure were simulated as constant values (see section 5.6). The average air conditions used to represent Extract and Supply modes are listed in Table 8.2, together with the heat absorbed at the evaporator (Q_{evap}), the evaporating temperature (T_{evap}) and the COP_H for each cycle, whereas the refrigerant operating data, consisting of enthalpies (i_r), pressures (P) and mass flow rates ($\dot{m}_r$), are summarised for both cycles in Table 8.3.

Table 8.2 – Annual average air conditions used to simulate the refrigeration cycles shown in Figure 8.8.

Cycle	$T_{a,in}$ (°C)	RH_{in} (%)	T_{evap} (°C)	Q_{evap} (kW)	COP_h
Extract Mode	20.0	50	3.5	775	3.62
Supply Mode	11.3	75	-3.4	738	3.18

8.3.3.3. Monthly Heat Pump COP

The COP_H of the HP can also be expressed by its monthly average values, which are shown in Figure 8.9, along with the percentage difference in heating COP between Extract and Supply modes for each month. Similarly to what was observed for the $COSP_H$, the difference in COP_H was much higher for colder months, with an average COP_H difference of 25% for the meteorological winter, whereas the average difference for summer was 6%.

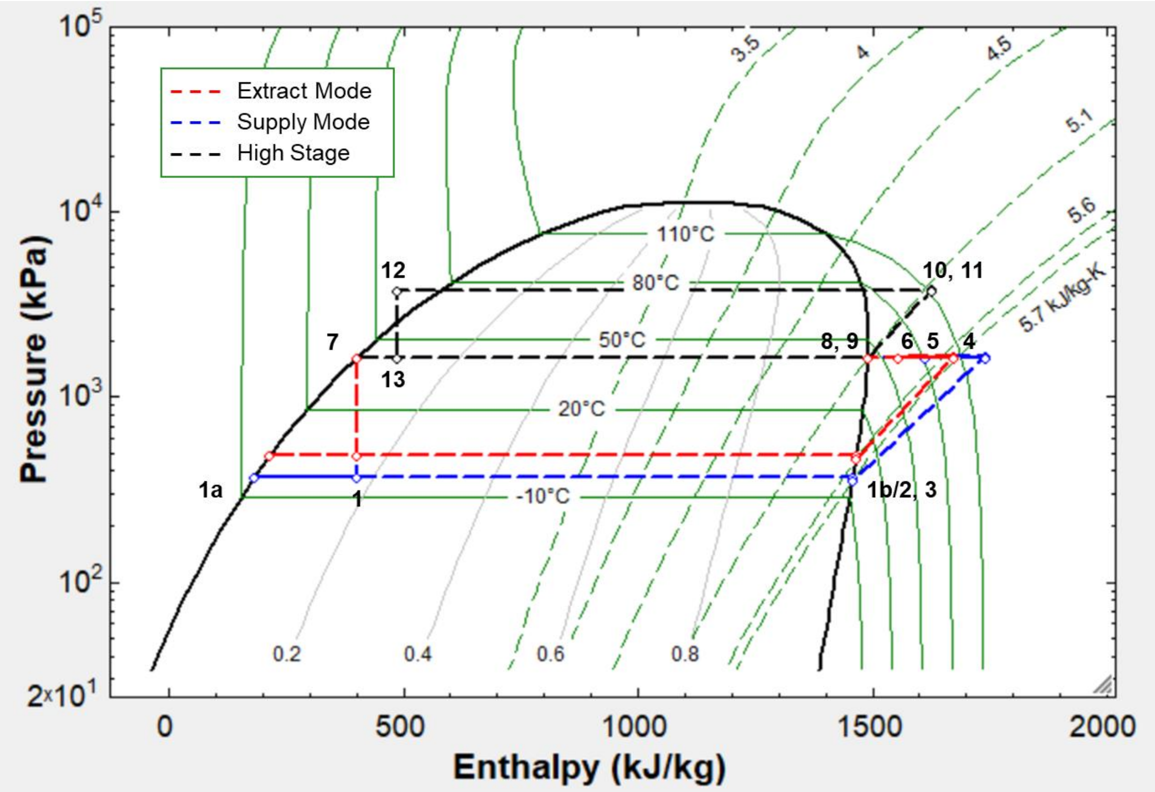

Figure 8.8 – Pressure-enthalpy chart for the HP considering typical Supply and Extract Mode operations.

Table 8.3 – Refrigerant operating data associated with the refrigeration cycles shown in Figure 8.8.

Cycle	Point	i_r (kJ/kg)	P (kPa)	$\dot{m}_r$ (kg/s)
Low stage Extract Mode	1	400.5	488.2	0.73
	1a	215.9	488.2	0.62
	1b/2	1466	488.2	0.11
	3	1466	469.4	0.73
	4	1674	1669	0.73
	5	1674	1643.7	0.73
	6	1549	1643	0.73
	7	400.5	1643	0.73
Low stage Supply Mode	1	400.5	377.7	0.70
	1a	184.2	377.7	0.58
	1b/2	1458	377.7	0.12
	3	1458	362.1	0.70
	4	1734	1669	0.70
	5	1734	1643.7	0.70
	6	1553	1643	0.70
	7	1490	1643	0.70
High stage Both modes	8	1490	1643	0.83
	9	1490	1637	
	10	1626	3811	
	11	1626	3794.1	
	12	485.5	3792	
	13	485.5	1643	

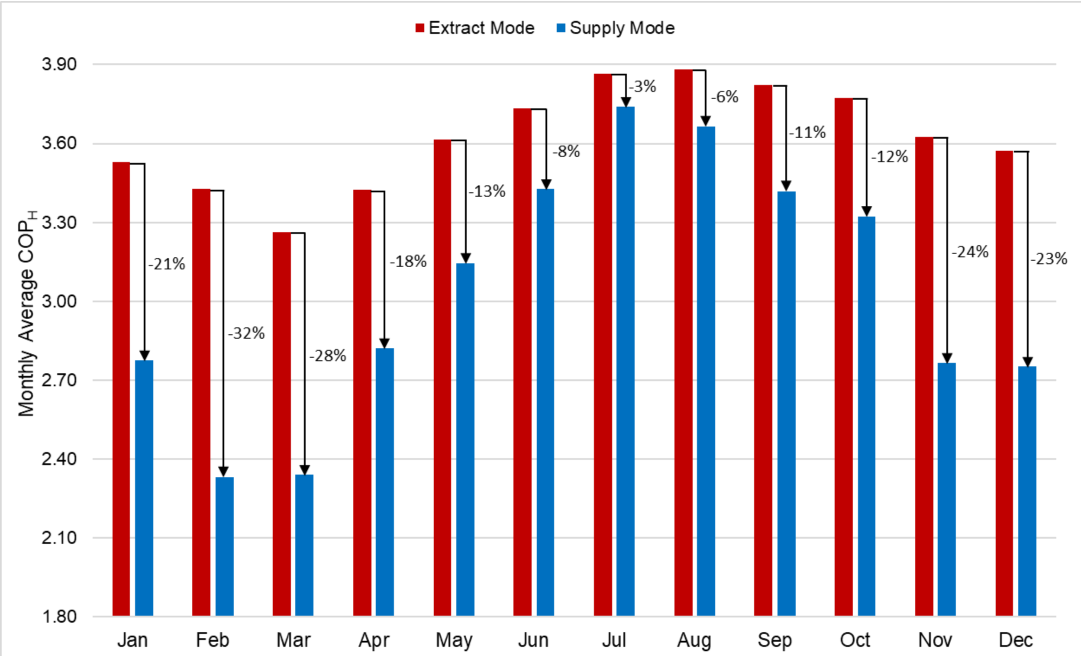

Figure 8.9 – Monthly average heating COP and its percentage differences for Supply and Extract modes.

8.3.3.4. Temperature and Humidity Impacts on COP

The difference in the calculated COP_H between Supply and Extract modes can be related to the influence of air inlet temperature ($T_{a,in}$) on HP performance, as heat source temperatures vary throughout the year and are dependent upon the operating mode of the reversible fan. Another relevant phenomenon for the analysis of heat recovery from humid air is condensation, as the presence of moisture can impact heat transfer and have an effect on important parameters of the WHR system, such as energy efficiency and cooling delivered.

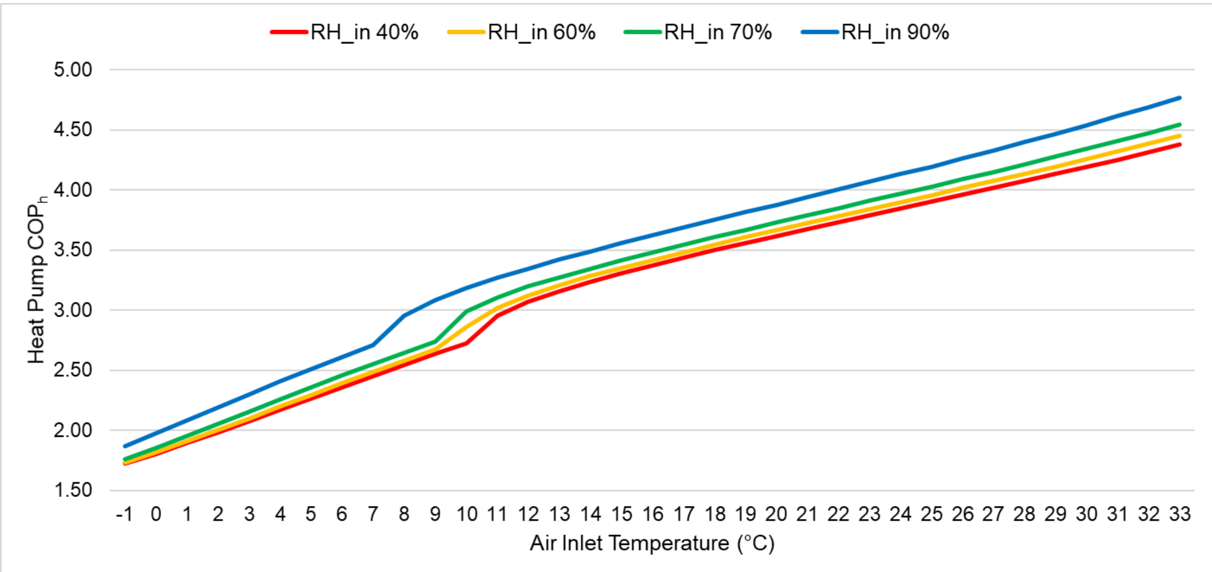

Figure 8.10 – Heating COP as a function of air inlet temperature for different RH values.

The impacts of air RH and temperature on HP performance were investigated based upon the modelled COP_H for the temperature range shown in Figures 8.1 and 8.2, and four different RH values (40%, 60%, 70% and 90%). This range covers most of the recorded values for RH_{in} and represents diverse coil conditions, varying from a fully dry coil surface for 40% RH_{in} to fully wet conditions for RH_{in} values of 90%. RH_{in} values of 60% and 70% were selected to represent partially wet conditions with different levels of condensate formation. Figure 8.10 shows the COP_H for the aforementioned temperature range and RH values, illustrating how efficiency increases with higher values of air temperature and RH. This is associated with the energy balances at the HRC and the evaporator, as warmer air means the coolant can circulate with higher temperatures, which in turn leads to an increase in evaporating temperature as well. Higher RH values also affect the energy balance as they change the conditions of the coil surface, with wet conditions leading to higher heat transfer coefficients and thus better performance.

Another relevant aspect of the curves is associated with a similar change in gradient observed for all RHs at air inlet temperatures ranging from 7 to 13°C. This is caused by a change in flow configuration due to the high coolant viscosities in that temperature range, which lead to lower Reynolds numbers and thus lower heat transfer coefficients. This is illustrated in Figure 8.11, which provides the relationship between air inlet temperature and average coolant temperatures for the analysed inlet RH values. The analysis shows that higher RH_{in} values yield higher coolant temperatures, meaning the coolant flow achieves the transitional and turbulent regimes at lower temperatures for higher values of RH_{in}. A transitional flow regime was obtained for coolant temperatures from -1.9°C to 3.9°C. This is achieved for an air inlet temperature of approximately 7°C for a RH of 90%, whilst the driest conditions (RH_{in} = 40%) led to transitional flow starting to develop at air temperatures of approximately 10°C.

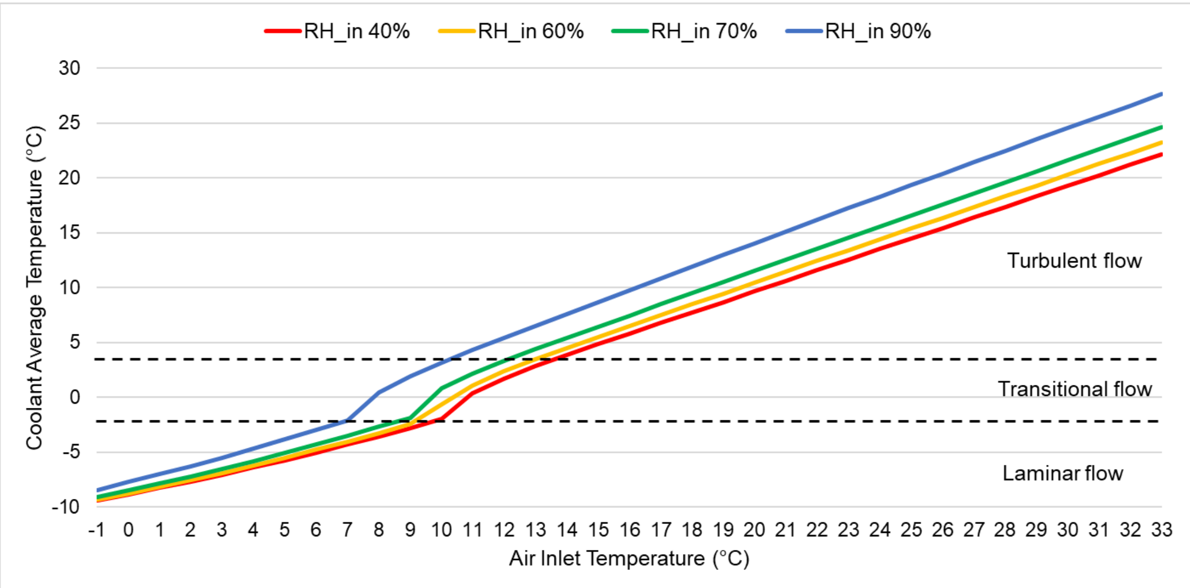

Figure 8.11 – Coolant average temperature as a function of air inlet temperature for different RH values.

As indicated in 5.4.4, convection is influenced by the type of flow that develops within the coils, which can be defined as either laminar, transitional or turbulent, with the latter being associated with higher heat transfer coefficients. As higher temperatures and RH values enhance heat transfer, the coolant can be circulated at higher temperatures without compromising the energy balances across the WHR system. A mixture of water with 30% PG concentration has high viscosities at low temperatures. As the Reynolds Number is a function of dynamic viscosity, laminar and transitional flow conditions are developed for low heat source temperatures, leading to a decrease in heat transfer coefficients when air inlet temperatures are lower. The relationship between air inlet temperature and the coolant heat transfer coefficient for different RH_{in} values is shown in Figure 8.12, highlighting the distinct curve gradients observed for the regions of laminar, transitional and turbulent flows.

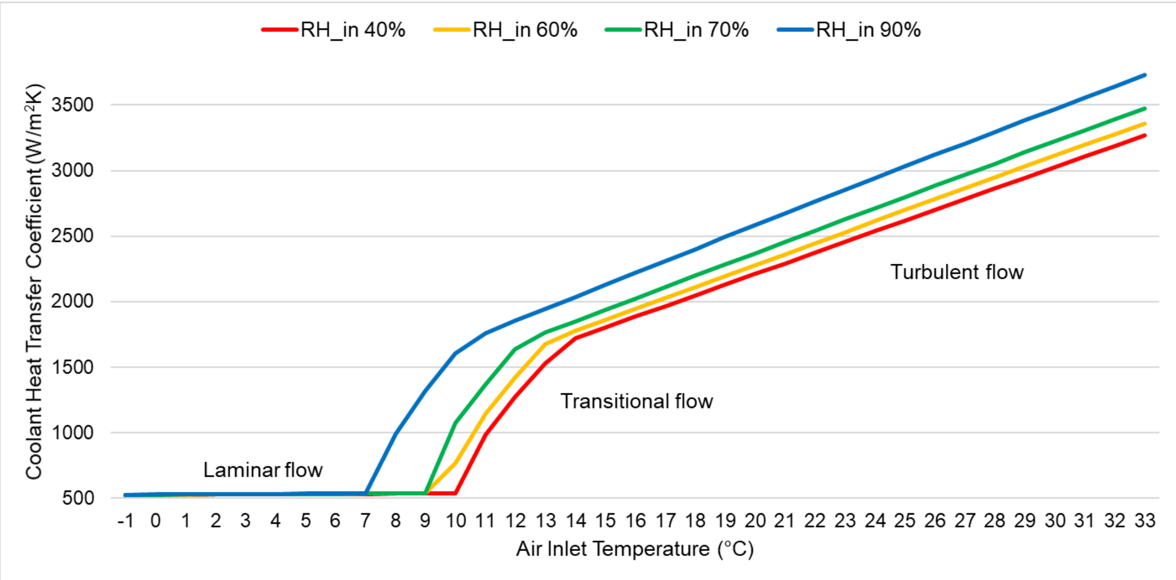

Figure 8.12 – Coolant heat transfer coefficient as a function of air inlet temperature for different RH values.

8.4. Heat Recovery

8.4.1. Coil Duty and Latent and Sensible Heat Shares

As demonstrated by Figure 8.4, the total heat recovered by the WHR system varies depending on the scenarios analysed, which are associated with different heat source conditions. As discussed in section 8.3.3.4, the occurrence of condensation due to high RH values leads to partially or fully wet surface conditions, which enhances heat transfer and affects the required coolant temperatures for heat to be recovered, impacting coil duty and system performance. This phenomenon can be represented by the shares of sensible and latent heat that are removed from the air stream during the heat recovery process. Figure 8.13 summarises the monthly heat recovered for Extract mode, highlighting the shares of latent and sensible heat, as well as the average monthly tunnel temperatures recorded, whereas Figure 8.14 provides the same information for Supply Mode heat recovery and the monthly ambient temperatures.

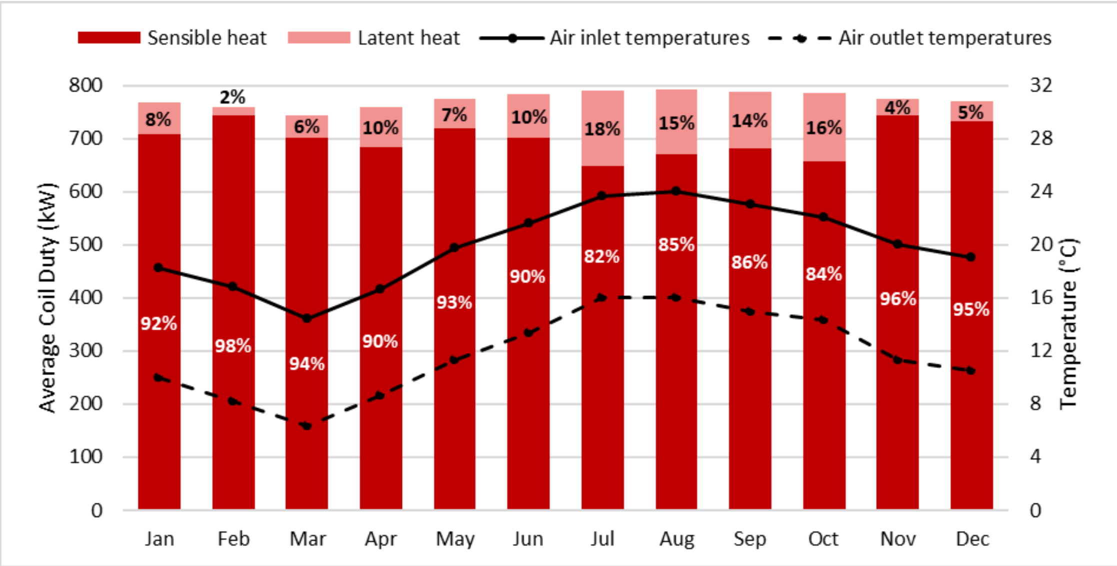

Figure 8.13 – Monthly average values for tunnel temperatures and total heat recovered in Extract Mode.

The annual average coil duty in Extract Mode was 774 kW, with an average latent heat share of 10%. The large share of sensible cooling is reflected in the air temperature difference across the coils (ΔT_a), with an annual average of 8.2 K. July and August, which had the highest monthly average temperatures of 23.6 and 24°C, respectively, also had the highest average duties of 791 and 792 kW. The hottest months also led to the highest predicted ΔT_a of 9.4 K. The highest percentages of latent heat within the total heat load were calculated for July and October, with values of 18% and 16%, respectively. The lowest value of coil duty (744 kW) was obtained for March, the coldest month in the data set. During the cold season, from November to March, the share of latent heat was lower, varying from 2% to 8% monthly.

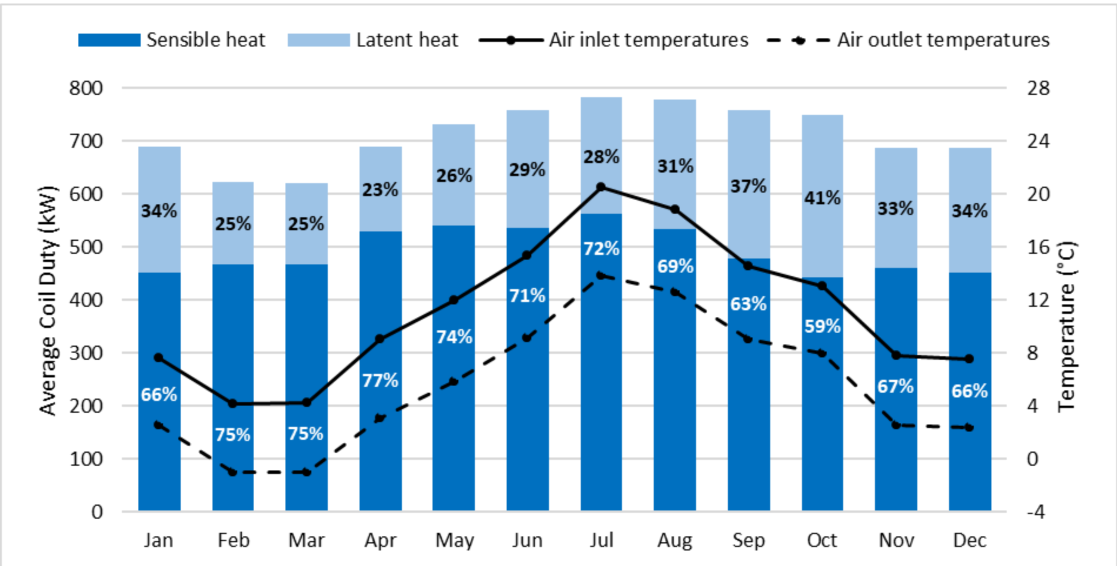

Figure 8.14 – Monthly average values for ambient temperatures and total heat recovered in Supply Mode.

Figure 8.14 shows that condensation has a much higher impact on heat recovery in Supply Mode, which had an annual average latent heat share of approximately 31%, leading to a lower average ΔT_a of 5.6 K over the year, with a minimum hourly temperature reduction of 3.5 K. This can be explained by the higher moisture contents of ambient air, which make condensation more likely to occur during Supply Mode operation. The highest percentages of latent heat were obtained for the months of September (37%) and October (41%), despite the coldest months being February and March. The annual average coil duty was also lower for Supply Mode (712 kW), a reduction of 8% when compared to the Extract Mode. The coldest months resulted in particularly low average coil duties, with 623 and 621 kW being calculated for February and March, respectively. The difference in coil duty obtained for Supply and Extract modes were not as significant for the warmest months, with July having an average duty of 782 kW in Supply, which is only 1.2% lower than the Extract Mode value.

8.4.1.1. Temperature and Humidity Impacts on Coil Duty

The analysis of the average coil duty highlights its sensitivity to the inlet air temperature. Additionally, the air RH at the coil inlet has a significant impact, as it can affect the shares of sensible and latent heat, as well as the overall heat transfer rate. This is illustrated in Figure 8.15, which shows how the coil duty increases with higher temperatures, regardless of RH values. As discussed, higher RH_{in} also leads to an increase in coil duty, which is related to higher heat transfer coefficient observed when the coil surface is wet (see Figure 8.12). The effects of flow configuration on coil duty can also be observed in Figure 8.15, as three distinct curve gradients were formed, characterising laminar, transitional and turbulent flow regions.

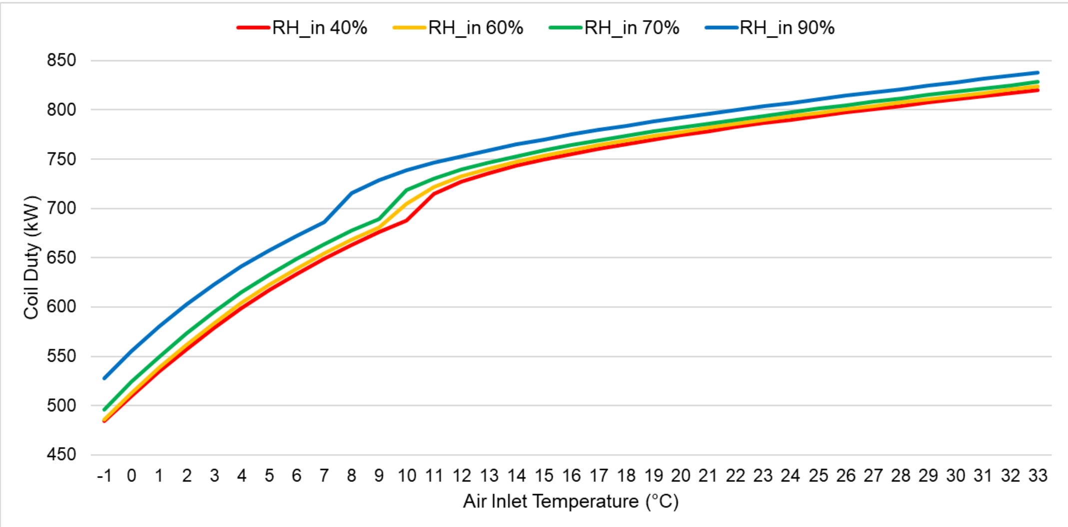

Figure 8.15 – Coil duty as a function of air inlet temperature for different RH values.

8.4.2. Condensation

The impacts of condensation can be analysed from the perspective of the sensible heat ratio (SHR), which provides the percentage of sensible heat transfer during the heat recovery process for different air inlet conditions, as illustrated in Figure 8.16. It can be seen that the SHR reduces for higher temperatures, when the coil duty is increased and condensation is more likely to take place. For a fully dry coil (RH_{in} = 40%), the heat transfer is entirely sensible for the analysed temperature range, whilst for the other conditions (partially and fully wet), the SHR decreases with an increase in temperature. Sensible heat transfer can be associated with a change in air temperature, whilst latent heat transfer is linked to the condensation of moisture onto the coil surface. This has important implications when analysing the cooling output from the WHR system, as the temperature reduction achieved is dependent upon the share of heat transfer that is sensible.

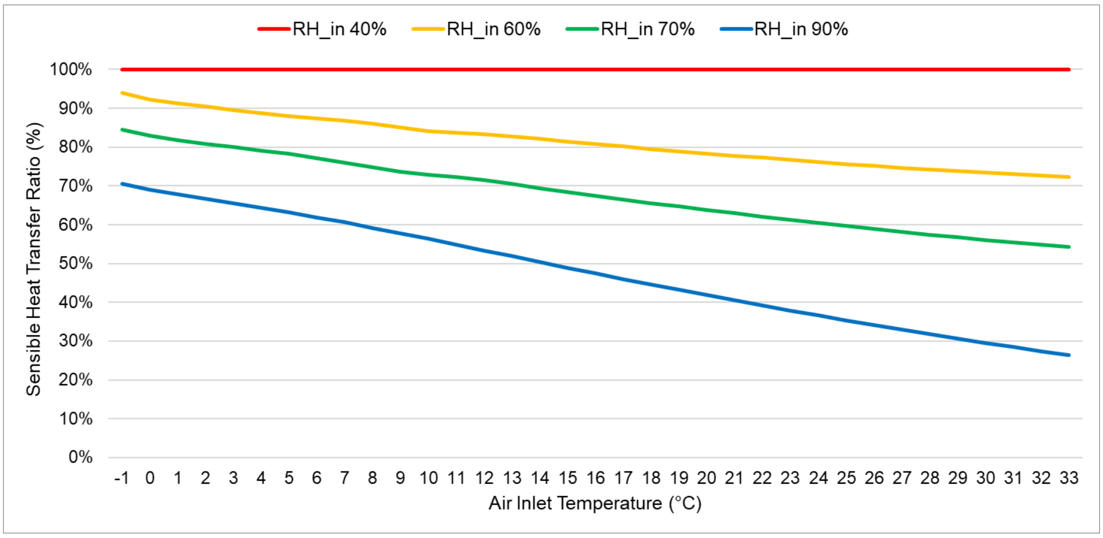

Figure 8.16 – SHR as a function of air inlet temperature for different RH values.

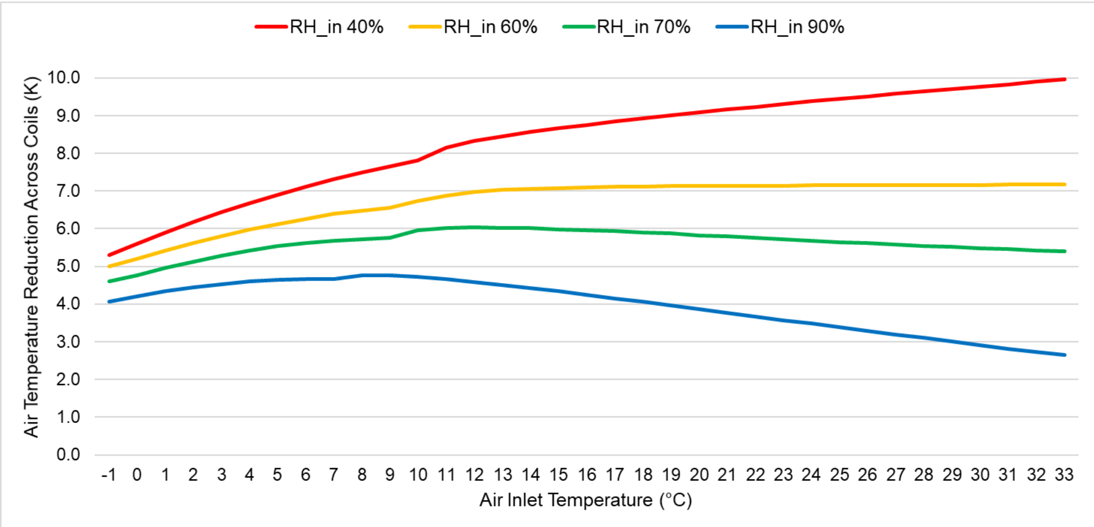

Figure 8.17 – Air temperature reduction across coils for different air inlet temperatures and RH values.

Figure 8.17 shows the air temperature reductions (ΔT_a) achieved at the coils for different air inlet temperature and RH values. As it can be seen, a fully dry condition (RH_{in} = 40%) leads to an increase in ΔT_a for higher temperatures, as they lead to an increase in coil duty, reaching values of up to 10 K. For a RH_{in} of 60%, ΔT_a also increases with temperature, going from 5 to 7.2 K, but with a smaller gradient as the share of latent heat also increases with temperature.

A similar profile is seen for RH_{in} = 70%, although ΔT_a experiences steeper reductions when the coil duty is increasing due to a decreasing SHR, which reaches its lowest value of 54% for the highest inlet air temperature (33°C). As for the fully wet condition (RH_{in} = 90%), the SHR decreases significantly at higher temperatures, reaching values as low as 26%, which leads to predominantly latent heat transfer and results in temperature reductions as low as 2.7 K for an inlet air temperature of 33°C.

Another way of representing the impacts of condensation and latent heat loads is by analysing the mass of condensate that is formed during the heat recovery process. This is illustrated in Figure 8.18, which shows the mass of condensate formed per hour for different values of temperature and RH. The mass of water condensed is inversely proportional to the SHR shown in Figure 8.16. Whilst a full dry surface is characterised by the absence of condensation, a fully wet condition with a RH_{in} of 90% can lead to up to 842 kg of water being condensed in an hour, based upon a condensation rate of 0.234 kg/s, which is calculated by the WHR model. For partially wet conditions, which are predominant in the model, the amount of water condensed is lower, but can still reach significant quantities, highlighting the importance of having a drainage system installed with the coils.

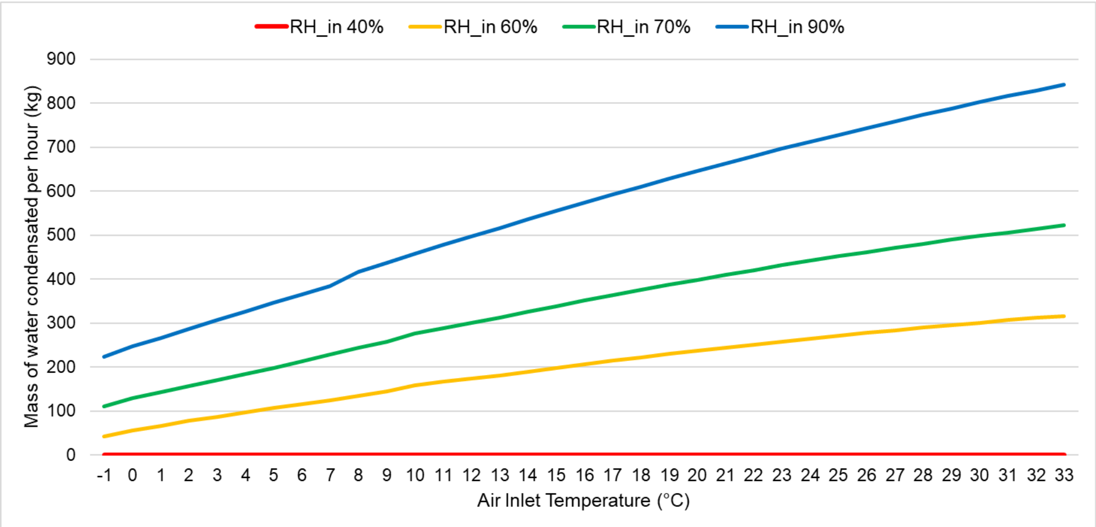

Figure 8.18 – Mass of condensate formed for different air inlet temperatures and RH values.

The occurrence of condensation varies significantly for Extract and Supply Mode operations, as latent cooling shares are much higher for the latter. This can be represented as in Figure 8.19, which shows the average mass of condensate that would be formed per hour for both operating modes over the year. As can be seen in Figure 8.19, Supply Mode leads to much greater levels of condensation, with an annual average of 311 kg per hour, or 5.19 kg per minute, and a maximum value of 433 kg per hour for October. As for Extract Mode, it leads to an average of 105 kg being formed per hour, which would be equivalent to 1.75 kg per minute, with a maximum value of 202 kg per hour being calculated for July.

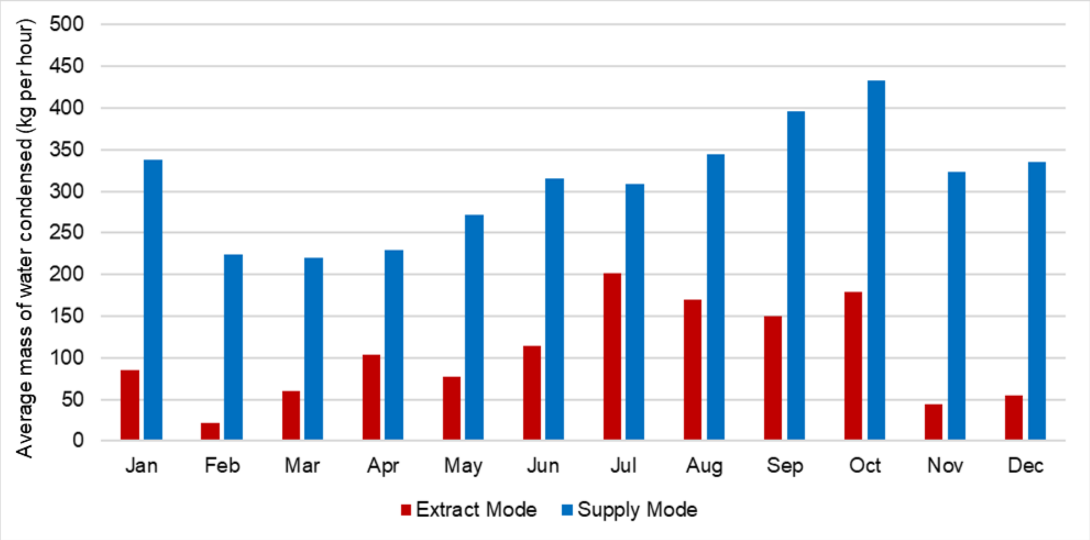

Figure 8.19 – Monthly averages for mass of condensate formed for Supply and Extract Modes.

8.4.3. Ventilation Shaft Air Flow Rates

The WHR model assumes that the volumetric flow rate of air across the coil is fixed at 70 m^3/s. In reality, this might fluctuate as a result of pressure variations caused by running trains. In order to analyse the impacts of lower flow rates on the efficiency of the WHR system, Figure 8.20 provides the $COSP_H$ for a range of air flow rates, from 70 to 35 m^3/s, considering full-load Extract Mode operation, with air temperature and RH of 20°C and 50%, respectively.

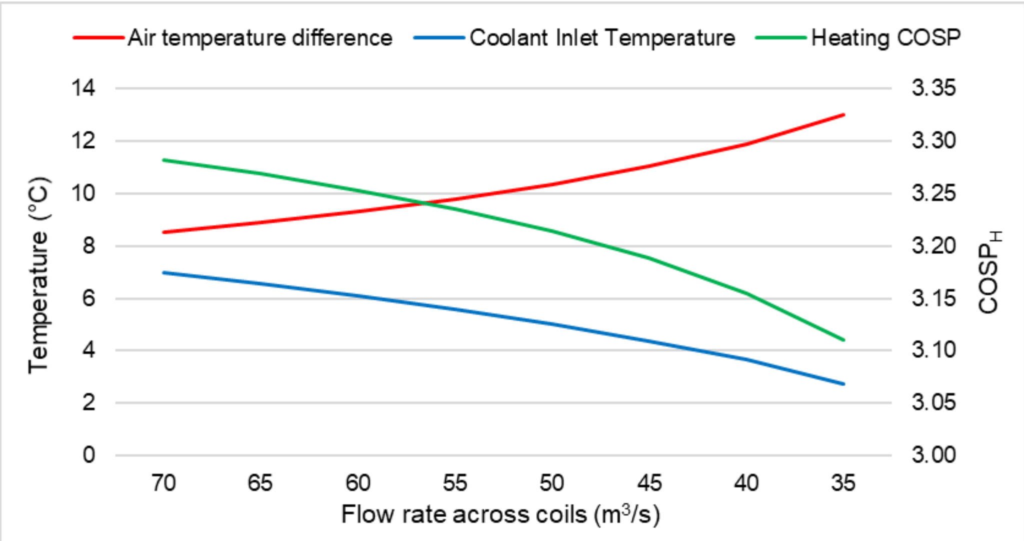

Figure 8.20 – Air temperature difference, coolant inlet temperature and heating COSP for different air flow rates.

The impacts of lower flow rates on coolant inlet temperatures, considering the PG 30% mixture, as well as on air temperature reduction (ΔT_a) across the coils were also considered. As it can be observed in Figure 8.20, lowering the flow rate to 35 m^3/s increases ΔT_a by 52%, going from 8.7 K to 13.2 K. In order to satisfy the energy balance, coolant inlet temperatures must also be lower, being reduced from 7°C to 2.75°C. This causes the HP COP to be reduced by almost 8%, leading to a 5.2% decrease in $COSP_H$, varying from 3.28 to 3.11 for the modelled conditions. Although the impact on efficiency is limited, reduced flow rates would lead to lower coolant temperatures, which could increase the risk of freezing. For particularly low temperatures, even a glycol mixture might not be enough to avoid freezing, meaning that the system would have to operate in a part-load configuration so as to avoid that risk.

8.5. Cooling Effect on the UR Environment

When operating in Supply Mode, the WHR system has the ability to provide cooled air to the UR environment, which may lead to reductions in air temperatures at tunnels and platforms. This cooling potential is the main benefit associated with Supply Mode operation, and a trade-off between system efficiency and cooling output must be analysed in order to identify the optimum operation for the WHR system. The energy efficiency of the WHR system has been discussed in section 8.3, which compared the performance of different operating modes, involving varying levels of cooling supply to the LU tunnels. This section investigates the impacts of this cooling provision based on the results of the SES UR model described in Chapter 7, which can simulate future reductions in peak temperatures for stations close to the ventilation shaft where the WHR system is installed.

8.5.1. Base Year Temperature and Humidity data

The SES model developed by TfL is calibrated to utilise 2006 weather data as the basis for simulations. As described in section 7.2.1, the UK climate projections from 2009 (UKCP09) are applied to this data set in order to model the future thermal environment of the LU, considering the influence of air and train dynamics on heat transfer within tunnels. The weather data utilised for the SES investigation were obtained from the Met Office (2019) and are shown in Figure 8.21, expressed in terms of daily average dry and wet-bulb temperatures.

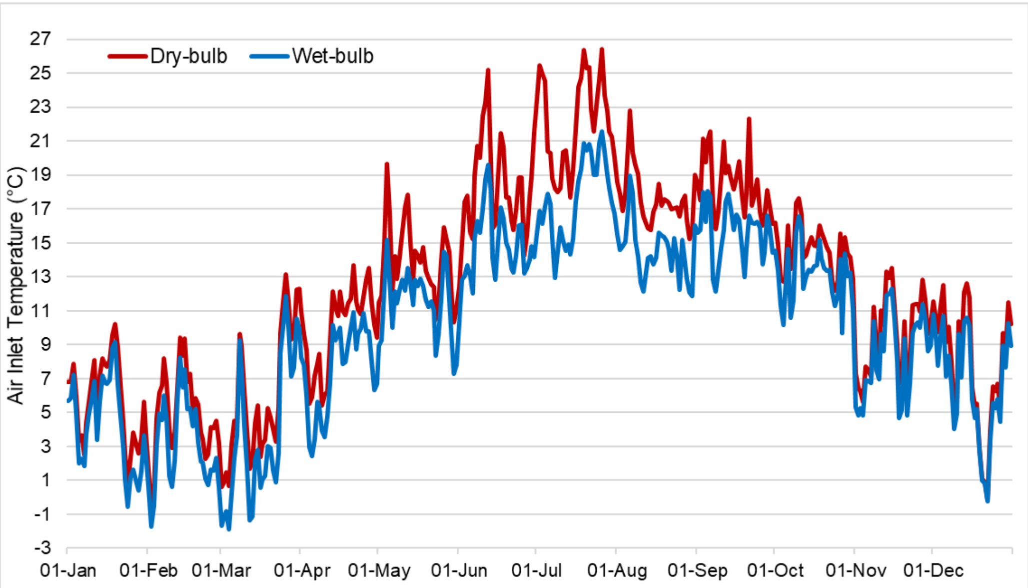

Figure 8.21 – Daily average dry and wet-bulb temperatures for the 2006 year data set (Met Office, 2019).

Similarly to the 2013/14 ambient temperature data (see Figure 8.2), the 2006 temperature data varied widely, with minimum and maximum hourly dry-bulb values of -4.2 and 33.6°C, respectively. The SD of the data set was 6.6°C, similar to the 2013/14 data, and the difference between dry and wet-bulb temperatures was low, with a yearly average of 2°C. The 2006 temperature and humidity data, as shown in Figure 8.21, were used in the WHR model to yield the conditions for air when leaving the HRC and entering the ventilation shaft.

8.5.2. Modelling Scenarios

The WHR system can provide different amounts of cooling over the span of a year depending on its operating conditions, which are associated with the possibility of operating the reversible fan in Extract and Supply modes for different lengths of time. As cooling is only provided during Supply Mode operation, different scenarios must be utilised to assess the impacts of operating in Supply during different periods. Therefore, this analysis considers the scenarios listed in Table 8.1 for the analysis of the cooling potential of the WHR system. As SES is unable to model a mixed operation of the City Road fan, Extract and Supply Mode scenarios were simulated separately and later combined by means of a weighted average, as described in section 7.5. Therefore, the SES simulations were performed for base scenarios of year-round operation in Extract and Supply modes. In order to represent the different amounts of cooling that can be delivered, different Supply Mode base scenarios were simulated by assuming that the WHR system would only provide cooling for a specific number of months, following the main modelling scenarios shown in Table 8.1. For instance, the base scenario B involves the provision of cooling only during the meteorological summer, so the coil was assumed to be running only from June to August, with ambient air being supplied for the remainder of the year. The SES base scenarios and their descriptions are provided in Table 8.4.

Table 8.4 – Base modelling scenarios for the SES investigation, based upon fan and coil operation modes.

Base Scenario		Fan Operating Conditions		Coil Operating Period	Description
		Short-term	**Long-term**		
A		Extract	Extract	N/A	Long-term and short-term simulations in Extract, coils may run but no cooling is provided.
B		Supply	Supply	Jun-Aug	Long-term and short-term simulations in Supply, cooling coils running from June to August.
C		Supply	Supply	May-Oct	Long-term and short-term simulations in Supply, cooling coils running from May to October.
D		Supply	Supply	Mar-Nov	Long-term and short-term simulations in Supply, cooling coils running from March to November.
E		Supply	Supply	Year-round	Long-term and short-term simulations in Supply, cooling coils running for the entire year.
F		Supply	Extract	Only short-term	Long-term in Extract and short-term in Supply, cooling coils running only during peak hours.
G		Supply	Supply	Off	Year-round operation in Supply, cooling coils not running (no cooling provided).

As can be seen from Table 8.4, the base scenarios A to F are used to represent different fan operating modes and cooling coil running periods. Scenarios A, B, C, D and E reflect the modelling scenarios described in Table 8.1, whereas scenario F represents the cooling effect of running in Supply Mode during the hottest period, but considering that the WHR system would operate in Extract Mode throughout the year. As for scenario G, its purpose is to serve as a basis for comparing the temperature reductions achieved with the cooling coils against the impacts of simply supplying ambient air to the tunnels, without any cooling delivery.

8.5.3. Inputs from WHR Model

The main input from the WHR model is the air temperature at the outlet of the HRC, which is considered as the supply temperature for the City Road vent shaft in the SES simulations. The supply temperature is calculated differently for short and long-term simulations, and specific values must be used for each of the scenarios in Table 8.4. The short-term simulations are carried out for the hottest week of the hottest year, meaning that supply temperatures are the same if the coil is running, particularly as it is assumed to be always on during the summer season for all scenarios involving cooling provision (B to F). In the case of long-term simulations, they represent the temperature variation over the entire year and are based upon annual averages of supply temperature, which depend upon the length of time the system is operating in Supply Mode. The supply temperatures for each base scenario from Table 8.4, calculated as described in section 7.3, are provided in Table 8.5 for morning and evening peaks associated with short and long-term simulations, considering the target year of 2030. Scenario A is not included in the analysis as Extract Mode does not involve supplying cooled air to the tunnels, which is also the case for the long-term simulations for Scenario F.

Table 8.5 – Ventilation shaft supply temperatures for the base scenarios used in the SES simulations for 2030.

Base Scenario	Long-term Supply Temperatures			Short-term Supply Temperatures	
	Annual Average	Morning Peak	Evening Peak	Morning Peak	Evening Peak
B	10.9°C	17.8°C	21.7°C	16.8°C	19.1°C
C	9.6°C	16.5°C	20.4°C		
D	8.3°C	15.1°C	19.0°C		
E	7.0°C	13.9°C	17.8°C		
F	N/A	N/A	N/A		
G	12.4°C	19.3°C	23.2°C	23.4°C	27.3°C

8.5.4. Initial Results from SES Investigation

The initial results from the SES investigation are related to the base scenarios described in Table 8.4. The analysis of the cooling performance was carried out for the stations of Angel, Old Street, King’s Cross and Moorgate. Initially, the base scenarios were compared for the 2030 temperature projections at the Northern Line platforms for the aforementioned stations.

The results for each Supply Mode scenario were compared to scenario A, which consisted of year-round operation in Extract Mode and corresponds to the baseline do-nothing scenario. The results for the target year of 2030 are provided in Figure 8.22, which shows how the cooling potential from the WHR system is quite significant, as all base scenarios that involve cooling provision led to greater temperature reductions (ΔTs) when compared to scenario G, which corresponds to year-round Supply operation without any cooling being delivered.

The cooling benefit is also quite localised, as only Angel and Old Street stations obtained significant temperature reductions, with little impact being observed for King's Cross and Moorgate stations. Compared to scenario A, the baseline Extract Mode case, and considering the scenarios with cooling provision in both short and long-terms (B, C, D and E), the average ΔT was of 5.95 K for Angel and 5.2 K for Old Street, whereas King's Cross and Moorgate had average ΔTs of 0.53 K and 0.27 K, respectively. The maximum ΔTs were achieved for scenario E; whilst Angel and Old Street had maximum ΔTs of 7.2 K and 6.3 K, respectively, while values of 0.7 and 0.5 K were predicted for King's Cross and Moorgate. Although the lower temperatures achieved for Angel can be due to its proximity to the City Road shaft, it is more likely that these results are linked to the tunnel airflow patterns, as lower temperatures were observed in the northbound direction even for scenarios without any cooling provision.

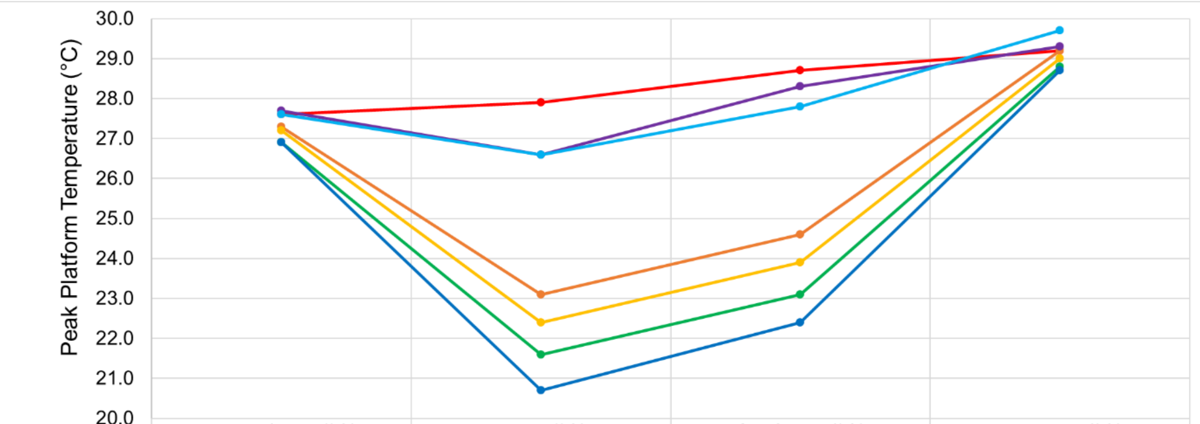

	King's Cross (°C)	Angel (°C)	Old Street (°C)	Moorgate (°C)
Scenario A	27.6	27.9	28.7	29.2
Scenario B	27.3	23.1	24.6	29.2
Scenario C	27.2	22.4	23.9	29.0
Scenario D	26.9	21.6	23.1	28.8
Scenario E	26.9	20.7	22.4	28.7
Scenario F	27.7	26.6	28.3	29.3
Scenario G	27.6	26.6	27.8	29.7

Figure 8.22 – SES simulation results for 2030, considering the base case scenarios described in Table 8.4.

The difference in cooling benefit amongst the base scenarios can be best analysed by discussing the results for a single station. When considering Angel station, the SES simulations predicted temperature reductions of up to 7.2 K (scenario E) against the baseline Extract Mode case (scenario A), which is achieved when 5,934 MWh of cooling is provided annually. Even for the lowest amount of cooling delivery (1,621 MWh/year), only during the summer months (scenario B), a reduction of 4.8 K would be achieved against the baseline scenario. The year-round supply of ambient air, represented by scenario G, which should already alleviate peak temperatures when compared to the baseline scenario, led to much lower benefits, with a ΔT of 1.3 K being observed for Angel. The long-term impacts of cooling are also quite significant, as scenario F, which involved long-term operation in Extract Mode, achieved much lower ΔTs, with a reduction of 1.3 K at Angel. This is equivalent to 27% of the ΔT achieved for Scenario B, which represents cooling provision throughout summer.

8.5.5. Results for a Combined Fan Operation

As SES is unable to model a mixed operation of the reversible fan, the combination of Supply and Extract Modes was modelled by means of a weighted average between simulations of year-round operation in each mode (see section 7.5), based upon the results shown in Figure 8.22. This involves creating a new set of scenarios, which reflect the main modelling scenarios described in Table 8.1. The new scenarios are able to differentiate the cooling benefit that is achieved through different periods of Supply Mode operation, whilst still enabling a comparison between the cooling and heating benefits associated with the WHR system. The combined operation scenarios, their corresponding base scenarios, weighting factors and results are summarised in Table 8.6. The weighting factors refer to the proportion of the year the system is running in each operating mode and are applied to the base scenarios to yield the platform temperatures for a combined operation. All results are provided in terms of peak platform temperatures for the target year of 2030 and are illustrated in Figure 8.23.

Table 8.6 – Different modelling scenarios for a combined fan operation, based upon weighted averages of year-round Extract and Supply Mode results.

Scenario	Base Scenarios (Figure 8.22)	Fan Operation	Weighting Factors		Peak Platform Temperatures in 2030			
			Extract	Supply	King's Cross	Angel	Old Street	Moorgate
1	A	12E/0S	1	0	27.6°C	27.9°C	28.7°C	29.2°C
2	A + B	9E/3S	0.75	0.25	27.5°C	26.7°C	27.7°C	29.2°C
3	A + C	6E/6S	0.5	0.5	27.4°C	25.2°C	26.3°C	29.1°C
4	A + D	3E/9S	0.25	0.75	27.1°C	23.2°C	24.5°C	28.9°C
5	E	0E/12S	0	1	26.9°C	20.7°C	22.4°C	28.7°C

The weighted average approach combines the long-term effects of Supply and Extract Mode operations, providing smoother temperature reductions than the base scenarios shown in Figure 8.22. As expected, the highest temperature reductions were observed for scenario 5, which involves year-round supply of cooling and is equivalent to the base scenario E, with calculated ΔTs of 6.3 and 7.2 K for Old Street and Angel stations, respectively. For scenarios 2, 3 and 4, which involve a combination of Extract and Supply modes, the average ΔTs, considering both adjacent stations, were of 1.1, 2.6 and 4.5 K, highlighting how the cooling benefit can be increased if the system operates for longer periods in Supply Mode.

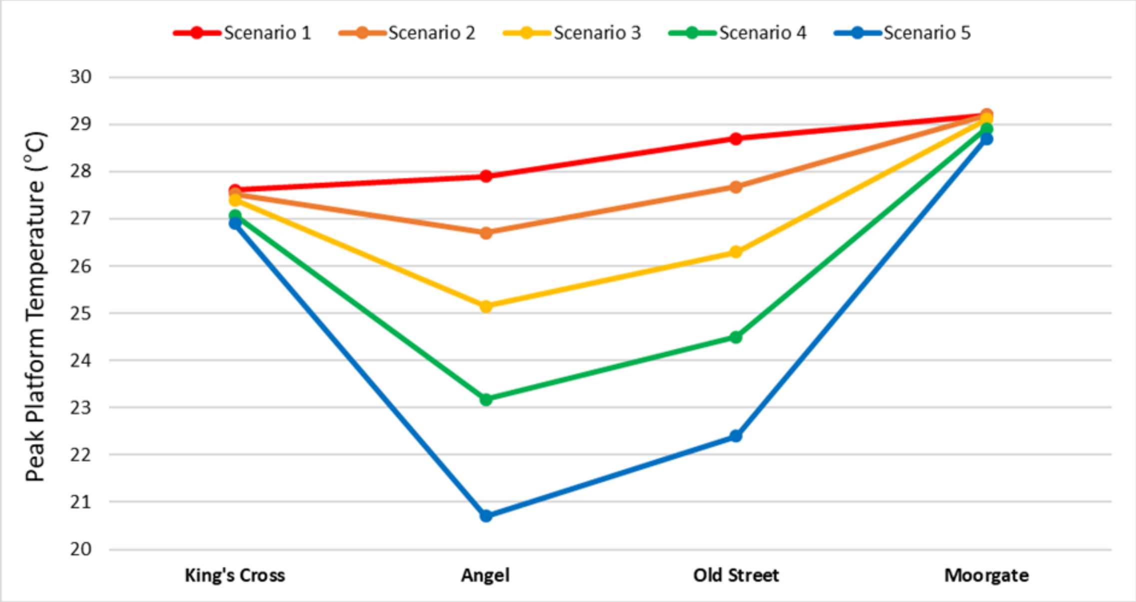

Figure 8.23 – Peak platform temperatures for the year of 2030 based upon weighted averages of Extract and Supply Mode SES simulations.

8.5.6. Peak Platform Temperatures in 2050

The cooling benefit is also analysed in terms of the projected peak platform temperatures for the year 2050, which demonstrates how the WHR system could help alleviating the effects of a warming climate. This investigation was carried out for 2050 scenarios equivalent to Scenarios 1 and 2 from Table 8.6, which represent, respectively, the baseline case and the provision of cooling only during the summer months, the most critical period in terms of thermal comfort in the LU. In order to model network conditions in 2050, the supply temperature inputs were adjusted to consider the expected increase in ambient temperatures from the UKCP09, and these are shown in Table 8.7 for Scenario 2, as Scenario 1 does not involve any cooling provision. The results obtained for the target years of 2030 and 2050 are then compared in Figure 8.24.

Table 8.7 – Ventilation shaft supply temperatures for Scenario 2, as used in the SES simulations for 2050.

Long-term Supply Temperatures			Short-term Supply Temperatures	
Annual Average	**Morning Peak**	**Evening Peak**	**Morning Peak**	**Evening Peak**
10.9°C	17.9°C	21.8°C	17.6°C	19.9°C

Based upon the $COSP_H$ values indicated in Figure 8.3, Scenario 2 would only cause an efficiency reduction of 1.2% compared to year-round operation in Extract Mode. The simulation results show that average peak platform temperatures are expected to increase by 2.7 K for the analysed stations between 2030 and 2050. These projections are associated with Scenario 1, where the fan would operate solely in exhaust and no cooling would be delivered to the LU tunnels. If cooling is provided during the summer months (Scenario 2), the average temperature increase by 2050 can be limited to 1.9 K against a scenario without cooling provision. If only the adjacent stations to the vent shaft are considered, where the cooling impact is highest, the rise in temperature would then be reduced to 1.3 K. For Angel station in particular, the provision of cooling during the summer months could potentially keep the evening peak temperature in 2050 within 1 K of the value predicted for 2030.

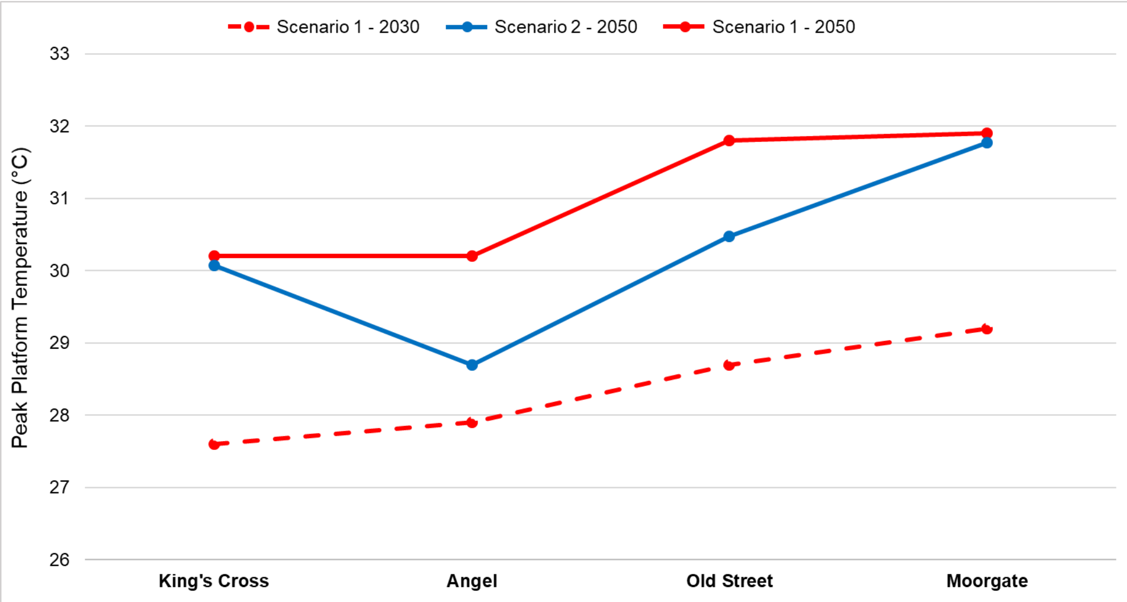

Figure 8.24 – SES simulation results for 2030 and 2050, considering the baseline Extract Mode (Scenario 1) and cooling provision during the summer months (Scenario 2).

The results for both 2030 and 2050 simulations demonstrate how the cooling provided by the WHR system could have significant impacts in terms of reducing LU station temperatures during peak service hours. These temperature reductions might lead to several tangible benefits for the LU, such as increasing the wellbeing of passengers and staff (Wen et al., 2020), reducing risk of train delays caused by high temperatures (Greenham et al., 2020), as well as enabling potential increases in service frequency and ridership.

8.6. Coolant Fluid and Freeze Protection

As described in section 5.5, the coolant represents the secondary working fluid utilised to transport the waste heat recovered at the HRC to the two-stage HP, where the heat is upgraded to an appropriate temperature for distribution. Different types of coolants can be utilised depending on the typical operating temperatures of the system. According to Melinder (2007), the secondary working fluid should have freezing security, good transport and heat transfer abilities, as well as low viscosities at the operating temperature range, which can affect the type of flow and the pressure drop in the system. The original design for the WHR system was based upon utilising water as the coolant (Islington Council, 2019). However, the possibility of operating in Supply Mode for longer periods throughout the year means that the coils would be exposed to lower temperatures, increasing the risk of coolant freezing.

Although ambient temperatures are below the freezing point of water only for 1% of the year, coolant temperatures must reach even lower values for heat to be captured from the airstream. Therefore, it might be necessary to use a freezing-point depressant (antifreeze) to keep the coolant from freezing within the coils under these conditions. However, the use of antifreeze mixtures comes at a cost of lowering the efficiency of the WHR system, as these mixtures generally have worse heat transfer properties than pure water. This section aims to compare the impacts of operating with antifreeze mixtures as opposed to the original system design.

8.6.1. Original System Design

The original system design was based upon utilising water as the coolant. In this case, the risk of freezing would be avoided by deploying an electric immersion heater, which would keep the coolant from freezing and damaging the HRC. This freeze protection (FP) circuit would only be operational for periods when the HP is switched off and ambient air temperatures are low enough to freeze the coolant if thermal equilibrium is reached. If water is to be used as the coolant, the energy consumption associated with the FP circuit (W_{FP}) must be included in the analysis of system performance, as shown by Equation 8.1, which is analogous to Equation 5.4 and calculates the energy used to keep the coolant at a given FP threshold ($T_{c,FP}$) above the air inlet temperature ($T_{a,in}$).

$$W_{FP} = \dot{m}_c C_{p,c}\left(T_{c,FP} - T_{a,in}\right) \tag{8.1}$$

Under these conditions, the HRC will therefore act as heating coils, which can be simulated with a dry surface. The modelling of the FP circuit must also define a logical framework for when the immersion heater should be utilised. This is based upon two additional temperature thresholds, one for the coolant temperature below which the HP stops ($T_{c,HP}$) and another being the air temperature at which the FP circuit is turned on ($T_{a,FP}$). Initially, the model runs normally based upon the air inlet conditions. If the energy balance calculates that the lowest coolant temperature within the system ($T_{c,in}$) is below the operational threshold of the HP ($T_{c,HP}$), the HP will be shut down. If the HP is not operational, the air inlet temperature must then be analysed against the FP starting threshold ($T_{a,FP}$). If $T_{a,in}$ is lower than $T_{a,FP}$, the immersion heater is turned on to heat the coolant so that its temperature at the coil outlet ($T_{c,out}$) is equal to $T_{c,FP}$. The flowchart shown in Figure 8.25 summarises the control procedure used by the FP model.

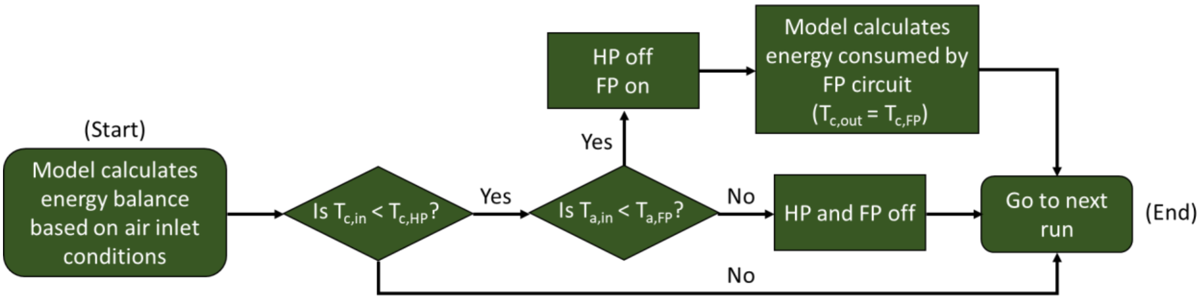

Figure 8.25 – Flowchart showing the control procedure of the FP model.

The energy consumption of the WHR system will vary depending upon the air conditions in both Extract and Supply modes, as well as on the thresholds chosen for the stopping and starting procedures for the HP and the FP circuit, respectively. Table 8.8 summarises different threshold values that will be modelled as part of the FP strategy. The initial HP shutdown threshold ($T_{c,HP}$) of 4°C is based upon the original system design (Islington Council, 2019). Additional scenarios with thresholds of 0°C and 1°C were also included to analyse the impact of lowering the threshold on system downtime and COP. For the FP circuit, values of 0°C and 1°C were also utilised to represent the starting threshold associated with the air temperature ($T_{a,FP}$) and the shutdown threshold associated with the coolant temperature ($T_{c,FP}$). In section 8.6.3, the overall system performance will be calculated for each of the scenarios shown in Table 8.8, both in Supply and Extract modes, and then compared against an antifreeze coolant counterfactual (see section 8.6.2).

Table 8.8 – Analysed temperature thresholds for the HP and FP control procedures.

Scenario	Coolant	$T_{c,HP}$ (°C)	$T_{a,FP}$ (°C)	$T_{c,FP}$ (°C)
W1	Water	0	0	0
W2	Water	1	1	1
W3	Water	4	0	0
W4	Water	4	1	1

8.6.2. Alternative Coolants

Melinder (2007) compared the performance of different aqueous solutions that can be used as secondary working fluids. Melinder's work included a comparison of different additives that could be used for a ground-source HP with operating temperatures ranging from -4 to 4°C. In this case, the author compared the performance of mixtures with different concentrations of ethyl alcohol (EA), propylene glycol (PG) and glycerol (GL). Other additives commonly utilised as antifreeze include salts, such as calcium chloride ($CaCl_2$) and sodium chloride (NaCl), as well as aqueous substances like ethylene glycol (EG) (ASHRAE, 2017). Melinder (2007) compared the aforementioned antifreeze mixtures based upon their volumetric heat capacity, kinematic viscosity, Reynolds number, pumping power requirements and heat transfer coefficients. Although the results showed that EA had, in general, the best volumetric heat capacity and viscosity among the coolant options analysed, it was highlighted that the correct coolant choice depends upon the specific operating conditions of each system, as well as on other factors such as cost and safety.

Therefore, simulations were carried out with the WHR model to analyse how different coolant alternatives would perform in terms of the $COSP_H$ and critical thermophysical properties under full-load conditions. These simulations considered the air temperature range shown in Figure 8.1 and Figure 8.2, and the annual average RH of 75% for ambient air, i.e. in Supply Mode operation, as described in 8.2. The comparison only considered aqueous antifreeze substances, as salts are highly corrosive with ferrous materials (Melinder, 2000). For that reason, the coolant options analysed consist of water with different concentrations of EA, EG, GL and PG. These were chosen as they were proposed by Melinder (2007) for a ground-source heat pump (GSHP) system, with the addition of EG, which is one of the most common substances used as a freezing-point depressant in refrigeration systems (ASHRAE, 2017).

Table 8.9 – Different coolant options, their freezing point and minimum operating air temperatures.

Coolant	Concentration in water (%)	Freezing point (°C)	Minimum air temperature (°C)
Ethyl Alcohol (EA)	10	-4.4	6.0
	20	-11.1	-1.0
	30	-20.1	
Ethylene Glycol (EG)	10	-3.4	7.0
	20	-8.0	2.0
	30	-14.6	-1.0
Glycerol (GL)	10	-2.3	8.0
	20	-5.6	5.0
	30	-9.7	1.0
Propylene Glycol (PG)	10	-2.9	7.0
	20	-7.2	3.0
	30	-12.8	-1.0
Pure Water	-	0	10.0

Initially, the different antifreeze substances were compared based upon their freezing point for different mass concentrations, as shown in Table 8.9, which also provides the minimum air temperature that each mixture would be able to operate at without freezing, as calculated by the energy balance from the WHR model. As seen in Table 8.9, utilising pure water as the coolant would mean that the system would be unable to operate for air temperatures below 10°C. For EG and PG, the system would be able to operate for the entire temperature range with a concentration of 30%. This can also be achieved with a concentration of 20% of EA, whilst GL would not be able to operate with air temperatures lower than 1°C. Therefore, a concentration of 30% will be considered for comparing all coolant mixtures except for EA, for which a concentration of 20% will be adopted in the following analyses. Figure 8.26 provides the $COSP_H$ for different air temperatures and the average ambient RH of 75%, obtained from the WHR model based upon the different coolant alternatives analysed.

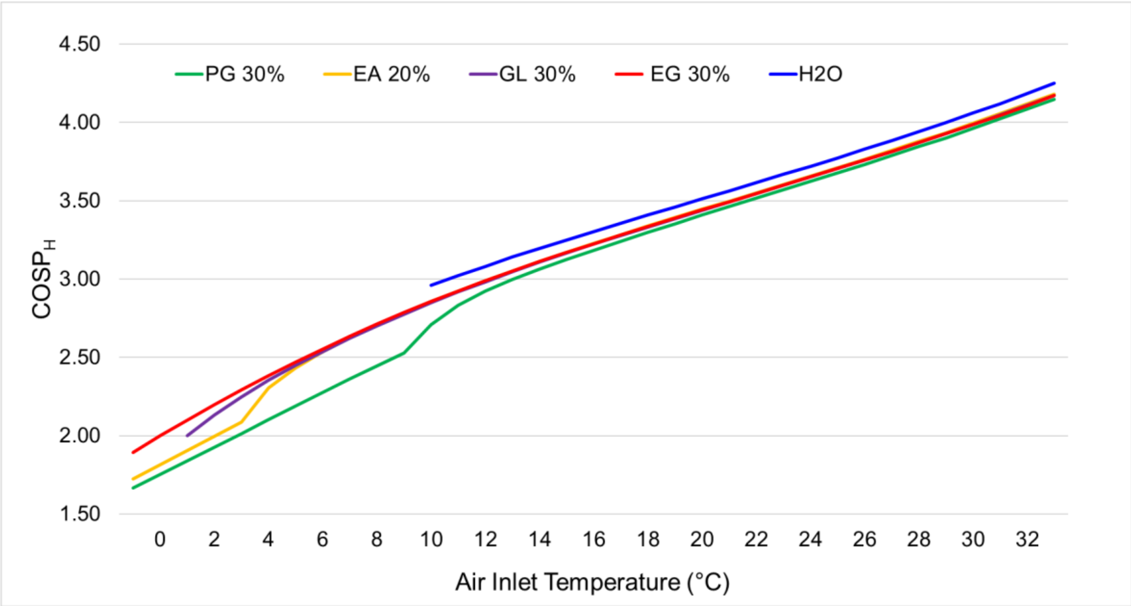

Figure 8.26 – $COSP_H$ for different coolant alternatives as a function of air inlet temperature for a RH of 75%.

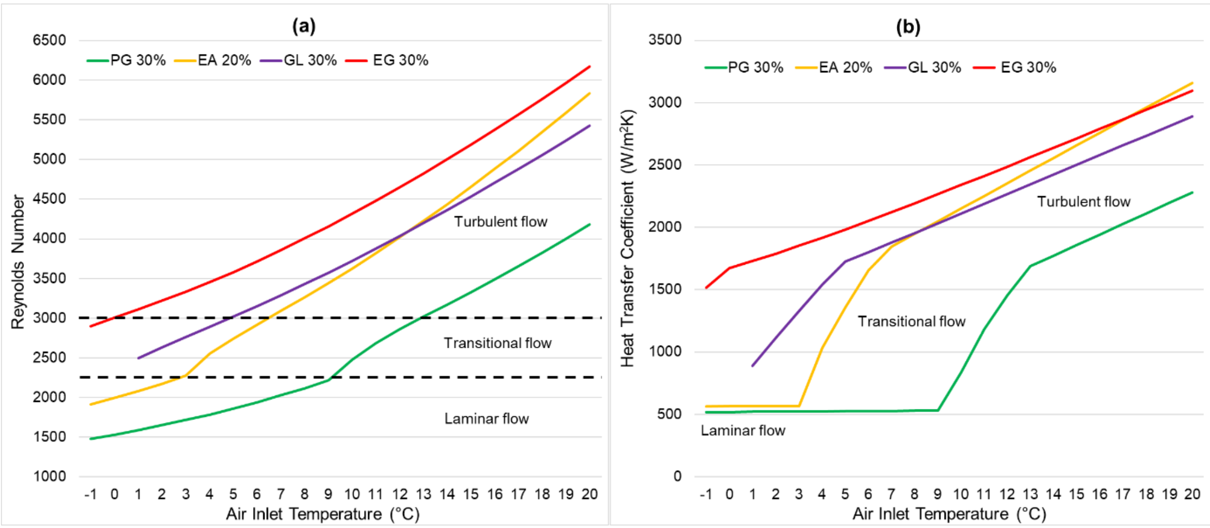

Figure 8.27 – Reynolds numbers (a) and heat transfer coefficients (b) for different coolant alternatives and air inlet temperatures.

As seen in Figure 8.26, water provides the best $COSP_H$, but would not be able to operate in a full-load condition for air temperatures below 10°C, as shown also in Table 8.9. The different mixtures behave similarly for higher air temperatures, above 13°C, with PG providing a slightly lower $COSP_H$. At lower temperatures, the effects of higher viscosities on the Reynolds number start to show. Transitional and laminar flow lead to lower heat transfer coefficients, meaning that higher temperature drops across the HRC are observed, resulting in lower coolant temperatures and a reduction in system efficiency. Laminar flow is observed for the PG and the EA mixtures for temperatures below 9 and 4°C, respectively, leading to lower efficiencies below those thresholds. The EG mixture only reaches a transitional flow at temperatures below 0°C, whilst GL is not able to operate with temperatures below 1°C and would lead to transitional flow for temperatures lower than 4°C. Figure 8.27 shows the Reynolds number (Re) and the coolant heat transfer coefficient (h_c) for the analysed coolant mixtures, highlighting how the different flow types affect heat transfer, which in turn impacts coolant temperatures and $COSP_H$ values.

Overall, the performance of each antifreeze mixture can be summarised by calculating a weighted average of the $COSP_H$ for the ambient temperature distribution shown in Figure 8.2. PG had the lowest average $COSP_H$ of 2.79, which is largely due to its high viscosity, which led to a greater likelihood of occurrence of laminar and transitional flows. EG achieved the best performance, with an average $COSP_H$ of 2.90, whilst both EA and GL had average $COSP_H$ values of 2.87. However, the choice of coolant is not only based upon their thermophysical properties, as other characteristics, such as toxicity, flammability, corrosiveness and cost, are equally relevant. For instance, EG is highly toxic and its use should be avoided for applications involving possible human contact (ASHRAE, 2017), such as the case for this WHR system, which captures waste heat from the ventilation infrastructure of a mass transportation system.

Despite achieving better performances than PG, EA and GL are not as widely used due to drawbacks associated with safety and costs. The main setback to the adoption of GL is its higher freezing points, meaning there is still risk of damage to the HRC due to coolant freezing on particularly cold days, even with a high mass concentration of 30%. Furthermore, the use of GL has been discontinued over the years in favour of EG due to cost considerations (Mbamalu, 2013), making it less common in refrigeration systems. On the other hand, EA is highly flammable, particularly when concentrated, and fire precautions must be in place when handling this substance (Stoecker, 1998). Heinonen et al. (1997) compared the performance of different antifreeze mixtures and showed that EA had high corrosion rates against copper, which is the material used for the HRC. It was also reported that PG had extremely low environmental, health, fire and corrosion risks (Heinonen et al., 1997). For those reasons, this investigation concluded that a water/PG mixture, with a concentration of 30%, was most appropriate to use as the coolant counterfactual to water when analysing system performance, as discussed in section 8.6.3.

8.6.3. Performance Comparison

After introducing the original system design and comparing different coolant alternatives, it was necessary to evaluate the benefits of using an antifreeze mixture against the original design. As mentioned in the previous section, PG with a concentration of 30% was chosen as the alternative coolant as it is a non-toxic, inflammable and non-corrosive substance, which can sustain the lower operating temperatures experienced in Supply Mode. The performance of the WHR system with the alternative coolant were analysed for the modelling scenarios 1 (year-round Extract Mode) and 5 (year-round Supply Mode), as described in Table 8.1, which represent the most extreme scenarios in terms of system performance and can highlight the advantages and disadvantages of utilising either one of these coolants (water or PG).

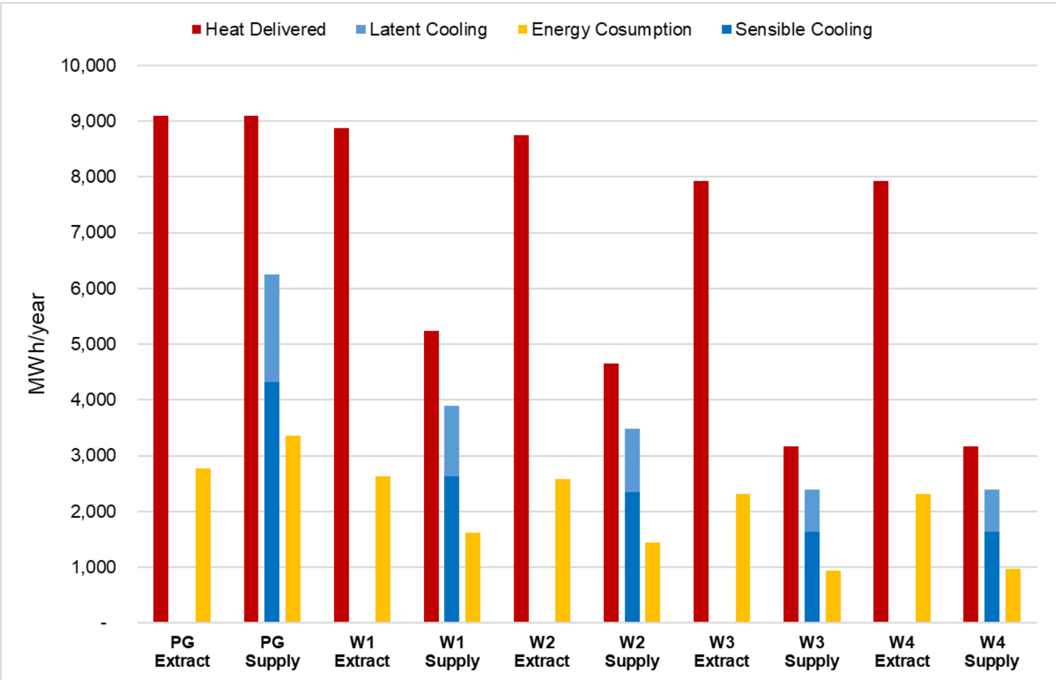

Figure 8.28 – Annual energy consumption and total heating and cooling for different coolants, control procedures and operating modes.

The different operating thresholds defined in Table 8.9 were also analysed, comparing how different control procedures, with varying temperature limits, would affect the efficiency and downtime of the WHR system. Figure 8.28 shows the annual performance of the WHR system in terms of its heating and cooling outputs, as well as its energy consumption, including the FP circuit if applicable. The cooling output was split between sensible and latent cooling to highlight the useful cooling produced, i.e. associated with a sensible cooling effect. The annual COSP and HP downtime for each scenario analysed is provided in Table 8.10.

Table 8.10 – COSP and HP downtime for the different scenarios analysed in Figure 8.28.

Scenario	PG		W1		W2		W3		W4	
	Extract	Supply	Extract	Supply	Extract	Supply	Extract	Supply	Extract	Supply
COSP	3.29	2.79	3.40	3.27	3.41	3.30	3.44	3.39	3.44	3.39
Downtime	0%	0%	2%	42%	4%	49%	13%	65%	13%	65%

Although utilising water can increase the COSP of the WHR system, it leads to an increase in system downtime, which is particularly critical when the system is operating in Supply Mode, as shown in Table 8.10. Even for the lowest HP shutdown temperature threshold ($T_{c,HP}$ = 0°C), corresponding to scenario W1, the system would not be able to operate in Supply Mode for

42% of the year, with downtime increasing with higher temperature thresholds. For instance, the amount of heat delivered in Supply Mode would be reduced by 49% for scenario W2 and 65% for scenarios W3 and W4, when compared to using a PG based coolant (see Figure 8.28). Extract mode is not as affected, particularly if the control procedure associated with scenario W1 is used, where the increase in COSP might make up for the downtime of 2%. Extract Mode is more significantly affected for the highest temperature threshold of 4°C in scenarios W3 and W4, which would lead to 13% less heat being supplied.

From the perspective of cooling delivery, which is only obtained when the system operates in Supply Mode, it can be seen from Figure 8.28 that the amount of cooling being supplied with scenario W1 is only 62% of what could be achieved using a PG mixture. For scenarios W2 and W3/W4, the cooling output would represent 56% and 38%, respectively, of the amount calculated for the PG counterfactual. This highlights the importance of using antifreeze coolants in order to maximise the cooling benefit that can be achieved with the system. In terms of the FP circuit, it would only be used during particularly cold days, presenting a minor fraction of the total energy consumption for the water scenarios, with a maximum share of 3% being observed for Scenario W4.

8.7. Conclusion

This chapter discussed the results from both the WHR and UR models, investigating the impacts of Extract and Supply Mode operations from the perspectives of energy efficiency and cooling potential. In Extract Mode, the annual average heating COSP can reach up to 3.38 depending on coolant choice. It has been observed that Supply Mode would increase system energy consumption by almost 21% for a year-round operation, as the WHR system would be subject to lower temperatures and require an antifreeze mixture to be used as coolant, with PG being identified as a suitable substance for this purpose. Supply Mode increases the share of latent cooling annually, leading to greater condensation rates at the HRC and lower temperature reduction across the coils.

However, significant cooling benefits can still be achieved, with a potential to reduce peak temperatures by up to 7.2 K for adjacent stations in 2030, which are associated with the potential of the WHR system to provide up to 5.93 GWh of cooling to the LU tunnels annually. One risk identified regarding Supply Mode operation is the reduction of system efficiency, as lower temperature air is used as the heat source. This could increase running costs for system operators, and a balance between cooling and heating benefits must be sought. The economic and environmental impacts of operating in Supply and Extract modes are discussed in detail in Chapter 9, providing insight into how leveraging the cooling benefit can be essential to making WHR an attractive opportunity for the future in the UK.

9. Evaluating the Benefits of WHR from Underground Railways

9.1. Introduction

This chapter describes an analysis of the potential benefits that could be achieved through waste heat recovery (WHR) from underground railways (URs). Based upon the concept and design of the Bunhill WHR system, this investigation is centred on a case study of a waste heat based HP connected to residential buildings via a district heating network (DHN). The case study aims to reproduce the operation of a heat network that runs entirely based on the WHR system, as opposed to the analyses of Chapter 8, which correspond to a continuous base-load operation of the heat pump (HP). The efficiency of the WHR system is evaluated considering the elements of flexibility and cooling, and its overall performance is then compared to gas boilers and air-source heat pump (ASHP) counterfactuals, in terms of potential carbon and cost savings, which are then applied to calculate the levelised cost of heat (LCH) and the carbon abatement costs (CAC) associated with each of the scenarios analysed. Furthermore, the analysis also accounts for the benefits of WHR to the wider energy system, in terms of reducing peak electricity demands, as well as its potential to tackle pollutant emissions, showcasing the full benefits that can be brought on by utilising waste heat from railway tunnels.

9.2. The Case Study

As mentioned previously, the case study used for this investigation is based upon the concept of the Bunhill WHR System. As the focus is on WHR, the combined heat and power (CHP) units installed at the energy centre for Bunhill 2 will not be included in the analysis, which investigates the performance of a HP that operates with waste heat from a LU ventilation shaft and supplies heat to a local DHN. In this case, the investigation considers a reduced heat demand that could be met with the HP alone, and this is associated with five housing estates in London that are connected to the Bunhill network. Figure 9.1 provides a map of the buildings that would be connected to the proposed network and their annual heat demands, which were taken from Table 4.1. The heat demands associated with buildings 01 and 02 have been added together as they are currently served by the same communal gas boiler and would be served by the same heat network substation. The hourly heat demand profiles for each of the buildings in Figure 9.1 were utilised to assess the costs of meeting the network heat demand with a 1 MW HP utilising waste heat from the LU, analogous to the one installed at the Bunhill 2 Energy Centre. Additional scenarios were simulated in order to account for the benefits of flexibility and cooling, and these will be further described in following sections, together with the assumptions used to model the counterfactuals of ASHPs and gas boilers.

Building Code	Annual Heat Demand (MWh)
01 and 02	2,527
03	1,497
04	468
05	919
Total	**5,411**

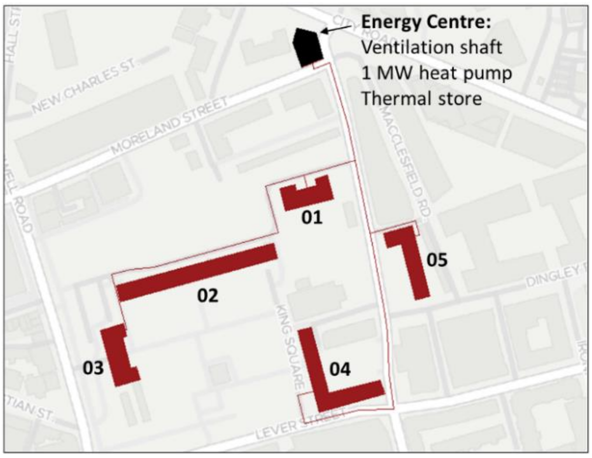

Figure 9.1 – The heat network modelled in this investigation and its connected buildings.

9.3. Simulating the Operation of the Heat Network

In order to simulate the operation of the proposed heat network, the commercial software tool energyPRO was utilised. As reviewed in section 2.14.2, energyPRO is a simulation tool that enables the techno-economic modelling of complex energy networks that may involve different energy vectors and conversion technologies, being ideally suited to perform optimisations of DHNs that involve the use of HPs with thermal energy storage (TES) (EMD, 2014). This optimisation procedure takes into account system capacity and efficiency, as well as electricity market conditions, to ensure that TES is used to avoid periods of higher electricity tariffs, shifting production to periods when costs are lower. The simulations in energyPRO are based upon a cost optimisation approach which follows a non-chronological order, ensuring timesteps with the highest priorities in terms of the cost of heat production are solved first (Østergaard and Andersen, 2021). Different resolutions can be applied, and this study is based upon hourly timesteps. The optimal solution is calculated from the following input data: heat demand profiles for all buildings connected to the network, capacity and efficiency of conversion technologies (e.g. HPs and boilers), characteristics of storage technologies, such as heat losses and useable volume, as well as data on the prices of the local electricity market. The modelling approaches for each of these inputs are described in the following sections.

9.3.1. Modelling Approach

The WHR model utilised for this investigation has been thoroughly described in Chapter 5, but it is important to understand how it is coupled with the energyPRO model of the heat network. Based upon the heat demand profiles for each of the buildings shown in Figure 9.1 and the hourly price of electricity, energyPRO determines if the WHR system should operate in a full load condition (1 MW of heat delivered), in a part-load condition (500 kW of heat delivered) or if only the thermal store should be used. This decision is also based upon hourly coefficient of system performance (COSP) values predicted by the WHR model based on air inlet conditions at the coils. Depending on the time of the year that is considered, the system could be operating in Supply Mode, which would also lead to the delivery of cooling to the railway tunnels. The energyPRO model yields hourly values for energy consumption and associated costs throughout the year for each WHR and counterfactual scenario. This takes into account the calculated efficiencies for the WHR system and the other conversion technologies, as well as the characteristics of the thermal stores and the heat network losses. The outputs from energyPRO are then combined with pumping power calculations to yield final values for carbon and cost savings, which are then combined with capital costs (CAPEX) figures to yield the LCH and CAC for each scenario. The relationship between WHR and energyPRO models is illustrated in Figure 9.2, highlighting their main inputs, outputs and interconnections.

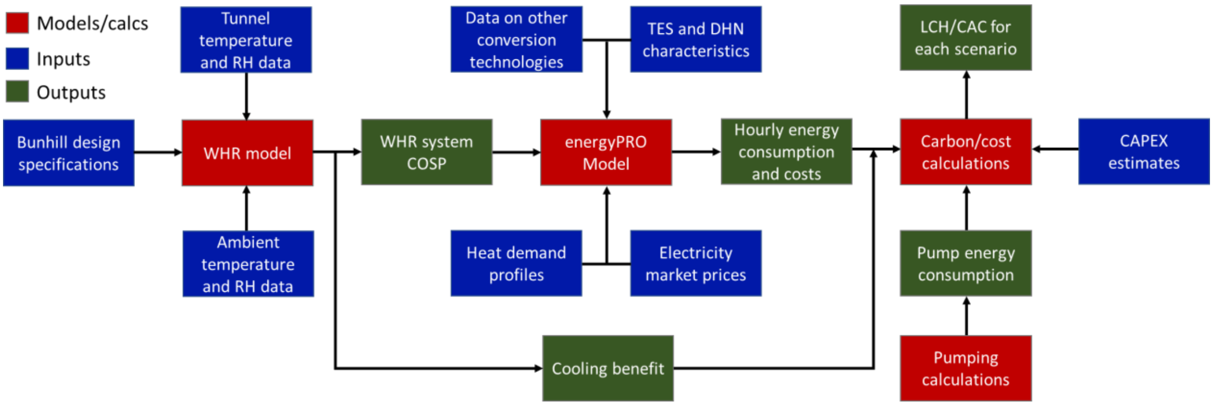

Figure 9.2 – Framework for the WHR and energyPRO models, highlighting inputs, outputs and interconnections.

9.3.2. Key Technical Assumptions

9.3.2.1. Modelling Air-source Heat Pumps

ASHPs are included in this investigation as a counterfactual that enables the comparison of the WHR system against a typical low-carbon technology, which is expected to take on a leading role as heating systems are decarbonised across the UK. For the purpose of this study, the coefficient of performance (COP) of the ASHP counterfactual is modelled exclusively as a function of ambient temperature (T_{amb}), using a correlation developed with data from a multinational manufacturer (R^2 = 0.977), as shown in Equation 9.1. Based upon the weather data utilised, the annual average COP for the ASHPs was 2.62.

$$COP_{ASHP} = -0.0011T_{amb}^2 + 0.0684T_{amb} + 2.0143 \tag{9.1}$$

9.3.2.2. Other Technologies and their Assumptions

Other technologies that were modelled as part of this investigation included gas boilers, which are used as a business-as-usual reference case, sensible TES tanks for providing flexibility, vent shaft chillers that represent the cooling counterfactual, as well as the DHN that distributes the generated heat to end users. The gas boilers were modelled considering a typical efficiency of 85%, whilst the heat network was modelled with assumed heat losses equivalent to 10% of the delivered heat, which is the maximum loss rate expected for district heating according to the UK Code of Practice for Heat Networks (CIBSE/ADE, 2020). The calculations of pumping power that would be required to deliver heat via the DHN, from the energy centre to each building substation, are detailed in section 9.3.3. The thermal stores were modelled by assuming that their useable volume is equal to their full capacity, and their heat losses were calculated using built-in energyPRO functions, considering the typical size and insulation for each TES tank modelled. The cooling benefit was assumed to be equivalent to the energy consumption that would be necessary for a typical ventilation shaft chiller system to deliver the same amount of cooling as the WHR system during its operation in Supply Mode. In this case, an average COP of 2.70 was estimated for the chiller system, considering an existing Transport for London (TfL) case study described in section 2.10, as well as fan and pumping power calculations similar to those carried out for the WHR model, which are described in sections 5.3 and 5.5, respectively.

9.3.3. Pumping Energy Calculations

Another relevant factor that needs to be accounted for when calculating the energy consumption associated with the WHR system is the pumping power required to distribute heat to the buildings connected to the DHN. The proposed network would consist of cross-linked polyethylene pipes and the size for each connecting branch was determined based on the peak heat demand of the buildings. The branches and their associated peak demands, including heat losses, together with their total lengths, considering flow and return pipework, are provided in Figure 9.3. As previously mentioned, buildings 01 and 02 would be served by the same substation located at building 01.

Branch	Length (m)	Pipe Size (mm)	Peak Demand (MW)
A-B	190	140	1.30
B-C	80	125	1.07
B-D	120	75	0.24
D-E	270	50	0.09
C-01	30	125	0.88
C-03	520	75	0.29
E-04	210	50	0.09
D-05	100	63	0.16
Total	**1,520 m**		

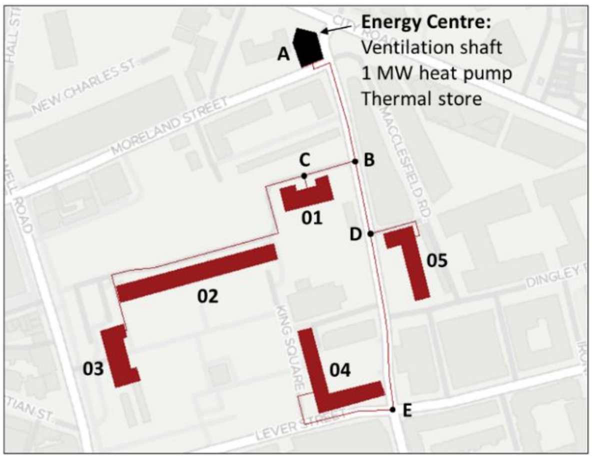

Figure 9.3 – The branches, their lengths and peak demands for the modelled heat network.

The approximate length of each branch was obtained using Google Maps, based on the route of the Bunhill Network (Islington Council, 2018). The proposed network would operate with the same flow and return temperatures as the Bunhill network, i.e. 75 and 55°C, respectively. This temperature difference (ΔT) and the peak demand values of each network branch (Q_{peak}), as shown in Figure 9.3, were then used to calculate the mass flow rates ($\dot{m}_{peak}$) necessary to meet the requirements of each connection during peak hours, considering the specific heat capacity of water ($C_{p,w}$) at the distribution temperatures, as shown in Equation 9.2.

$$\dot{m}_{peak} = \frac{Q_{peak}}{C_{p,w}\Delta T} \tag{9.2}$$

Based on the calculated flow rates, the pipe sizes for each branch were determined by following pipe sizing guidelines established by the UK's Heat Network Code of Practice (CIBSE/ADE, 2020). This consisted of choosing appropriate pipe diameters to make sure that peak flow velocities would not be higher than the typical velocities provided by the Code. The peak flow velocity (v_{peak}) can be calculated based on the pipe cross sectional area (A_{pipe}), as well as the water mass flow rate and its density (ρ_w), as shown in Equation 9.3.

$$v_{peak} = \frac{\dot{m}_{peak}}{\rho_w A_{pipe}} \tag{9.3}$$

After the pipe sizes are determined, the pumping power required to operate the heat network on an hourly basis can be calculated, utilising the methodology described in section 5.5. In this case, heat demand profiles and the heat losses rate are used to calculate flow rates and velocities for every timestep. A pipe roughness of 0.0015 mm was assumed and the head losses were calculated considering the fittings and component pressure losses described in Appendix H. An assumed static head of 10 metres was also considered in calculations.

9.3.4. Energy Tariffs and Operational Expenditure (OPEX)

The energyPRO model of the proposed heat network is based upon an optimisation problem where the objective function is the cost of heat production. Therefore, energy tariffs for both natural gas and electricity are required as inputs to the simulation. The cost of natural gas was assumed as £28.90 per MWh, whilst the detailed pricing structure for the electricity market in London had to be used in order to model the flexible operation of the heat network. For this investigation, 2019 electricity price data for the UK spot market were utilised. All electricity import levies were then applied according to their periods of applicability, considering 2019 values, yielding the final hourly prices that were used as inputs to energyPRO. Table 9.1 defines and summarises all the charges considered in terms of price per unit (£/MWh). The FIT, CfD, CMC and AAHEDC were combined and modelled as a single charge as they do not have specific periods of application. As Triads only apply during the 3 half-hourly periods of highest electricity demand, which are not pre-determined, they were modelled so as to avoid 3-hour periods likely to have higher demands during the winter season (warning periods). In addition to energy costs, the OPEX estimates also include maintenance costs, which were assumed to be a fixed annual value equivalent to a 1% share of the initial capital investment required for each simulated scenario.

Table 9.1 – The assumed prices for levies used to calculate hourly electricity tariffs in simulations.

Charge	Price per MWh	Period	Description
Red Distribution Use of System (DUoS)	£47.44	11:00 – 14:00 16:00 – 19:00	Applied to avoid the higher costs of distributing electricity during peak hours (weekdays only).
Renewable Obligation (RO)	£18.60	All times	Penalty for the supply of non-renewable electricity (depends on the grid % of renewable generation).
Feed-in Tariff (FIT)	£12.95	All times	Charge to cover scheme that supports distributed generation of renewable electricity.
Contracts for Difference (CfD)			Charge to cover scheme that supports generation of low-carbon electricity.
Capacity Market Charges (CMC)			Charge to support capacity market investments.
Assistance for Areas with High Electricity Distribution Costs (AAHEDC)			Charge to replenish the costs of providing electricity in particularly remote areas.
Climate Change Levy	£8.47	All times	Charge to incentivise reduction in energy consumption and associated emissions.
Triad Warning Periods	£874 – £1,748	3-hour peaks	Applied during the expected 20 most intensive 3h periods of demand from November to February.

9.3.5. Carbon Factors

Based upon the results from the energyPRO simulations, it was also possible to calculate the carbon emissions associated with the energy consumption predicted for each modelled scenario. This was achieved by considering the carbon intensities for electricity and natural gas, which were derived from the latest central projections from BEIS (2020c), considering commercial/public sector use over a 20-year period (2021-2040). This led to average carbon factors of 0.184 kgCO_2e/kWh and 0.140 kgCO_2e/kWh for natural gas and electricity, respectively, reflecting the expected decarbonisation of the electricity grid in the coming years.

9.4. Estimation of Capital Expenditure (CAPEX)

The estimation of capital costs was based on typical benchmarks for the main components for each of the technologies included in this analysis. Most benchmarks utilised were taken from the GreenSCIES project, as reported by Revesz et al. (2020). As GreenSCIES involves an ambient loop network, this investigation used pipework cost estimates from a report by DECC (2015), the UK Government department for energy prior to BEIS. The benchmark used for the WHR system, which excludes the costs of upgrading with a HP, was obtained from cost of capture estimates that fed into the UK's NCA on nationwide opportunities for developing district energy networks (see section 2.7.7). Replacement expenditure (REPEX) associated with new gas boilers were also obtained from the GreenSCIES project, whilst the benchmark used for ASHPs is based upon quotes from suppliers in London, as reported in (Carbon Trust, 2020). The benchmarks utilised to estimate capital costs are shown in Table 9.2.

Table 9.2 – Capital cost benchmarks used for different system components and their applicability to each technology investigated.

Components	Benchmarks	Applicability		
		WHR	ASHP	Gas Boilers
WHR system	£834/kW	✓		
WHR HP	£500/kW	✓		
ASHP	£1,150/kW		✓	
HP connection	25% of HP cost	✓	✓	
Gas boiler REPEX	£75/kW			✓
Thermal store	£1,000/m^3	✓		
Plant pipework	£750/m	✓	✓	✓
Pumps and valves	£20,000/plant	✓	✓	✓
Heat network	£243/MWh	✓		
Plate heat exchanger	£15,000/unit	✓	✓	✓
Heat meters	£1,000/unit	✓	✓	✓
Contingency	20% of CAPEX	✓	✓	✓

9.5. Figures of Merit

As mentioned in 9.1, the concepts of LCH and CAC are used in this investigation to evaluate the advantages of WHR as a tool for decarbonisation, being compared to the low-carbon counterfactual of ASHPs, based on a business-as-usual reference case of communal gas boilers. The LCH is a common metric used to represent the net present cost per unit of energy over the lifetime of a generating asset, as described by Wang (2018) and shown in Equation 9.4. As for the CAC, it represents the cost-effectiveness of a mitigation measure and can be applied to compare different technologies in terms of the cost per metric tonne of carbon avoided over their lifetime (Ibrahim and Kennedy, 2016), as shown in Equation 9.5. Both LCH and CAC figures are based upon the net present cost (NPC) of heat, a parameter calculated from CAPEX estimations, which include necessary investments and any avoided upfront costs (relating to gas boilers), as well as annual OPEX cash flows, which must be brought to a present value based on a discount rate of i and a life cycle of n years, as shown in Equation 9.6. All scenarios are compared based upon a 20-year design life and an assumed discount rate of 3.5%.

$$Levelised\ cost\ of\ heat\ (LCH) = \frac{Net\ present\ cost\ of\ heat}{Total\ energy\ output\ over\ lifetime} \tag{9.4}$$

$$Carbon\ abatement\ cost\ (CAC) = \frac{Net\ present\ cost\ of\ heat}{Total\ carbon\ savings\ over\ lifetime} \tag{9.5}$$

$$Net\ present\ cost\ of\ heat\ (NPC) = \mathrm{CAPEX} + \mathrm{OPEX}\ \frac{1-(1+i)^{-n}}{i} \tag{9.6}$$

9.6. Investigation A: TES and the Flexible Operation of the WHR System

9.6.1. Introduction to Investigation A

Flexibility is expected to play a key role in the process of heat electrification, and several studies have identified the benefits of exploiting time-of-use tariffs, as discussed in 2.11.2.

However, there is little evidence of how flexibility can be linked with waste heat to maximise the cost and carbon savings of DHNs. Therefore, investigation A looks at how different volumes of sensible TES affect the LCH achieved by a WHR system, considering both operational and capital costs. The carbon benefits of TES will also be analysed in terms of the CAC for the system that can be achieved with different thermal store sizes. Only sensible TES tanks were considered in this analysis as this was the thermal storage technology adopted for both Bunhill 1 and 2 phases.

Table 9.3 – A list of the Investigation A scenarios based upon their heat source, size of TES and description.

Scenario	Heat Source	Total Capacity	TES Volume	Description
A0	Gas Boilers	1.4 MW	0	Do-nothing scenario. Used as a reference case with gas boilers only, no heat network.
A1	WHR System	1 MW	50 m^3	HP operating with waste heat from the LU and a 50m^3 store.
A2	WHR System	1 MW	100 m^3	HP operating with waste heat from the LU and a 100m^3 store.
A3	WHR System	1 MW	150 m^3	HP operating with waste heat from the LU and a 150m^3 store.
A4	WHR System	1 MW	200 m^3	HP operating with waste heat from the LU and a 200m^3 store.
A5	WHR System	1 MW	0	HP operating with waste heat from the LU and no storage (gas boilers used to meet peaks).
A6	ASHPs	1.4 MW	0	Each building having its own ASHP, with a total capacity of 1.4 MW and no heat network.

The hourly heat demand profiles for each of the buildings in Figure 9.1 were utilised to assess the costs of meeting the network heat demand with thermal storage tanks of different volumes coupled with a 1 MW HP utilising waste heat from the LU. For this investigation, the energy centre was modelled with thermal store volumes of 50, 100, 150 and 200 m^3 and also a scenario without TES, when gas boilers would be used to help meeting demands during peak periods. These scenarios were compared to a reference case where the heat demand for each building would be met with a communal gas boiler, and in this case a total heat output capacity of 1.4 MW would be needed to meet peak demands. Additionally, a scenario where each building would have its own ASHP, with a combined capacity of 1.4 MW, was included in the analysis as a low-carbon counterfactual. A list of the modelled scenarios is provided in Table 9.3. As investigation A aims to look at the benefits of operating the WHR system flexibly through TES, no cooling benefit is included and only Extract Mode operation is considered.

9.6.2. Results and Discussion from Investigation A

9.6.2.1. Cost Savings

Based upon the spot market prices for 2019 and the levies and taxes described in Table 9.1, energyPRO was utilised to yield the annual energy costs for each of the scenarios described in Table 9.3. The pumping energy consumption calculations, described in section 9.3.3, were also included in the analysis. The results from these simulations are shown in Figure 9.4, highlighting the costs associated with gas and electricity. The latter can be distinguished between the costs for running the HP and the costs associated with the pumping energy required to operate the heat network.

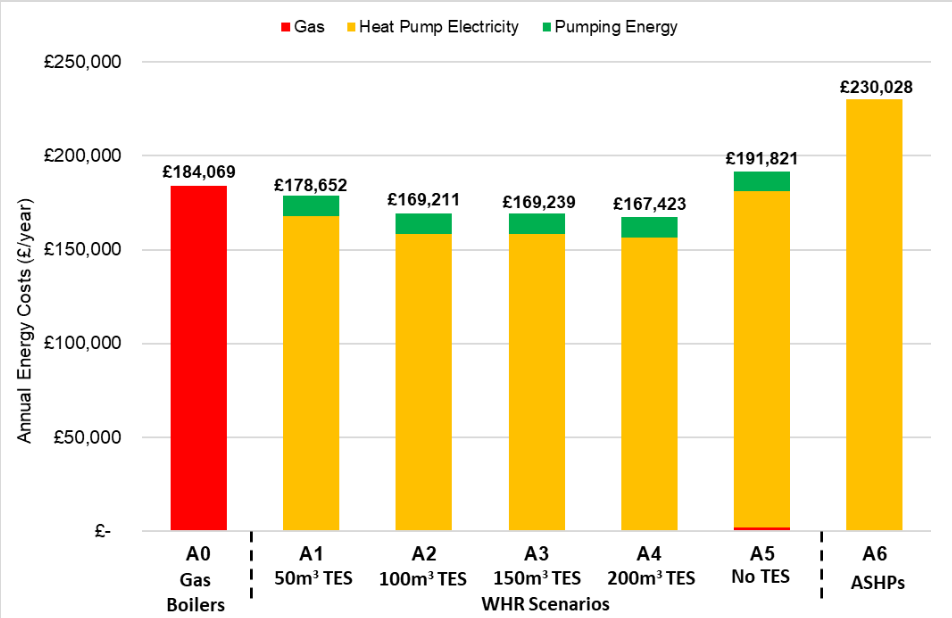

Figure 9.4 – Modelled annual energy running costs for each of the scenarios from Table 9.3.

As it can be seen from Figure 9.4, the WHR system, when coupled with TES, would lead to lower annual energy running costs against gas boilers and the ASHP scenario. The lowest energy costs were achieved for scenario A4, a reduction of around 9% against the reference case (A0), as the largest thermal store allows the WHR system to produce heat away from periods when charges such as DUoS and Triads apply. The inability to operate flexibly in the scenario without TES (A5), means that top up heat from gas boilers would still be needed to meet the annual peaks in demand. The ASHP resulted in the highest costs, with an increase of 25% against scenario A0, which is considered to be due to the lack of flexibility and their lower COPs when compared to WHR scenarios.

9.6.2.2. Carbon Savings

Based on results from energyPRO simulations and the estimated pumping energy requirements, it is possible to calculate the carbon emissions associated with the energy consumption predicted for each scenario. This is achieved by considering the carbon intensity of electricity and natural gas, which is based on average carbon factors introduced in 9.3.5. The calculated annual carbon emissions for the scenarios from Table 9.3 are illustrated in Figure 9.5, which shows how all scenarios involving electrification would lead to significant carbon savings against the reference case (A0), ranging from 74.3% for Scenario A6 to 78.5% for Scenario A1. This is due to the greater efficiency of HPs when compared to gas boilers, with the potential to achieve significant emission reductions depending on the carbon intensity of the electricity grid. The highest savings achieved for Scenario A1 are due to a lower use of electricity annually, as the WHR system would be able to operate with a higher average COSP. All WHR scenarios led to similar carbon savings, which were slightly smaller for scenario A5, as it also involved using gas boilers to help meet network demands during peak hours.

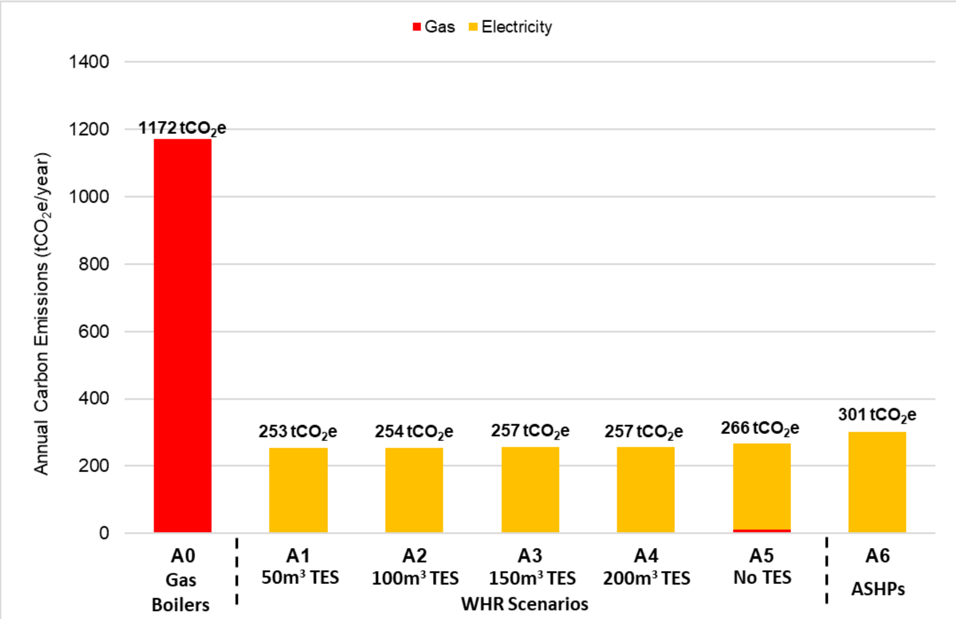

Figure 9.5 – Modelled annual carbon emissions for each of the scenarios from Table 9.3.

9.6.2.3. Capital and Maintenance Costs

The capital cost benchmarks introduced in 9.4 were used to estimate the investment costs associated with each scenario described in Table 9.3. These were then used to calculate the NPC of heat, which is an input to the LCH and CAC calculations. Furthermore, annual maintenance costs equivalent to a 1% share of the CAPEX were assumed for each scenario. Both capital and maintenance cost estimates are listed in Table 9.4.

Table 9.4 – The estimated capital and maintenance costs for all Investigation A scenarios.

Scenario	A0	A1	A2	A3	A4	A5	A6
CAPEX (x1,000)	£245	£3,307	£3,367	£3,427	£3,487	£3,247	£2,534
Annual Maintenance	£2,448	£33,065	£33,665	£34,265	£34,865	£32,465	£25,338

9.6.2.4. Levelised Cost of Heat

The analysis of the LCH for all scenarios listed in Table 9.3 can be found in Figure 9.6. It is important to emphasise that the capital and operational costs associated with the reference case (A0) were deducted from all low-carbon scenarios, as these would avoid the need to invest in new gas boilers and the OPEX of meeting heat demands with natural gas. Therefore, the LCH for Scenario A0 was not included in the analysis. Figure 9.6 shows how Scenario A2, which is associated with the coupling of a 100 m^3 TES tank with the WHR system, leads to the lowest LCH (£30.99/MWh) amongst the waste heat based scenarios. This represents a reduction of 5.2% in the LCH when compared to Scenario A5 (£32.70), where no thermal storage is applied and some gas top-up is required to cover peak demands. When compared to the ASHPs, all WHR scenarios led to higher LCH values, which can be linked with the high capital costs associated with heat networks and the WHR system, as most WHR scenarios were able to achieve lower OPEX values (see Figure 9.4).

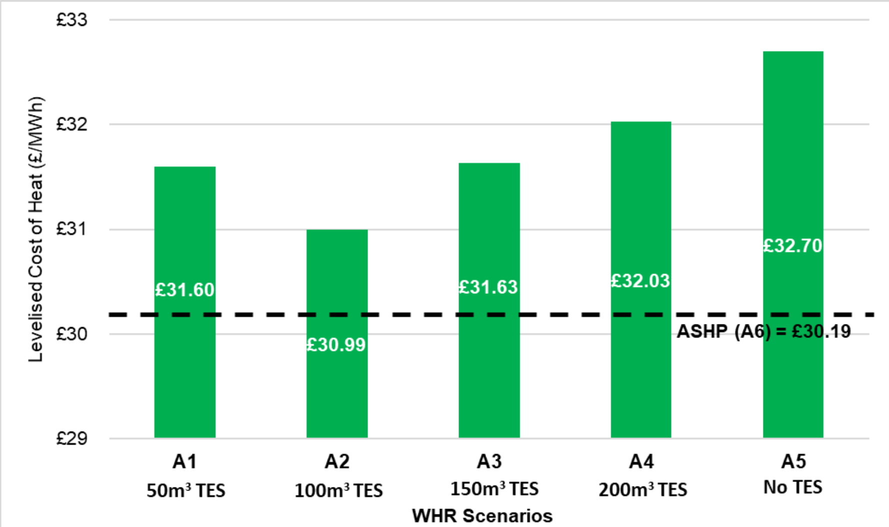

Figure 9.6 – The calculated values of LCH for each of the scenarios from Table 9.3.

The high LCH achieved for WHR can also be linked to the low costs of gas (£28.9/MWh) when compared to electricity, which had an annual average tariff of £95.72 per MWh. This means that even the best performing WHR scenario (A2) would increase heating costs by around 3.1 pence per kWh against the reference case. As for the ASHP scenario, its lower estimated CAPEX means it would achieve a lower LCH when compared to waste heat scenarios, even though ASHPs have higher operational costs, reaching a LCH value that would be 3.02 p/kWh higher than the reference case.

9.6.2.5. Carbon Abatement Costs

The CAC, which are illustrated in Figure 9.7, only consider low-carbon scenarios, as these are compared against the reference case (Scenario A0) when calculating their respective carbon savings. As seen in Figure 9.7, thermal storage can help in reducing the costs of decarbonisation, achieving lower CAC than ASHPs in all scenarios but A4, which had the largest TES tank (200 m^3) and therefore higher CAPEX. This is due to the greater efficiencies of waste heat based HPs and the ability of TES to shift heat production to periods when electricity costs are lower. The lowest CAC was observed for Scenario A2, where a 100 m^3 store would achieve a cost of £182.7 per tCO_2e avoided. This is 2.6% lower than the CAC calculated for the ASHPs counterfactual. The highest CAC was obtained for Scenario A5 (£195.1/tCO_2e), which does not include any TES and therefore is unable to operate flexibly.

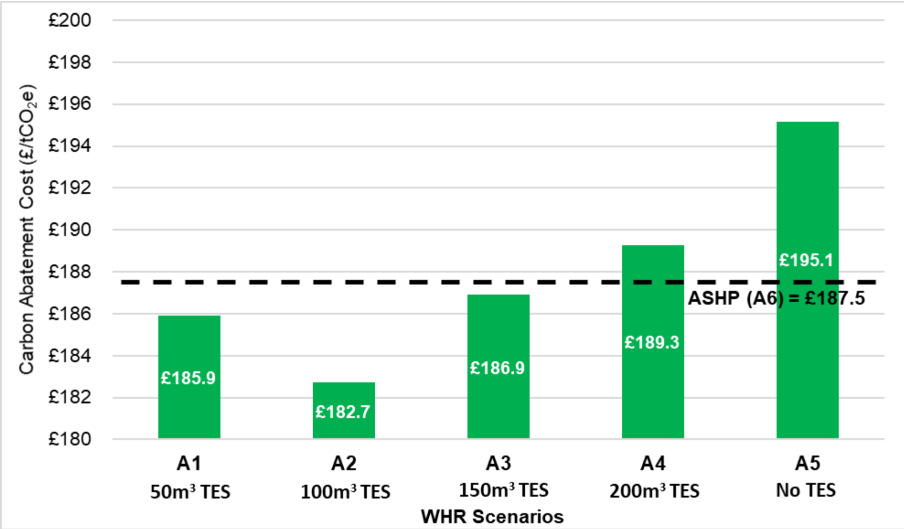

Figure 9.7 – The calculated CAC for each of the low-carbon scenarios from Table 9.3.

9.6.3. Summary of Findings from Investigation A

Investigation A highlighted how flexibility is able to reduce the costs of operating a waste heat based DHN, reducing the calculated LCH, which in turn increases the cost effectiveness of waste heat as a decarbonisation measure. However, low-carbon heat networks still have long payback periods and would lead to higher costs than the counterfactuals analysed. This is due to their high CAPEX and to the price disparity between gas and electricity in the UK. For that reason, the UK government has been incentivising district heating schemes through policies such as the Green Heat Network Fund (GHNF) (BEIS, 2021d). This investigation has indicated that there must be a balance between OPEX savings and capital investment, as Scenario A2, with a 100 m^3 thermal store, led to the best results amongst the WHR scenarios analysed.

The carbon analysis showed how the higher efficiency of WHR, together with the flexibility of TES, could result in lower CAC, as Scenario A2 was able to achieve a reduction of almost 3% when compared to the low-carbon counterfactual of ASHPs. This emphasises how, even with a higher levelised cost, waste heat from the LU could still provide an efficient means of decarbonising heat due to its potential to achieve significant carbon savings. Furthermore, the cost effectiveness of WHR could be even higher if its other benefits are also explored, such as cooling and the reduction in peak demand for electricity. This is investigated in the following sections, highlighting how secondary benefits can be crucial to reduce the LCH and CAC associated with the WHR system, increasing its competitiveness.

9.7. Investigation B: Incorporating the Cooling Benefit

9.7.1. Introduction to Investigation B

As discussed in Chapter 8, the cooling potential of the WHR system could be significantly beneficial to the LU environment, helping to reduce station temperatures during peak hours in the future. This benefit can also be analysed from carbon and cost perspectives, which could increase the feasibility of WHR systems compared with conventional heating technologies. The aim of Investigation B is to build upon the results from Investigation A, evaluating how Supply Mode operation and its associated cooling benefit would impact the levelised cost of heat (LCH) and carbon abatement costs (CAC) for the WHR system. Therefore, the cost and carbon savings were calculated based on the energy consumption of a ventilation shaft chiller system that would provide the same amount of cooling, considering the assumptions described in section 9.3.2.

In this case, two different periods of cooling provision through Supply Mode operation were considered: either for the 3 months of the meteorological summer (June to August) or for 6 months, from May to October. The system would operate for the remainder of the year in Extract Mode in order to take advantage of the higher LU tunnel temperatures during the winter, providing high heating efficiency throughout the year whilst still delivering a significant amount of cooling during the warmer months. As the flexible operation of the heat network might reduce the cooling output from the WHR system, four different scenarios were modelled. These combine the different periods of cooling supply with either no TES or with the best performing scenario from Investigation A, which corresponds to a TES volume of 100 m^3. All WHR scenarios modelled as part of Investigation B are listed in Table 9.5.

Table 9.5 –The Investigation B scenarios based on their capacity, size of TES, operating mode and description.

Scenario	Capacity	TES Volume	Operating Mode	Description
B1	1 MW	0	Extract: 9 months Supply: 3 months	HP operating with waste heat from the LU connected to a heat network, with cooling delivered for 3 months (June to August) but no flexibility provided.
B2	1 MW	0	Extract: 6 months Supply: 6 months	HP operating with waste heat from the LU connected to a heat network, with cooling delivered for 6 months (May to October) but no flexibility provided.
B3	1 MW	100 m^3	Extract: 9 months Supply: 3 months	HP operating with waste heat from the LU connected to a heat network, with flexibility provided by a 100m^3 thermal store and cooling delivered for 3 months (June to August).
B4	1 MW	100 m^3	Extract: 6 months Supply: 6 months	HP operating with waste heat from the LU connected to a heat network, with flexibility provided by a 100m^3 thermal store and cooling delivered for 6 months (May to October).

One particularly important aspect of the WHR model is the coolant that is considered as the heat recovery fluid during simulations. For scenarios where the fan runs exclusively in Extract Mode, as in Investigation A, the WHR system is modelled with water as the coolant. However, when Supply Mode operation is also required, an antifreeze mixture must be utilised in order for heat to be recovered from ambient air, which can fall to much lower temperatures than tunnel air. In this case, as described in section 8.6, the coolant considered is a propylene glycol (PG) and water mixture, with a concentration of 30%. The choice of coolant, as well as the heat source used (tunnel or ambient air), have significant impacts on the system's energy efficiency. This is highlighted in Table 9.6, which shows the modelled COSP for the different WHR scenarios, highlighting the fan operating conditions and the coolant used in each case.

Table 9.6 – Annual COSP modelled for the WHR scenarios, according to heat source and coolant type.

Operating Mode	Heat Source	Corresponding Scenarios	Coolant	Annual COSP
Extract: year-round	Tunnel air	A1 to A5	Water	3.38
Extract: September to May Supply: June to August	Ambient and tunnel air	B1 and B3	PG 30%	3.24
Extract: November to April Supply: May to October	Ambient and tunnel air	B2 and B4	PG 30%	3.15

9.7.2. Results and Discussion from Investigation B

9.7.2.1. Cooling Outputs

The impacts of cooling were included in the analysis by amending the WHR system's COSP according to its operating mode, with the Supply Mode COSP being used during the period when cooling is being delivered. Therefore, the HP running times were still determined based on the energyPRO simulations, but the system would operate with a different COSP in Supply Mode. Therefore, the final cooling output for each scenario would depend on the number of hours the WHR system would operate in Supply Mode, which in turn varies according to the heat demand of the network and the use of the TES tank. The total cooling delivered for each of the scenarios from Table 9.5 are provided in Table 9.7.

Table 9.7 – Periods of operation in Supply Mode and total cooling delivered for Investigation B scenarios.

Scenarios	B1	B2	B3	B4
Period in Supply Mode	Jun-Aug	May-Oct	Jun-Aug	May-Oct
Total Cooling Delivered	448 MWh/year	1497 MWh/year	435 MWh/year	1468 MWh/year

9.7.2.2. Cost Savings

The energy costs for all Investigation B scenarios are shown in Figure 9.8, highlighting the contributions of both gas and electricity, as well as the savings from the cooling that could be displaced. The cooling displacement was calculated based on the cooling outputs from Table 9.7 and the COP for the vent shaft chiller system used as a counterfactual (see 9.3.2). Once again, the costs associated with pumping energy for the heat network are also included, along with top-up gas boilers for the scenarios without TES. The combined net energy costs for each scenario are also presented, along with the energy costs modelled for the reference case (A0) and the ASHP counterfactual (A6).

Figure 9.8 demonstrates how cooling can help with reducing the net energy costs associated with the WHR system considerably, particularly when flexible operation through TES is also applied, as minimum costs of £142,145 were achieved for Scenario B4. Energy cost savings of up to 22.8% and 38.2% were obtained against Scenarios A0 and A6, respectively. It can also be observed in Figure 9.8 that the maximum cooling benefit would be achieved for Scenario B2, when the HP would have to operate more frequently as no TES would be available. This made Scenario B2 the second least costly amongst the scenarios analysed, with net annual energy running costs of £157,121, leading to reductions of 14.6% and 31.7% against Scenarios A0 and A6, respectively. Without any TES, supplying cooling for only three months (Scenario B1) is the only analysed case that would not be less costly than the reference case, with a slight increase of 0.6% in annual energy costs.

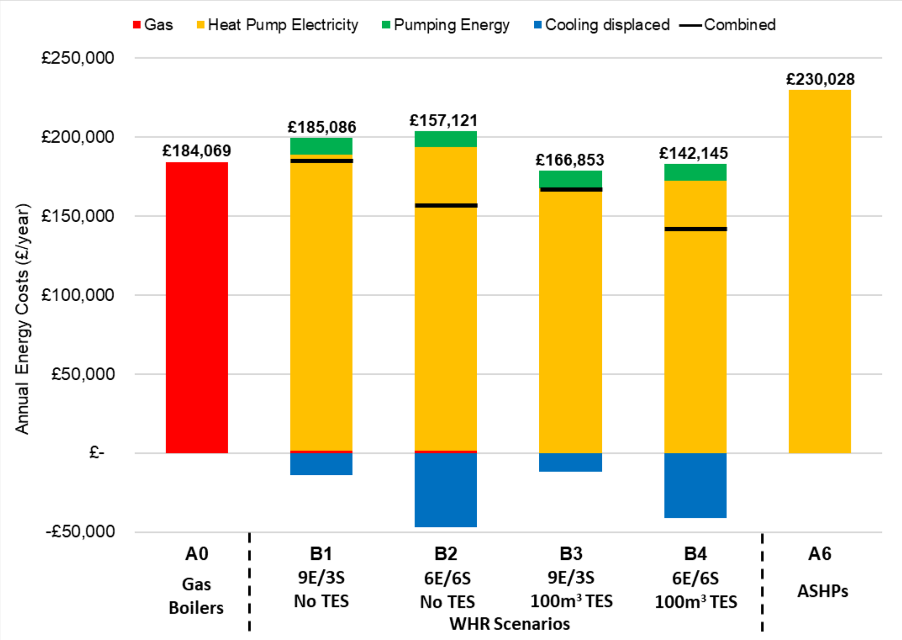

Figure 9.8 – Modelled annual energy running costs for the scenarios from Table 9.5 and counterfactuals.

9.7.2.3. Carbon Savings

A similar approach was carried out to calculate the carbon emissions associated with the cooling provision for the scenarios from Investigation B. In this case, the cooling outputs for each scenario, as described in Table 9.7, were divided by the assumed COP of 2.70 for the vent shaft chiller counterfactual. The modelled energy consumption was then multiplied by the average carbon factor for electricity (see 9.3.5) to yield the emission savings from cooling. The total carbon emissions for each of the Investigation B scenarios, together with the results for Scenarios A0 and A6, are illustrated in Figure 9.9. It can be observed that cooling can further enhance the carbon savings achieved with WHR. Overall, the savings achieved ranged from 77.9% for Scenario B1, to 82.6% for Scenario B4, which achieved the best results amongst the scenarios analysed. When compared against Scenario A2, Scenario B4 would reduce annual carbon emissions by 50.9 tCO_2e, increasing the savings against the reference case (A0) by 4.3%. As both scenarios involve a 100 m^3 thermal store, this reflects the benefits of operating the WHR system in Supply during the warmer months of the year. When compared to ASHPs, Scenario B4 would emit 97.6 tCO_2e less, which is equivalent to an increase of 8.3%

in carbon savings when both are compared to the reference case of communal gas boilers. This highlights how WHR can be a key technology for reducing emissions, particularly when both its heating and cooling benefits are taken into account.

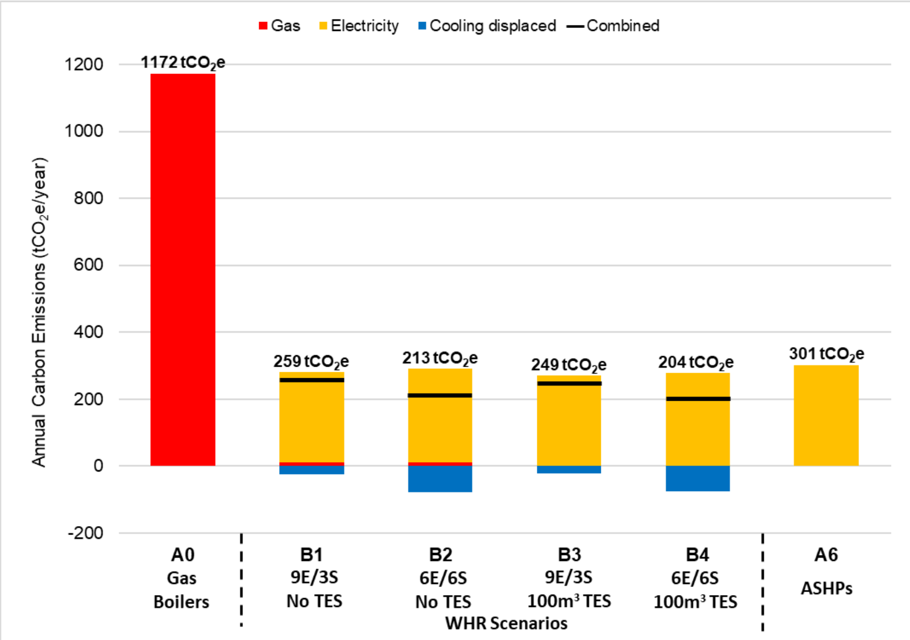

Figure 9.9 – Modelled annual carbon emissions for the scenarios from Table 9.5 and counterfactuals.

9.7.2.4. Levelised Cost of Heat

For calculating the LCH for the scenarios from Investigation B, the capital and maintenance costs for the WHR system with a 100 m^3 thermal store and without any storage were utilised, based upon the values described in section 9.6.2.3. Similarly to Investigation A, the cost savings achieved by moving away from gas boilers are also included in the cash flow when calculating the net present cost of heat. The values of LCH for all scenarios from Investigation B are illustrated in Figure 9.10, which also includes Scenario A6 for comparison purposes.

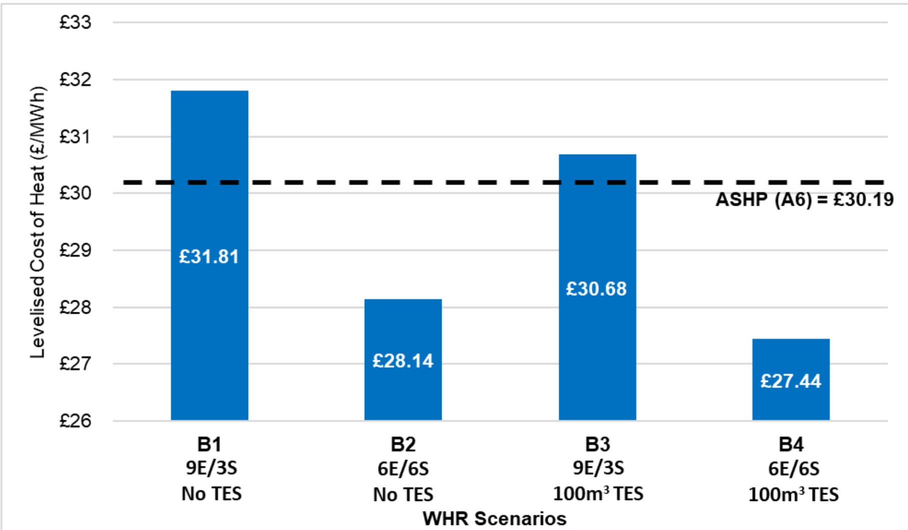

Figure 9.10 – The calculated values of LCH for each of the scenarios from Table 9.5.

Due to the cooling benefit, the LCH could be reduced significantly, even though the WHR system would operate with a lower COSP in Supply Mode. If cooling is delivered for a 6 month period, which is equivalent to the original design of the Bunhill WHR System, a LCH lower than ASHPs would be achieved. If coupled with a 100 m^3 store (Scenario B4), the LCH would be £27.44 per MWh, a value that is 9.1% lower than the LCH for ASHPs (A6). When compared to Scenario A2, where the WHR system is coupled with 100 m^3 of TES and operates solely in Extract Mode, the LCH could be reduced by up to £3.55 per MWh (11.5%) with cooling.

9.7.2.5. Carbon Abatement Costs

The CAC for each of the Investigation B scenarios are illustrated in Figure 9.11, along with the CAC obtained for the ASHP scenario (A6). As seen in Figure 9.11, all scenarios except for B1 led to a reduction in decarbonisation costs when compared to Scenario A6. This highlights the importance of combining cooling and flexibility in order to achieve greater value for money with the WHR system. The scenarios involving 6 months of cooling proved to be the most beneficial, with Scenario B4 once again achieving the best results, with a CAC of £153.3 per tCO_2e. When Scenarios B2 and B4 are compared to their analogous scenarios from Investigation A, i.e. without any cooling provision, savings of £36.46/tCO_2e and £29.45/tCO_2e are achieved, respectively. This means cooling could reduce the CAC by 18.7% when no TES is applied (B2) and by 16.1% when 100 m^3 of thermal storage is included (B4). When compared to ASHPs, the best performing scenario (B4) was able to reduce CAC by £34.27 per tCO_2e (18.3%).

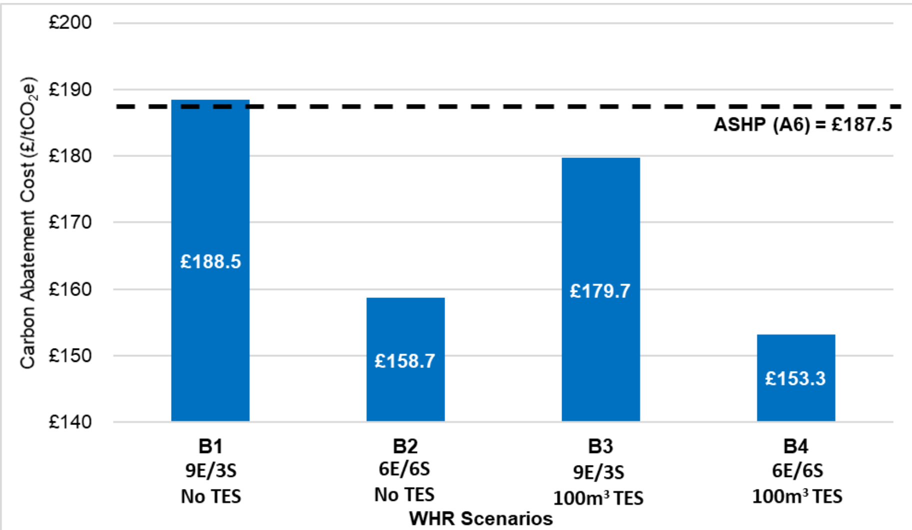

Figure 9.11 – The calculated CAC for each of the scenarios from Table 9.5.

9.7.3. Summary of Findings from Investigation B

The results from Investigation B highlight the importance of the secondary benefit of cooling in terms of increasing the cost effectiveness of the WHR system. A mixed operation of the system, in both Extract and Supply modes, is able to reduce the costs per unit of heat delivered, which also leads to a lower cost per tonne of CO_2e avoided. These benefits can be even greater when the system is able to operate flexibly with TES. However, one potential issue is that the recipient of the cooling benefit would be the railway operator, whilst the heat network operator would be the stakeholder having to bear the higher costs of producing low-carbon heat using electricity as fuel. For instance, when analysing the scenarios that involve 100m^3 of TES, the operation in Supply Mode for 6 months would increase electricity costs by 8%, or approximately £14,000 annually, whilst the cooling benefit that could be achieved has a value of £41,057. Therefore, it is essential that all stakeholders agree on how the system should be operated from an early stage, establishing a balance between running costs and cooling provision, so that the project can be successful in claiming all of its potential benefits. Furthermore, current and future policies are expected to provide much needed support for low-carbon heat networks in the coming years, reducing the high capital costs associated with district heating. This would incentivise WHR schemes to play a significant role in the decarbonisation of heat, whilst also enabling secondary benefits to be exploited.

9.8. Investigation C: Implications to the Wider Energy System

9.8.1. Introduction to Investigation C

As discussed in Chapter 2, electrification through the use of HPs provides a great opportunity for decarbonising heat, particularly as the supply of electricity from renewable generating sources has increased significantly over recent years and is expected to keep growing in the future. However, this opportunity comes with a great challenge, which is associated with the need to upgrade the generation, transmission and distribution capacities of the electricity grid in order to support the growth in demand. This makes energy efficiency and flexibility measures of significant importance, as they help alleviate stress on the electricity grid and reduce the investment costs required to increase network capacity.

The aim of Investigation C is to analyse how the efficiency of the WHR system, as well as its flexible operation, would impact the wider energy system by reducing peak electricity demands associated with heating provision for the buildings shown in Figure 9.1 when compared to ASHPs. As discussed in 2.11.2, the Carbon Trust (2021) quantified the benefits of flexibility by estimating that a reduction of 61 GW in peak electricity demand would reduce energy system costs by £16.7 billion per year. For the purpose of this investigation, this figure has been used to yield a benchmark on the economic impact of peak demand reductions, which can be expressed as £273,770 per MW of peak demand annually. If the estimations from Piclo Energy (2020) are used, a benchmark of £303,333 per MW/year is obtained, which represents an approximate increase of 10% against the Carbon Trust values. The former benchmark has been utilised for this analysis as it represents a more conservative approach. In order to represent the different possible operations of the WHR system, the scenarios from Investigation B, as well as the best performing Scenario from Investigation A (A2), have been used as the basis for Investigation C, and the resulting scenarios are detailed in Table 9.8.

Table 9.8 – A summary of the main features for each of the Investigation C scenarios.

Scenario	Capacity	TES Volume	Operating Mode	Peak Demand	Description
C1	1 MW	100 m^3	Extract: 12 months	329 kW	Same as Scenario A2, but now including wider system benefits.
C2	1 MW	0	Extract: 9 months Supply: 3 months	407 kW	Same as Scenario B1, but now including wider system benefits.
C3	1 MW	0	Extract: 6 months Supply: 6 months	460 kW	Same as Scenario B2, but now including wider system benefits.
C4	1 MW	100 m^3	Extract: 9 months Supply: 3 months	424 kW	Same as Scenario B3, but now including wider system benefits.
C5	1 MW	100 m^3	Extract: 6 months Supply: 6 months	490 kW	Same as Scenario B4, but now including wider system benefits.

9.8.2. Results and Discussion from Investigation C

9.8.2.1. Peak Demand Reductions

This investigation is based upon the modelled peak demand values for the scenarios analysed, shown in Table 9.8. The peak demand represents the maximum hourly power required to run the system in each scenario, and the values obtained are based on the operating schedule determined by energyPRO and the calculated COSP values from the WHR model. The benefits are then calculated utilising the aforementioned benchmark and by comparing the predicted peak demand for each WHR scenario against the hourly peak demand of 593 kW simulated for the ASHP counterfactual, where the total peak demand to be met with the ASHPs consists of the sum of the individual peak demands for each building.

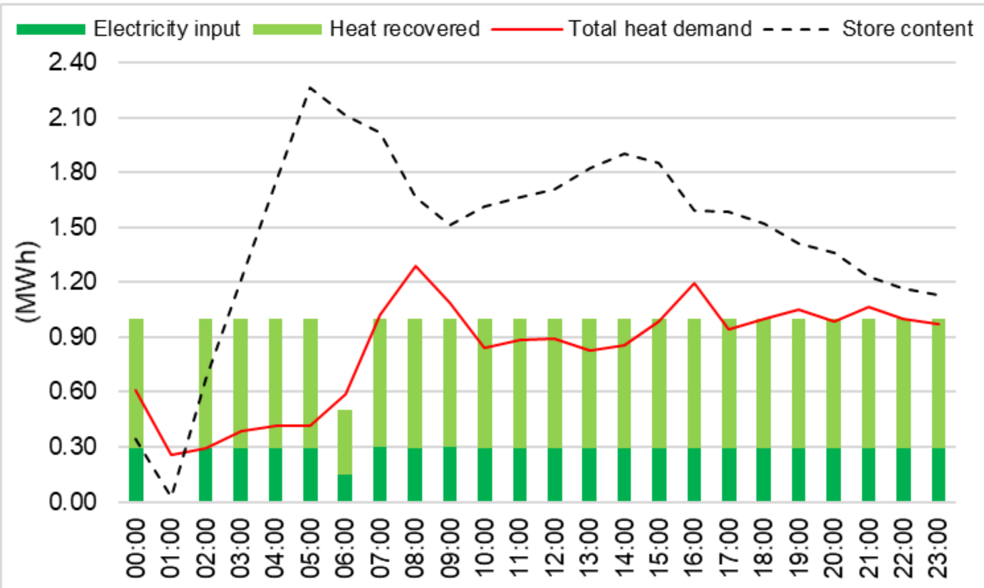

Figure 9.12 – Heat demand and generation profile for Scenario A2/C1 (WHR system coupled to a 100 m^3 store).

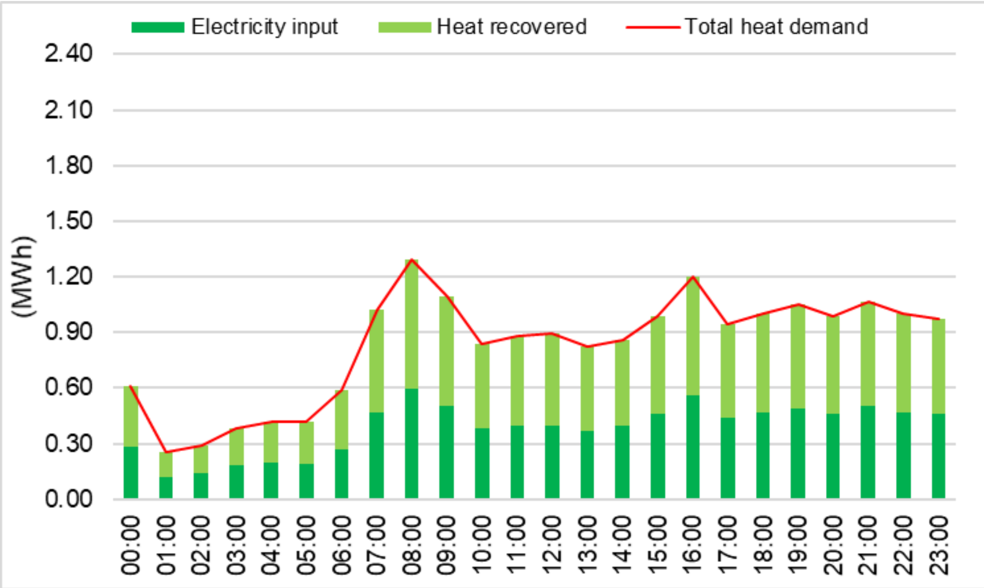

Figure 9.13 – Heat demand and generation profile for Scenario A6 (Communal ASHPs with no storage).

Due to its flexibility and higher efficiency, the WHR system is able to operate using less electricity when meeting network demands, thus having a lower peak demand, as illustrated in Figure 9.12. As for the ASHPs counterfactual, their lower efficiency and lack of TES mean they have to operate with varying capacities when meeting the heat demands for each building, consuming more electricity from the grid during peak periods, as shown in Figure 9.13. Both figures are based upon the day when ASHPs would reach their highest electricity consumption, on 8 February. On that particular day, the peak demand for the WHR system was 297 kW (07:00), as opposed to 593 kW (08:00) for the ASHPs.

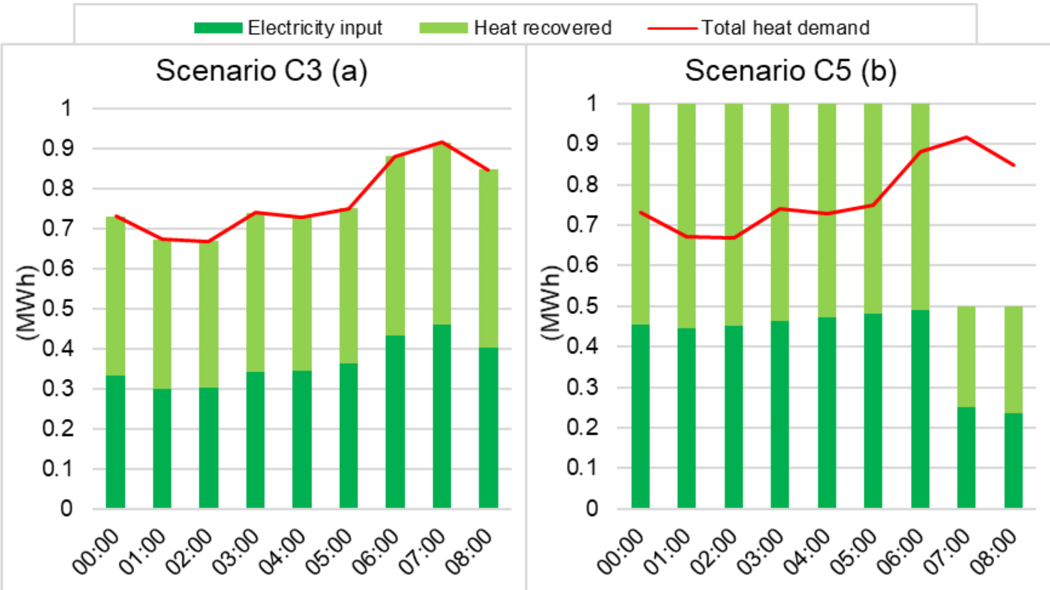

Figure 9.14 – Heat demand and generation profile for Scenarios C3 (a) and C5 (b).

When operating in Supply Mode, the WHR system has a lower COSP and therefore requires more electricity to produce 1 MW of heat. This is also highlighted in Table 9.8, with scenarios with greater cooling outputs leading to higher electricity peak demands. It is also interesting to notice how the cooling scenarios that involved flexibility (C4 and C5), led to higher peak demands than scenarios with the same cooling delivery but no flexibility (C2 and C3). This is illustrated in Figure 9.14, which shows the heat demand and generation profiles for Scenarios C3 (no TES) and C5 (100 m^3 of TES) on the first 8 hours of 30 October, when the COSP reaches values as low as 1.99. As it can be noticed, the lack of flexibility means that the WHR system would have a varying output in Scenario C3, whilst Scenario C5 leads to a stable operation, whether it is at full or partial load. This leads to Scenario C5 producing more thermal energy than C3 during a one hour interval, therefore requiring more electricity as the COSP was modelled only as a function of heat source conditions.

9.8.2.2. Levelised Cost of Heat

Similarly to the previous studies, Investigation C also evaluates the wider system benefits in terms of their impacts on the levelised costs heat and the CAC for each scenario. Based on the benchmark introduced in 9.8.1 and the simulated peak demands for each scenario, as shown in Table 9.8, the overall savings in terms of reduced network upgrade investments were calculated on an annual basis and these values were added to the NPC calculations. As system wide benefits are only applicable in a context of electrification, the gas boiler reference case was not included in the analysis, so it compares the potential savings that could be achieved by a WHR system against the electric alternative of ASHPs. The resulting LCH values for each scenario from Investigation C are provided in Figure 9.15.

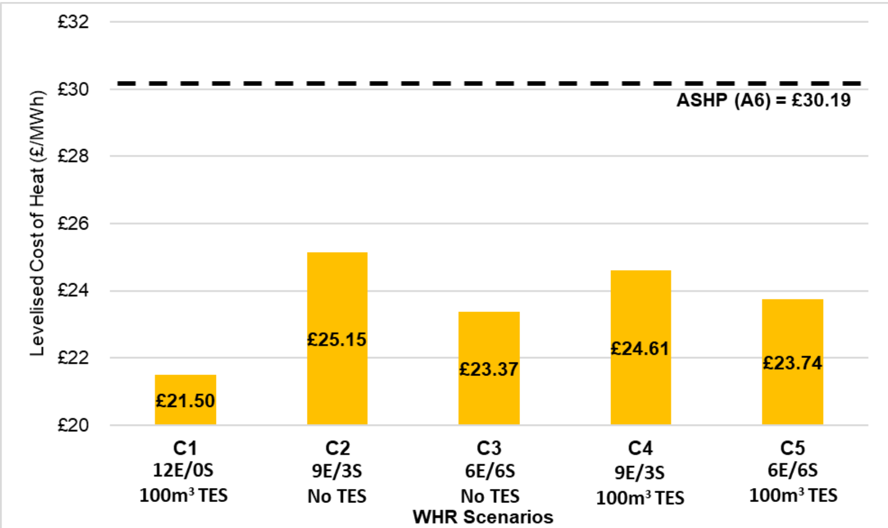

Figure 9.15 – The calculated values of LCH for each of the scenarios from Table 9.8.

As seen in Figure 9.15, the incorporation of system wide benefits could reduce the LCH for the WHR system markedly, with the lowest value (£21.50/MWh) being achieved for Scenario C1, which does not involve any cooling, as the higher efficiency of Extract Mode leads to lower power demands during peak hours, with a potential benefit of £72,328 annually. The LCH for scenario C1 represents a reduction of 28.8% against the ASHPs counterfactual. The cooling scenarios, which operate with lower COSPs when running in Supply Mode, achieved higher LCH values, ranging from £23.37/MWh for Scenario C3 to £25.15/MWh for Scenario C2, which still represent considerable savings when compared to ASHPs. Due to the higher peak demand observed when Supply Mode is combined with flexibility, the lowest savings amongst the cooling scenarios were obtained for Scenario C5, with a calculated system wide benefit of £28,145 per annum.

9.8.2.3. Carbon Abatement Costs

The CAC were also calculated for each of the Scenarios from Table 9.8, considering the savings estimated for the wider energy system when calculating the NPC of heat. The results of the CAC analysis are illustrated in Figure 9.16. Once again, the higher efficiency of the WHR system when operating solely in Extract Mode leads to much greater savings for the wider energy system, resulting in the lowest CAC of £126.7 per tCO_2e avoided. This represents savings of 32.4% when compared to the low-carbon counterfactual of ASHPs. The scenarios where cooling is provided led to higher costs than Scenario C1, ranging from £131.8 to £149 per tonne of CO_2e saved, which again can be explained by the lower COSP obtained when the system operates in Supply Mode, leading to greater electricity consumption and peak demands, as detailed in section 9.8.2.1.

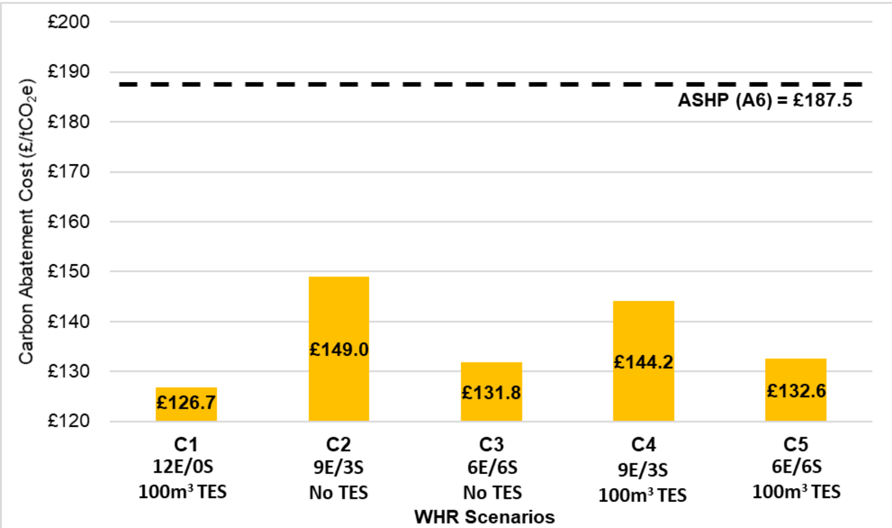

Figure 9.16 – The calculated CAC for each of the scenarios from Table 9.8.

9.8.3. Summary of Findings from Investigation C

Investigation C provides interesting insights into the importance of considering wider energy system impacts when analysing the benefits that can be achieved with WHR, as the high efficiencies obtained with waste heat could potentially reduce the investment costs required to upgrade the electricity grid in the future. Results from this analysis showed how the potential cost savings from wider system benefits could be higher than the cost savings achieved through the provision of cooling to the LU tunnels. However, this investigation did not consider the potential benefits of displacing the electricity demand from vent shaft chiller systems, which could increase the overall benefit of the cooling scenarios considerably. It is also important to highlight that benefits to the wider energy system cannot be directly claimed by operators of the WHR system, being more suited for consideration in policy design rather than as an instrument to increase the financial attractiveness of WHR systems. Nevertheless, Investigation C demonstrated how waste heat can be crucial in enabling a cost effective transition to a net-zero energy system, emphasising how benefits that are often overlooked should be incorporated when assessing the impacts of DHNs involving waste heat.

9.9. Air Quality Improvement

Another benefit that can be achieved with HP systems compared to conventional gas heating systems is the reduction in emission of harmful gases, which can help to improve the quality of air locally. As introduced in section 2.11.3, DEFRA provides guidelines for assessing the economic impacts of common air pollutants, such as nitrogen oxides (NO_x) and sulphur dioxide (SO_2), and these can be used to yield air quality damage costs for different fuels, as reported in (BEIS, 2020c). The replacement of business-as-usual gas heating by HPs eliminates direct NO_x and SO_2 emissions that result from the burning of natural gas in boilers. The UK's National Atmospheric Emissions Inventory (NAEI, 2019) provides emission factors for the combustion of natural gas in the residential sector, with benchmarks of 69.7 and 1.08 mg/kWh being associated with NO_x and SO_2, respectively.

Considering the total heat demand associated with the buildings connected to the modelled network, which is equivalent to 5,411 MWh per year, and the efficiency assumed for gas boilers of 85%, the replacement of communal gas heating for an electric heating system would reduce annual direct emissions by 443 kg for NO_x and by 7 kg for SO_2, helping to improve air quality for the local community. Furthermore, the higher energy efficiency associated with the WHR system means it would require less electricity than ASHPs while meeting the same heat demand, leading to lower indirect emissions, which result from the use of thermal power plants for the production of electricity. Therefore, utilising a WHR system would enable air pollution to be addressed both directly at a local level and indirectly by reducing the consumption of electricity required to meet the heat demands of the district heating system.

9.10. Conclusion

This Chapter investigated the potential benefits that could be claimed by operating a heat network based on WHR from the LU, highlighting the advantages of using waste heat particularly when compared to business-as-usual and low-carbon counterfactuals, which were represented by communal gas boilers and ASHPs, respectively. Initially, the impacts of flexibility were analysed by comparing how different thermal energy storage (TES) volumes would affect the LCH produced by the WHR system, as well the costs for each tonne of CO_2e it would avoid. The best performing scenario, for a 100 m^3 store, would increase the LCH against both counterfactuals, which is mostly due to the price disparity between gas and electricity in the UK as well as the high capital costs associated with district heating. However, the greater carbon savings achieved with waste heat meant the WHR system was able to reduce the CAC by approximately 3% in comparison with ASHPs.

The investigation proceeded to analyse the impacts of cooling, which represents a significant secondary benefit associated with the WHR system. Based on different operating conditions, the cooling benefit was quantified, with and without flexibility, and then compared to the low-carbon counterfactual utilising the same metrics (LCH and CAC). Overall, flexibility was able to provide great additional value to system performance, but cooling proved to be more effective in terms of reducing the LCH and CAC, with savings of approximately 9% and 18%, respectively, being achieved when compared to ASHPs. Considering a 100 m^3 thermal store and 6 months of Supply Mode operation, cooling could reduce the LCH for the WHR system by 11.5%. It is important to highlight that this analysis was carried out using energy prices from 2019, prior to the energy crisis of 2021-22, which was caused mainly by an increase in natural gas prices across Europe. Therefore, WHR schemes, which are based on energy efficiency and low-carbon heat, will become increasingly relevant and cost-effective over the next years.

Lastly, the impacts of waste heat in terms of reducing peak electricity demands and improving air quality were also analysed. The operation of the system in Extract Mode, particularly if coupled with TES, was able to achieve a greater peak demand reduction than the scenarios involving cooling provision through Supply Mode operation, as a higher seasonal COSP is obtained in Extract Mode. In terms of impacts to the wider energy system, a higher heating efficiency means less power is required during peak periods, alleviating stress on the grid and potentially reducing investment costs necessary to upgrade the generation, transmission and distribution capacities of the electricity network. As for air quality, the higher efficiencies of the WHR system would lead to lower emissions of harmful pollutants when compared to both the gas boiler reference case and the low-carbon counterfactual of ASHPs. The results from this investigation highlight the need for policy makers to recognise the benefits that can be claimed through the development of waste heat based DHNs, as these represent an effective means of minimising decarbonisation costs through the flexible integration of heating and cooling. This would also help improve air quality and alleviate stress on the electricity grid as the UK moves towards a clean energy future.

10. Waste Heat Recovery and the Potential for Replication

10.1. Introduction

This thesis has investigated the benefits of waste heat recovery (WHR) from underground railways (URs) based upon a case study of a single ventilation shaft of the London Underground (LU) network. However, this technology could be replicated at other locations across London, the UK and abroad. The potential for WHR from several UR systems in Europe has been investigated by the ReUse Heat project, as detailed in section 2.7.7. However, their study considered that heat would be recovered only at stations, with heat source temperatures being assumed to vary from 15 to 30°C throughout the year for all locations. Their proposed system would involve installing air-to-water heat pumps (HPs) to recover heat by reducing exhaust air temperature down to 5°C, with an assumed flow rate of 30 m^3/s.

There are currently four UR systems in the UK, namely in the cities of Glasgow, Newcastle, Liverpool and London. However, the Merseyrail network, in Liverpool, has a short underground section and no data were available from the Glasgow Subway, so only the URs in Newcastle and London were considered in this investigation. Therefore, specific data from the LU and the Tyne and Wear Metro were used together with the WHR model to calculate how much waste heat could be recovered from all feasible vent shafts belonging to these systems. This entailed replicating the typical conditions for both networks in order to calculate achievable coefficients of performance (COPs), which were then used to estimate the total heat demand that could be met with waste heat from URs in England. Based on the approach developed in Chapter 9, the potential carbon and cost savings that could be obtained are also estimated.

10.2. Methodology

The methodology used to determine the waste heat potential from the Newcastle and London UR systems was based upon the number of ventilation shafts for both networks and their typical volumetric flow rates. Additionally, temperature and relative humidity (RH) data were used to calculate how much heat could be recovered from each network, utilising the Bunhill 2 design and the WHR model as the basis for calculations. As discussed in section 5.4.2, the heat would be recovered from humid air, so the heat transfer process can be related to a change in enthalpy on the air side, as shown in Equation 10.1. The inlet air enthalpy ($i_{a,in}$) can be calculated based on humidity and temperature data, and the outlet air enthalpy ($i_{a,out}$) is determined as part of the energy balance calculated by the WHR model.

$$Q_{rec} = \dot{m}_a \Delta i_a = \dot{m}_a (i_{a,in} - i_{a,out}) \tag{10.1}$$

$$\dot{m}_a = \dot{V}_a \rho_a \tag{10.2}$$

Therefore, the model was used to obtain the average change in enthalpy (Δi_a) for the different air conditions experienced at both the Tyne and Wear Metro and the LU systems. The mass flow rates were calculated based on volumetric flow rate data ($\dot{V}_a$) and air density (ρ_a), as shown in Equation 10.2. Despite the occurrence of condensation, the mass flow rate was assumed to be constant as air travels through the coils, since results from the WHR model have shown that the mass of condensate formed per second is always below 0.2% of the inlet air mass flow rate. Equation 10.1 was then used to yield the average heat recovered per single vent shaft, which was then scaled up to the total number of shafts. The WHR model was also used to derive heating and cooling COSP values for different operating modes, and these were applied to yield the total heat output as well as the cost and carbon savings that could be obtained if waste heat was recovered from all feasible vent shafts.

10.3. London Underground

10.3.1. Estimation of Waste Heat Output

The potential for recovering waste heat from the LU has been estimated using the WHR model, which is based on the data set described in 8.2. It has been reported (Gilbey et al., 2011) that there may be 113 ventilation shafts with potential for heat recovery in the LU network, consisting of 58 station shafts with an average flow rate of 28 m^3/s, and 55 mid-tunnel shafts with an average flow rate of approximately 53 m^3/s. This implies an average air flow rate of approximately 40 m^3/s from LU ventilation shafts. As discussed in section 2.9.4, a recent report from Transport for London (TfL, 2020b) has identified 55 vent shafts as feasible for WHR, and their approximate locations are highlighted in Figure 10.1.

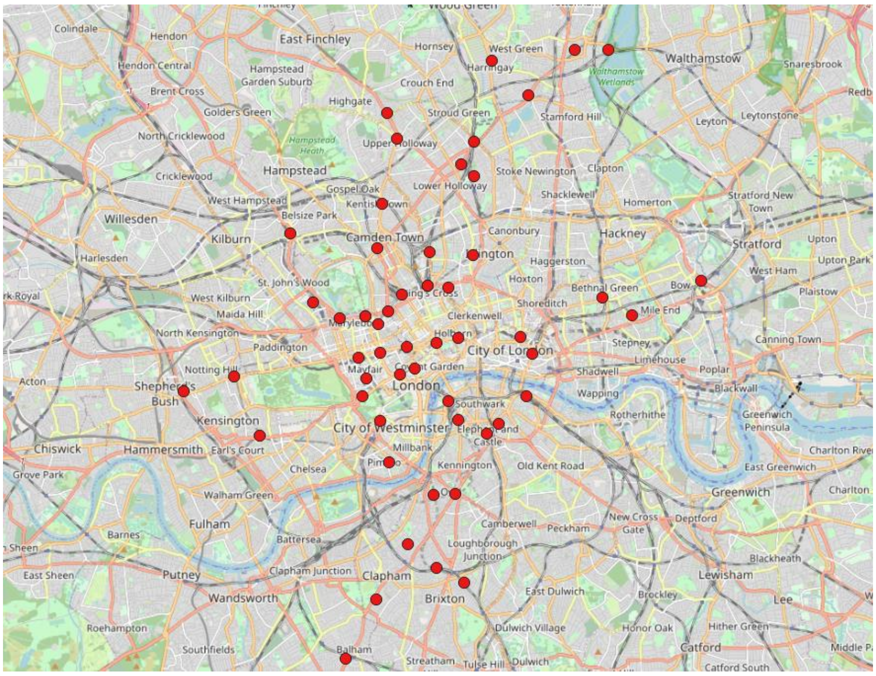

Figure 10.1 – The locations of feasible vent shafts for WHR in London (Adapted from TfL, 2020b).

Although temperature and RH may vary at different locations across the Underground network, data from the City Road ventilation shaft were utilised to quantify the potential for heat recovery from the 55 locations shown in Figure 10.1. Results from the WHR model provide the annual average enthalpy difference associated with the heat recovery process and this is shown in Table 10.1. By considering the average flow rate of 40 m^3/s and density for humid air, which is approximately 1.2 kg/m^3, it is possible to calculate how much waste heat could be recovered, which is also highlighted in Table 10.1, together with the heating and cooling COSPs obtained for Extract Mode operation, which are used to estimate the potential heat output from the LU. In order to determine the heat recovery potential for a combined operation with 6 months in Supply Mode, from May to October, the heating and cooling COSPs for such condition are also considered. The average enthalpy change for a combined operation is lower than that of Extract Mode, as the heat source temperatures recorded for Supply Mode reduce the coil capacity, as discussed in 8.4.1. Due to its lower average COSPs, a combined operation also recovers less heat for the same amount of heat delivered.

Table 10.1 – Parameters used for estimating the potential of WHR from the LU.

Operation	Δi_a	$\dot{m}_a$	**Heat Recovered**		$COSP_H$	$COSP_C$	**Heat Delivered**	
			Single	**Total**			**Single**	**Total**
12E/0S	9.34 kJ/kg	48 kg/s	448 kW	24.6 MW	3.38	2.55	593 kW	32.6 MW
6E/6S	8.97 kJ/kg	49 kg/s	435 kW	23.9 MW	3.15	2.31		

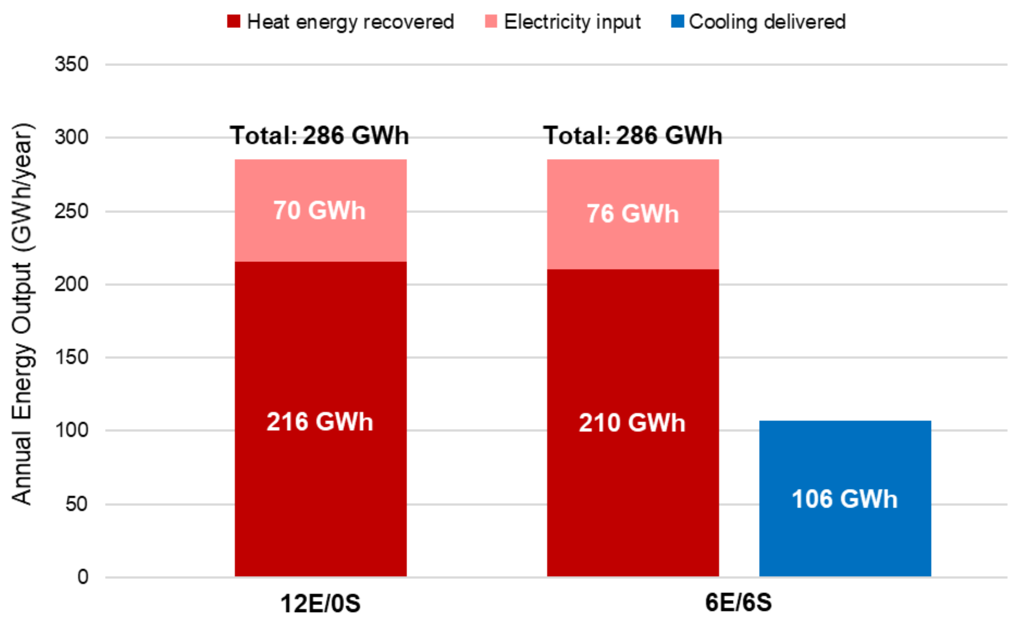

Figure 10.2 – The potential for heat recovery from the LU for Extract Mode and a combined operation, which includes a cooling benefit.

Based on the values shown in Table 10.1, it is possible to calculate the total amount of waste heat that could be recovered from the LU vent shafts, as well as how much energy could be delivered via a district heating network (DHN) after upgrading the waste heat with a HP. These calculations assume that ventilation shafts operate continuously, i.e. 8760 hours per year, however, in reality some downtime would be needed for routine maintenance. Based on these calculations, the waste heat potential for LU ventilation shafts was estimated at 216 GWh per annum, as shown in Figure 10.2. The total amount of thermal energy that could be delivered, after upgrading with HPs with the same performance as the one used for Bunhill 2, would be of 286 GWh per year. If these systems were to operate in Supply Mode during the warmer months, from May to October, the total energy consumption would increase by 8.6%, but this would also provide a benefit of delivering 106 GWh per year of cooling to the different lines of the Underground network through the vent shafts highlighted in Figure 10.1.

10.3.2. Potential Carbon and Cost Savings

In order to investigate the benefits of recovering waste heat from all feasible ventilation shafts of the LU network, calculations of potential carbon and cost savings were carried out, based upon the simulation results described in Chapter 9. These simulations analysed the performance of the WHR system when coupled with thermal energy storage (TES), either operating only in Extract Mode or in a combined mode, with up to 6 months of cooling supply to the LU tunnels. The best performing scenarios in both cases, i.e. with (B4) and without (A2) cooling, were used as the basis for calculations, with a pro-rata approach based on HP capacity being used to determine the costs and emissions for an average size ventilation shaft, using the parameters listed in Table 10.1. Therefore, the annual carbon emissions and energy costs per shaft, which are shown in Table 10.2, were calculated considering the average flow rate of 40 m^3/s and its associated system capacity of 593 kW.

Table 10.2 – Annual energy costs and associated carbon emissions for an average LU ventilation shaft.

Operation	Capacity (kW)	Energy Costs (£/year)				CO_2e Emissions (tCO_2e/year)		
		Heat Pump	Pumping	Cooling	Total	Electricity	Cooling	Total
12E/0S	593	£93,949	£6,422	0	**£100,371**	151	0	**151**
6E/6S	593	£102,248	£6,422	-£24,354	**£84,316**	166	-45	**121**

Based on the results from Table 10.2, the cost and carbon savings against communal gas boilers and air-source heat pumps (ASHPs) were calculated. A pro-rata approach was used to obtain the annual costs and emissions for both counterfactuals. For ASHPs, costs and carbon emissions totalled, respectively, £136,446 and 179 tCO_2e per annum. In the case of gas boilers, their annual costs and carbon emissions were calculated as £109,184 and 695 tCO_2e, respectively. The costs and carbon calculations for each technology were then scaled up for the 55 locations in order to estimate the benefit that could be achieved against communal ASHPs and gas boilers if waste heat were recovered from all 55 ventilation shafts.

The costs and carbon emissions associated with energy use, calculated for each technology, are illustrated in Figure 10.3.

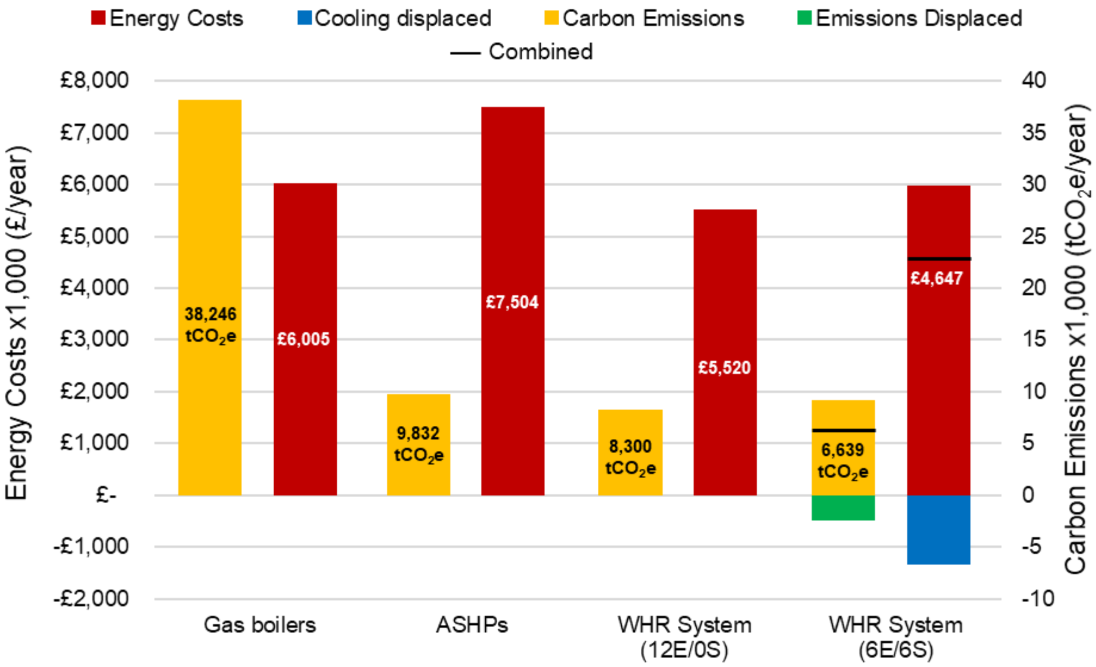

Figure 10.3 – The calculated annual energy costs and carbon emissions for WHR from the LU and its counterfactuals.

As seen in Figure 10.3, the potential savings that could be achieved if WHR systems were developed for the vent shafts identified by TfL are considerable. In terms of annual energy costs, WHR would lead to £484,733 (8.1%) of savings against gas boilers, which could be further increased to £1,367,743 (22.8%) per year if cooling is also delivered. When compared to ASHPs, using the WHR systems would result in £1,984,115 (26.4%) of annual cost savings in Extract Mode, with additional savings of £883,011 achieved if the system operates for half the year in Supply Mode, reducing energy costs by 38.2% against ASHPs. As for environmental performance, the high energy efficiency of the WHR system, coupled with the low carbon intensity of the electricity grid in the future, would lead to significant reductions in carbon emissions. When compared to gas boilers, waste heat from the LU would lead to annual carbon savings of 29,946 tCO_2e (78.3%) in Extract Mode, whilst a combined operation with cooling would lead to savings of 31,606 tCO_2e (82.6%) per year. Furthermore, WHR would be able to reduce emissions by 1,524 to tCO_2e (15.5%) against communal ASHPs, with savings of 3,184 tCO_2e (32.4%) being achieved for a combined operation.

10.4. Tyne and Wear Metro

10.4.1. Estimation of Waste Heat Output

A similar approach has been developed for the Tyne and Wear Metro, an underground transport network connecting the cities of Newcastle and Sunderland in North East England.

The network operator, Nexus, provided data on typical flow rates and locations for the ventilation shafts belonging to the network (Nexus, 2020). Overall, there are 10 ventilation shafts spread across central Newcastle, with an average volumetric flow rate of 50 m^3/s. The approximate locations of the Tyne and Wear Metro vent shafts are shown in Figure 10.4.

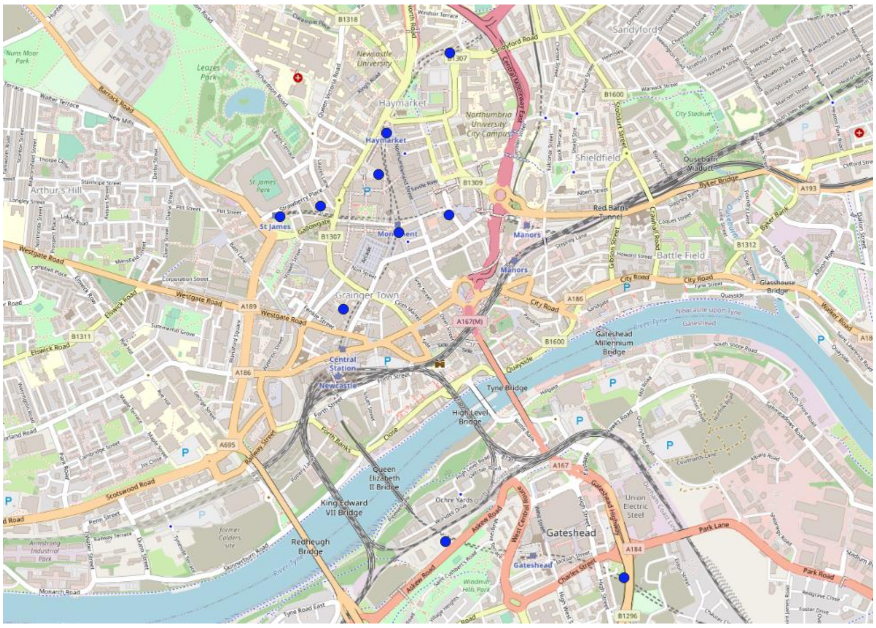

Figure 10.4 – The locations of feasible vent shafts for WHR in Newcastle.

Nexus reported that winter temperatures on the Tyne and Wear Metro typically vary from 11.5 to 15°C (2020), but detailed data for a one year period was not available, so a correlation between ambient (T_{amb}) and tunnel (T_{tun}) temperatures developed using LU data has been utilised to calculate network temperatures for Newcastle. The correlation is shown in Equation 10.3 and is based on monthly average temperatures and has a R^2 value of 0.8356, and the resulting tunnel temperatures calculated for the Newcastle network, which agree with the information provided by the system operator, are listed in Table 10.3. The calculations were based on 2013 mean monthly temperature data provided by the Met Office (2019) for the weather station of Albemarle, the closest that captured mean temperature data in that year.

$$T_{tun} = -0.0155 \times T_{amb}^2 + 0.08846 \times T_{amb} + 12.373 \qquad (10.3)$$

Table 10.3 – Ambient temperatures and calculated network temperatures for the Tyne and Wear Metro system.

Monthly Temperatures	Jan	Feb	Mar	Apr	May	Jun	Jul	Aug	Sep	Oct	Nov	Dec
Mean Ambient (°C)	2.8	2.7	1.5	6.3	9.7	12.8	17	15.6	12.3	11.0	5.0	5.6
Mean Tunnel (°C)	14.7	14.6	13.7	17.3	19.5	21.2	22.9	22.4	20.9	20.2	16.4	16.8

In order to estimate the potential for WHR from the Tyne and Wear Metro, the WHR model was run utilising the average monthly temperatures from Table 10.3, and considering average RH values of 75% to represent Supply Mode conditions and a RH of 50% to represent Extract Mode, based on the data described in section 8.2. The results provide the average enthalpy change associated with the heat recovery process for two operation regimes, year-round Extract Mode and a mixed operation with 6 months in Supply. The average vent shaft flow rate is then applied to yield the WHR potential, and this is provided in Table 10.4, together with the heating and cooling COSPs obtained for the aforementioned operational regimes.

Table 10.4 – Parameters used for estimating the potential of WHR from the Tyne and Wear Metro.

Operation	Δi_a	$\dot{m}_a$	Heat Recovered		$COSP_H$	$COSP_C$	Heat Delivered	
			Single	Total			Single	Total
12E/0S	9.19 kJ/kg	60 kg/s	554 kW	5.54 MW	3.30	2.47	741 kW	7.41 MW
6E/6S	8.75 kJ/kg	61 kg/s	535 kW	5.35 MW	3.03	2.19		

Based on the average enthalpy difference and the mass flow rates modelled for the typical Tyne and Wear ventilation shaft, the potential heat recovered from a single shaft was calculated as 554 kW in Extract Mode and as 535 kW for a combined 50/50 operation. The annual averages of heating and cooling COSPs were then utilised to yield the figure of 741 kW as the heat that could be delivered if a Bunhill-like system was installed at a ventilation shaft in Newcastle. By considering a continuous operation, the potential for WHR and associated cooling supply were estimated, as illustrated in Figure 10.5.

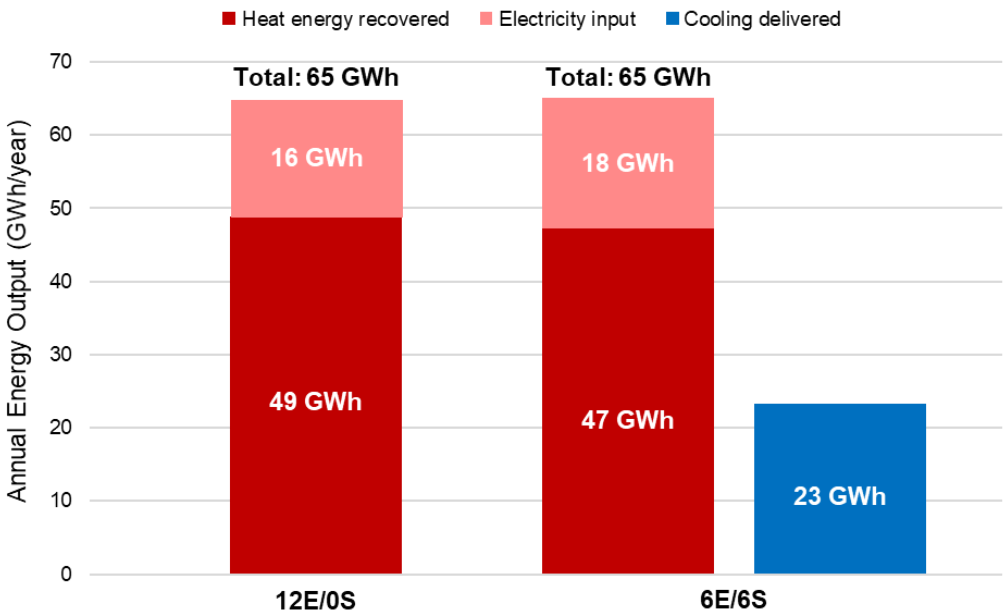

Figure 10.5 – The potential for heat recovery from the Tyne and Wear Metro for Extract Mode and a combined operation, which includes a cooling benefit.

10.4.2. Potential Carbon and Cost Savings

Similarly to the approach used for the LU, the potential carbon and cost savings that could be achieved by recovering waste heat from the Tyne and Wear Metro were calculated utilising the simulation results from Chapter 9, as these also included the benefits of cooling and flexibility. Once again, the results from scenarios A2 and B4 underpin the calculations, which are based on the estimated system capacity for an average size vent shaft, using the parameters listed in Table 10.4. Therefore, the annual carbon emissions and energy costs per shaft, which are shown in Table 10.5, were obtained by considering an average flow rate of 50 m^3/s and its associated system capacity of 741 kW.

Table 10.5 – Annual energy costs and associated carbon emissions for an average Tyne and Wear vent shaft.

Operation	Capacity (kW)	Energy Costs (£/year)				CO_2e Emissions (tCO_2e/year)		
		Heat Pump	Pumping	Cooling	Total	Electricity	Cooling	Total
12E/0S	741	£117,408	£8,026	0	**£125,434**	189	0	**189**
6E/6S	741	£127,780	£8,026	-£30,435	**£105,371**	207	-56	**151**

Based on the estimated system capacity from Table 10.5, the annual operational costs and emissions for both gas and ASHP counterfactuals were calculated utilising a pro-rata approach. For ASHPs, the operating costs and carbon emissions were estimated as £170,517 and 223 tCO_2e per annum. As for gas boilers, the annual operational expenditure (OPEX) and carbon emissions were calculated to be £136,448 and 869 tCO_2e, respectively. The cost and carbon calculations for each technology were then scaled up for the 10 locations in order to represent the benefit that could be achieved against communal ASHPs and gas boilers if waste heat were recovered from all ventilation shafts, as shown in Figure 10.6.

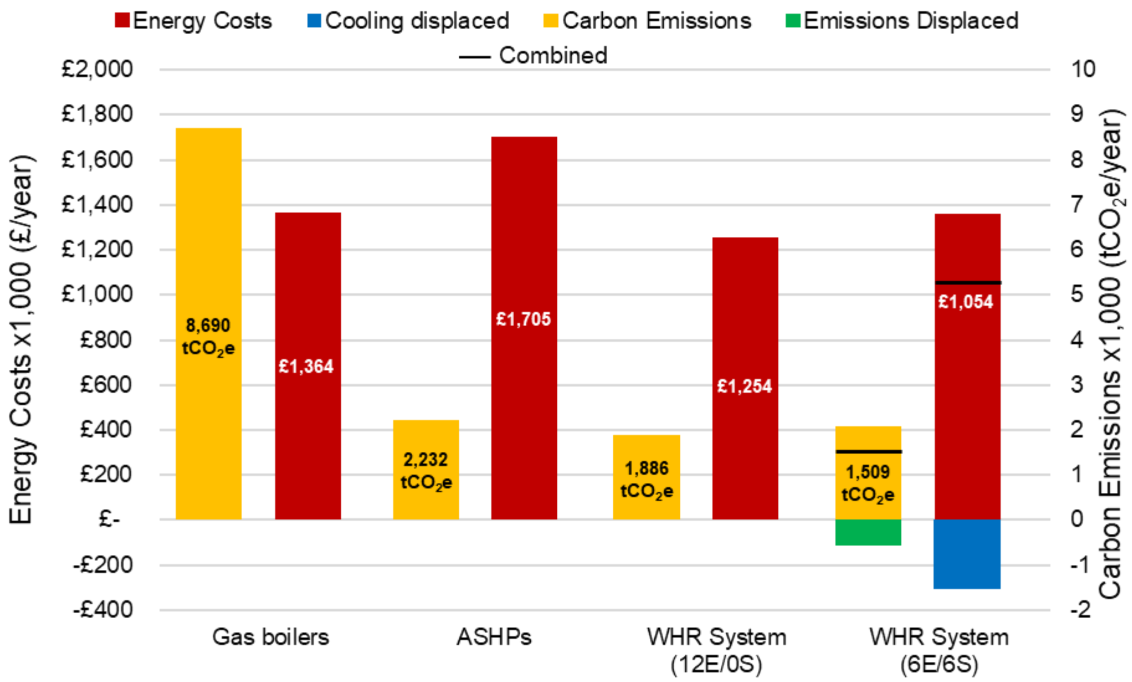

Figure 10.6 – The calculated annual energy costs and carbon emissions for WHR from the Tyne and Wear Metro and its counterfactuals.

In terms of energy costs, implementing WHR at all ventilation shafts would lead to £110,141 of annual savings against gas, with an almost 3-fold increase being observed if cooling is also delivered, reaching £310,778 of cost savings per year. When compared to ASHPs, WHR leads to £450,830 of annual cost savings in Extract Mode, with additional savings of £200,592 being achieved in a combined Extract/Supply operation, an approximate increase of 45%. As for carbon emissions, exploiting waste heat from the Tyne and Wear Metro would lead to annual reductions of 6,804 tCO_2e against gas boilers, considering only Extract Mode operation, with the cooling benefit from Supply Mode increasing savings to 7,182 tCO_2e per year. The carbon savings obtained against ASHPs were also significant, reaching 346 tCO_2e per year for Extract Mode only operation. In a combined operating mode, the cooling benefit would more than double the achievable carbon savings, resulting in reductions of around 723 tCO_2e per annum.

10.5. Conclusion

The replication studies were aimed at highlighting the significant potential URs have as low-carbon energy sources for heat networks in England. This involved estimating how much heat could be recovered from the LU and Tyne and Wear Metro transport systems, using the Bunhill WHR system as a reference case, with approximately 30 MW of waste heat being calculated as the combined potential for both networks. This would correspond to an annual heat output of approximately 351 GWh from ventilation shafts, considering that HPs would be used to upgrade the heat to a distribution temperature of 75°C. If the cooling potential behind WHR is also considered, annual cost and carbon benefits of around £1.7 million and 39 $ktCO_2e$ could be achieved against conventional heating systems based on communal gas boilers. These benefits could be even greater if waste heat is exploited through heat networks that operate at lower distribution temperatures, such as 4GDH and 5GDHC systems, as this would reduce heat network losses and allow HPs to operate with lower pressure ratios. Furthermore, WHR systems could be used to meet base loads of larger heat networks with a number of heat sources, instead of operating as the single source of energy, which is likely to increase the feasibility of WHR from URs due to economies of scale and improve the resilience of the DHN.

However, the opportunity for WHR from ventilation shafts also comes with challenges. Vent shafts typically have limited space for installing heat recovery equipment, and existing fans might not have sufficient capacity to cope with the additional pressure drop of coils fitted in the air path. Furthermore, the cooling potential, which helps to improve the economics of waste heat considerably, might not be beneficial at all locations, particularly for the Tyne and Wear Metro, which experiences lower temperatures across the year. Nevertheless, cooling can be a critical benefit for cities with UR systems in warmer countries, and demands are expected to grow significantly, even in milder climates, as global surface temperatures increase. Additionally, as ventilation shafts are often located in close proximity to potential end users, WHR systems of this type offer a great opportunity for the decarbonisation of heat in cities.

11. Conclusion and Further Studies

11.1. Introduction

The work described in this thesis has involved an investigation of the performance of a first-of-its-kind system that recovers waste heat from a London Underground (LU) ventilation shaft. This research project was motivated by the potential of this novel system to deliver significant carbon savings whilst helping to reduce costs associated with the decarbonisation of heating systems. One of the main advantages of the waste heat recovery (WHR) system is its bivalency, as the reversible fan enables operation in either Extract or Supply Modes, unlocking the potential for cooling to also be delivered. This was highlighted in the critical literature review, which analysed different studies on heat recovery from underground railways (URs) and concluded that there was a need to further investigate the full benefits of utilising waste heat from this source, particularly from the perspectives of cooling and flexibility. This knowledge gap served as the basis for the research questions that were introduced in Chapter 3, and the conclusions which are described in this chapter.

The performance of the WHR system has been investigated based on its energy efficiency when coupled with thermal energy storage (TES) and connected to a district heating network (DHN). Furthermore, the cooling benefit when operating in Supply Mode has been quantified in both economic and environmental terms, with a focus on understanding the thermal interactions between the WHR system and the LU environment. The research work was underpinned by a mathematical model of the WHR system, which was coupled with two other models, namely: of the LU environment and of the DHN. This approach enabled the demonstration of the full benefits potentially achieved through recovering waste heat from URs and the final conclusions to this thesis are provided in this chapter, along with recommendations for future work that should be performed in this field of research in order to build upon the findings of this investigation.

11.2. Research Questions and Findings

11.2.1. Performance Analysis and Optimisation Opportunities

Due to delays in the commissioning process, it was not possible to collect experimental data from the Bunhill 2 Energy Centre for a long period of operation, which would have enabled the assessment of the seasonal performance of the WHR system. The main challenge contributing to the issue was that the two-stage heat pump (HP) had to adapt itself to a wider range of vent shaft air temperatures, particularly since testing was carried out in Extract Mode during the summer, as discussed in Chapter 6. As the HP operates at an intermediate pressure set point, it is unable to deal with high evaporating temperatures and small low-stage pressure lifts. In the case of highly variant heat source temperatures, the flexibility of a one-stage HP could be beneficial (even if the overall COSP compared to a two-stage HP might be marginally reduced), particularly if the WHR system were set to operate with lower distribution temperatures.

The experimental data collected were used to validate the WHR model developed, which was applied to evaluate system performance for different operating conditions, providing insight into how potential benefits could be maximised. The heating coefficient of system performance ($COSP_H$) varied from 2.79 to 3.38, depending on the operating mode in which the reversible fan was set and which coolant was used, with a potential cooling output of up to 5.93 GWh per annum being estimated for year-round Supply Mode operation. This significant cooling benefit can only be exploited if an antifreeze additive is used for the coolant; utilising a propylene glycol (PG) mixture with a mass concentration of 30% has been recommended. The risk of freezing could also be avoided by operating at part-load conditions during colder periods, but this would reduce the total cooling output that the WHR system could deliver.

As Supply Mode operation would increase energy consumption by 20.9% when compared to year-round Extract Mode operation, a balance between heating and cooling benefits must be sought, as the recipient of the cooling benefit is the railway operator, whilst the DHN operator is the stakeholder who has to bear the higher costs of producing low-carbon heat using electricity as fuel. Operating for 3 or 6 months in Supply Mode can deliver 1.62 or 3.18 GWh of cooling per year, respectively, whilst only increasing energy consumption by 1.4% and 4.6% compared with a continuous operation in Extract Mode. Furthermore, the coupling of the WHR model with a heat network model enabled the evaluation of the cost and carbon savings of the system for different TES capacities. This highlighted the benefits of operating the WHR system flexibly, which could reduce the levelised cost of heat (LCH) by up to 5.2% compared with a scenario without flexibility. If both cooling and flexibility are considered, the savings in LCH could be up to 16.1%.

11.2.2. Comparison Against Typical Technologies for Heating and Cooling

The full benefits that can be achieved from the WHR system were investigated by combining the WHR model results with an energyPRO model of a heat network. This approach enabled utilising time-of-use energy tariffs to investigate the benefit of operating the HP flexibly, and different scenarios were compared based on calculations for the LCH and the carbon abatement costs (CAC). The results for the WHR system were than compared against conventional and low-carbon heating counterfactuals, represented by communal gas boilers and air-source heat pumps (ASHPs), respectively. In addition, the cooling benefit was calculated considering the WHR system would displace a vent shaft chiller system, similar to the one described in section 2.10. In terms of carbon savings, the potential benefits of WHR are significant, with reductions of up to 969 and 98 tCO_2e/year achieved against gas boilers and ASHPs, assuming a 50/50 Supply/Extract operation that delivers cooling to the LU tunnels from May to October. These results can be translated into CAC savings, with a reduction of £34.27 per tCO2e (18.3%) achieved against the ASHP counterfactual, confirming how WHR from URs can help reduce the costs of decarbonisation.

As for energy costs, the combination of flexibility with cooling delivery through Supply Mode leads to significant savings compared with both gas boilers (22.8%) and ASHPs (38.2%). However, the high capital costs associated with WHR systems and heat networks mean that the LCH for the best performing scenario is still very high when considering gas boilers as the reference case, with an excess cost of £27.44 per MWh of heat delivered. This indicates the need for strong future policies to level the playing field between low-carbon heat sources and business-as-usual fossil fuel technologies. Nonetheless, the WHR system is still able to lower the costs of heat production against ASHPs by £3.55 per MWh (9.1%), which is due to the greater efficiency and higher level of flexibility that can be achieved through WHR.

11.2.3. Potential Impacts on the London Underground Environment

The cooling potential of using the WHR system in Supply Mode has been investigated by simulating how future LU network temperatures would be affected, utilising a bespoke modelling tool based upon the SES platform. A novel approach combining Engineering Equation Solver (EES) and Subway Environment Simulation (SES) models was developed and used to simulate peak platform temperature for stations near the City Road ventilation shaft in the target years of 2030 and 2050, considering both latent and sensible cooling effects. The cooling output associated with Supply Mode operation resulted in significant reductions in platform temperatures, particularly for the stations adjacent to the ventilation shaft (Angel and Old Street), while negligible reductions were observed at King's Cross and Moorgate.

For 2030, the highest reductions were obtained for year-round Supply Mode operation, where the continuous supply of cooling could potentially reduce peak temperatures by 7.2 K at Angel and 6.3 K at Old Street. For scenarios involving a combination of Extract and Supply modes, the average ΔTs, considering both adjacent stations, varied from 1.1 to 4.5 K, which highlighted how the cooling benefit could be increased if the system operated for longer periods in Supply Mode. For the 2050 analysis, the results showed it would be possible to alleviate the expected increase in platform temperatures by 1.5 K and 1.3 K for Angel and Old Street, respectively, just by providing cooling during the summer. These temperature reductions might lead to several tangible benefits for LU, such as increasing the wellbeing of passengers and staff, reducing the risk of train delays caused by high temperatures, as well as unlocking the potential for service frequency and ridership to be increased.

11.2.4. Secondary Benefits of Recovering Waste Heat from Underground Railways

The benefits of waste heat are commonly expressed in terms of energy efficiency gains, but this investigation has emphasised how WHR can explore value streams such as flexibility and cooling to reduce the costs of heat production, helping to increase the competitiveness of low-carbon heating when compared to business-as-usual technologies. Furthermore, this research analysed how WHR could lead to a reduction in peak electricity demands associated with heating systems, and help to improve air quality by lowering emissions of nitrogen oxides (NO_x) and sulphur dioxide (SO_2) pollutants.

With the planned wide-scale electrification of the heating and transport sectors in the UK, significant upgrades will be required to allow the electricity grid to cope with increasing levels of demand. The higher energy efficiency and flexibility achieved through the combination of WHR and TES could therefore make an important contribution to alleviating stress on the grid, potentially reducing the investment costs necessary to upgrade the generation, transmission, and distribution capacities of the electricity network. This investigation has demonstrated how annual peak demands could be reduced by up to 44% if the WHR system is the chosen decarbonisation measure compared with communal ASHPs serving individual buildings. Based on previously published figures, this peak demand reduction, for the buildings considered in the analysis, could be associated with annual savings of up to £72,328 for the wider energy system. The higher heating efficiencies obtained through WHR also lead to lower emissions of harmful pollutants when compared to both the gas boiler reference case and the low-carbon counterfactual of ASHPs. These results emphasise the need for policy makers to recognise the benefits obtained through the development of DHNs utilising waste heat, as they represent an effective means of minimising the costs of electrification whilst also improving air quality and, thus, benefitting the local community.

11.2.5. The Replication Potential for WHR from Underground Railways

Lastly, this thesis has investigated the prospects for WHR from URs in England, which was achieved by evaluating the potential for replication of WHR at feasible ventilation shafts across the country. The analysis focused on calculating the potential waste heat output from other ventilation shafts belonging to the underground transport systems of London and Newcastle. If WHR systems were installed at every feasible location, around 30 MW of heat could be recovered from these transport networks, providing 351 GWh of heat energy annually. By considering that these systems would be connected to heat networks similar to the one described in Chapter 9, the combination of WHR from both Newcastle and London UR systems could lead to annual cost savings of £1.68 and £3.52 million compared with communal gas boilers and ASHPs, respectively. In terms of carbon emissions, the respective savings against the aforementioned counterfactuals would be of 38.7 and 3.9 ktCO_2e per year. If these WHR systems were connected to heat networks operating with lower distribution temperatures, such as 4GDH and 5GDHC systems, the potential savings could be even higher. Furthermore, if the HPs were used to meet the base loads of larger networks, the energy output from the system would be greater, as more of the recoverable heat would be used. This could help reduce heat production costs and increase the competitiveness of WHR from URs, although this configuration could possibly lead to fossil fuels being used in periods of peak demand.

11.3. Recommendations for Future Work

11.3.1. Seasonal Performance Analysis

This investigation involved analysing the benefits available from harnessing waste heat from URs based on the development of a mathematical model of the WHR system. This model has been validated against experimental and manufacturer's data for the main components of the system, namely the heat recovery coils (HRC) and the HP. Once the Bunhill WHR System is operating normally, experimental data should be collected and used to assess its seasonal performance.

11.3.2. Heat Network Types and Distribution Temperatures

The benefits of waste heat have been analysed based on the Bunhill 2 concept, which involved lowering the temperatures of a 3GDH network to 55/75°C to accommodate the WHR system. Waste heat from URs can also be exploited by networks operating at lower temperatures, such as 4G and 5G systems, which could increase system efficiency by allowing the HP to operate with a smaller pressure ratio; a performance comparison for different heat network topologies should therefore be investigated in further research. Additionally, as this research was focused on decarbonisation, it was assumed that the WHR system would be used as the single energy source for a heat network when, in reality, it might make commercial sense for the HP to be used to meet the base demand of a larger network. For this reason, it is recommended that the benefits of such a configuration be evaluated in future studies.

11.3.3. Heat Pump Design

The HP installed at the Bunhill 2 energy centre is a two-stage system utilising ammonia as the refrigerant. The toxicity of ammonia might incur additional costs associated with health and safety equipment, therefore testing the HP system performance using alternative refrigerants, such as non-toxic hydrofluoroolefin (HFO) blends with low flammabilities (e.g. R448a, R449a and R515b), is recommended for further studies. Lower flow temperatures, as discussed in section 11.3.2, could enable the utilisation of a single-stage HP, which would operate more flexibly when dealing with the wide air temperature fluctuation of the ventilation shaft, and the benefits of single-stage systems should also be investigated in future work.

11.3.4. Measuring Impacts of Supply Mode Operation

The cooling benefits potentially achieved through Supply Mode operation have been analysed through simulating the future impacts of the WHR system on the LU environment, with significant peak temperature reductions being calculated for stations adjacent to the City Road ventilation shaft. It is recommended that station temperatures be monitored when the WHR system operates in Supply Mode, as this could reveal the actual cooling benefit obtained and be used to further validate the approach developed as part of the Heat FUEL project.

11.3.5. Impacts of Antifreeze Mixtures on Pumping Power

The research described in this thesis discussed the energy efficiency implications of utilising an antifreeze mixture during Supply Mode operation from a heat transfer perspective. However, an alternative coolant could also lead to an increase in viscous friction throughout the coolant loop, affecting pumping energy consumption. It is therefore recommended that these impacts be investigated in future studies.

11.3.6. Additional Counterfactuals

The research detailed in this thesis was aimed at comparing the performance of the WHR system against typical technologies used for heating and cooling. In future work, it would be beneficial to include comparisons with emerging heating technologies, such as hydrogen, and other low-carbon counterfactuals, such as biomass, electric boilers and individual ASHPs. Additionally, the benefits of recovering waste heat from railway tunnels should be compared against other urban waste heat sources such as sewers, electricity substations, and data centres. This would allow evaluating the heat recovery potential for each of these sources, indicating what should be prioritised from both technical and non-technical perspectives. Other cooling alternatives, such as platform air-handling units (PAHUs) and groundwater schemes, should also be compared to mechanical cooling solutions and investigated to assess their potential for WHR.

11.3.7. Impacts to the Local and Wider Energy System

A more detailed analysis of the impacts of deploying a large district-scale WHR system as opposed to smaller individual or communal HPs should also be the focus of further work. This would contribute to a more accurate estimation of the benefits to the wider energy system both at local and national scales, considering any connection and reinforcement costs incurred. A more detailed investigation on the benefits of flexibility in terms of avoiding the use of marginal fossil fuel power plants should also be carried out, as this would indicate how the coupling of WHR and TES could reduce the overall costs and emissions related to electricity generation.

11.3.8. Whole Life-Cycle Carbon Assessment

As this thesis aimed to investigate the operational performance of the WHR system, only carbon emissions resulting from energy use have been considered when evaluating the environmental benefits of recovering waste heat from URs. However, the calculation of embodied carbon is an important step in a holistic environmental assessment, which must become the standard practice for net zero purposes. Embodied carbon, which accounts for the CO_2e emissions resulting from manufacturing and construction processes, is expected to become increasingly relevant for electric heating systems as operational carbon emissions are reduced due to the decarbonisation of the electricity grid. Therefore, it is recommended that whole life-cycle carbon emissions, which combine embodied and operational elements, are considered in future research on WHR schemes. This is particularly relevant for district heating projects, since, while they involve constructing large material-intensive infrastructures, they can also result in embodied carbon savings due to economies of scale in comparison with individual heating systems.

11.3.9. Social Impacts and Sustainability

Social value is another important aspect of WHR schemes that should be investigated further. A truly sustainable energy system should deliver economic, environmental and social benefits. As discussed in this thesis, some of the social impacts that could be achieved with the WHR system include reducing the costs of heat production, tackling air pollution, and alleviating the risk of heat stress related issues for LU passengers. Lower heat production costs could cut down energy bills and help to reduce fuel poverty, whilst tackling air pollution and overheating on the LU could lead to significant health benefits. However, the investigation carried out with the UR model has indicated that the cooling benefits from the WHR system are mostly limited to adjacent stations, meaning mitigation measures would also be required at other locations in order to achieve network-wide benefits that would impact LU passengers on a larger scale. Further understanding of how social benefits could be quantified is needed, and this should also be addressed in future studies.

12. References

Adam, D., Hofinger, J. & Ostermann, N., 2001. Utilization of geothermal energy from railway tunnels. Proceedings of the 15th International Conference on Soil Mechanics and Geotechnical Engineering, Istanbul, Turkey.

Adam, D. & Markiewicz, R., 2009. Energy from Earth-Coupled Structures, Foundations, Tunnels and Sewers.. Géotechnique 59, 229-236.

The Association for Decentralised Energy (ADE), 2018. Market Report: Heat Networks in the UK. Available online: https://www.theade.co.uk/resources/publications/market-report-heat-networks-in-the-uk [Accessed 04/11/18].

Allegrini, J., Orehounig, K., Mavromatidis, G., Ruesch, F., Dorer, V. & Evins, R., 2015. A review of modelling approaches and tools for the simulation of district-scale energy systems. Renewable and Sustainable Energy Reviews 52, 1391-1404.

Ampofo, F., Maidment, G. & Missenden, J., 2004. Underground railway environment in the UK, Part 2: Investigation of heat load. Applied Thermal Engineering, 24(5), 633-645.

Ampofo, F., Maidment, G. & Missenden, J., 2011. Application of Groundwater Cooling Scheme for London Underground Network. International Journal of Refrigeration 34, 2042-2049.

Arpagaus, C., Bless, F., Schiffmann, J. & Bertsch, S., 2016. Multi-temperature heat pumps: A literature review. International Journal of Refrigeration 69, 437-465.

The American Society of Heating, Refrigerating and Air-Conditioning Engineers (ASHRAE), 2017. ASHRAE Handbook - Fundamentals. SI edition. Atlanta, GA, USA.

The American Society of Heating, Refrigerating and Air-Conditioning Engineers (ASHRAE), 2020. ASHRAE Handbook - HVAC Systems and Equipment. SI edition. Atlanta, GA, USA.

AVEVA, 2019. District Energy Management. Available online: https://sw.aveva.com/operate-and-optimise/continuous-process/district-energy-management [Accessed 17/09/19].

Ayub, Z., 2003. Plate Heat Exchanger Literature Survey and New Heat Transfer and Pressure Drop Correlations for Refrigerant Evaporators. Heat Transfer Engineering 24, 3-16.

AZO Materials, 2013. Stainless Steel Grade 254 SMO™ (UNS S31254). Available online: https://www.azom.com/article.aspx?ArticleID=9157 [Accessed 16/12/20].

Barla, M., Di Donna, A. & Perino, A., 2016. Application of Energy Tunnels to an Urban Environment. Geothermics 61, 104-113.

Bibri, S. E. & Krogstie, J., 2017. Smart sustainable cities of the future: An extensive interdisciplinary literature review. Sustainable Cities and Society 31, 183-212.

Botelle, M., Payne, K. & Redhead, B., 2010. Squeezing the heat out of London's Tube. Proceedings of the Institution of Civil Engineers 163(3), 114-122.

Brandl, H., 2006. Energy Foundations and Other Thermo-Active Ground Structures. Géotechnique 56, 81-122.

Buffa, S., Cozzini, M., D'Antoni, M., Baratieri, M. & Fedrizzi, R., 2019. 5th generation district heating and cooling sysems: A review of existing cases in Europe. Renewable and Sustainable Energy Reviews 104, 504-522.

Buhmann, P., Moormann, C., Westrich, B., Pralle, N. & Friedemann, W., 2016. Tunnel Geothermics — A German Experience with Renewable Energy Concepts in Tunnel Projects. Geomechanics for Energy and the Environment 8, 1-7.

Bünning, F., Wetter, M., Fuchs, M. & Müller, D., 2018. Bidirectional low temperature district energy systems with agent-based control: Performance comparison and operation optimization. Applied Energy 209, 502-515.

C40 Cities, 2019. Why Cities? Available Online: https://www.c40.org/why_cities [Accessed 14/03/19].

Carbon Trust, 2020. Heat pump retrofit in London. Available online: https://www.carbontrust.com/resources/heat-pump-retrofit-in-london [Accessed 17/06/21].

Carbon Trust, 2021. Flexibility in Great Britain. Available online: https://www.carbontrust.com/resources/flexibility-in-great-britain [Accessed 25/06/21].

Climate Change Committee (CCC), 2019. Net Zero - The UK's Contribution to Stopping Global Warming. Available online: https://www.theccc.org.uk/publication/net-zero-the-uks-contribution-to-stopping-global-warming/ [Accessed 19/05/19].

Climate Change Committee (CCC), 2020. Sixth Carbon Budget. Available online: https://www.theccc.org.uk/publication/sixth-carbon-budget/ [Accessed 14/10/21].

Cebon, D., 2020. Hydrogen for heating? Available online: https://www.csrf.ac.uk/blog/hydrogen-for-heating/ [Accessed 15/10/21].

Çengel, Y. A. & Boles, M. A., 2011. Thermodynamics - An Engineering Approach. 7th Ed. New York, NY, USA.

Chartered Institution of Building Services Engineers (CIBSE), 2020. CP1 – Heat networks: Code of Practice for the UK, London, UK.

Cipolla, S. & Maglionico, M., 2014. Heat recovery from urban wastewater: Analysis of the variability of flow rate and temperature.. Energy and Buildings 69, 122-130.

Committee on the Medical Effects of Air Pollutants (COMEAP), 2019. Particulate air pollution on London Underground: health effects. Available online: https://www.gov.uk/government/publications/particulate-air-pollution-on-london-underground-health-effects [Accessed 22/06/19].

COMSOL, 2019. COMSOL Multiphysics. Available online: https://uk.comsol.com/ [Accessed 14/09/19].

Cross, D., Hughes, B., Ingham, D. & Ma, L., 2015. A validated numerical investigation of the effects of high blockage ratio and train and tunnel length upon underground railway aerodynamics. Journal of Wind Engineering and Industrial Aerodynamics 146, 195-206.

Culha, O., Gunerhan, H., Biyik, E., Ekren, O. & Hepbasli, A., 2015. Heat exchanger applications in wastewater source heat pumps for buildings: A key review.. Energy and Buildings 104, 215-232.

Davies, G., Boot-Handford, N., Grice, J., Dennis, W., Rami, R., Nicholls, A. & Maidment, G., 2017. Metropolitan Integrated Cooling and Heating. ASHRAE Winter Conference, Las Vegas, NV, USA.

Davies, G., Maidment, G. & Tozer, R., 2016. Using data centres for combined heating and cooling: An investigation for London. Applied Thermal Engineering 94, 296-304.

Davies, G., Revesz, A., Davenport, A., Yazadzhiyan, B. & Maidment, G., 2019a. Electrical cable tunnel cooling combined with heat recovery in cities. CIBSE Technical Symposium, Sheffield, UK.

Davies, G., Boot-Handford, N., Curry, D., Dennis, W., Ajileye, A., Revesz, A. & Maidment, G., 2019b. Combining cooling of underground railways with heat recovery and reuse. Sustainable Cities and Society 45, 543-552.

Department for Business, Energy and Industrial Strategy (BEIS), 2016. Heat meter accuracy testing. Available online: https://www.gov.uk/government/publications/heat-meter-accuracy-testing [Accessed 31/03/22].

Department for Business, Energy and Industrial Strategy (BEIS), 2018. Heat Networks Investment Project, Introduction to the Scheme. Available online: https://www.gov.uk/government/publications/heat-networks-investment-project-hnip-scheme-overview [Accessed 21/11/18].

Department for Business, Energy and Industrial Strategy (BEIS), 2020a. Digest of UK Energy Statistics (DUKES) 2020. Available online: https://www.gov.uk/government/statistics/digest-of-uk-energy-statistics-dukes-2020 [Accessed 18/08/20].

Department for Business, Energy and Industrial Strategy (BEIS), 2020b. The ten point plan for a green industrial revolution. Availble online: https://www.gov.uk/government/publications/the-ten-point-plan-for-a-green-industrial-revolution [Accessed 26/10/21].

Department for Business, Energy and Industrial Strategy (BEIS), 2020c. Green Book supplementary guidance: valuation of energy use and greenhouse gas emissions for appraisal. Available online: https://www.gov.uk/government/publications/valuation-of-energy-use-and-greenhouse-gas-emissions-for-appraisal [Accessed 04/04/21].

Department for Business, Energy and Industrial Strategy (BEIS), 2021a. Provisional UK greenhouse gas emissions national statistics 2020. Available online: https://www.gov.uk/government/statistics/provisional-uk-greenhouse-gas-emissions-national-statistics-2020 [Accessed 23/06/21].

Department for Business, Energy and Industrial Strategy (BEIS), 2021b. Heat and buildings strategy. Available online: https://www.gov.uk/government/publications/heat-and-buildings-strategy [Accessed 26/10/21].

Department for Business, Energy and Industrial Strategy (BEIS), 2021c. Green Homes Grant: make energy improvements to your home. Available online: https://www.gov.uk/guidance/apply-for-the-green-homes-grant-scheme [Accessed 26/10/21].

Department for Business, Energy and Industrial Strategy (BEIS), 2021d. Green Heat Network Fund (GHNF) Transition Scheme. Available online: https://www.gov.uk/government/publications/green-heat-network-fund-ghnf-transition-scheme [Accessed 26/10/21].

Department for Business, Energy and Industrial Strategy (BEIS), 2021e. Opportunity areas for district heating networks in the UK: second National Comprehensive Assessment. Available online: https://www.gov.uk/government/publications/opportunity-areas-for-district-heating-networks-in-the-uk-second-national-comprehensive-assessment [Accessed 18/10/21].

Department of Energy and Climate Change (DECC), 2015. Assessment of the costs, performance and characteristics of UK heat networks. Available online: https://www.gov.uk/government/publications/assessment-of-the-costs-performance-and-characteristics-of-uk-heat-networks [Accessed 02/07/21].

Department for Environment, Food and Rural Affairs (DEFRA), 2021a. Emissions of air pollutants in the UK - Summary. Available online: https://www.gov.uk/government/statistics/emissions-of-air-pollutants/emissions-of-air-pollutants-in-the-uk-summary [Accessed 29/10/21].

Department for Environment, Food and Rural Affairs (DEFRA), 2021b. Assess the impact of air quality. Available online: https://www.gov.uk/government/publications/assess-the-impact-of-air-quality/air-quality-appraisal-damage-cost-guidance [Accessed 29/10/21].

Demirel, Y. & Gerbaud, V., 2018. Nonequilibrium Thermodynamics. 4th Ed. Lincoln, NE, USA.

District Energy Initiative, 2019. What is District Energy?. Available online: http://www.districtenergyinitiative.org/what-district-energy [Accessed 29/03/19].

Dragoni, F., Baig, S., Perris, D., Boot-Handford, N., Paurine, A., Gilbey, M., Wegner, M. & Maidment, G., 2016. An Investigation of Cooling Unit Performance on the London Underground Railway Network. CIBSE Technical Symposium, Edinburgh, UK.

Duffy, S., 2018. Opportunities to Utilise Transport for London's Secondary Heat Sources. CIBSE Technical Symposium, London, UK.

Dundee Tunnel Research, 2019. Thermotun – Software. Available online: http://www.thermotun.com/thermotun/ [Accessed 27/12/19].

Ebrahimi, K., Jones, G. & Felischer, A., 2014. A review of data center cooling technology, operating conditions and the corresponding low-grade waste heat recovery opportunities. Renewable and Sustainable Energy Reviews 31, 622-638.

Element Energy and Imperial College London, 2014. Infrastructure in a low-carbon energy system to 2030. Available online: https://www.theccc.org.uk/publication/infrastructure-in-a-low-carbon-energy-system-to-2030-by-element-energy-and-imperial/ [Accessed 02/11/21].

Element Energy, 2021. Development of trajectories for residential heat decarbonisation to inform the Sixth Carbon Budget. Available online: https://www.theccc.org.uk/publication/development-of-trajectories-for-residential-heat-decarbonisation-to-inform-the-sixth-carbon-budget-element-energy/ [Accessed 14/10/21].

Elmahdy, A. H. & Mitalas, G. P., 1977. A simple model for cooling and dehumidifying coils for use in calculating energy requirements for buildings. ASHRAE Transactions 83(2), 103-117.

EMD, 2014. energyPRO - Simulate, analyse and optimise operations of energy plants. Available online: https://www.emd.dk/energypro [Accessed 30/06/21].

Energy and Climate Intelligence Unit (ECIU), 2020. Gas boilers and NOx: the hidden emitter. Available online: https://eciu.net/analysis/reports/2020/gas-boilers-and-nox-the-hidden-emitter [Accessed 29/10/21].

Energy Systems Catapult (ESC), 2020a. Decarbonisation of Heat: Why It Needs Innovation. Available online: https://es.catapult.org.uk/brochures/decarbonisation-heat [Accessed 20/06/21].

Energy Systems Catapult (ESC), 2020b. Storage & Flexibility Net Zero Series: Thermal Energy Storage for Heat Networks. Available online: https://es.catapult.org.uk/reports/storage-and-flexibility-thermal-energy-storage-for-heat-networks/ [Accessed 03/01/21].

Euroheat and Power, 2015. Statistics Overview. Available online: http://www.euroheat.org/wp-content/uploads/2016/03/2015-Country-by-country-Statistics-Overview.pdf [Accessed 04/11/18].

Euroheat and Power, 2019. District Energy Explained. Available online: https://www.euroheat.org/knowledge-hub/district-energy-explained/ [Accessed 29/03/19].

European Environment Agency (EEA), 2018. Renewable Energy in Europe - 2018. Recent Growth and Knock-on Effects. Available online: https://www.eea.europa.eu/publications/renewable-energy-in-europe-2018 [Accessed 17/05/19].

Fang, H., Xia, J. & Jiang, Y., 2015. Key issues and solutions in a district heating system using low-grade industrial waste heat.. Energy 86, 589-602.

F-Chart Software, 2019. EES Overview. Available online: http://fchartsoftware.com/ees/index.php [Accessed 15/09/19].

Franzius, J. N. & Pralle, N., 2011. Turning segmental tunnels into sources of renewable energy. Proceedings of the Institution of Civil Engineers - Civil Engineering 164(1), 35-40.

Gabrielaitiene, I., Bøhm, B. & Sunden, B., 2007. Modelling temperature dynamics of a district heating system in Naestved, Denmark—A case study. Energy Conversion and Management 48(1), 78-86.

GEA Refrigeration, 2021. Private Communication. London, UK.

Ge, Y. & Tassou, S., 2014. Control optimizations for heat recovery from CO2 refrigeration systems in supermarket.. Energy Conversion and Management 78, 245-252.

Ghoubali, R., Byrne, P., Miriel, J. & Bazantay, F., 2014. Simulation study of a heat pump for simultaneous heating and cooling coupled to buildings. Energy and Buildings 72, 141-149.

Gilbert, T., 2013. Aerodynamic Effects of High Speed Trains in Confined Spaces. PhD Thesis. University of Birmingham, Birmingham, UK.

Gilbey, M., Duffy, S. & Thompson, J., 2011. The Potential for Heat Recovery from London Underground Stations and Tunnels. CIBSE Technical Symposium, Leicester, UK.

Greater London Authority (GLA), 2018a. London Environment Strategy. Available online: https://www.london.gov.uk//what-we-do/environment/london-environment-strategy [Accessed 30/10/18].

Greater London Authority (GLA), 2018b. Population and Household Projections. Available online: https://data.london.gov.uk/dataset/projections [Accessed 13/03/19].

Greater London Authority (GLA) and Buro Happold, 2013. London's Zero Carbon Energy Resource - Secondary Heat, London, UK.

Gnielinski, V., 1976. New Equations for Heat and Mass Transfer in Turbulent Pipe and Channel Flow. International Chemical Engineering 16(2), 359-68.

Greenham, S., Ferranti, E., Quinn, A. & Drayson, K., 2020. The impact of high temperatures and extreme heat to delays on the London Underground rail network: An empirical study. Meteorological Applications 27(3), 1910.

GreenSCIES, 2020. Green Smart Community Integrated Energy Systems. Available online: https://www.greenscies.com/ [Accessed 19/06/20].

Hammond, G. & Norman, J., 2014. Heat recovery opportunities in UK industry. Applied Energy 116, 387-397.

Hazi, A., Hazi, G. & Vernica, S., 2013. Opportunity study for heat recovery from large power transformers in substations. Termotehnica 1, 9-12.

Heat Roadmap Europe, 2019. The legacy of Heat Roadmap Europe 4. Available online: https://heatroadmap.eu/ [Accessed 17/05/19].

Heinonen, E. W., Wildin, M. W., Beall, A. N. & Tapscott, R. E., 1997. Assessment of Antifreeze Solutions for Ground-Source Heat Pump Systems. ASHRAE Transactions 103(2), 747-756.

Hinojosa, L. R., Day, A. R., Maidment G. G., Dunham, C. & Kirk, P., 2007. A comparison of combined heat and power feasibility models. Applied Thermal Engineering 27(13), 2166-2172.

History House, 2020. When was London's Underground nicknamed the Tube?. Available online: https://historyhouse.co.uk/articles/the_tube.html [Accessed 25/08/2020].

Holman, J. P., 2010. Heat Transfer. 10th Ed. New York, USA.

Hornbeck, R. W., 1965. An All-Numerical Method for Heat Transfer in the Inlet of a Tube. ASME, Paper 65-WA/HT-36.

Howarth, R. W. & Jacobson, M. Z., 2021. How green is blue hydrogen? Energy Science & Engineering 9, 1676-87.

Ibrahim, N. & Kennedy, C., 2016. A Methodology for Constructing Marginal Abatement Cost Curves for Climate Action in Cities. Energies 9(4), 227.

International Energy Agency (IEA), 2018a. World Energy Outlook 2018 - Executive Summary. Available online: https://www.iea.org/weo2018/ [Accessed 17/05/19].

International Energy Agency (IEA), 2018b. IEA World Energy Balances 2018. Available online: https://webstore.iea.org/world-energy-balances-2018 [Accessed 17/05/19].

International Energy Agency (IEA), 2018c. Energy Efficiency: Buildings. Available online: https://www.iea.org/topics/energyefficiency/buildings/ [Accessed 17/05/19].

International Energy Agency (IEA), 2021. Net Zero by 2050 - A Roadmap for the Global Energy Sector. Available online: https://www.iea.org/reports/net-zero-by-2050 [Accessed 15/10/21].

Imperial College London and Sohn Associates, 2014. Management of Electricity Distribution Network Losses - Appendices. Available online: https://www.westernpower.co.uk/downloads/4847 [Accessed 10/06/19].

Incropera, F. P., DeWitt, D. P., Bergman, T. L. & Lavine, A. S., 2002. Fundamentals of Heat and Mass Transfer. 6th Ed. New York, NY, USA.

The Intergovernmental Panel on Climate Change (IPCC), 2018. Special Report - Global Warming of 1.5 °C. Available online: https://www.ipcc.ch/sr15/ [Accessed 15/03/19].

IPU, 2019. CoolPack. Available online: https://www.ipu.dk/products/coolpack/ [Accessed 16/09/21].

Islington Council, 2018. Islington Council's GIS System. Available online: https://www.islington.gov.uk/map [Accessed 16/11/18].

Islington Council, 2019. Private Communication. London, UK.

Islington Council, 2020. Climate emergency. Available online: https://www.islington.gov.uk/environment-and-energy/climate-emergency [Accessed 17/03/22].

Islington Council, 2021. Bunhill Heat and Power. Available online: https://www.islington.gov.uk/environment-and-energy/energy/bunhill-heat-network [Accessed 25/02/22].

Jones, P., Dunham, C. & Davidson, C., 2019. A roadmap to achieve 5th generation heat networks in the UK. CIBSE Technical Symposium, Sheffield, UK.

Jones, W. P., 1973. Air Conditoning Engineering. 5th Ed. Oxford, UK.

Kakaç, S., Liu, H. & Pramuanjaroenkij, A., 2012. Heat Exchangers - Selection, Rating, and Thermal Design. 3rd Ed. Boca Raton, FL, USA.

Kakaç, S., Shah, R. K. & Aung, W., 1987. Handbook of Single-Phase Convective Heat Transfer. New York, NY, USA.

Kastl, B. K., 2012. Dehumidifying Coil Models for Energy Simulation and Design. Master Thesis. Oklahoma State University, Stillwater, OK, USA.

Khan, M. S., Khan, T. S., Chyu, M.-C. & Ayub, Z. H., 2014. Evaporation heat transfer and pressure drop of ammonia in a mixed configuration chevron plate heat exchanger. International Journal of Refrigeration 41, 92-102.

Khan, T. S., Khan, M. S., Chyu, M.-C. & Ayub, Z. H., 2010. Experimental investigation of single phase convective heat transfer coefficient in a corrugated plate heat exchanger for multiple plate configurations. Applied Thermal Engineering 30(8), 1058-1065.

Kumar, H., 1984. The Plate Heat Exchanger: Construction and Design. Institute of Chemical Engineering Symposium Series 86, 1275-88.

Kwon, O., Cha, D. & Park, C., 2013. Performance evaluation of a two-stage compression heat pump for disrict heating using waste energy. Energy 57, 275-281.

Law, R., Harvey, A. & Reay, D., 2013. pportunities for low-grade heat recovery in the UK food processing industry. Applied Thermal Engineering 53, 188-196.

Lund, H., Østergaard, P. A., Nielsen, T. B., Werner, S., Thorsen, J. E., Gudmundsson, O., Arabkoohsar, A. & Mathiesen, B. V., 2021. Perspectives on fourth and fifth generation district heating. Energy 227, 120520.

Lund, H., Werner, S., Wiltshire, R., Svendsen, S., Thorsen, J. E., Hvelplund, F. & Mathiesen, B. V., 2014. 4th Generation District Heating (4GDH): Integrating smart thermal grids into future sustainable energy systems. Energy 68, 1-11.

Madani, H., Claesson, J. & Lundqvist, P., 2011. Capacity control in ground source heat pump systems: Part I: modeling and simulation. International Journal of Refrigeration, 34(6), 1338-1347.

Maidment, G. G., 1998. Optimisation of Environmental Conditions for Unwrapped Chilled Foods on Display. PhD Thesis. London South Bank University, London, UK.

Marques, C., Dunham, C., Matabuena, R., Revesz, A., Maidment, G., Jones, P. & Lagoeiro, H., 2021. Integration of High Temperature Heat Networks with Low Carbon Ambient Loop Systems. ASHRAE Winter Conference.

Mbamalu, V. C., 2013. Glycerin and the Market. PhD Thesis. The University of Tennessee, Chattanooga, TN, USA.

Meesenburg, W., Markussen, W. B., Ommen, T. & Elmegaard, B., 2020. Optimizing control of two-stage ammonia heat pump for fast regulation of power uptake. Applied Energy, 271, 115126.

Melinder, Å., 2000. Update on Secondary Refrigerants for Indirect Systems. Available online: https://www.researchgate.net/publication/237462358 [Accessed 29/01/21].

Melinder, Å., 2007. Thermophysical Properties of Aqueous Solutions Used as Secondary Working Fluids. PhD Thesis. Royal Institute of Technology KTH, Stockholm, Sweden.

Meteorological Office (Met Office), 2018. UK Climate Projections (UKCP). Available online: https://www.metoffice.gov.uk/research/approach/collaboration/ukcp/ [Accessed 08/01/21].

Meteorological Office (Met Office), 2019. Private Communication. London, UK.

Milnes, M., 2010. The Mathematics of Pumping Water. AECOM Design Build and The Royal Academy of Engineering. Available online: https://www.stem.org.uk/resources/elibrary/resource/25398/mathematics-pumping-water [Accessed 03/01/20].

Mitchell, J. W. & Braun, J. E., 2013. Principles of Heating, Ventilation and Air Conditioning in Buildings. 1st Ed. USA.

Moody, L. F. & Princeton, N. J., 1944. Friction Factors for Pipe Flow. Transactions of the American Society of Mechanical Engineers (ASME) 66, 671-84.

Mortada, A., 2016. Energy Efficient Passenger Comfort in Underground Subway Environments. PhD Thesis. University of Cambridge, Cambridge, UK.

Mortada, A., Choudhary, R. & Soga, K., 2018. Multi-dimensional simulation of underground subway spaces coupled with geoenergy systems. Journal of Building Performance Simulation 11(5), 517-37.

Muley, A. & Manglik, R. M., 1999. Experimental Study of Turbulent Flow Heat Transfer and Pressure Drop in a Plate Heat Exchanger With Chevron Plates. Journal of Heat Transfer 121(1), 110-117.

National Atmospheric Emissions Inventory (NAEI), 2019. Emission factors detailed by source and fuel. Available online: https://naei.beis.gov.uk/data/ef-all-results?q=151786 [Accessed 16/02/22].

Naphon, P. & Wongwises, S., 2005. Heat transfer coefficients under dry- and wet-surface conditions for a spirally coiled finned tube heat exchanger. International Communications in Heat and Mass Transfer 32(3), 371-385.

Nellis, G. & Klein, S., 2008. Heat Transfer. 1st Ed. New York, NY, USA.

Nexus - Transport for Tyne and Wear, 2020. Private Communication. Newcastle, UK.

Nicholson, D., Chen, Q., Silva, M., Winter, A. & Winterling, R., 2014. The Design of Thermal Tunnel Energy Segments for Crossrail, UK.. Proceedings of the Institution of Civil Engineers 167(3), 118-134.

Ninikas, K., Hytiris, N., Emmanuel, R., Aaen, B. & Younger P. L., 2016. Heat recovery from air in underground transport tunnels. Renewable Energy 96, 843-849.

Ninikas, K., Hytiris, N., Emmanuel, R. & Aaen, B., 2019. The Performance of an ASHP System Using Waste Air to Recover Heat Energy in a Subway System. Clean Technologies 1(1), 154-163.

Offor, H. U. & Alabi, S. B., 2016. An Accurate and Computationally Efficient Explicit Friction Factor Model. Advances in Chemical Engineering and Science 6, 237-45.

Office of Gas and Electricity Markets (Ofgem), 2020. Non-Domestic Renewable Heat Incentive (RHI). Available online: https://www.ofgem.gov.uk/environmental-programmes/non-domestic-rhi [Accessed 06/04/21].

Østergaard, P. A. & Andersen, A. N., 2016. Booster heat pumps and central heat pumps in district heating. Applied Energy 184, 1374-1388.

Østergaard, P. A. & Andersen, A. N., 2021. Variable taxes promoting district heating heat pump flexibility. Energy 221, 119839.

Pattijn, P. & Baumans, A., 2017. Fifth-generation thermal grids and heat pumps: A pilot project in Leuven, Belgium. Heat Pumping Technologies 35(2), 53-57.

Pellegrini, M. & Bianchini, A., 2018. The Innovation Concept of Cold District Heating Networks: A Literature Review. Energies 11(1), 236-251.

Piclo Energy, 2020. Modelling the GB Flexibility Market. Part 1: The Value of Flexibility. Available online: https://piclo.energy/publications/Value+of+Flexibility.pdf [Accessed 02/11/21].

Polzot, A., D'Agaro, P. & Cortella, G., 2017. Energy Analysis of a Transcritical CO2 Supermarket Refrigeration System with Heat Recovery.. Energy Procedia 111, 648-657.

ReUseHeat, 2020. ReUseHeat Project. Available online: https://www.reuseheat.eu/ [Accessed 18/10/21].

Revesz, A., 2017. Modelling of the Thermal Interactions of Underground Railways with Nearby Vertical Ground Heat Exchangers in an Urban Environment. PhD Thesis. London South Bank University, London, UK.

Revesz, A., Chaer, I., Thompson, J., Mavroulidou, M., Gunn, M. & Maidment, G., 2016. Ground Source Heat Pumps and Their Interactions with Underground Railway Tunnels in an Urban Environment: A Review. Applied Thermal Engineering 93, 147-154.

Revesz, A., Chaer, I., Thompson, J., Mavroulidou, M., Gunn, M. & Maidment, G., 2019. Modelling of Heat Energy Recovery Potential from Underground Railways with Nearby Vertical Ground Heat Exchangers in an Urban Environment. Applied Thermal Engineering, 147, 1059-1069.

Revesz, A., Jones, P., Dunham, C., Davies, G., Marques, C., Matabuena, R., Scott, J. & Maidment, G., 2020. Developing novel 5th generation district energy networks. Energy 201, 117389.

Rohsenow, W., Hartnett, J. & Cho, Y., 1998. Handbook of Heat Transfer. New York, NY, USA.

Rowe, J. M. & Paul, J. D., 2022. Cooling the London Underground: Evaluating the use of groundwater and subterranean river water. Sustainable Cities and Society 76, 103531.

Ruesch, F. & Haller, M., 2017. Potential and limitations of using low-temperature district heating and cooling networks for direct cooling of buildings. Energy Procedia 122, 1099-1104.

Safa, A. A., Fung, A. S. & Kumar, R., 2015. Performance of two-stage variable capacity air source heat pump: Field performance results and TRNSYS simulation. Energy and Buildings 74, 80-90.

Schmidt, D., Kallert, A., Blesl, M., Svendsen, S., Li, H., Nord, N. & Sipilä, K., 2017. Low Temperature District Heating for Future Energy Systems. Energy Procedia 116, 26-38.

Shah, R. K. & London, A. L., 1978. Laminar Forced Convection in Ducts. New York, NY, USA.

SPC Coils, 2020. SPC Online Coils Selector. Available online: https://coil.spc-hvac.co.uk/ [Accessed 07/10/20].

Stoecker, W. F., 1998. Industrial Refrigeration Handbook. New York, NY, USA.

Stoecker, W. F. & Jones, J. W., 1982. Refrigeration and air conditioning. 2nd Ed. New York, NY, USA.

Transport for London (TfL), 2017. Tube Temperature Measurements.. Available online: https://tfl.gov.uk/corporate/transparency/freedom-of-information/foi-request- etail?referenceId=FOI-2633-1617 [Accessed 09/09/20].

Transport for London (TfL), 2019a. Facts and Figures. Available online: https://tfl.gov.uk/corporate/about-tfl/what-we-do/london-underground/facts-and-figures [Accessed 14/01/19].

Transport for London (TfL), 2019b. Private Communication. London, UK.

Transport for London (TfL), 2020a. A Brief History of the Underground. Available online: https://tfl.gov.uk/corporate/about-tfl/culture-and-heritage/londons-transport-a-history/london-underground/a-brief-history-of-the-underground [Accessed 24/08/20].

Transport for London (TfL), 2020b. Early Market Engagement - TfL Waste Heat Opportunities. Available online: https://procontract.due-north.com/Advert?advertId=91605c8a-5d89-ea11-80ff-005056b64545 [Accessed 27/10/21].

The National Archives, 1946. Improving London's Transport - Flickr. Available online: https://www.flickr.com/people/nationalarchives/ [Accessed 25/08/20].

THERMOS Project, 2019. THERMOS (Thermal Energy Resource Modelling and Optimisation System). Available online: https://www.thermos-project.eu/home/ [Accessed 14/09/19].

Thompson, J. A., 2006. Sustainable cooling of underground railways through enhancement of the heat sink effect. PhD Thesis. London South Bank University, London, UK.

Thompson, J., Maidment, G. & Missenden, J., 2006a. Modelling low-energy cooling strategies for underground railways. Applied Energy 83, 1152-1162.

Thompson, J., Maidment, G., Missenden, J. & Ampofo, F., 2006b. Evaluation of Underground Railway Networks Operating Sustainable Cooling Systems. Available online: https://www.researchgate.net/publication/228781277_Evaluation_of_underground_railway_networks_operating_sustainable_cooling_systems [Accessed 16/09/19].

Thonon, B., 1995. Design Method for Plate Evaporators and Condensers. 1st International Conference on Process Intensification, BHR Group Conference Series 18, 37-47.

Threlkeld, J. L., 1962. Thermal Environmental Engineering. 1st Ed. Englewood Cliffs, NJ, USA.

Tran, C. T., Rivière, P., Marchio, D. & Arzano-Daurelle, C., 2012. Refrigerant-based measurement method of heat pump seasonal performances. International Journal of Refrigeration 35(6), 1583-1594.

TRNSYS, 2019. TRNSYS - Transient System Simulation Tool. Available online: http://www.trnsys.com/index.html [Accessed 16/09/19].

U.S. Department of Transportation, 2002. Subway Environmental Design Handbook, Volume II. Subway Environmental Simulation Computer Program, Version 4.1, New York, NY, USA.

Union internationale des transports publics (UITP), 2018. World Metro Figures 2018. Available online: https://www.uitp.org/world-metro-figures-2018 [Accessed 06/06/19].

UK Energy Research Centre (UKERC), 2020. Heat decarbonisation in the UK - National scenarios vs practical local options. Available online: https://ukerc.ac.uk/news/heat-decarbonisation-in-the-uk-national-scenarios-vs-practical-local-options/[Accessed 29/07/21].

United Nations Department of Economic and Social Affairs (UN DESA), 2018. World Urbanization Prospects: The 2018 Revision, New York, NY, USA.

United Nations Climate Change (UNCC), 2021. COP 26. Available online: https://ukcop26.org/ [Accessed 13/10/21].

Vahterus, 2020. Introduction to Vahterus Plate and Shell Heat Exchanger Technology. Available online: https://vahterus.com/products/pshe-technology/ [Accessed 15/12/20].

Vardy, A. E., 1996a. Aerodynamic Drag on Trains in Tunnels Part 1: Synthesis and Definitions. Proceedings of the Institution of Mechanical Engineers, Part F: Journal of Rail and Rapid Transit 210(1), 29-38.

Vardy, A. E., 1996b. Aerodynamic Drag on Trains in Tunnels Part 1: Prediction and Validation. Proceedings of the Institution of Mechanical Engineers, Part F: Journal of Rail and Rapid Transit 210(1),. 39-49.

Vasilyev, G. P., Popov, M. I., Gornov, V. F., Shapkin, P. V. & Kolesova, M. V., 2019. Using Tunnel Air Heat in the Heat and Cold Supply Systems of Subway Facilities. Thermal Engineering 66(11), 812-21.

Wahlroos, M., Pärssinen, M., Rinne, S., Syri, S. & Manner, J., 2018. Future views on waste heat utilization - Case of data centers in Northern Europe. Renewable and Sustainable Energy Reviews 82, 1749-1764.

Wang, J. & Hihara, E., 2003. Prediction of air coil performance under partially wet and totally wet cooling conditions using equivalent dry-bulb temperature method. International Journal of Refrigeration 26(3), 293-301.

Wang, Z., 2018. Heat pumps with district heating for the UK's domestic heating: individual versus district level. Energy Procedia 149, 354-62.

Wanniarachchi, A. S., Ratnam, U., Tilton, B. E. & Dutta-Roy, K., 1995. Approximate Correlations for Chevron-Type Plate Heat Exchangers. ASME National Heat Transfer Conference, New York, NY, USA.

Wen, Y., Leng, J., Shen, X., Han, G., Sun, L. & Yu, F., 2020. Environmental and Health Effects of Ventilation in Subway Stations: A Literature Review. International Journal of Environmental Research and Public Health 17(3), 1084.

Werner, S., 2017. International review of district heating and cooling. Energy 137, 617-631.

WSP, 2018. MICAH Impact on Tunnel Temperatures, London, UK.

Ziemele, J., Kalnins, R., Vigants, G., Vigants, E. & Veidenbergs, I., 2018. Evaluation of the industrial waste heat potential for its recovery and integration into a fourth generation district heating system. Energy Procedia 147, 315-21.

Žukauskas, A., 1972. Heat Transfer from Tubes in Cross Flow. Advances in Heat Transfer 8, 93-160.

Appendix A – Review of Modelling Tools

There is a wide number of modelling tools reported in current literature that have been used to analyse the performance of energy systems. Some can be applied to provide a holistic analysis, including energy generation, distribution and demand, whilst others are capable of analysing one specific part in more detail. This research project aimed to analyse the efficiency of the WHR system, so a combination of software tools that can provide a comprehensive analysis of the performance of this energy system was deployed. The developed WHR model is able to calculate energy balances for each of the main components of the WHR plant, based upon the heat transfer regimes that characterise heat recovery and HPs. One of the critical parameters analysed was the heat being recovered at the coils. As the amount of heat being extracted depends on the varying air conditions, the system operates in a transient manner. However, in order to facilitate the analysis and reduce computational effort, the model could be broken down into several steady state analyses that relate to specific time intervals. Therefore, the tool selected had to allow either a transient analysis of the system or operate with hourly or smaller time steps. Different software tools that could potentially be used to develop the WHR model were reviewed and a summary of this analysis is provided in Table A.1. The tools were compared according to different parameters, which are as follows:

- **Application:** a short description of the functionalities of the software tool analysed;
- **Utility:** a highlight of software features that could be useful for this investigation;
- **Level:** the scale for which the tool was developed, which can be either of the following:
    - **Local:** the software is focused on the analysis of small energy systems or components (e.g. heat sources, HPs, generation plants);
    - **District**: the software is focused on the holistic analysis of energy systems (e.g. district energy networks, communal systems, microgrids);
- **Granularity:** the smallest time step that can be applied with the analysed tool;
- **Flexibility:** an indication based on reviewed studies of how much the tool allows users to edit models and introduce components, which can be either of the following:
    - **Low:** unable to edit components;
    - **Medium:** editing of components is limited;
    - **High:** components can be edited freely.
- **Validation:** how the analysed model was validated according to one or more reviewed case studies;
- **Connectivity:** the format in which results can be exported/generated;
- **Availability:** if the tool is open i.e. available to users at no cost (free) or requires a paid-for license (commercial).

Table A.1 – A review of simulation tools that can be used to model WHR systems and district energy networks.

Tool	Application	Utility	Level	Granularity	Flexibility	Validation	Connectivity	Availability	References
CitySim	Building energy simulation tool that calculates building energy performance based on a resistor-capacitor thermal model	Estimating heating and cooling demand for buildings	Local	Hourly	Low	Experimental Data	Results can be exported to spreadsheets	Free	Walter & Kämpf (2015) Allegrini et al. (2015)
Coolpack	Uses EES to model refrigeration cycles based on user defined parameters	Refrigeration cycle analysis, component sizing, energy analysis and optimisation	Local	NA	Low	Not reported	Cycle diagrams can be printed as pdf files	Free	IPU (2019)
EES	Numerical equation solving based on written code	Can be used in different applications, including for analysing energy systems and heat transfer phenomena	Local	Sub-hourly	High	Experimental data	Results can be exported to text files and spreadsheets	Commercial	F-Chart Software (2019) Ghoubali et al. (2014) Madani et al. (2011)
EnergyPlus	Modelling energy consumption and water use for buildings and their energy systems	Energy consumption and generation for single buildings	Local	Sub-hourly	Medium	Experimental data	Results are exported as text files	Free	Allegrini et al. (2015) EnergyPlus (2019) Jeon et al. (2010)
EnergyPRO	Techno-economic optimisation of complex energy systems, combining electrical and thermal energy	Financial analysis of systems that involve the provision of electricity and/or thermal energy	District	Sub-hourly	Medium	Not reported	Results can be exported to spreadsheets	Commercial	Hinojosa et al. (2017) Revesz et al. (2020) Østergaard & Andersen (2019)
RETScreen	A spreadsheet based tool for feasibility and performance analysis of clean energy systems	Energy efficiency, renewable energy and cogeneration projects for buildings	Local or District	Monthly	Low	Experimental data and comparison to other tools	Detailed data outputs, but format not specified	Free	Allegrini et al. (2015) NRCan (2019) Lee et al. (2012)
Termis	Numerical simulation and optimisation of district energy networks	Achieving energy efficiency by manipulating operating parameters	District	Sub-hourly	Low	Experimental data	Results can be exported as GIS layers or to spreadsheets	Commercial	AVEVA (2019) Allegrini et al. (2015) Gabrielaitiene et al. (2007)
Thermos	Techno-economic analysis and routing of heat networks based on Geographic Information System (GIS) mapping	Feasibility study for district heating	District	Yearly	Low	Not reported	Results exportation as GIS files in future versions	Trial/Free	THERMOS (2019)
TRNSYS	Simulation and analysis of a variety of transient systems	Mostly applied to model thermal and electrical energy systems	Local or District	Sub-hourly	High	Experimental data	Results can be exported as spreadsheets and code can be used in other tools	Commercial	TRNSYS (2019) Allegrini et al. (2015) Safa et al. (2015)

Appendix B – WHR Model EES Code

```
$UnitSystem SI Mass kJ C kPa

Function p_drop (op_mode) {function to calculate fan pressure drop (Pa)}
 If (op_mode) = 1 Then {if operating in Extract, pressure drop is 105.9 Pa}
p_drop = 105.9 [Pa]
Else {if operating in Supply, pressure drop is 106.2 Pa}
p_drop = 106.2 [Pa]
Endif
End

Function lmxd (X_1,X_2) {function to prevent negative LMTD}
If (X_1/X_2) = 1 Then {prevents natural log equal to 0}
lmxd = 0
Goto 1
Else
If (X_1/X_2) < 0 Then {prevents a negative natural log}
lmxd = 0
Goto 1
Endif
Endif
lmxd = (X_2 - X_1)/ln(X_2/X_1) {log mean temperature/enthalpy difference}
1:
End

Function c1_thonon (BETA) {function to determine Thonon coefficient C1 based on chevron angle}
If BETA =< 30 Then
c1_thonon = 0.2964
Else
If (30<BETA) and (BETA=< 45) Then
c1_thonon = 0.2964+(0.2998-0.2964)*(BETA-30)/15
Else
If (45< BETA) and (BETA=<60) Then
c1_thonon = 0.2267+(0.2998-0.2267)*(60-BETA)/15
Else
If (60<BETA) and (BETA=<75) Then
c1_thonon = 0.1+(0.2267-0.1)*(75-BETA)/15
Else
If BETA > 75 Then
c1_thonon = 0.1
Endif
Endif
Endif
Endif
Endif
End

Function m_thonon (BETA) {function to determine Thonon coefficient m based on chevron angle}
If BETA =< 30 Then
m_thonon = 0.7
Else
If (30<BETA) and (BETA=< 45) Then
m_thonon = 0.645+(0.7-0.645)*(45-BETA)/15
Else
If (45< BETA) and (BETA=<60) Then
m_thonon = 0.631+(0.645-0.631)*(60-BETA)/15
Else
If (60<BETA) and (BETA=<75) Then
m_thonon = 0.631+(0.687-0.631)*(BETA-60)/15
Else
If BETA > 75 Then
m_thonon = 0.687
Endif
Endif
Endif
```

```
Endif
Endif
End

{INPUTS}
T_a_in {air inlet temperature (C)}
RH_in {air inlet relative humidity (dim)}
Operation_mode {Select operation mode: 1 for Extract, 0 for Supply}

{GENERAL PROPERTIES}
P_atm = 101.3 [kPa] {Atmospheric pressure}

{HEAT EXCHANGER}
"Coil geometry"
d_tube_ext = 0.012 [m] {tube external diameter}
t_tube = 0.0004 [m] {tube thickness}
d_tube_int = d_tube_ext - 2*t_tube {tube internal diameter (m)}
r_tube_int = d_tube_int/2 {tube internal radius (m)}
r_tube_ext = d_tube_ext/2 {tube external radius (m)}
A_face = L_coil*H_coil {coil face area (m2)}
L_coil = 4.75 [m] {coil length}
H_coil = 6.04 [m] {coil height}
D_coil = 0.29 [m] {coil depth}
N_rows = 12 [dim] {number of rows in each bank}
N_tubes = 2*25+2*26+2*28 [dim] {number of tubes per row (tubes high)}
S_L = 0.033 [m] {longitudinal coil pitch}
S_T = 0.0381 [m] {transversal coil pitch}
S_D = sqrt(S_L^2+(S_T/2)^2) {diagonal coil pitch (m)}
A_in = pi#*d_tube_int*L_coil*N_rows*N_tubes {total internal tube area (m2)}
A_out = pi#*d_tube_ext*L_coil*N_rows*N_tubes {total external tube area (m2)}
EPSILON_tube = 0.0000015 [m] {absolute roughness factor for copper pipes}
m = 0.6 [dim] {constant for calculating Nusselt number of air flow through a bank of tubes - Incropera}
C_1 = 0.35*(S_T/S_L)^0.2 {constant for Nusselt number of air flow through a bank of tubes - Incropera (dim)}
C_2 = 0.97+0.02/3 {correction factor for banks with 12 rows (interpolation between factors for 10 and 13 rows)}
A_tubes = (pi#*(d_tube_ext^2)/4)*N_tubes*N_rows {total tube cross section area per fin (m2)}
A_fin = 2*D_coil*H_coil - A_tubes {total sum area of fins (excluding tubes) for two banks (m2)}
d_fin = 2*sqrt(S_L*S_T/pi#) {diameter of the circular fin equivalent of a squared fin (m)}
L_fin = d_fin/2 - d_tube_ext/2 {fin length per single tube (m)}
s_fin = 0.00635 [m] {spacing gap between fins based on a fin density of 4 fpi}
t_fin = 0.00015 [m] {fin thickness}
N_fins = L_coil/g_fin {number of fins per bank based on a fin density of 4 fpi (dim)}
A_coil = A_fin*N_fins+A_out {total coil surface area, including fins (m2)}

"Fin efficiency"
i_c_sat_in = enthalpy(AirH2O, T=T_c_in, R=1, P=P_atm) {enthalpy for saturated air at the coolant inlet
temperature (kJ/kg)}
i_c_sat_out = enthalpy(AirH2O, T=T_c_out, R=1, P=P_atm) {enthalpy for saturated air at the coolant outlet
temperature (kJ/kg)}
C_ef = (i_c_sat_in - i_c_sat_out)/(converttemp(C,K,T_c_in) - converttemp(C,K,T_c_out)) {effective specific
heat for cooling coils (kJ/(kg*K)}
m_fin_d = sqrt(2*h_a/(k_t*t_fin)) {m =2*h/(k*t) for dry coils (1/m)}
ETA_fin_d = tanh(L_fin*m_fin_d)/(L_fin*m_fin_d) {fin efficiency (dim)}
ETA_o_d = 1 - (A_fin*N_fins/A_coil)*(1-ETA_fin_d) {global fin efficiency (dim)}
m_fin_w = sqrt(2*h_a*C_ef/(k_t*t_fin*C_p_a)) {m =2*h*Cs/(k*t*Cpa) for wet coils (1/m)}
ETA_fin_w = tanh(L_fin*m_fin_w)/(L_fin*m_fin_w) {fin efficiency (dim)}
ETA_o_w = 1 - (A_fin*N_fins/A_coil)*(1-ETA_fin_w) {global fin efficiency (dim)}

"Convection inside tube"
V_dot_tube = V_dot_c/(N_tubes*1.5) {volumetric flow rate of coolant for each tube based on type of circuit from
manufacturer (m3/s)}
V_dot_c = m_dot_c/average(density(Water,T=T_c_in,P=600[kPa]),density(Water,T=T_c_out,P=600[kPa]))
{coolant volumetric flow rate (m3/s)}
v_tube = V_dot_tube/(pi#*(d_tube_int^2)/4) {coolant flow velocity inside tubes (m/s)}
Re_tube =
v_tube*average(density(Water,T=T_c_in,P=600[kPa]),density(Water,T=T_c_out,P=600[kPa]))*d_tube_int/MU_
c {Reynolds number for coolant flow inside coils (dim)}
```

```
MU_c = average(viscosity(Water,T=T_c_in,P=600[kPa]),viscosity(Water,T=T_c_out,P=600[kPa])) {viscosity of the coolant (kg/(m*s))}
Pr_c = average(prandtl(Water,T=T_c_in,P=600[kPa]),prandtl(Water,T=T_c_out,P=600[kPa])) {Prandtl number for the coolant (dim)}
Call pipeflow_nd(Re_tube,Pr_c,L_coil/d_tube_int, EPSILON_tube/d_tube_int: ,Nu_c,f_c) {function to determine the Nusselt number for a constant wall heat flux (dim)}
k_c = average(conductivity(Water,T=T_c_in,P=600[kPa]),conductivity(Water,T=T_c_out,P=600[kPa])) {conductivity of coolant (W/(m*K))}
h_c = Nu_c*k_c/d_tube_int {convective heat transfer coefficient for flow inside coils (W/(m2*K)}
R_c = 1/(A_in*h_c) {coolant side thermal resistance (K/W)}

"Fouling resistance for closed-loop treated water"
XI_f = foulingfactor('Closed-loop treated water') {fouling factor for the coolant flowing inside the coils}
R_f = XI_f/(2*pi#*r_tube_int*L_coil*N_rows*N_tubes) {thermal resistance associated with fouling inside the tubes (K/W)}

"Conduction through tube walls"
k_t = average(conductivity(Copper,T=T_c_in),conductivity(Copper,T=T_c_out)) {conductivity of tube wall at inlet and outlet temperatures (W/(m*K)}
R_t = ln(r_tube_ext/r_tube_int)/(2*pi#*k_t*L_coil*N_rows*N_tubes) {thermal resistance to conduction through the tube walls (K/W)}

"Convection through a bank of tubes"
v_a = V_dot_a/A_face {air velocity through coil banks (m/s)}
v_a_max = S_T*v_a/(S_T-d_tube_ext) {maximum air velocity function for air flow through coils (m/s)}
Re_a = v_a_max*average(density(AirH2O,T=T_a_in,R=RH_in,P=P_atm),density(AirH2O,T=T_a_out,R=RH_out,P=P_atm))*d_tube_ext/MU_a {Reynolds number for air flow through coils (dim)}
MU_a = average(viscosity(AirH2O,T=T_a_in,R=RH_in,P=P_atm),viscosity(AirH2O,T=T_a_out,R=RH_out,P=P_atm)) {viscosity of air going through coils (kg/(m*s))}
Pr_a = average(prandtl(AirH2O,T=T_a_in,R=RH_in,P=P_atm),prandtl(AirH2O,T=T_a_out,R=RH_out,P=P_atm)) {Prandtl number for air going through coils (dim)}
Pr_a_w = average(prandtl(AirH2O,T=T_c_in,R=RH_in,P=P_atm),prandtl(AirH2O,T=T_c_out,R=RH_out,P=P_atm)) {Prandtl number at wall temperature for air going through coils (dim)}
Nu_a = C_1*C_2*(Re_a^m)*(Pr_a^0.36)*((Pr_a/Pr_a_w)^0.25) {Nusselt number for air flow across coils (dim) - Zukauskas (Incropera)}
k_a = average(conductivity(AirH2O,T=T_a_in,R=RH_in,P=P_atm),conductivity(AirH2O,T=T_a_out,R=RH_out,P=P_atm)) {conductivity of air going through coils (W/(m*K))}
h_a = Nu_a*k_a/d_tube_ext {convective heat transfer coefficient for air flow across coils (W/(m2*K))}
R_a_d = 1/(ETA_o_d*A_coil*h_a) {air side thermal resistance associated with dry coils (K/W)}
R_a_w = C_p_a*convert(kJ/(kg*K),J/(kg*K))/(ETA_o_w*A_coil*h_a) {air side enthalpic resistance associated with wet coils ((J/kg)/W)}

"Heat transfer calculations - dry surface"
U_d =1/(A_coil*(R_a_d+R_t+R_f+R_c)) {dry surface heat transfer coefficient for coils based on outside area (W/(m2*K)}
UA_d = U_d*A_coil*convert(W/K,kW/K) {UA value for dry coils (kW/K)}
dT_1 = T_a_x - T_c_x {outlet approach temperature for coils (K)}
dT_2 = T_a_in - T_c_out {inlet approach temperature for coils (K)}
Q_d = X*UA_d*LMTD {heat recovered from coils (kW)}
    LMTD = lmxd(dT_1,dT_2) {log mean temperature difference for coils}
Q_d = m_dot_a*C_p_a*(T_a_in - T_a_x) {sensible heat transfer on air side for dry coil fraction X (kW)}
Q_d = m_dot_c*C_p_c*(T_c_out - T_c_x) {sensible heat transfer on coolant side for dry coil fraction X (kW)}

"Point of condensation"
T_dp = dewpoint(AirH2O,T=T_a_in, R=RH_in, P=P_atm) {dew point of air at inlet conditions (C)}
(T_a_x - T_dp)/R_a_d = (T_dp - T_c_x)/(R_f+R_t+R_c) {calculation of air and coolant conditions for a surface temperature equal to the dew point of air}

"Heat transfer calculations - wet surface"
R_o_w = R_a_w + C_ef*convert(kJ/(kg*K),J/(kg*K))*(R_t+R_f+R_c) {wet surface overall enthalpic resistance for coils based on outside area ((J/kg)/W)}
```

```
U_w =1/(A_coil*R_o_w) {wet surface energy transfer coefficient for coils based on outside area (W/(m2*(J/kg))}
UA_w = U_w*A_coil*convert(W/(J/kg),kW/(kJ/kg)) {UA value for wet coils (kW/(kJ/kg))}
dE_1 = i_a_out - i_c_sat_in {outlet approach temperature for coils (K)}
dE_2 = i_a_x - i_c_sat_x {inlet approach temperature for coils (K)}
Q_w = (1-X)*UA_w*LMED {heat recovered from coils (kW)}
   LMED = lmxd(dE_1,dE_2) {log mean temperature difference for coils}
i_a_x = enthalpy(AirH2O,T=T_a_x, w=OMEGA_in, P=P_atm) {enthalpy of air at point of condensation (kJ/kg)}
i_c_sat_x = enthalpy(AirH2O,T=T_c_x, R=1, P=P_atm) {enthalpy of air at point of condensation (kJ/kg)}
Q_w = (i_a_x*m_dot_a) - (i_a_out*(m_dot_a-(m_w_c*convert(kg/h,kg/s)))) {heat transfer on air side for wet coil fraction (kW)}
Q_w = m_dot_c*C_p_c*(T_c_x - T_c_in) {heat transfer on coolant side for wet coil fraction (kW)}

"Air side heat transfer"
V_dot_a = 70 [m^3/s] {air volumetric flow rate}
RHO_a = density(AirH2O,T=T_a_in,R=RH_in,P=P_atm) {air density at inlet conditions (kg/m3)}
m_dot_a = V_dot_a*RHO_a {air mass flow rate (kg/s)}
C_p_a =
average(specheat(AirH2O,T=T_a_in,R=RH_in,P=P_atm),specheat(AirH2O,T=T_a_out,R=RH_out,P=P_atm))
{air specific heat at inlet conditions (kJ/(kg*K)}
Q_sen = C_p_a*((T_a_in*m_dot_a)-(T_a_out*(m_dot_a-(m_w_c*convert(kg/h,kg/s))))) {sensible cooling to the air stream (kW)}
SHR = Q_sen/Q_rec {sensible heat ratio for heat recovery process (dim)}

"Air inlet conditions"
i_a_in = enthalpy(AirH2O,T=T_a_in,R=RH_in,P=P_atm) {enthalpy of air at inlet conditions (kJ/kg)}
OMEGA_in = humrat(AirH2O,T=T_a_in,R=RH_in,P=P_atm) {moisture content of air at inlet conditions (kg/kg)}
m_dot_a_d = m_dot_a/(1+OMEGA_in) {mass flow rate of dry air (kg/s)}

"Air outlet conditions"
EPSILON_w = (i_a_x - i_a_out)/(i_a_x - i_c_sat_in) {enthalpy effectiveness for the coils (dim)}
EPSILON_w = (OMEGA_in - OMEGA_out)/(OMEGA_in - humrat(AirH2O,h=i_c_sat_in,R=1,P=P_atm))
{humidity effectiveness for the coils (dim)}
T_a_out = temperature(AirH2O,h=i_a_out,w=OMEGA_out,P=P_atm) {air outlet temperature (C)}
RH_out = relhum(AirH2O,T=T_a_out,w=OMEGA_out,P=P_atm) {moisture content of air at outlet conditions (kg/kg)}
m_w_c = (OMEGA_in - OMEGA_out)*m_dot_a_d*convert(kg/s,kg/h) {mass of condensate generated per hour (kg/h)}

"Coolant side heat transfer"
m_dot_c = 37.6 [kg/s] {coolant mass flow rate}
C_p_c = average(specheat(Water,T=T_c_in,P=600[kPa]),specheat(Water,T=T_c_out,P=600[kPa])) {specific heat of coolant at inlet conditions (kJ/(kg*K))}
Q_rec = Q_d + Q_w {coolant side heat recovery (kW)}

{HEAT PUMP}
"Refrigerant"
R$='Ammonia'
"EVAPORATOR 1-2"
Q_rec = Q_evap {heat recovered at coils is equal to heat absorbed at evaporator (kW)}
dT_evap_1 = T_c_in - T_evap {outlet approach temperature for evaporator (K)}
dT_evap_2 = T_c_out - T_evap {inlet approach temperature for evaporator (K)}
Q_evap = UA_evap*LMTD_evap {heat transfer at evaporator (kW)}
UA_evap = U_evap*A_evap {UA value for evaporator (kW/K)}
U_evap = (1/(1/h_r_evap+1/h_c_evap+R_plate_evap))*convert(W/(K*m2),kW/(K*m2)) {overall heat transfer coefficient for evaporator (kW/(K*m2))}
   LMTD_evap = lmxd(dT_evap_1,dT_evap_2) {log mean temperature difference for evaporator (K)}
x_r_1a = 0 {quality of refrigerant at evaporator inlet - saturated liquid (dim)}
x_r_2 = 1 {quality of refrigerant at evaporator inlet - saturated vapour (dim)}
P_evap = pressure(R$,T=T_evap,x=x_r_1a) {evaporating pressure [kPa]}
i_r_1a = enthalpy(R$,T=T_evap,x=x_r_1a) {refrigerant enthalpy at evaporator inlet (kJ/kg)}
i_r_2 = enthalpy(R$,T=T_evap,x=x_r_2) {refrigerant enthalpy at evaporator outlet (kJ/kg)}
m_dot_r_1a = m_dot_r_2 {mass balance at evaporator (kg/s)}
Q_evap = m_dot_r_1a*(i_r_2 - i_r_1a) {heat absorbed by refrigerant at evaporator (kW)}

"PHE geometry"
BETA_evap = 60 [degrees] {chevron angle for evaporator plates}
```

N_plate_evap = 342 [dim] {number of plates in evaporator}
d_plate_evap = 0.556 [m] {plate diameter for evapator}
d_plate_evap_imp = d_plate_evap***convert**(m,ft) {plate diameter for evapator - imperial units (ft)}
t_plate_evap = 0.0008 [m] {plate thickness for evaporator}
A_plate_evap = 0.26 [m2] {area per plate for evaporator}
L_plate_evap = 1.015 [m] {plate patch length for evaporator (m)}
A_evap = N_plate_evap*A_plate_evap {surface area for evaporator (m2)}
d_nozzle_evap = 0.1143-2*0.00602 {nozzle diameter for evaporator (m)}
A_nozzle_evap = pi#*(d_nozzle_evap/2)^2 {nozzle area for evaporator (m2)}
A_proj_evap = pi#*(d_plate_evap/2)^2 - 2*A_nozzle_evap {projected area for evaporator (m2)}
PHI_evap = A_plate_evap/A_proj_evap {surface enlargement factor for evaporator (dim)}
w_plate_evap = (pi#*(d_plate_evap/2)^2)/d_plate_evap {plate width for evaporator, considering a fictitious squared area (m)}
p_plate_evap = L_plate_evap/N_plate_evap {plate pitch for evaporator (m)}
b_plate_evap = p_plate_evap - t_plate_evap {channel spacing for evaporator (m)}
d_evap = 2*b_plate_evap/PHI_evap {hydraulic diameter for evaporator (m)}
d_evap_imp = d_evap***convert**(m,ft) {hydraulic diameter for evaporator - imperial units (ft)}
N_p_evap = 1 {number of passes for evaporator (dim)}
N_cp_evap = (N_plate_evap - 1)/(2*N_p_evap) {number of channels per pass for evaporator (dim)}

"Refrigerant flow"
G_r_evap = m_dot_r_1a/(N_cp_evap*b_plate_evap*w_plate_evap) {refrigerant mass flux for evaporator (kg/(m2*s))}
k_r_1a = **conductivity**(R$,***T***=T_evap,***x***=x_r_1a) {conductivity for liquid refrigerant at evaporator (W/(m*K))}
k_r_1a_imp = k_r_1a***convert**(W/(m*K),BTU/(hr*ft*R)) {conductivity for liquid refrigerant at evaporator - imperial units (BTU/(hr*ft*R))}
MU_r_1a = **viscosity**(R$,***T***=T_evap,***x***=x_r_1a) {viscosity for liquid refrigerant at evaporator}
i_f_g_evap = **enthalpy_vaporization**(R$,***T***=T_evap) {heat of vaporisation at evaporating temperature (kJ/kg)}
i_f_g_evap_imp = i_f_g_evap***convert**(kJ/kg,BTU/lb_m) {heat of vaporisation at evaporating temperature - imperial units (BTU/lb_m)}
P_crit = **p_crit**(R$) {critical pressure for refrigerant (kPa)}
Re_r_1a = G_r_evap*d_evap/MU_r_1a {Reynolds number for liquid refrigerant at evaporator (dim)}
h_r_evap_imp =
0.1121*(k_r_1a_imp/d_evap_imp)*(((Re_r_1a^2)*i_vap_evap_imp/d_plate_evap_imp)^0.4124)*((P_evap/P_crit)^0.12)*((65/BETA_evap)^0.35) {convective heat transfer coefficient for refrigerant flowing through evaporator - imperial units (BTU/(hr*ft2*R)}
h_r_evap = h_r_evap_imp***convert**(BTU/(hr*ft2*R),W/(m2*K)) {convective heat transfer coefficient for refrigerant flowing through evaporator (W/(m2*K)}

"Coolant flow"
G_c_evap = m_dot_c/(N_cp_evap*b_plate_evap*w_plate_evap) {coolant mass flux for evaporator (kg/(m2*s))}
Re_c_evap = G_c_evap*d_evap/MU_c {Reynolds number for coolant at evaporator (dim)}
C1_evap = **c1_thonon**(BETA_evap) {function to determine Thonon coefficient C1}
m_evap = **m_thonon**(BETA_evap) {function to determine Thonon coefficient m}
Nu_c_evap = C1_evap*(Re_c_evap^m_evap)*(Pr_c^(1/3)) {Nusselt number for coolant at evaporator based on Thonon correlation (dim)}
k_c_evap = **average**(**conductivity**(***Water***,***T***=T_c_in,***P***=600[kPa]),**conductivity**(***Water***,***T***=T_c_out,***P***=600[kPa])) {conductivity for coolant at evaporator (dim)}
h_c_evap = Nu_c_evap*k_c_evap/d_evap {convective heat transfer coefficient for coolant flowing through evaporator (W/(m2*K)}

"Plate resistance"
k_plate_evap = 14 [W/(m*K)] {plate conductivity as per design specs}
R_plate_evap = t_plate_evap/k_plate_evap {conductive thermal resistance for evaporator plates ((m2*K)/W)}

"LOW-STAGE SUCTION LINE 2-3"
DELTAP_2_3 = 0.013***convert**(bar,kPa) {design pressure drop across low-stage suction line (kPa)}
P_ls_suction = **p_sat**(R$,***T***=T_evap - 1[C]) - DELTAP_2_3 {low-stage compressor suction pressure based on superheat of 1K (kPa)}
m_dot_r_3 = m_dot_r_1b + m_dot_r_2 {mass balance at low-stage suction line (kg/s)}

"LOW-STAGE COMPRESSOR 3-4"
P_rat = P_int/P_evap {low-stage compressor pressure ratio (dim)}
ETA_comp_ls = -0.0383*(P_rat^2) + 0.2287*P_rat + 0.5448 {low-stage compressor isentropic efficiency based on pressure ratio and design specs (dim)}
ETA_comp_ls = (i_r_4s - i_r_3)/(i_r_4 - i_r_3) {isentropic efficiency of low-stage compressor (dim)}

i_r_3 = i_r_2 {enthalpy of refrigerant at low-stage compressor inlet (kJ/kg)}
s_r_3 = **entropy**(R$,***h***=i_r_3,***P***=P_ls_suction) {specific entropy at low-stage compressor inlet conditions (kJ/(kg*K)), considering a superheat of 1K}
i_r_4s = **enthalpy**(R$,***s***=s_r_3,***P***=P_ls_discharge) {enthalpy for an isentropic compression (kJ/kg)}
W_comp_ls = m_dot_r_4*(i_r_4 - i_r_3) {work input into the low-stage compressor (kW)}
T_r_4 = **temperature**(R$,***h***=i_r_4,***P***=P_ls_discharge) {refrigerant temperature ap=600[kPa]t low-stage compressor outlet (C)}

"LOW-STAGE DISCHARGE LINE 4-5"
DELTAP_4_5 = 0.253***convert**(bar,kPa) {design pressure drop across low-stage discharge line (kPa)}
P_ls_discharge = P_int + DELTAP_4_5 + DELTAP_ds_ls {low-stage compressor discharge pressure (kPa)}
m_dot_r_4 = **average**(m_dot_r_3,m_dot_r_5) {mass balance at low-stage discharge line (kg/s)}

"LOW-STAGE DESUPERHEATER 5-6"
m_dot_w = 12.4 [kg/s] {mass flow rate of hot loop water}
T_w_5 = 55 [C] {water temperature at low-stage desuperheater inlet}
UA_ds_ls = 4.796 [kW/K] {UA value for low-stage desuperheater (kW/K)}
dT_ds_ls_1 = T_r_6 - T_w_5 {outlet approach temperature for low-stage desuperheater (K)}
dT_ds_ls_2 = T_r_5 - T_w_6 {inlet approach temperature for low-stage desuperheater (K)}
Q_ds_ls = UA_ds_ls*LMTD_ds_ls {heat transfer at low-stage desuperheater (kW)}
LMTD_ds_ls = **lmxd**(dT_ds_ls_1,dT_ds_ls_2) {log mean temperature difference for low-stage desuperheater (K)}
C_p_w_ds_ls = **average**(**specheat**(***Water***,***T***=T_w_5,***P***=600[kPa]),**specheat**(***Water***,***T***=T_w_6,***P***=600[kPa])) {average specific heat of water flowing through the low-stage desuperheater}
Q_ds_ls = m_dot_w*C_p_w_ds_ls*(T_w_6 - T_w_5) {heat absorbed by water at low-stage desuperheater (kW)}
Q_ds_ls = m_dot_r_5*(i_r_5 - i_r_6) {heat absorbed by refrigerant at low-stage desuperheater (kW)}
i_r_5 = i_r_4 {refrigerant temperature at low-stage desuperheater inlet (kJ/kg)}
T_r_5 = **temperature**(R$,***h***=i_r_5,***P***=P_int+DELTAP_ds_ls) {enthalpy of refrigerant at low-stage desuperheater inlet (kJ/kg)}
T_r_6 = **temperature**(R$,***h***=i_r_6,***P***=P_int) {refrigerant enthalpy at low-stage desuperheater outlet (kJ/kg)}
m_dot_r_5 = m_dot_r_6 {mass balance at low-stage desuperheater (kg/s)}
DELTAP_ds_ls = 0.7 [kPa] {design pressure drop across low-stage desuperheater (kPa)}

"LOW-STAGE EXPANSION VALVE AND SEPARATOR 7-1"
m_dot_r_7 = m_dot_r_1 {mass balance at low-stage expansion valve (kg/s)}
m_dot_r_1 = m_dot_r_1a + m_dot_r_1b {mass balance at low-stage expansion valve outlet (kg/s)}
i_r_7 = **enthalpy**(R$,***P***=P_int,***x***=x_r_7) {refrigerant enthalpy at low-stage expansion valve inlet (kJ/kg)}
x_r_7 = 0 {refrigerant quality at low-stage expansion valve inlet (dim)}
i_r_7 = i_r_1 {refrigerant enthalpy conservation at low-stage expansion valve (kJ/kg)}
x_r_1 = **quality**(R$,***P***=P_evap,***h***=i_r_1) {refrigerant quality at low-stage expansion valve outlet (dim)}
m_dot_r_1b = x_r_1*m_dot_r_1 {mass flow rate of refrigerant going from low-stage expansion valve to evaporator (kg/s)}

"SEPARATOR 6,7,8,13"
T_int = 42 [C] {Separator temperature}
P_int = **p_sat**(R$,***T***=T_int) {Saturation pressure at separator temperature (kPa)}
m_dot_r_6 + m_dot_r_13 = m_dot_r_7 + m_dot_r_8 {mass balance at separator (kg/s)}
m_dot_r_6*i_r_6 + m_dot_r_13*i_r_13 = m_dot_r_7*i_r_7 + m_dot_r_8*i_r_8 {energy balance at separator (kW)}

"HIGH-STAGE SUCTION LINE 8-9"
DELTAP_8_9 = 0.059***convert**(bar,kPa) {design pressure drop across high-stage suction line (kPa)}
P_hs_suction = P_int - DELTAP_8_9 {high-stage compressor suction pressure with no superheat (kPa)}
m_dot_r_8 = m_dot_r_9 {mass balance at high-stage suction line (kg/s)}
i_r_8 = **enthalpy**(R$,***P***=P_int,***x***=x_r_8) {enthalpy of refrigerant at high-stage separator exit - saturated vapour (kJ/kg)}
x_r_8 = 1 {quality of refrigerant at high-stage separator exit - saturated vapour (dim)}

"HIGH-STAGE COMPRESSOR 9-10"
ETA_comp_hs = 0.88 [dim] {isentropic efficiency of high-stage compressor (dim)}
ETA_comp_hs = (i_r_10s - i_r_9)/(i_r_10 - i_r_9) {isentropic efficiency of low-stage compressor (dim)}
i_r_9 = i_r_8 {refrigerant enthalpy at high-stage compressor inlet (kJ/kg)}
s_r_9 = **entropy**(R$,***h***=i_r_9,***P***=P_hs_suction) {specific entropy at high-stage compressor inlet conditions (kJ/(kg*K))}
i_r_10s = **enthalpy**(R$,***s***=s_r_9,***P***=P_hs_discharge) {enthalpy for an isentropic compression (kJ/kg)}
W_comp_hs = m_dot_r_10*(i_r_10 - i_r_9) {work input into the high-stage compressor (kW)}

T_r_10 = **temperature**(R$,***h***=i_r_10,***P***=P_hs_discharge) {refrigerant temperature at high-stage compressor outlet (C)}

"HIGH-STAGE DISCHARGE LINE 10-11"
DELTAP_10_11 = 0.1605***convert**(bar,kPa) {design pressure drop across high-stage discharge line (kPa)}
P_hs_discharge = P_cond + DELTAP_10_11 + DELTAP_cond {high-stage compressor discharge pressure (kPa)}
m_dot_r_10 = **average**(m_dot_r_9,m_dot_r_11) {mass balance at high-stage discharge line (kg/s)}

"CONDENSER 11-12"
T_w_12 = 75 [C] {water temperature at condenser inlet}
T_w_11 = T_w_6 {water temperature at condenser outlet}
UA_cond = 76.55 [kW/K] {UA value for condenser (kW/K)}
dT_cond_1 = T_r_12 - T_w_11 {outlet approach temperature for condenser (K)}
dT_cond_2 = T_r_11 - T_w_12 {inlet approach temperature for condenser (K)}
Q_cond = UA_cond*LMTD_cond {heat transfer at condenser (kW)}
LMTD_cond = **lmxd**(dT_cond_1,dT_cond_2) {log mean temperature difference for condenser (K)}
C_p_w_cond = **average**(**specheat**(***Water***,***T***=T_w_12,***P***=600[kPa]),**specheat**(***Water***,***T***=T_w_11,***P***=600[kPa])) {average specific heat of water flowing through the condenser}
Q_cond = m_dot_w*C_p_w_cond*(T_w_12 - T_w_11) {heat absorbed by water at condenser (kW)}
P_cond = **p_sat**(R$,***T***=T_cond) {condensing pressure (kPa)}
DELTAP_cond = 2.1 [kPa] {design pressure drop across high-stage heat exchangers (kPa)}
T_cond = T_w_12 + 1 {condensing temperature}
Q_cond = m_dot_r_12*(i_r_11 - i_r_12) {heat rejected by refrigerant at condenser (kW)}
i_r_11 = i_r_10 {refrigerant enthalpy at condenser inlet (C)}
T_r_11 = **temperature**(R$,***h***=i_r_11,***P***=(P_cond+DELTAP_cond)) {refrigerant enthalpy at condenser inlet (kJ/kg)}
i_r_12 = **enthalpy**(R$,***T***=T_r_12,***P***=P_cond) {refrigerant temperature at condenser outlet (kJ/kg)}
m_dot_r_11 = m_dot_r_12 {mass balance at condenser (kg/s)}

"HIGH-STAGE EXPANSION VALVE 12-13"
m_dot_r_12 = m_dot_r_13 {mass balance at high-stage expansion valve (kg/s)}
i_r_12 = i_r_13 {refrigerant enthalpy conservation at high-stage expansion valve (kJ/kg)}
x_r_13 = **quality**(R$,***P***=P_int,***h***=i_r_13) {refrigerant quality at high-stage expansion valve (dim)}

"COEFFICIENT OF PERFORMANCE"
ETA_m = 0.92 [dim] {compressor average motor efficiency (dim)}
W_hp = (W_comp_ls + W_comp_hs)/ETA_motor {Total heat pump work input is equal to the sum of work input to low-stage and high-stage compressors divided by motor efficiency(kW)}
Q_out = Q_cond + Q_ds_ls {Total heat pump output is equal to the sum of heat outputs from heat exchangers (kW)}
COP_h = Q_out/W_hp {heating COP (dim)}
COP_c = COP_h - (1*ETA_m) {cooling COP (dim), accounting for the motor efficiency}
COP_c = Q_evap/W_hp {cooling COP (dim)}

{FAN}
"Fan power consumption"
ETA_f = 0.595 [dim] {fan efficiency of 59.5%}
W_f = DELTAP_f*V_dot_a/ETA_f***convert**(W,kW) {fan additional power consumption associated with pressure drop (kW)}
DELTAP_f = **p_drop**(Operation_mode) {function to calculate fan pressure drop (kPa)}

{COOLANT LOOP}
"Pumping power consumption"
W_p = (H_total*g#*m_dot_c)/(ETA_p)***convert**(W,kW) {pump power consumption for the coolant loop (kW)}
ETA_p = 0.5 [dim] {pump efficiency of 50%}
H_total = H_static + H_components + H_dynamic {total head loss to be overcome (m)}

"Static head loss calculation"
H_static = 5 [m] {static head the pump needs to overcome, assuming a height of 5 metres}

"Heat exchanger head loss calculation"
H_components = H_coils + H_evap {total head loss associated with main connections of coolant loop (m)}
H_coils = (DELTAP_c_coils***convert**(kPa,Pa))/(g#***average**(**density**(***Water***,***T***=T_c_in,***P***=600[kPa]),**density**(***Water***,***T***=T_c_out,***P***=600[kPa]))) {head loss associated with heat recovery coils (m)}
DELTAP_c_coils = 134 [kPa] {coolant pressure loss through the heat recovery coils}

H_evap =
(DELTAP_c_evap***convert**(kPa,Pa))/(g#***average**(**density**(***Water***,***T***=T_c_in,***P***=600[kPa]),**density**(***Water***,***T***=T_c_out,***P***=600[kPa]))) {head loss associated with evaporator (m)}
DELTAP_c_evap = 20 [kPa] {coolant pressure loss through the evaporator}

"Dynamic head loss calculation"
H_dynamic = (K_total*(v_loop^2))/(2*g#) {the Darcy Weisbach equation for calculating dynamic head loss (m)}

"flow velocity calculation"
v_loop = V_dot_c/A_loop {coolant velocity across the loop (m/s)}
A_loop = (d_loop^2)*pi#/4 {coolant loop pipe cross section area (m2)}
d_loop = 0.1541 [m] {coolant loop pipe diameter (m)}

"Head loss coefficient calculation"
K_total = K_fit + K_loop {total head loss coefficient (dim)}

"Head loss coefficient for pipe fittings"
K_fit = K_in + K_90 + K_45 + K_but + K_nr + K_out {total head loss coefficient for pipe fittings (dim)}
K_in = 2*0.05 {head loss coefficient for 2 inlet bellmouth valves}
K_90 = 10*0.75 {head loss coefficient for 10 90deg bends}
K_45 = 6*0.3 {head loss coefficient for 6 45deg bends}
K_but = 2*0.3 {head loss coefficient for 2 butterfly valves}
K_nr = 2*1 {head loss coefficient for 2 non-return valves}
K_out = 2*0.2 {head loss coefficient for 2 outlet bellmouth valves}

"Head loss coefficient for coolant loop length"
K_loop = f_loop*L_loop/d_loop {total head loss coefficient associated with loop length (dim)}
L_loop = 20 [m] {assumed total loop length of 20 metres}
Call **pipeflow_nd**(Re_loop,Pr_c,L_loop/d_loop, EPSILON_loop/d_loop: ,,f_loop) {fuction to determine friction coefficient associated with coolant flow through the loop (dim)}
EPSILON_loop = 0.000046 [m] {absolute roughness factor for stainless steel pipes}
Re_loop =
v_loop***average**(**density**(***Water***,***T***=T_c_in,***P***=600[kPa]),**density**(***Water***,***T***=T_c_out,***P***=600[kPa]))*d_loop/MU_c
{Reynolds number for coolant flow within the loop (dim)}

{SYSTEM EFFICIENCY}
"Heating and cooling Coefficient of System Performance (COSP)"
W_total = W_hp + W_f + W_p {total work input into the system (kW)}
COSP_h = Q_out/W_total {heating COSP (dim)}
COSP_c = Q_evap/W_total {cooling COSP (dim)}

Appendix C – WHR Model Results for Average Monthly Conditions

Table C.1 – Results from the WHR model for full-load Extract Mode operation, with water used as coolant (part I).

Month	Coil Condition	T_a_in (C)	RH_in	T_dp (C)	ω_in (kg/kg)	i_a_in (kJ/kg)	Ta_x (C)	i_a_x (kJ/kg)	T_a_out (C)	RH_out	ω_out (kg/kg)	i_a_out (kJ/kg)	T_c_out (C)	T_c_in (C)	i_c_sat_in (kJ/kg)	T_c_out (C)	i_c_sat_out (kJ/kg)	Nu_a	Re_a	h_a (W/m^{2}K)	Nu_c	Re_c
January	Partial	18.27	50%	7.68	0.0065	34.85	10.88	27.35	9.66	85%	0.006341	25.66	7.03	6.12	20.83	11.04	31.74	37.72	2916	77.68	118.3	13203
February	Dry	16.82	42%	3.85	0.0050	29.50	0.00	0.00	7.87	76%	0.00498	20.43	0.00	4.75	0.00	9.63	0.00	37.96	2947	77.77	115.8	12663
March	Partial	14.43	47%	3.27	0.0048	26.57	5.95	17.98	5.72	84%	0.004764	17.71	2.70	2.55	13.94	7.36	23.40	38.29	2989	77.9	111.9	11815
April	Partial	16.63	50%	6.17	0.0059	31.55	9.36	24.16	8.11	85%	0.005706	22.49	5.51	4.61	17.82	9.48	28.08	37.95	2946	77.77	115.6	12608
May	Partial	19.71	48%	8.40	0.0068	37.16	11.32	28.63	10.73	85%	0.006776	27.86	7.81	7.40	23.49	12.36	34.97	37.54	2893	77.61	120.5	13712
June	Partial	21.60	52%	11.33	0.0084	42.91	14.76	35.93	13.12	86%	0.008031	33.45	10.65	9.33	27.74	14.34	40.18	37.23	2854	77.49	123.8	14498
July	Partial	23.64	57%	14.63	0.0104	50.19	18.34	44.76	15.91	86%	0.00972	40.57	13.91	11.69	33.31	16.76	47.06	36.9	2810	77.37	127.8	15477
August	Partial	23.99	54%	14.12	0.0101	49.67	17.69	43.23	15.76	86%	0.009571	40.03	13.42	11.73	33.42	16.80	47.19	36.88	2809	77.36	127.8	15496
September	Partial	23.03	53%	12.94	0.0093	46.78	16.45	40.06	14.66	86%	0.008899	37.21	12.25	10.75	31.03	15.79	44.23	37.03	2827	77.41	126.2	15083
October	Partial	22.07	55%	12.62	0.0091	45.29	16.25	39.35	14.05	86%	0.008584	35.80	11.90	10.01	29.30	15.04	42.10	37.14	2841	77.46	125	14779
November	Dry	20.02	45%	7.74	0.0065	36.69	0.00	0.00	10.84	81%	0.006538	27.37	0.00	7.71	0.00	12.68	0.00	37.51	2890	77.59	121.1	13838
December	Partial	19.07	47%	7.51	0.0064	35.47	10.23	26.48	10.01	84%	0.006417	26.22	6.96	6.82	22.26	11.75	33.47	37.64	2906	77.65	119.5	13478

Table C.2 – Results from the WHR model for full-load Extract Mode operation, with water used as coolant (part II).

Month	Coil Condition	h_c (W/m^{2}K)	U_d (W/m^{2}K)	UA_d (kW/K)	Q_d (kW)	X	U_w (W*kg/m^2*J)	UA_w (kW/[kJ/kg])	ε_w	Q_w (kW)	Q_rec (kW)	SHR	Q_sen (kW)	m_cond (kg)	T_evap (C)	h_r_evap (W/m^{2}K)	h_c_evap (W/m^{2}K)	U_evap (kW/m^{2}K)	UA_evap (kW/K)	P_evap (kPa)	i_r_1a (kJ/kg)	ir_2 (kJ/kg)
January	Partial	6083	56.48	158.1	633.8	74.7%	0.0424	118.8	0.26	142.4	776.1	95%	739.3	52.02	3.845	4856	4406	2.041	181.4	494.9	217.7	1466
February	Dry	5926	56.4	157.9	0	0.0%	0.0000	0	0.00	0	770	100%	770	0	2.431	4764	4337	2.01	178.7	470	211.1	1465
March	Partial	5672	56.26	157.5	735.9	95.0%	0.0443	124.1	0.07	23.17	759	100%	755.6	4.897	0.164	4613	4225	1.958	174.1	432.2	200.6	1462
April	Partial	5910	56.39	157.9	627.1	74.6%	0.0433	121.1	0.26	142.2	769.3	96%	734.9	48.76	2.285	4755	4330	2.006	178.4	467.5	210.4	1465
May	Partial	6227	56.54	158.3	716.5	87.1%	0.0417	116.8	0.15	65.03	781.5	98%	766.9	20.62	5.159	4940	4469	2.069	184	518.9	223.8	1467
June	Partial	6443	56.63	158.5	581.4	66.3%	0.0406	113.5	0.30	207.7	789.1	91%	721.2	95.17	7.149	5066	4564	2.111	187.7	557	233	1469
July	Partial	6702	56.73	158.8	448.7	50.7%	0.0391	109.4	0.37	349	797.7	82%	655.2	198.7	9.569	5217	4677	2.162	192.2	606.2	244.4	1472
August	Partial	6707	56.73	158.8	532.1	59.8%	0.0390	109.3	0.33	265.8	797.9	87%	696.5	141.4	9.615	5220	4679	2.162	192.3	607.2	244.6	1472
September	Partial	6599	56.69	158.7	557.1	62.9%	0.0397	111.1	0.32	237.3	794.3	89%	709.6	118.5	8.602	5156	4632	2.141	190.4	586.2	239.8	1471
October	Partial	6519	56.66	158.6	494.4	55.8%	0.0401	112.3	0.35	297.2	791.6	86%	682	153.4	7.849	5109	4597	2.126	189	570.9	236.3	1470
November	Dry	6262	56.56	158.4	0	0.0%	0.0000	0	0.00	0	782.7	100%	782.7	0	5.479	4960	4484	2.076	184.6	524.9	225.3	1468
December	Partial	6161	56.52	158.2	756.7	95.2%	0.0421	117.8	0.06	22.32	779.1	99%	775	5.695	4.556	4902	4440	2.056	182.8	507.8	221	1467

Table C.3 – Results from the WHR model for full-load Extract Mode operation, with water used as coolant (part III).

Month	Coil Condition	m_r_1a (kg/s)	m_r_1b (kg/s)	Q_ds_ls (kW)	i_r_5 (kJ/kg)	i_r_6 (kJ/kg)	T_w_6 (C)	T_r_5 (C)	T_r_6 (C)	m_r_5 (kg/s)	Q_cond (kW)	i_r_11 (kJ/kg)	i_r_12 (kJ/kg)	T_r_11 (C)	T_r_12 (C)	m_r_12 (kg/s)	COP_c	COP_h	W_hp (kW)	W_system (kW)	COSP_c	COSP_h	Q_out (kW)
January	Partial	0.622	0.107	89.02	1671	1549	56.72	103.5	59.91	0.728	949.3	1626	485.5	113	58.81	0.833	2.72	3.64	285	315	2.46	3.30	1038.3
February	Dry	0.614	0.109	94.68	1681	1550	56.83	107	60.13	0.724	943.7	1626	485.8	113	58.88	0.828	2.64	3.56	291.7	321.7	2.39	3.23	1038.4
March	Partial	0.602	0.113	105	1698	1551	57.03	113.6	60.5	0.715	933.3	1626	486.4	113	59	0.819	2.50	3.42	303.6	333.6	2.28	3.11	1038.3
April	Partial	0.613	0.110	95.29	1682	1550	56.84	107.4	60.15	0.723	943	1626	485.8	113	58.89	0.827	2.63	3.55	292.4	322.4	2.39	3.22	1038.3
May	Partial	0.628	0.104	84.18	1664	1549	56.62	100.5	59.72	0.732	954.2	1626	485.2	113	58.76	0.837	2.80	3.72	279.2	309.2	2.53	3.36	1038.4
June	Partial	0.638	0.100	77.42	1653	1548	56.49	96.39	59.44	0.738	960.9	1626	484.8	113	58.68	0.842	2.91	3.83	270.9	300.9	2.62	3.45	1038.3
July	Partial	0.650	0.095	69.85	1641	1547	56.35	91.9	59.1	0.745	968.5	1626	484.3	113	58.59	0.849	3.05	3.97	261.6	291.5	2.74	3.56	1038.4
August	Partial	0.650	0.095	69.72	1640	1547	56.34	91.82	59.1	0.745	968.6	1626	484.3	113	58.59	0.849	3.05	3.97	261.4	291.4	2.74	3.56	1038.3
September	Partial	0.645	0.097	72.81	1645	1547	56.4	93.64	59.24	0.742	965.5	1626	484.5	113	58.63	0.846	3.00	3.92	265.2	295.2	2.69	3.52	1038.3
October	Partial	0.642	0.099	75.17	1649	1547	56.45	95.04	59.34	0.740	963.2	1626	484.6	113	58.65	0.844	2.95	3.87	268.2	298.2	2.66	3.48	1038.4
November	Dry	0.630	0.103	83.05	1662	1548	56.6	99.79	59.67	0.733	955.3	1626	485.1	113	58.75	0.838	2.82	3.74	277.8	307.8	2.54	3.37	1038.4
December	Partial	0.625	0.105	86.36	1667	1549	56.67	101.8	59.8	0.731	952	1626	485.3	113	58.78	0.835	2.76	3.68	281.8	311.8	2.50	3.33	1038.4

Table C.4 – Results from the WHR model for full-load Supply Mode operation, with a PG 30% mixture used as coolant (part I).

Month	Coil Condition	T_a_in (C)	RH_in	T_dp (C)	ω_in (kg/kg)	i_a_in (kJ/kg)	Ta_x (C)	i_a_x (kJ/kg)	T_a_out (C)	RH_out	ω_out (kg/kg)	i_a_out (kJ/kg)	T_c_out (C)	T_c_in (C)	i_c_sat_in (kJ/kg)	T_c_out (C)	i_c_sat_out (kJ/kg)	Nu_a	Re_a	h_a (W/m^{2}K)	Nu_c	Re_c
January	Wet	7.62	82%	4.75	0.0053	21.00	0	0	2.68	92%	0.004195	13.20	0.00	-4.55	1.85	0.25	9.87	39.03	3083	78.19	14.13	2244
February	Partial	4.20	76%	0.35	0.0039	13.93	3.51	13.24	-0.90	89%	0.003118	6.89	-3.58	-7.55	-2.64	-3.15	4.07	39.57	3155	78.4	14.07	1890
March	Partial	4.25	74%	0.03	0.0038	13.76	3.191	12.69	-0.97	89%	0.003085	6.73	-3.90	-7.62	-2.74	-3.23	3.94	39.58	3155	78.4	14.07	1883
April	Partial	9.06	69%	3.68	0.0049	21.49	7.18	19.58	3.23	87%	0.004131	13.60	-0.62	-4.28	2.27	0.55	10.38	38.87	3064	78.12	14.14	2278
May	Partial	12.00	69%	6.50	0.0060	27.18	10.21	25.37	5.88	88%	0.005072	18.64	4.71	0.65	10.55	5.80	20.18	38.46	3009	77.97	41.96	2944
June	Partial	15.35	70%	9.92	0.0076	34.60	13.62	32.85	9.39	88%	0.006467	25.71	8.39	4.14	16.91	9.43	27.96	37.95	2944	77.78	50.84	3484
July	Partial	20.47	65%	13.67	0.0098	45.33	17.4	42.2	14.03	87%	0.008682	36.02	12.33	8.73	26.37	14.15	39.66	37.25	2854	77.51	60.49	4284
August	Partial	18.80	70%	13.22	0.0095	42.89	16.88	40.93	12.95	88%	0.008197	33.69	11.86	7.61	23.93	13.00	36.63	37.44	2879	77.58	58.15	4080
September	Partial	14.57	78%	10.78	0.0080	34.97	14.32	34.71	9.41	90%	0.006615	26.10	9.33	4.19	17.00	9.48	28.08	38	2950	77.8	50.94	3492
October	Wet	13.02	82%	10.02	0.0076	32.37	0.00	0.00	8.06	92%	0.006177	23.63	0.00	3.03	14.81	8.28	25.39	38.22	2977	77.89	48.47	3306
November	Wet	7.77	80%	4.54	0.0052	20.96	0	0	2.76	90%	0.004147	13.16	0.00	-4.57	1.82	0.23	9.83	39.01	3081	78.18	14.13	2242
December	Wet	7.50	82%	4.63	0.0053	20.77	0.00	0.00	2.56	92%	0.004158	12.99	0.00	-4.66	1.69	0.14	9.67	39.04	3085	78.2	14.13	2231

Table C.5 – Results from the WHR model for full-load Supply Mode operation, with a PG 30% mixture used as coolant (part II).

Month	Coil Condition	h_c (W/m^{2}K)	U_d (W/m^{2}K)	UA_d (kW/K)	Q_d (kW)	X	U_w (W*kg/m^2*J)	UA_w (kW/[kJ/kg])	ε_w	Q_w (kW)	Q_rec (kW)	SHR	Q_sen (kW)	m_cond (kg)	T_evap (C)	h_r_evap (W/m^{2}K)	h_c_evap (W/m^{2}K)	U_evap (kW/m^{2}K)	UA_evap (kW/K)	P_evap (kPa)	i_r_1a (kJ/kg)	ir_2 (kJ/kg)
January	Wet	539	0	0	0	0.0%	0.0218	60.99	0.41	685.4	685.4	64%	439.1	349.8	-8.619	3900	2059	1.251	111.2	307.5	160.3	1452
February	Partial	533	30.58	85.6	61.57	10.0%	0.0231	64.74	0.40	565	626.6	73%	458.1	240.7	-11.64	3512	1947	1.169	103.9	271.8	146.5	1449
March	Partial	533	30.57	85.59	95	15.2%	0.0232	64.83	0.39	529.8	624.8	75%	468.8	222.8	-11.71	3502	1944	1.167	103.7	271.1	146.2	1449
April	Partial	539	30.7	85.96	166	23.7%	0.0217	60.78	0.35	523.3	689.2	75%	515.2	247.3	-8.342	3929	2068	1.258	111.8	310.9	161.5	1453
May	Partial	1615	46.14	129.2	156.3	20.7%	0.0340	95.23	0.45	582.5	738.8	73%	536.5	286.4	-3.204	4373	2250	1.369	121.7	380.4	185.1	1459
June	Partial	1969	48.25	135.1	149.7	19.9%	0.0341	95.52	0.45	610.8	760.6	68%	518	341.5	0.463	4633	2377	1.442	128.2	437	202	1463
July	Partial	2363	49.94	139.8	262	33.0%	0.0330	92.32	0.39	520	782	71%	551.8	321.6	5.281	4948	2546	1.534	136.4	521.2	224.3	1468
August	Partial	2267	49.59	138.8	164.5	22.0%	0.0333	93.28	0.43	612.7	777.2	65%	504.1	382.2	4.108	4873	2505	1.511	134.4	499.6	218.9	1466
September	Partial	1974	48.29	135.2	21.95	3.2%	0.0341	95.5	0.49	738.9	760.8	59%	450.2	436.9	0.5153	4637	2379	1.443	128.3	437.9	202.2	1463
October	Wet	1874	0	0	0	0.0%	0.0343	95.95	0.50	754.3	754.3	58%	434.7	450.4	-0.7048	4553	2337	1.419	126.2	418.3	196.6	1461
November	Wet	538	0	0	0	0.0%	0.0218	61	0.41	685.1	685.1	65%	445.3	340.6	-8.639	3898	2058	1.251	111.2	307.2	160.2	1452
December	Wet	538	0	0	0	0.0%	0.0218	61.07	0.41	683.8	683.8	64%	439.1	347.6	-8.727	3888	2055	1.248	111	306.2	159.8	1452

Table C.6 – Results from the WHR model for full-load Supply Mode operation, with a PG 30% mixture used as coolant (part III).

Month	Coil Condition	m_r_1a (kg/s)	m_r_1b (kg/s)	Q_ds_ls (kW)	i_r_5 (kJ/kg)	i_r_6 (kJ/kg)	T_w_6 (C)	T_r_5 (C)	T_r_6 (C)	m_r_5 (kg/s)	Q_cond (kW)	i_r_11 (kJ/kg)	i_r_12 (kJ/kg)	T_r_11 (C)	T_r_12 (C)	m_r_12 (kg/s)	COP_c	COP_h	W_hp (kW)	W_system (kW)	COSP_c	COSP_h	Q_out (kW)
January	Wet	0.530	0.121	182.5	1837	1557	58.52	167.9	62.52	0.652	855.8	1626	491.4	113	59.96	0.755	1.79	2.71	383.6	413.3	1.66	2.51	1038.3
February	Partial	0.481	0.117	250.8	1979	1560	59.84	223.4	63.41	0.598	787.5	1626	496.2	113	60.88	0.697	1.40	2.32	447.5	477.1	1.31	2.18	1038.3
March	Partial	0.480	0.116	253	1984	1560	59.88	225.3	63.43	0.596	785.3	1626	496.3	113	60.91	0.695	1.39	2.31	449.5	479.1	1.30	2.17	1038.3
April	Partial	0.534	0.121	178.2	1829	1557	58.44	164.6	62.44	0.655	860.2	1626	491.1	113	59.9	0.758	1.82	2.74	379.4	409.1	1.69	2.54	1038.4
May	Partial	0.580	0.118	125	1732	1553	57.41	126.7	61.14	0.698	913.3	1626	487.7	113	59.24	0.803	2.27	3.19	325.5	355.2	2.08	2.92	1038.3
June	Partial	0.603	0.113	103.6	1695	1551	57	112.6	60.45	0.716	934.8	1626	486.3	113	58.98	0.820	2.52	3.44	301.9	331.6	2.29	3.13	1038.4
July	Partial	0.629	0.104	83.75	1663	1549	56.61	100.2	59.7	0.733	954.6	1626	485.1	113	58.75	0.837	2.81	3.73	278.7	308.3	2.54	3.37	1038.4
August	Partial	0.623	0.106	88.03	1670	1549	56.7	102.8	59.87	0.729	950.3	1626	485.4	113	58.8	0.833	2.74	3.66	283.8	313.5	2.48	3.31	1038.3
September	Partial	0.604	0.113	103.3	1695	1551	56.99	112.4	60.44	0.716	935	1626	486.3	113	58.98	0.821	2.52	3.44	301.6	331.3	2.30	3.13	1038.3
October	Wet	0.596	0.115	109.6	1706	1551	57.11	116.5	60.65	0.711	928.8	1626	486.7	113	59.05	0.815	2.44	3.36	308.7	338.3	2.23	3.07	1038.4
November	Wet	0.530	0.121	182.8	1838	1557	58.53	168.2	62.53	0.651	855.5	1626	491.4	113	59.96	0.754	1.78	2.70	384	413.6	1.66	2.51	1038.3
December	Wet	0.529	0.121	184.3	1841	1557	58.55	169.3	62.55	0.650	854.1	1626	491.5	113	59.98	0.753	1.78	2.70	385.3	415	1.65	2.50	1038.4

Appendix D – SES Tunnel Geometry and General Parameters

In order to understand the physical principles behind SES, it is essential to review how the UR network is schematically represented in simulations. The network must be broken down into specific components that can be easily modelled, enabling the subprogrammes to calculate the thermal and aerodynamic interactions within tunnels. SES divides an UR system into four main components: sections, nodes, segments and subsegments. A brief introduction to these components is provided below:

- **Sections:** represent a specific length of tunnel in which air flow is uniform;
- **Nodes:** consist of the connecting points between tunnel sections;
- **Segments:** represent tunnel lengths with uniform geometric parameters and air velocities;
- **Subsegments:** represent smaller divisions of segments where air temperature and humidity can be assumed as constant.

Figure D.1 provides examples of tunnel sections and their associated nodes and segments. The detailed description of these components, their purpose and simulating procedure used is provided in the following subsections.

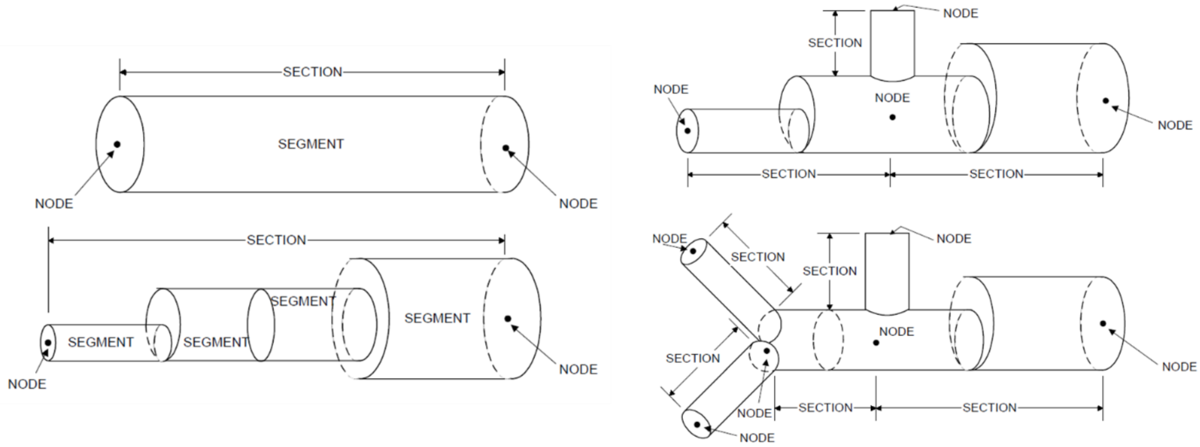

Figure D.1 – Examples of sections and their components as simulated by SES (U.S. Department of Transportation, 2002).

Segments and Subsegments

Segments

Segments represent the basic geometric unit for the simulation of air flows in SES. They consist of both line and ventilation shaft segments and are defined by their uniform geometric properties, which are their type (tunnel or station), length, cross section area, perimeter and roughness length. Due to their uniform geometry, segments are assumed to develop uniform air velocities when no trains are passing within them. Line segments consist of UR (running) tunnels, whilst ventilation shaft segments are structures that enable the movement of air between the tunnels and atmosphere, possibly containing a fan, or structures that connect two different line segments, such as stairways and walkways for the movement of passengers. Both running tunnels and ventilation shaft structures can consist of several segments, depending on their length, cross section area and perimeter.

Subsegments

Segments represent the basic unit for the analysis of air movement within tunnels. However, when modelling temperature and humidity, another basic unit must be introduced, particularly as these parameters can vary over the length of a single tunnel segment. Therefore, SES divides segments into one or more subsegments, representing units of independent temperature and humidity that can reflect small-scale variations in sensible and latent heat transfer, increasing the accuracy of simulations.

Sections, Junctions, Nodes and Portals

Sections and Junctions

Sections represent a specific tunnel length over which air moves at a uniform flow rate. The combination of different interconnected sections makes up the UR network. A section might consist of one or more segments, with different segments developing different air velocities due to their different geometries. A specific segment may comprise an entire section, but it cannot be part of more than one section. Just as for segments, sections can be of the line or ventilation shaft type. A section can be connected to other sections or to the atmosphere. The air flow rates specific to sections are obtained from the aerodynamic subprogramme of SES. When more than two sections meet, their connection is referred to as a junction.

Nodes and Portals

Nodes represent the connection points between sections. A specific node may be attached to up to five sections, and it is defined as a portal when connected to the atmosphere, where trains can either leave or enter the tunnelled network. As for ventilation shafts, its atmosphere nodes are referred to as “openings to the atmosphere”. Nodes are points at which the laws of mass and energy conservation are applied. Therefore, SES is able to connect different tunnel sections by calculating mass and energy balances at nodes.

Appendix E – SES Train Simulation and Performance

The calculation of heat loads within an UR system involves determining the amount of heat being released by trains, ancillary equipment and passengers. As shown in section 2.9.3, the operation of trains represents the main source of heat within a UR environment, whilst also having a significant impact on the air flow patterns within the tunnels. It is therefore imperative to understand how the routes, speed and acceleration of the trains within URs affect heat release and air speeds within the system. This involves calculating train movement patterns and acceleration, which consists of considering the force balance between resistances to train movement, such as rolling friction and aerodynamic drag, as well as the traction forces associated with train propulsion systems. This section describes the main resistances to train acceleration and their associated calculation methods, as well as how motor performance and work output have been estimated in the UR model. Another critical aspect considered in the UR model is the vehicle braking cycle, as braking is the main source of heat dissipation within a UR system (Ampofo et al., 2004). SES enables the modelling of train braking systems considering the use of regenerative braking when estimating heat dissipation. The modelling of train braking cycles is also discussed in this section.

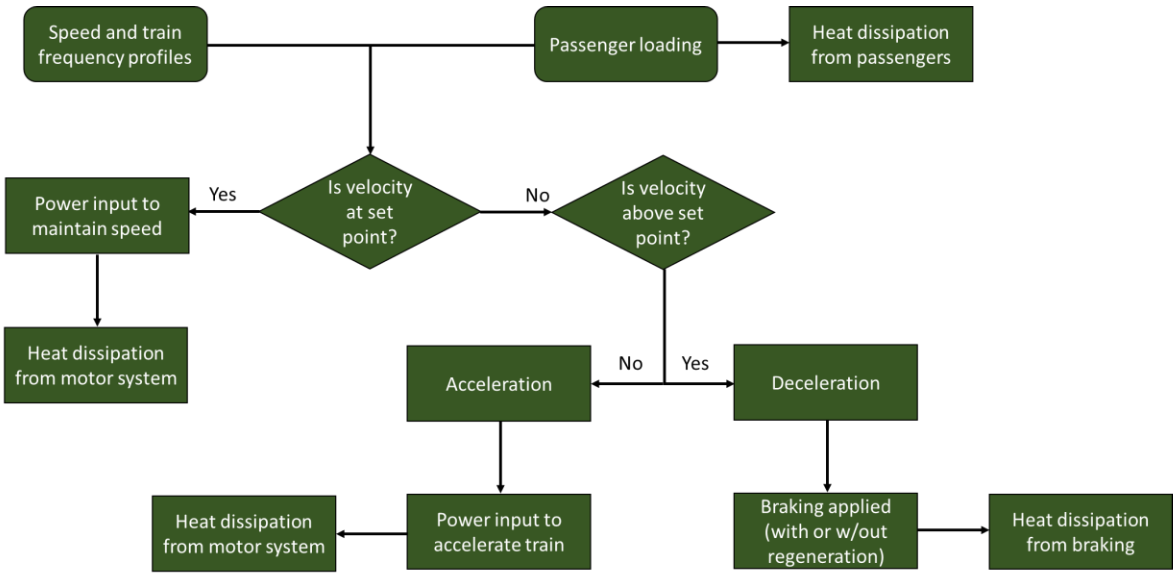

Figure E.1 – The UR model framework for calculating heat loads due to train movement within tunnels.

The UR model utilises a specific logical framework in order to simulate the movement of trains within the tunnels and calculate their associated heat loads. Initially, based on train frequency and speed profiles supplied by the user, the programme computes train resistances, analysing if trains should accelerate or decelerate based upon pre-established criteria of train frequency and associated set point velocities for travelling and approaching stations. If continued acceleration is necessary to meet train frequency, the programme calculates how much motor power is required for that purpose. If trains must decelerate, the programme then calculates the stopping time and velocity reduction based on user-specified braking rates. The programme also calculates the heat dissipation associated with braking, which can be reduced if regenerative braking is applied. Finally, when trains reach the set point velocity, no acceleration is required and the programme only considers the power consumption needed to maintain speed. The UR model also computes any heat dissipation associated with passengers and auxiliary systems, as well as changes in passenger loading of trains at each station, based upon estimates from the UK Department for Transport. The logical framework of the UR model, based upon the methodology of SES, is shown in Figure E.1.

Routing and Train Operating Modes

The initial step for simulating the movement and performance of trains is to determine their routes through the network of tunnels. Routes represent paths taken by trains in tunnels and contain information on train scheduling, track profiles, location of stops (typically stations) and coasting points along the network. The scheduling data determines train frequencies (headways) and the types of trains used for a specific route. The track profile involves a description of the physical properties of a given route, such as grade, curvature and speed limits. Line segments, as defined in Appendix D, can have one or more routes passing through them. These routes can operate in the same or in opposite directions. All trains operating on the same route must adhere to the same set of specifications, which can only be associated with a single route. If each train travelling upon a track passes through the same line segments and stops at the same locations for the same stopping periods, then only one route is required to simulate that track.

Each route must therefore be associated with trackway parameters, e.g. track curvature, grade and maximum train velocity. These parameters can vary along a route, and track sections are defined as route lengths across which these parameters remain constant. These track sections are used only for the purpose of establishing the routes and are different from the air movement sections defined in Appendix D. The only parameter that can vary within a single route is train scheduling, as different types of trains and headways can be used to meet travel demands for the same route. The user must specify train scheduling and trains can be dispatched onto routes as groups. A train group consists of one or more trains of the same type which operate on a specific route with the same headway. The SES train performance subprogramme is able to compute the location, velocity and acceleration of any given train as it moves along a specific route. These calculations are time-dependent and trains can be found in any of five different operating modes: accelerating at full power, maintaining a constant speed, braking (decelerating), coasting (moving without power input) and stopped.

Resistances to Train Movement

In order to calculate the force balance associated with a specific operating mode, the main resistances to train movement must be known. These resistances are mainly associated with train acceleration and rolling, as well as the aerodynamic drag resulting from the movement of air caused by train motion. All resistances are associated with physical parameters of the trains and are described in the following subsections.

Acceleration and Rolling Resistances

The acceleration and rolling resistances are associated with train motion and are a function of the total mass of the train. In SES, a train is considered as one or more cars which operate as a single unit (U.S. Department of Transportation, 2002). The total train mass (m_{tr}) is a function of the total number of cars (N_{cars}) and their average masses ($\overline{m}_{car}$), as shown in Equation E.1. A car can be either powered or not, and the mass associated with the propulsion system must be accounted for in the calculations. The car mass is also defined by the type of train being simulated, which in this case is the 1995 rolling stock used for the Northern Line.

$$m_{tr} = N_{cars}\overline{m}_{car} \tag{E.1}$$

$$\overline{m}_{car} = f_{acc}\overline{m}_{car,e} + m_{pas} \tag{E.2}$$

The calculation of train mass depends upon the type of resistance being analysed. The acceleration resistance of rotating parts can be considered through the utilisation of an acceleration resistance factor (f_{acc}). This factor can be applied directly to the average empty mass of the car ($\overline{m}_{car,e}$) and added to the mass of the passengers aboard the car (m_{pas}) to yield the average car mass ($\overline{m}_{car}$), as shown in Equation E.2. The acceleration resistance factor should be disregarded when calculating movement resistances associated with track grades and train rolling. In this case, a f_{acc} value of unity can be utilised. The scheduled train stops, defined as part of the routing process, are used to determine any changes in passenger loading of trains along the route, as the number of persons entering or leaving the train affect its mass and inertia. When estimating these loading variations, transport planning data is used to forecast the use of public transport in the future, as shown in (TfL, 2017), which highlights how rail and Underground boardings are expected to increase by 54% from 2015 to 2041.

Aerodynamic Drag

In UR systems, the aerodynamic drag represents the motion resistance of the air surrounding the running trains. Drag forces are associated with shear and normal stresses that act across all train surfaces, being computable by applying specific drag coefficients for each surface. The shear stress caused by skin friction is dominant on the sides, bottom and roof of the train, whilst the front/nose and the back/tail of the train are predominantly subject to normal stress.

The frontal drag coefficient varies according to the type of train and some examples of typical values are provided in the SES handbook (U.S. Department of Transportation, 2002). According to Vardy (1996a), the frontal or back drag force ($F_{d,f}$) acting on a train is a function of the drag coefficient (C_d), the density of tunnel air (ρ_a), as well as air velocity in front of the train ($v_{a,f}$) and train frontal area ($A_{tr,f}$). The formula for frontal drag is shown in Equation E.3, which can also be used to calculate the back drag force by applying a drag coefficient associated with the rear of the train instead of its front.

$$F_{d,f} = \frac{1}{2} C_d \rho_a A_{tr,f} v_{a,f}^2 \tag{E.3}$$

The remaining drag forces ($F_{d,s}$) are associated with the skin friction across the train surfaces, and can be expressed in terms of the skin friction coefficient ($f_{d,s}$), the side or roof surface area of the trains ($A_{tr,s}$), and the annular velocity that develops between the tunnel walls and the train surfaces ($v_{a,s}$), as shown in Equation E.4 (Vardy, 1996a). The train skin friction coefficient is also used to calculate the head losses for line segments with running trains. The coefficient has been experimentally measured in field observations, with typical values ranging from 0.009 to 0.015 (U.S. Department of Transportation, 2002). SES uses a median of 0.012 as the typical skin friction coefficient for modern trains.

$$F_{d,s} = \frac{1}{2} f_{d,s} \rho_a A_{tr,s} v_{a,s}^2 \tag{E.4}$$

Tractive Effort

The tractive effort of trains is associated with their propulsion system, which may consist of direct current (DC) or alternating current (AC) electric motors. TfL utilises different rolling stocks for each Underground line, with the Northern Line operating with the 1995 rolling stock, which is equipped with AC motors fed by a 630 V DC supply system consisting of third and fourth rails. The conversion from DC to AC is carried out with insulated-gate bipolar transistor converters. Based upon the type of motor and motor performance data, SES is able to calculate the tractive effort available from the motors for a given operating mode (see Figure E.1) and speed profiles. The tractive effort is then applied to determine the power consumption of the trains and their associated heat losses, as detailed in the SES manual.

Train Braking Systems

Braking represents the main source of heat dissipation within a UR environment, as the kinetic energy associated with train motion must be transformed to bring the vehicle to standstill. Most UR trains use their propulsion motors for braking, during which the motors act as generators, converting the kinetic energy of the train into electrical energy. The use of motors as generators causes a drag force to act on the vehicle, reducing its velocity. This method of braking is known as dynamic braking, and the types of dynamic braking systems simulated in the UR model are described in the following subsections.

Rheostatic Braking

Rheostatic braking is a type of dynamic braking that involves dissipating the train's kinetic energy in a controlled manner. This is achieved by dissipating the electricity generated in the dynamic braking process as heat through a resistor grid. Some of the train's kinetic energy is directly converted into heat as part of the braking process, mainly due to friction losses, whilst the remainder is first converted into electricity before being rejected as heat. This method of braking is not very efficient, particularly as energy is dissipated from the resistor grid and released as waste heat. This thermal energy represents the main source of heat in the UR environment (U.S. Department of Transportation, 2002). The resistor grids typically consist of metallic coils or tubes that are arranged in banks and located beneath the vehicle, rejecting heat by convection and radiation (Mortada, 2016), as shown in Equation E.5.

$$Q_{RG} = Q_{RG,c} + Q_{RG,r} \tag{E.5}$$

The heat release by convection can be calculated as shown in Equation E.6, where $A_{RG,c}$ represents the effective resistor grid convective area, as shown in Figure E.2, and h_{RG} the convective heat transfer associated with the resistor grid, which can be calculated assuming that the grid behaves as a bank of tubes (see section 5.4.6). The term T_{RG} is the average temperature of the resistor grid, whilst T_a represents the average tunnel air temperature.

$$Q_{RG,c} = h_{RG} A_{RG,c} (T_{RG} - T_a) \tag{E.6}$$

As for radiation, its associated heat transfer can be calculated as shown in Equation E.7, where $A_{RG,r}$, ε_{RG}, σ and T_w represent, respectively, the resistor effective radiation area, its emissivity, the Stefan-Boltzmann Constant, and the tunnel wall temperature. SES calculates $A_{RG,r}$ of the resistor grid by considering the resistor grid to be enclosed in an imaginary rectangular box (U.S. Department of Transportation, 2002), as shown in Figure E.2.

$$Q_{RG,r} = A_{RG,r} \varepsilon_{RG} \sigma (T_{RG}^4 - T_w^4) \tag{E.7}$$

$$T_{RG} = \frac{41.22 N_{cars} \overline{m}_{car,e} V_{max}^2}{\bar{t} N_{cars,p} (A_{RG,c} + A_{RG,r})} + T_a \tag{E.8}$$

The temperature of the resistor grid (T_{RG}) is dependent upon several factors, including whether the resistor grid is operating in a state of thermal equilibrium. This state is typically achieved after a couple of braking cycles have taken place, which may vary according to the thermal inertia of the resistor grid and the kinetic energy of the train (U.S. Department of Transportation, 2002). Overall, the average temperature of the resistor grid can be estimated as shown in Equation E.8, where V_{max} represents the average maximum velocity a train can achieve between two stops, $\bar{t}$ is the average dwell and travel time between two stops, and $N_{cars,p}$ is the number of powered cars per train (U.S. Department of Transportation, 2002).

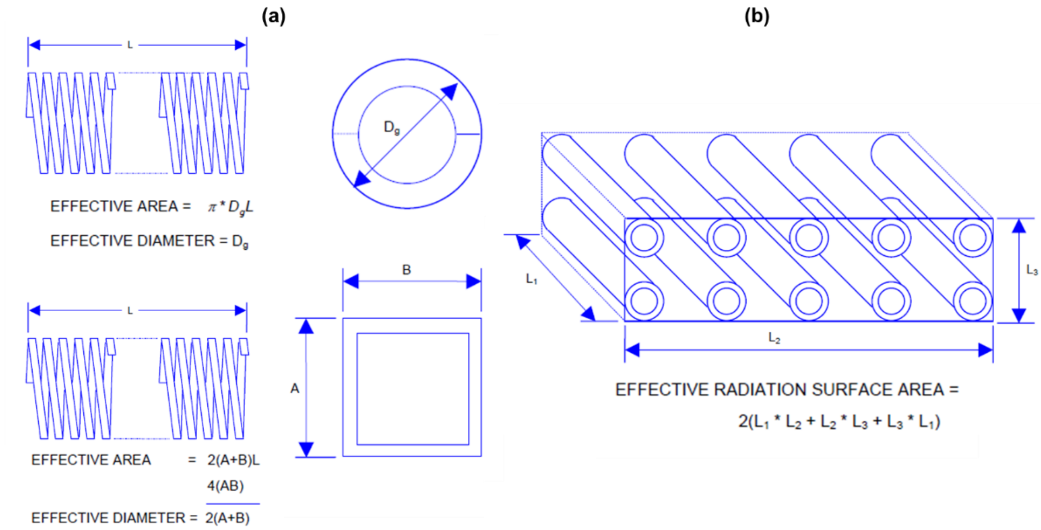

Figure E.2 – Schematics for the calculation of the effective resistor area for (a) convection and (b) radiation (U.S. Department of Transportation, 2002).

Regenerative Braking

Regenerative braking is a sustainable alternative to rheostatic braking where part of the electricity generated during braking is supplied back into the distribution system. Regenerative braking allows the braking electricity to be utilised to power auxiliary equipment or another train operating near the braking vehicle. When the electrical output from the braking cycle exceeds the power demands for on-board equipment and nearby trains, the train controls are able to switch the braking system to a rheostatic mode. The amount of energy recoverable from regenerative braking depends upon the type of UR system being analysed. When modelling regenerative braking on SES, the user must provide the regenerative efficiency (η_{reg}) as an input. The regenerative efficiency is the ratio between total energy regenerated (W_{reg}) and the total energy available for regeneration (W_{tot}), as shown in Equation E.9.

$$\eta_{reg} = \frac{W_{reg}}{W_{tot}} \qquad \text{(E.9)}$$

The total energy available for regeneration is equal to the total mechanical energy (comprising both kinetic and potential energy) for the train in relation to the stopping point, minus all the friction losses. The regenerative efficiency is associated with a single train, but an average value for the entire rolling stock can be used to represent the overall benefit of regeneration. For the Northern Line models, the average regenerative efficiency is assumed as 60% (TfL, 2019b). As a result of this type of braking system, less heat will be introduced into the tunnels and less electricity will be required to power the trains and their auxiliary equipment.

Appendix F – SES Aerodynamic Phenomena

The thermal environment in railway tunnels is highly influenced by aerodynamics, as the movement of air drives the convective transfer of heat and moisture throughout the system. The main factors that influence air flow patterns in a UR environment are mechanical ventilation provided by fans and the piston effect, caused by the mass of air dislocated as trains move. Buoyancy, drag and head losses are other prominent factors that affect air flows and velocities. The airflow in tunnels is transient in nature and depends upon the train movement patterns. Therefore, the position, velocity and acceleration data from the train performance subprogramme are used to calculate energy balances associated with air movement, which consists of the difference between energy added to the flow (piston effect and mechanical ventilation) and energy lost mainly due to friction and drag. The piston effect is evaluated based upon train and tunnel geometries, and aerodynamic differential equations are integrated forward in time to provide continuous readings of aerodynamic drag, air velocities and flow rates in tunnels, ventilation shafts and stations. Appendix F describes the methodology used to estimate the movement of air for both vent shaft and line segments.

Aerodynamic Nodes

As mentioned in Appendix D, the UR network is broken down into tunnel sections of constant air flow rate. As SES assumes the flow within UR tunnels to be turbulent and incompressible, the relation between air flow rate and head loss can be calculated by applying Bernoulli's principle of energy conservation, as shown in Figure F.1 for points 1 and 2 of a given section.

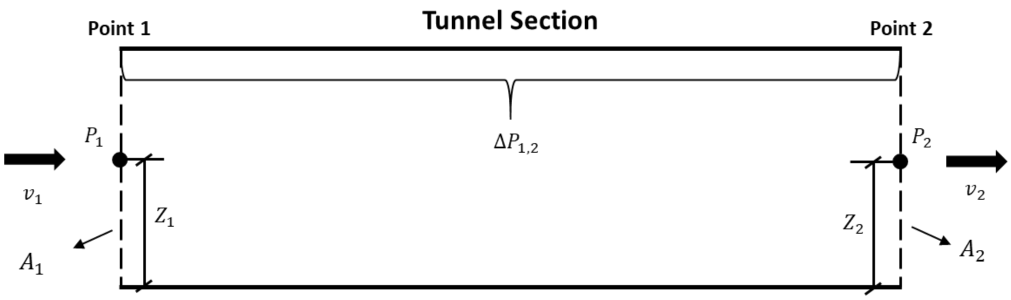

Figure F.1 – The energy components of air flowing from point 1 to 2 within a given tunnel section.

The energy conservation principle, applied to the section shown in Figure F.1, leads to Equation F.1, which involves the potential, kinetic and pressure components associated with air flow over a given tunnel section. The total pressure difference ($\Delta P_{1,2}$) combines the energy losses due to friction with energy gains over the section, which can be associated with the movement of trains, buoyancy, and mechanical ventilation.

$$P_1 + \rho g Z_1 + \frac{1}{2}\rho v_1^2 = P_2 + \rho g Z_2 + \frac{1}{2}\rho v_2^2 + \Delta P_{1,2} \tag{F.1}$$

For the control volume between points 1 and 2, the principle of mass continuity applies and the incompressibility assumption means that the density can be assumed as constant, meaning that volumetric air flow rates will remain the same. As the volumetric flow rate is the product of cross-sectional area and velocity, the velocity of flow and its associated kinetic head will vary based upon a change in cross-sectional area, as shown in Equation F.2.

$$\dot{V} = A_1 v_1 = A_2 v_2 \tag{F.2}$$

The point where sections meet are defined as aerodynamic nodes, at energy and mass conservation balances are calculated. These equations are integrated over a user defined time-step to yield the varying air flow rates for each section and the air velocities observed in each tunnel segment. Sections can be one of two types: either ventilation shaft sections or line sections, as introduced in Appendix D. The factors that influence fluid flow for these sections are different and will be further detailed in the subsections below.

Air Flow in Ventilation Shaft Segments

For ventilation shafts and similar structures in which there is no train movement (e.g. staircases, halls, passageways), airflow can be calculated based upon forced ventilation, buoyancy effects and head losses across a given section. The difference in pressure between two different points within a tunnel, as shown in Equation F.1, can also be expressed in terms of a head difference (ΔH) between these two points, based upon the relationship shown in Equation F.3, where ρ represents the fluid density and g is the acceleration due to gravity. For a vent shaft segment, the head difference is associated with the head gains due to the presence of fans (H_{fan}) and the occurrence of buoyancy (H_{buo}), as well the head losses across the section due to friction (H_{fr}) and minor losses (H_m), as shown in Equation F.4.

$$\Delta H = \frac{\Delta P}{\rho g} \tag{F.3}$$

$$\Delta H = H_{fr} + H_m + H_{fan} + H_{buo} \tag{F.4}$$

Head Losses

One of the main factors associated with airflow calculation is the energy lost as the air travels through the tunnels. The airflow within tunnels can be treated as any fluid flow within pipes or ducts and, in these cases, the energy losses are commonly referred to as head losses. These losses are either associated with viscous friction along the tunnel walls or with abrupt changes in area or turns within the tunnels. In SES, head losses are calculated separately for each segment, as their different geometries and velocities yield different values of head loss. These are then combined to provide the overall head loss for a given tunnel section.

Friction Losses along Tunnels

Many empirical correlations have been develop for calculating head losses associated with viscous friction (H_{fr}). A widely used correlation is the Darcy-Weisbach equation, which is a function of the tunnel friction factor for a given segment (f), its length (L), hydraulic diameter (D), as well as of the air velocity in the tunnel (v) and the acceleration due to gravity (g), as shown in Equation F.5 (Moody and Princeton, 1944).

$$\mathrm{H}_{fr} = f\,\frac{L}{D}\,\frac{v^2}{2g} \tag{F.5}$$

The SES program applies Moody and Princeton's diagram (1944) to compute the friction factor for each tunnel section based upon the tunnel hydraulic diameter and its Reynolds number, as well as the roughness length of the tunnel, which must be provided by the user. The roughness length of the tunnel is the average height of the uniform protuberances from the tunnel walls which can be either uniform or ribbed, when they are spaced widely enough so that the surface cannot be considered uniform, as shown in Figure F.2.

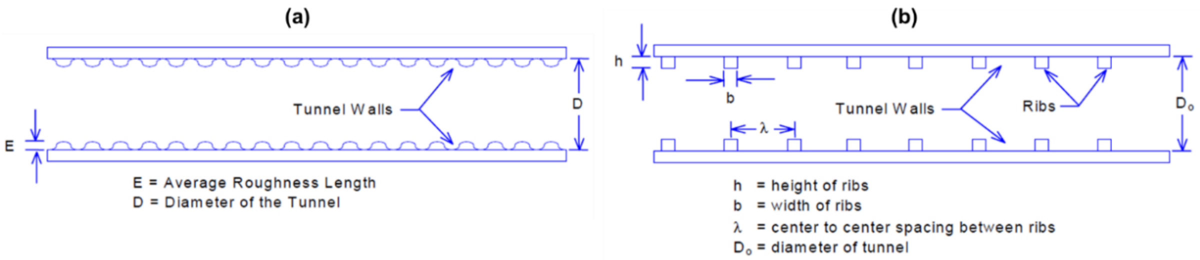

Figure F.2 – Profile of tunnels with uniform (a) and ribbed (b) roughness lengths (adapted from U.S. Department of Transportation, 2002).

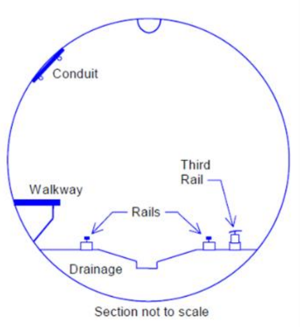

(1) Subperimeter Identification	(2) Percentage of Perimeter	(3) Roughness Characteristics: Relative* Roughness	λ^{**}/D	h^{**}/D	(4) f_t	(5) Weighted Contribution to Total f_t (2 x 4)
Pipe supports	11%	---	0.61	0.01	0.051	0.0056
Rail and pads	4%	---	0.09	0.015	0.037	0.0015
Catwalk and supports	4%	---	0.24	0.15	0.135	0.0054
Third rail and supports	2%	---	0.3	0.04	0.22	0.0044
Concrete wall surface	79%	0.0002	---	---	0.014	0.0111
					Weighted tunnel friction factor:	0.028

*Calculation using Moody's Diagram
**Calculation based upon Figure 6.9

Figure F.3 – Friction factor calculation for a line segment with different roughness lengths (adapted from U.S. Department of Transportation, 2002).

For ribbed tunnels, SES is also able to compute the friction factor (f) based upon its geometrical parameters, which are shown in Figure F.2. It is commonly the case that a given tunnel segment may have different roughness lengths along each of its inner surfaces. One example is the difference between tunnel walls and trackbeds, which have different lengths of roughness for the same line segment. SES is able to overcome this challenge by allowing the perimeter of a segment to be entered as separate lengths, each with its own roughness value.

This approach is able to combine ribbed and uniform roughness lengths into a weighted average value for a single line segment. An example of a typical cross section of a railway tunnel is shown in Figure F.3, which also demonstrates how the friction factor for that particular section can be calculated.

Minor Losses

In SES, the head losses that occur due to sudden changes in geometry, such as enlargement, contractions and turns, are referred to as minor losses. One practical way to model these losses is to express them in terms of friction losses by applying an equivalent tunnel length, which represents the length the air would have to travel in order to lose the same amount of energy as it loses when there is a change in area or turn. This methodology is analogous to the approach used for calculating the pumping power requirements of the coolant loop in section 5.5.1, as shown in Equation F.6.

$$H_m = \frac{K_m v^2}{2g} \tag{F.6}$$

Equation F.6 yields the minor head loss for an abrupt change in flow (H_m) as a function of the minor head loss coefficient (K_m), the velocity of the air flow in the segment (v), and the acceleration due to gravity (g). The SES aerodynamic subprogramme calculates the head loss across the UR network utilising Equation F.6, with only the head loss coefficient being provided by the user for each line and vent shaft segment. A list of typical minor head losses and their associated coefficients, as used in SES calculations, is provided in the SES handbook (U.S. Department of Transportation, 2002).

Fan Operation

Ventilation shafts are widely used across the LU network to guarantee the circulation of fresh air across the tunnels. These shafts often rely on the use of fans, which can operate in Exhaust/Extract or Supply modes. In SES, fans are modelled according to the air volumetric flow rate that is moved by the fan ($\dot{V}_f$ in Figure F.4). This value is equal to the sum of air flows that go to each of the tunnel directions ($\dot{V}_{f,1}$ and $\dot{V}_{f,2}$), as shown in Figure F.4, which provides an example for a Supply Mode fan configuration. In SES, the fan operation is simulated based upon fan performance curves, which are commonly available from manufacturers. These curves enable the pressure gains to the air stream to be calculated based upon the volumetric flow rate of the fan. For the fan used as part of the WHR system, the performance curves are shown in Figure F.5 (TfL, 2019b). As the fan is 100% reversible, the same performance curve can be utilised for operation in Extract and Supply modes. It is common for fans to operate with an approximately constant volumetric flow rate, although some variation can be caused by disturbances such as the train piston effect. In this case, the performance curves are checked to ensure pressure and flow rate variations are within fan operating limits at all times.

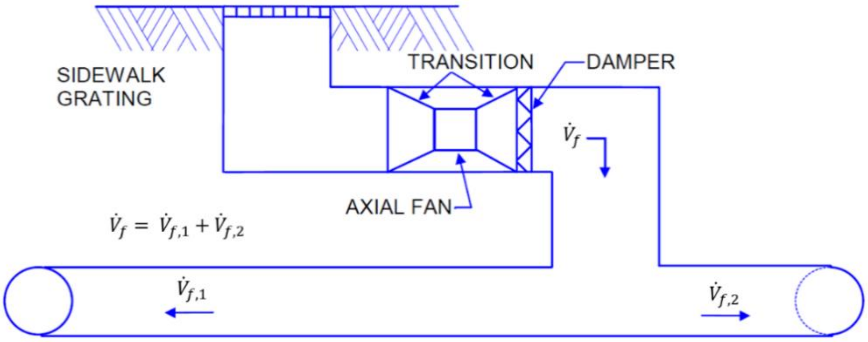

Figure F.4 – Example of tunnel air flows for a conventional Supply fan (adapted from U.S. Department of Transportation, 2002).

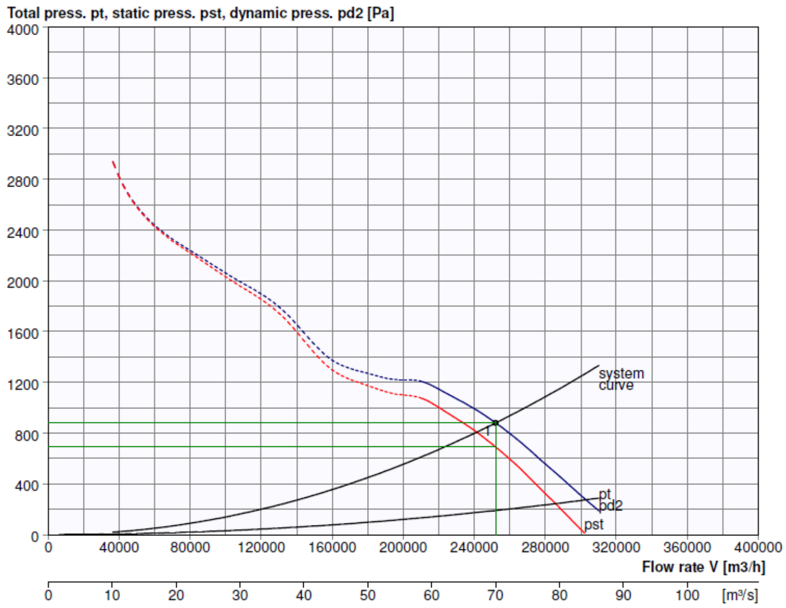

Figure F.5 – Performance curves for the fan installed for the WHR system (TfL, 2019b).

Buoyancy

Buoyancy represents the movement of air associated with the stack effect, being particularly applicable for ventilation shaft sections without fans, which are commonly referred to as draught relief shafts. Buoyancy is primarily caused by a variation in density and can be accounted for by noting that changes in density are inversely proportional to changes in air temperature (U.S. Department of Transportation, 2002). According to Mortada (2016), who developed a UR model based upon SES principles, the buoyancy head for a segment (H_{buo}) can be calculated by applying Equation F.7. This equation is a function of the difference in temperature between air in a given tunnel segment (T_{seg}) and ambient air (T_{amb}), as well as the stack height for the segment (Z_{seg}).

$$H_{buo} = Z_{seg}(1 - \frac{T_{amb}}{T_{seg}}) \qquad \text{(F.7)}$$

Air Flow in Line Segments

The modelling of line segments involves greater complexity as it also requires simulating train movement. In addition to the friction and minor losses, the air flow rates for line segments are significantly impacted by the piston effect and aerodynamic drag, which leads to head losses associated with the front, rear and sides of the train. As for the piston effect, its associated compressibility effects lead to a variation of air static and dynamic pressures, meaning that different flow rates can be observed when a train is passing through a given segment. SES is able to calculate the aerodynamics of line segments by breaking them into different regions, each with its own flow rate and velocity, as shown by the example in Figure F.6.

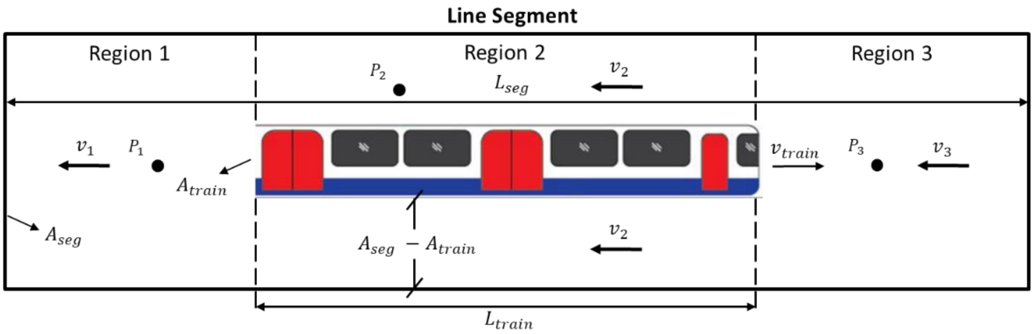

Figure F.6 – The different regions and their parameters for calculating pressure differences in line segments (adapted from Mortada (2016) and Vardy (1996a)).

Equation F.1 is still applicable for the different air flow regions shown in Figure F.6. The pressure difference (ΔP) in this case must be analysed for each region, based upon friction and minor head losses, as well as the pressure losses/gains due to aerodynamic drag and the piston effect. The additional pressure losses associated with air flowing in region 2 must take into account both the tunnel and the train skin friction coefficients. The pressure losses/gains associated with drag and the piston effect will be discussed in the following subsections.

Aerodynamic Drag

The change in total pressure due to aerodynamic drag (ΔP_{drag}) can be calculated based upon a pressure loss coefficient associated with either the front ($K_{d,front}$) or back ($K_{d,back}$) of a train, as shown in Equations F.8 and F.9 (Vardy, 1996a), respectively. These equations represent the drag effects on the example shown in Figure F.6, where the difference in potential head along the segment is neglected. The drag pressure loss coefficients for either the front or the back of the train (K_d) can be calculated based upon the drag coefficients introduced in Appendix E and the segment (A_{seg}) and train (A_{train}) cross-sectional areas, as shown in Equation F.10 (Vardy, 1996a).

$$\Delta P_{drag,front} = P_3 + \frac{1}{2}\rho v_3^2 - P_2 + \frac{1}{2}\rho v_2^2 = K_{d,front}\frac{1}{2}\rho v_2^2 \tag{F.8}$$

$$\Delta P_{drag,back} = P_2 + \frac{1}{2}\rho v_2^2 - P_1 + \frac{1}{2}\rho v_1^2 = K_{d,back}\frac{1}{2}\rho v_2^2 \quad \text{(F.9)}$$

$$C_d = K_d / \frac{A_{train}}{A_{seg}}(1 - \frac{A_{train}}{A_{seg}})^2 \quad \text{(F.10)}$$

The Piston Effect

The piston effect is characterised by the train induced air flows in tunnels, as the movement of trains within tunnels creates high and low pressure regions at the front and back of the vehicle, respectively (Cross et al., 2015). Gilbert (2013), who studied the aerodynamics of high-speed trains in confined spaces such as tunnels, highlighted how the static pressure changes when a train is passing through a given control volume, as shown in Figure F.7.

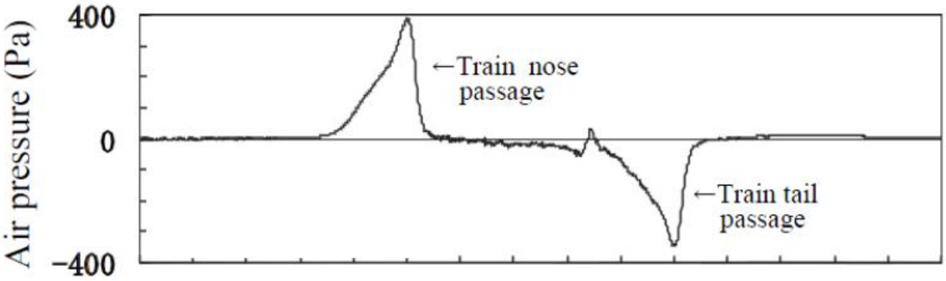

Figure F.7 – Typical static pressure changes at front and back of train as it passes through a partially enclosed space (Gilbert, 2013).

This piston effect is described as the formation of pressure waves within tunnels in the work of Vardy (1996a). The propagation of a wave can be calculated based on the static pressures and air velocities both upstream (point 1 in Figure F.8) and downstream (point 2 in Figure F.8) of the wavefronts, which are formed both at the front and rear of the train. The pressure difference associated with a wavefront can be derived based on the principles of mass and energy conservation for a given line segment (Vardy, 1996b). According to Vardy (1996b), the pressure change due to the piston effect can be calculated based on the upstream (v_1) and downstream (v_2) velocities, as well as on the local speed of sound upstream to the wavefront (c_1), as shown in Equation F.11. The calculation of the velocities developed due to the piston effect are outside the scope of this investigation and can be found in the work of Gilbert (2013).

$$\Delta P_{piston} = P_2 - P_1 = P_1 c_1 (v_2 - v_1) \quad \text{(F.11)}$$

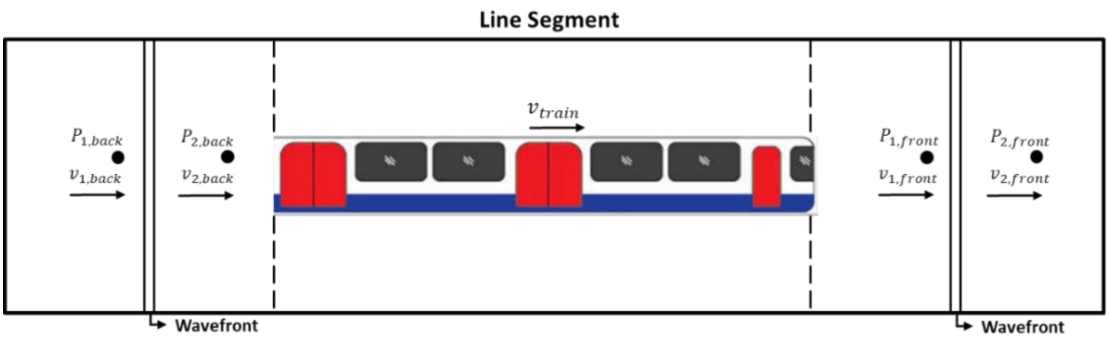

Figure F.8 – Static pressure and flow velocities for piston effect wavefronts (adapted from Vardy, 1996b).

Appendix G – SES Heat Sink Effect

As demonstrated in Chapter 7, temperatures in URs are determined based upon the system geometry, the operation of train, ventilation and mechanical systems, as well as on the heat generation within the network and outside weather conditions. One additional factor that affects the development of tunnel air temperatures is the heat transfer between tunnel air, walls and its surrounding soil. This factor is known as the soil heat sink effect and requires specific modelling, particularly as tunnel air temperatures can influence the soil's capability to either absorb or reject heat. Another singularity of the heat sink effect as opposed to the phenomena analysed by the other subprogrammes is its timescale. The aero and thermodynamic simulations are run on a second-by-second basis, providing short-term results associated with the UR characteristics for a specific moment in time. On the other hand, the heat sink effect must be modelled for a longer period of time, as changes in wall temperatures are a result of prolonged exposure to tunnel air temperatures. Therefore, the heat sink subprogramme must consider daily and annual variations of tunnel air temperature in order to yield the wall surface temperatures for the tunnel structures in the long-term.

This makes both short-term and long-term simulations interdependent, as the aerodynamic and temperature/humidity subprogrammes must consider the wall temperatures when calculating tunnel air temperatures, which are in turn used to predict the wall temperature development in the long-term. Therefore, average values for short-term simulations are used to produce wall temperature values over the long-term, which are then applied to short-term simulations to analyse the UR environment in the worst-case scenario, which corresponds to the hottest week of the hottest year in the simulation. The worst-case scenario is considered in simulations as it represents the critical period with regard to thermal comfort in the LU environment. These calculations rely upon thermal property data for the tunnel structure and its surrounding soil, as well as on temperature data for the soil and ambient air.

Tunnel Wall Temperatures

During short-term SES simulations, the surface temperature distribution along the tunnel walls remains essentially invariant. However, these temperature can vary throughout the year due to variations in the UR system utilisation and ambient conditions. The heat sink calculations consider the thermal inertia and long-term heat transfer to produce a corrected wall surface temperature distribution that can be applied to analyse the UR environment in the short-term. For these calculations to take place, SES utilises airflows and heat loads calculated from short-term simulations, daily and annual temperature variations, as well as thermal properties of the tunnel structure and surrounding soil.

Heat Transfer through Tunnel Walls

As SES assumes the air flow to be fully turbulent and incompressible, the heat transfer through the tunnel walls can be calculated similarly to the pipe flow configuration described in sections 5.4.4 and 5.4.5, which involve internal convection and wall conduction for tubes, respectively. In this case, the tunnelled environment can be modelled as demonstrated in Figure G.1.

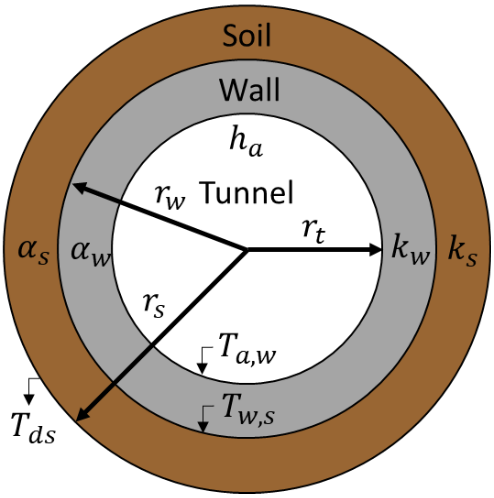

Figure G.1 – Schematic of the tunnel wall, its surrounding soil and their relevant parameters (adapted from Mortada, 2016).

The tunnel wall temperature can be determined by calculating the energy balance between the tunnel air and the surrounding soil, where the boundary conditions relate to the temperature at the air/wall interface ($T_{a,w}$) and the soil deep sink temperature (T_{ds}). In this case, Fourier's law of conduction can be applied for both soil and wall in its differential form, as shown in Equations G.1 and G.2, respectively (Mortada, 2016).

$$\frac{\partial T_w}{\partial t} = \alpha_w \left(\frac{\partial^2 T_w}{\partial r^2} + \frac{1}{r}\frac{\partial T_w}{\partial r}\right) \tag{G.1}$$

$$\frac{\partial T_s}{\partial t} = \alpha_s \left(\frac{\partial^2 T_s}{\partial r^2} + \frac{1}{r}\frac{\partial T_s}{\partial r}\right) \tag{G.2}$$

The initial conditions for modelling assume that both wall and soil are at the deep sink temperature ($T_w = T_s = T_{ds}$). The calculation of the energy balance is then based upon heat transfer across the tunnel wall surface, which assumes that the convective heat transfer from the tunnel air is equal to the conductive heat transfer into the tunnels walls, at steady-state, as shown in Equation G.3. The energy balance for the wall/soil interface is based upon the conductive heat transfer from the tunnel wall into the soil, as shown in Equation G.4. The calculations must then adhere to another boundary condition, which defines that the soil temperature (T_s) tends to the deep sink temperature (T_{ds}) at a point where the distance from the centre of the tunnel is r_s, as shown in Equation G.5.

$$h_a(T_a - T_{a,w}) = \frac{1}{r_t}(T_{a,w} - T_{w,s})\frac{k_w}{\ln(r_w/r_t)} \quad \text{(G.3)}$$

$$(T_{a,w} - T_{w,s})\frac{k_w}{\ln(r_w/r_t)} = (T_{w,s} - T_{ds})\frac{k_s}{\ln(r_s/r_w)} \quad \text{(G.4)}$$

$$\lim_{r \to r_s} T_s = T_{ds} \quad \text{(G.5)}$$

Ambient Temperature Fluctuations

The tunnel air temperature (T_a) must be determined in order for the heat transfer through the tunnel walls to be calculated. The long-term simulations associated with the heat sink effect must consider the fluctuation of tunnel air temperature throughout the year, which is a function of ambient temperature and can therefore be modelled based upon annual temperature amplitude. As mentioned in 7.2.1, the SES model used by TfL is based upon 2006 climate data that is calibrated for the target year in the simulation. The annual ambient temperature amplitudes projected for 2030 and 2050 are, respectively, 6.87°C and 7°C (TfL, 2019b).

Furthermore, the daily ambient temperature amplitude must also be considered, as the wall temperature will vary depending on which period of the day is of interest. As SES simulations are typically carried out to represent the worst-case scenario (1% exceedance temperature), the daily fluctuation can be represented in terms of evening and morning peak temperatures, which are associated with daily service peaks, when train frequency is at 24 TPH, as opposed to 20 TPH for interpeak periods. The evening peak corresponds to the period between 16:00 and 19:00 during weekdays, whereas the morning peak consists of the period from 07:00 to 10:00. For the projected 2030 temperatures, the evening tunnel air peak temperature that would only be exceeded 1% of the time is 27.3°C, whilst the morning peak temperature for the same exceedance criteria is 23.4°C. By considering both annual and daily variations, SES is able to model the heat sink effect and estimate tunnel wall temperatures during peak hours.

Soil and Wall Thermal Properties

The computation of the heat sink effect requires the soil and wall thermal properties to be known. The typical materials used for tunnel linings are either cast iron or concrete, whilst the surrounding soil consists predominantly of London Clay (Revesz, 2017). The material properties used for the tunnel walls, as well as for the typical soil surrounding LU tunnels, have been described in detail by Revesz (2017) and are shown in Table G.1.

Table G.1 – Typical material and soil properties for LU tunnels (adapted from Revesz, 2017).

Material	Thermal Conductivity (W/m*K)	Thermal Diffusivity (m^2/s)	Density (kg/m^3)	Specific Heat Capacity (J/kg*K)
Cast Iron	52	1.7×10^{-7}	7272	420
Concrete	1.1	5.2×10^{-7}	2400	880
London Clay	1.3	8.5×10^{-7}	1920	797

Appendix H – Inputs for Pumping Energy Calculations

In order to calculate the total pumping energy consumption for the heat network, it is necessary to take into account the pressure losses for the pipework, including fittings, as well as the loss of pressure associated with specific components such as valves and heat exchangers. The pressure losses from components were determined based on the design values of the Bunhill WHR System, and the pressure losses associated with valves and other network devices were obtained from the works of Milnes (2010) and Davies et al. (2019a). These assumed pressure loss values are listed in Table H.1.

Table H.1 – Pressure losses associated with heat exchangers and valves assumed for the heat network.

Component/Valve	Location	No. of Items	Unitary ΔP (kPa)	Total ΔP (kPa)
Condenser	Heat Pump	1	140	140
PHE	Substations	5	20	100
Strainers	Heat Network	3	45	135
Motorised Valves	Heat Network	1	100	100
Balancing Valves	Heat Network	1	45	45
			Total	**520 kPa**

The fittings considered for all branches of the network and their associated head loss coefficients (K) are listed in Tables H.2 to H.9. These were obtained from the work of Milnes (2010) and the head loss coefficients associated with pipe expansion and reduction, assuming a squared fitting, can be calculated with Equations H.1 and H.2, respectively.

$$K_{expansion} = (1 + 0.8f_{in})\left[1 - \left(\frac{D_{in}}{D_{out}}\right)^2\right]^2 \qquad \text{(H.1)}$$

$$K_{reduction} = (0.6 + 0.48f_{in})\left(\frac{D_{in}}{D_{out}}\right)^2\left[\left(\frac{D_{in}}{D_{out}}\right)^2 - 1\right] \qquad \text{(H.2)}$$

Table H.2 – Head loss coefficients for heat network branch D-05.

Fitting Item	Location	No. of Items	K-value	Total K-value per item
Inlet Pipe (Bellmouth)	Substation	1	0.05	0.05
90° Bend (Short Radius)	Macclesfield Road	2	0.75	1.5
Butterfly Valve (Fully Open)	Substation	1	0.3	0.3
Non-return Valve	Substation	1	1	1
Outlet Pipe (Bellmouth)	Substation	1	0.2	0.2
			Total	**3.05**

Table H.3 – Head loss coefficients for heat network branch E-04.

Fitting Item	Location	No. of Items	K-value	Total K-value per item
Inlet Pipe (Bellmouth)	Substation	1	0.05	0.05
90° Bend (Short Radius)	Lever Street, King Square	4	0.75	3
Butterfly Valve (Fully Open)	Substation	1	0.3	0.3
Non-return Valve	Substation	1	1	1
Outlet Pipe (Bellmouth)	Substation	1	0.2	0.2
			Total	**4.55**

Table H.4 – Head loss coefficients for heat network branch C-03.

Fitting Item	Location	No. of Items	K-value	Total K-value per item
Inlet Pipe (Bellmouth)	Substation	1	0.05	0.05
90° Bend (Short Radius)	King Square	8	0.75	6
Butterfly Valve (Fully Open)	Substation	1	0.3	0.3
Non-return Valve	Substation	1	1	1
Outlet Pipe (Bellmouth)	Substation	1	0.2	0.2
			Total	**7.55**

Table H.5 – Head loss coefficients for heat network branch C-01.

Fitting Item	Location	No. of Items	K-value	Total K-value per item
Inlet Pipe (Bellmouth)	Substation	1	0.05	0.05
Butterfly Valve (Fully Open)	Substation	1	0.3	0.3
Non-return Valve	Substation	1	1	1
Outlet Pipe (Bellmouth)	Substation	1	0.2	0.2
			Total	**1.55**

Table H.6 – Head loss coefficients for heat network branch D-E.

Fitting Item	Location	No. of Items	K-value	Total K-value per item
90° Bend (Short Radius)	Point E	2	0.75	1.5
			Total	**1.5**

Table H.7 – Head loss coefficients for heat network branch B-C.

Fitting Item	Location	No. of Items	K-value	Total K-value per item
Tee	Point C	2	1	2
Pipe Reduction BC-03	Point C	1	3.02	3.02
Pipe Expansion 03-BC	Point C	1	0.42	0.42
			Total	**5.44**

Table H.8 – Head loss coefficients for heat network branch B-D.

Fitting Item	Location	No. of Items	K-value	Total K-value per item
Tee	Point D	2	1	2
Pipe Reduction BD-DE	Point D	1	1.77	1.77
Pipe Expansion DE-BD	Point D	1	0.32	0.32
Pipe Reduction BD-05	Point D	1	0.38	0.38
Pipe Expansion 05-BD	Point D	1	0.09	0.09
			Total	**4.56**

Table H.9 – Head loss coefficients for heat network branch A-B.

Fitting Item	Location	No. of Items	K-value	Total K-value per item
Inlet Pipe (Bellmouth)	Heat Pump	1	0.05	0.05
90° Bend (Short Radius)	Moreland Street	4	0.75	3
Pipe Reduction AB-BC	Point B	1	0.20	0.20
Pipe Expansion BC-AB	Point B	1	0.04	0.04
Pipe Reduction AB-BD	Point B	1	5.38	5.38
Pipe Expansion BD-AB	Point B	1	0.52	0.52
Tee	Point B	2	1	2
Butterfly Valve (Fully Open)	Heat Pump	1	0.3	0.3
Non-return Valve	Heat Pump	1	1	1
Outlet Pipe (Bellmouth)	Heat Pump	1	0.2	0.2
			Total	**12.70**